The Dissertation Committee for Lindsay Lowe Worthington Certifies that this is the approved version of the following dissertation:

New Geophysical Parameters for Understanding the Evolution of the St. Elias Orogen, Southern Alaska

Committee:

Sean P.S. Gulick, Supervisor

Harm J.A. van Avendonk

Terry L. Pavlis

Brian K. Horton

Mark Cloos

Luc L. Lavier

New Geophysical Parameters for Understanding the Evolution of the St. Elias Orogen, Southern Alaska

by

Lindsay Lowe Worthington, B.A.

Dissertation

Presented to the Faculty of the Graduate School of

The University of Texas at Austin

in Partial Fulfillment

of the Requirements

for the Degree of

Doctor of Philosophy

The University of Texas at Austin

December 2010

Dedication

To my family.

Acknowledgements

Many people devoted their time and energy to help make this work possible. Thank you to my advisor, Sean Gulick, for his boundless energy and encouragement. I have learned so much from his abilities to remain calm and positive under pressure, to approach science with enthusiasm and to always find time to provide support to his many students. I don't think I will ever fully grasp how fortunate I have been to have someone like Sean as my advisor. Thank you to my committee members: Terry Pavlis, for his leadership and vision in guiding STEEP research, for his work in helping prepare the included manuscripts for publication, for his encouragement and hospitality whenever I've traveled to El Paso; Harm van Avendonk, for his patience in teaching me the art of refraction seismology, and his encouragement and steady attitude whenever I came running with a perceived crisis; Brian Horton, for his reminders to 'consider the skeptic,' his thorough comments on this dissertation and lively discussion during STEEP group meetings at UTIG; Mark Cloos, whose comments and questions kept me questioning my assumptions; and Luc Lavier, for his insight into broader tectonic problems and his candid career advice. I appreciate their willingness to serve on my committee and I hope that I can become a worthy colleague.

Many other scientists have served as mentors during my graduate career. I thank: Gail Christeson for being a role model in work ethic, technical know-how, and sarcasm; Ron Bruhn for taking me under his wing high in the bear-infested Don Miller Hills; Ken Ridgway for his encouragement and interest in my work; and Bix Magnani for showing me how much fun science can be.

My friends have been such an important part of my life in Austin. The commiseration and camaraderie of my fellow graduate students has been invaluable. I especially thank Bobby Reece who has endured my tears and my rough drafts like a champ. His work ethic and genuine excitement about our field is inspiring. I cannot imagine these last few years without him. I also thank the ultimate Frisbee community in Austin, UT women's ultimate and Showdown, for support, encouragement, laughs upon laughs, downtown adventures and regional championships that helped me forget about my studies for a while.

My family has been so supportive. My mother always told me I could be anything I wanted to be…I don't know if she had this in mind. Doug, who understood my interest in math, and for his late night homework-checking and science project-helping. My grandparents, Morrie and Marian, who are inspirations for their hard-work and sense of humor. My sisters, Amy and Annie, I'm glad to share so many memories. My father, step-mom and my brothers for their encouragement.

Lastly, and most importantly, I want to thank my husband, Travis. He has been my steadfast cheerleader and never doubted me, even when I doubted myself. He has taken care of me and our home with so much love. Thank you.

New Geophysical Parameters for Understanding the Evolution of The St. Elias Orogen, Southern Alaska

Publication No._____

Lindsay Lowe Worthington, Ph.D.

The University of Texas at Austin, 2010

Supervisor: Sean P.S. Gulick

The St. Elias Orogen is the result of oblique collision and flat-slab subduction in the Gulf of Alaska between North America (NA) and the Yakutat microplate (YAK). Extensive glaciation and a complex tectonic environment make this region a unique case study in which to examine the details of terrane accretion and the possible coupled influence of climate and tectonic drivers on the structural and topographic evolution of an orogenic wedge. The dataset for this project includes: 3 multi-channel seismic reflection surveys (~4000 km total seismic reflection data) and a ~450 km-long wide-angle seismic refraction profile.

Reflection seismic profiles across the offshore YAK-NA deformation front, provide constraints for quantifying Pleistocene deformation recorded in the glaciomarine Yakataga formation. Growth strata and kinematic fold analysis allow comparison of relative timing of fault activity, which reveals temporal and spatial shifting of

deformation within the margin towards the onshore eastern corner of the orogen. This information is important not only for the development of regional tectonic models, but also for understanding how climatic shifts may have affected the evolution of margin architecture during Pleistocene glacial-interglacial periods.

Joint tomographic inversion of coincident reflection and refraction profiles constrains YAK crustal velocity and thickness. The offshore YAK crust ranges in thickness from 15 to 35 km, considerably thicker than normal oceanic crust. The crustal thickness and velocity structure support an oceanic plateau origin for the YAK microplate. Crustal velocity and structure are continuous across the YAK shelf except for a regional dip of the top of YAK crust of ~3° to the west. Moho arrivals across the profile do not mimic the dipping trajectory of the basement, indicating that the offshore YAK crust is doorstop-shaped, thinning in the convergence direction. This geometry leads to the following implications for the YAK-NA collision: first, uplift and deformation have intensified through time as successively thicker, more buoyant YAK crust attempts to subduct; second, current topography, exhumation and deformation patterns are partially controlled by underlying crustal geometry of converging YAK crust.

Table of Contents

List of Tables

List of Figures

Chapter 1: Introduction

The Gulf of Alaska margin is one of the most tectonically active regions in the world due to the combined interactions between the Pacific and North American tectonic plates and the Yakutat microplate (Figure 1.1). The margin forms a corner geometry where relative motion of the Pacific Plate with respect to North America transitions from right-lateral strike-slip motion on the Fairweather Fault to convergence at the Aleutian subduction zone (Figure 1.1). This transition is complicated by oblique convergence of the allochthonous Yakutat microplate (Lahr and Plafker, 1980; Plafker, 1987).

Convergence between the Yakutat microplate and North America has resulted in more than 10 Myr of flat-slab subduction. The flat-slab segment projects ~500 km landward from the Yakutat-North America deformation front, an offshore-onshore thrust across the Yakutat shelf (Figure 1.1), at a subduction angle of ~6° (Eberhart-Phillips et al., 2006; Gulick et al., 2007) causing regional uplift across southern Alaska. The Yakutat-North America plate interface is also the site of major earthquakes, including the M9.2 Alaska earthquake in 1964 (Shennan, 2009; Shennan et al., 2009) (Figure 1.2).

The Yakutat-North America margin is also the site of the coastal St. Elias Mountains. A relationship between YAK-NA convergence and St. Elias orogenesis is often inferred, though the details of this relationship are unclear. The St. Elias orogen displays the highest coastal relief on the planet: Mt. St. Elias (Figure 1.1) rises more 5500 m above sea level over a horizontal distance of 25 km (Gulick et al., 2007). The orogen

also boasts the highest concentration of peaks higher than 4300 m in North America (Meigs and Sauber, 2000). Offshore deformation is concentrated within the Pamplona Zone fold-thrust belt that comprises the western portion of the offshore Yakutat microplate and the frontal St. Elias orogenic wedge (Bruns, 1983b; Plafker, 1987) (Figure 1.3).

The St. Elias orogen is the most extensively glaciated active mountain belt in the world (Spotila and Meigs, 2004) and is home to two of the world's largest temperate glaciers, the Bering Glacier and the Malaspina Glacier (Figure 1.3). Glacial troughs up to 150 km long and 15 km wide are present on the coastal plain and continental shelf, influencing the construction of the continental terrace by glaciomarine sedimentation that began by ~5.5 Ma (Carlson, 1989; Lagoe et al., 1993; Prueher and Rea, 1998; Rea and Snoeckx, 1995). Studies of sedimentation rates in the Gulf of Alaska margin (e.g., Jaeger et al., 1998; Sheaf et al., 2003; Spotila et al., 2004) indicate that the orogen is eroding at the highest rates on earth, averaging 0.76 mm/year over the last 6 million years (Lagoe et al., 1993) and ~5.1 mm/yr during the Holocene (Sheaf et al., 2003).

The Gulf of Alaska margin and the St. Elias orogen serve as a natural laboratory for gaining insight into tectonic processes and climate-tectonic interactions for several reasons. First, more than 10 km of marine sediments record tectonic and climatic signatures during the last ~6 Ma, since the onset of alpine glaciation in the region (Lagoe et al., 1993; Lagoe and Zellers, 1996; Rea and Snoeckx, 1995). This record provides a unique opportunity to study climatic and tectonic interaction and feedback. Investigation of structural evolution in the Gulf of Alaska is especially compelling in light of evidence

revealing feedback connections between mass redistribution by erosional/depositional processes and orogenic wedge development (e.g., Hilley et al., 2004; Malavieille, 2010; Pavlis et al., 1997; Roe et al., 2006; Simpson, 2010; Whipple, 2009; Whipple and Meade, 2006). Second, southern Alaska is composed of several exotic, geologically distinct, tectonostratigraphic terranes (e.g., Bruns, 1983a; Plafker, 1987; Plafker et al., 1994) (Figure 1.2). Current Yakutat-North America convergence may act as a modern analog for processes that have constructed much of the continental crust in southeast Alaska. Third, the margin may be the only modern example of an oceanic plateau collision (Christeson et al., 2010; Eberhart-Phillips et al., 2006; Gulick et al., 2007; Pavlis et al., 2004) and is a rare example of flat-slab subduction in an accretionary margin. Further study of tectonic and structural responses provides insight into the combined effects of these margin characteristics.

1.1. BACKGROUND AND STATE OF KNOWLEDGE

1.1.1 Yakutat Geology

The unsubducted Yakutat microplate is bounded on the south by the Transition fault, on the west by the Kayak Island Zone suture, to the east by the Fairweather transform fault and on the north by the Chugach-St. Elias fault (Figure 1.3). Yakutat basement west of the Dangerous River Zone (DRZ) is a Paleogene-early Eocene oceanic plateau, based on offshore dredging of basalts at the continental slope and combined results of geophysical studies that constrain Yakutat thickness and crustal velocity

structure (Christeson et al., 2010; Eberhart-Phillips et al., 2006; Ferris et al., 2003; Gulick et al., 2007; Plafker, 1987) (Figure 1.3). East of the DRZ, outcrop studies and offshore dredging results indicate that Yakutat basement may be a continental fragment, though crustal structure at depth and total thickness is unknown (Plafker, 1987) (Figure 1.3).

The >15 km thick Yakutat Cenozoic sedimentary cover west of the DRZ consists of the St. Elias foreland fold-thrust belt between the Pamplona Zone deformation front and the Chugach-St. Elias fault (Figure 1.3). These rocks are primarily siliciclastic marine and glaciomarine strata interbedded with volcanics and coal beds (Plafker et al., 1994). The youngest Yakataga Formation forms more than 6 km of the cover sequence and dates from the onset of St. Elias glaciation in the late-Miocene (~5.5 Ma) to the present (Plafker et al., 1994).

1.1.2 Regional Tectonics

The Yakutat terrane was excised from western Canada (Plafker, 1987; Plafker et al., 1994) or the United States Pacific Northwest (Bruns, 1983a), when the Queen Charlotte-Fairweather transform stepped inboard, forming the eastern boundary of the Yakutat microplate (Figure 1.3). Yakutat-North America convergence began when the leading edge of the microplate encountered the Aleutian trench ~20-10 Ma (Plafker et al., 1994; Rea and Snoeckx, 1995). In the last ~6 Ma, the Yakutat terrane has been lodged into the “subduction corner,” adjacent to the Bering Glacier (Figure 1.1), constructing the present high topography and initiating extensive alpine and tidewater glaciation (Lagoe et

al., 1993; Lagoe and Zellers, 1996; Rea et al., 1995; Rea and Snoeckx, 1995; Zellers, 1995).

Prior to YAK convergence, southern Alaska experienced the collision and accretion of multiple terranes during the early Mesozoic through the early Eocene (Bruns, 1983a; Lahr and Plafker, 1980; Plafker, 1987; Plafker et al., 1994) (Figure 1.4). These collisions were part of the larger terrane accretion process that has formed the North American-Canadian Cordillera (e.g., Coney et al., 1980; Dickinson, 2004). Two of these previously accreted terranes, the Chugach and Prince William (Figure 1.4), are a subduction complex welded onto the continent when the Kula-Farallon ridge subducted beneath the margin, resulting in high temperature, low pressure metamorphism (Pavlis et al., 2004; Plafker et al., 1994). These metamorphic assemblages provide a backstop for the current subduction of the Yakutat microplate; accretion and upper plate deformation associated with Yakutat subduction is limited to areas south and east of this backstop. The distinctive sedimentary cover of the Yakutat terrane, along with the presence of the metamorphic backstop allows a clear definition of the onshore portion of the Yakutat-North America suture, locally identified as the Chugach-St. Elias fault, throughout most of the orogen (Bruhn et al., 2004; Pavlis et al., 2004) (Figure 1.3). Offshore, the suture is not clearly defined due to high sediment load and complex fault morphology (Pavlis et al., 2004; Plafker et al., 1994), though it may be located in the offshore Kayak Island Zone (Figure 1.3). Currently, the active offshore Yakutat-North America plate boundary is located on the décollement that daylights at the eastern extent of the Pamplona Zone. This geometry implies that the St. Elias foreland is a wide, flat thrust zone between the

Chugach-St. Elias fault and the Pamplona Zone deformation front. The Yakutat-Pacific boundary is located on the currently inactive Transition Fault (Gulick et al., 2007).

GPS data characterize current relative plate motion in the YAK-NA margin, indicating that the Yakutat microplate convergences with North America at ~47 mm/yr (Elliot et al., 2010) (Figure 1.1). This rate of convergence is similar to the Pacific-North America convergence vector of ~50 mm/yr, but the direction of plate motion is ~5 degrees more easterly (Elliott et al., 2010; Fletcher and Freymueller, 1999). Accommodation of Yakutat-North America convergence remains unconstrained with respect to which geologic structures are affected and how deformation proceeds. Euler pole models and associated reconstructions (Pavlis et al., 2004) for plate motions conclude that the orogen has absorbed ~240-300 km of convergence during the last 6 Ma. In this reconstruction, the offshore Pamplona Zone absorbs only a small fraction of the total convergence, suggesting that the bulk of neotectonic deformation occurs farther towards the interior of the margin, west of Kayak Island (Bruhn et al., 2004; Pavlis et al., 2004). Restorations based on surface geology and offshore seismic data yield shortening estimates over the last 6 Myr ranging from 36 km (Wallace, 2008) to 82 km (Meigs et al., 2008). These estimates highlight a discrepancy between observed and predicted convergence, leaving significant shortening unaccounted for across the margin.

1.1.3 Glacial History and Climate Impacts on Orogenesis

The glacial history of the Gulf of Alaska margin has been constructed through a combination of surface outcrop sampling (e.g., Lagoe et al., 1993; Lagoe and Zellers,

1996), subsurface coring (White et al., 1997), scientific drilling (Prueher and Rea, 1998; Rea et al., 1995; Rea and Snoeckx, 1995) and industry well-cuttings (Lagoe et al., 1993; Lagoe and Zellers, 1996; Zellers, 1995). A summary of glacial history and the associated sediment record is shown in Figure 1.5. Alpine glaciation in the margin may have initiated as early as ~7 Ma (Lagoe et al., 1993) and was well underway by 5.5 Ma (Lagoe et al., 1993; Rea and Snoeckx, 1995; White et al., 1997), when elevation of the Chugach-St. Elias mountain belt was sufficient to trap precipitation from storms generated in the Gulf of Alaska. Initial onset of tidewater glaciation, Lagoe et al.'s (1993) "Glacial Interval A", is linked to the appearance of ice-rafted debris (IRD) at DSDP Site 178 from 4.3-2.4 Ma (Lagoe et al., 1993) and at ODP Site 887 from ~5 Ma (Krissek, 1995) to 4.3 Ma (Rea and Snoeckx, 1995) (Figure 1.5).

A reduction in glaciomarine sedimentation correlating with the ~4.5-2.8 Mid-Pliocene Warm Period (MPW) (Shackleton et al., 1995) is observed in marine and non-marine records, though timing varies between different locales in the Gulf of Alaska region. In outcrop and continental shelf samples, the MPW lasts from 4.2 Ma to 3.5-3.0 Ma (Lagoe and Zellers, 1996). At ODP Site 887, the MPW lasts from 3.6-2.8 Ma (Rea et al., 1995; Rea and Snoeckx, 1995). Renewed onset of intense glaciation after ~3 Ma, "Glacial Interval B" (Lagoe et al., 1993), is characterized by an increase in IRD accumulation at 2.6 Ma within deep-sea records (Lagoe et al., 1993; Prueher and Rea, 1998) and by thick successions (22 m) of diamictite in outcrop (Lagoe et al., 1993).

At ~1 Ma, the rate of terrigenous sedimentation doubles, likely due to widespread glacial advance associated with the Mid-Pleistocene Transition that carved a series of U-

shaped sea valleys to the shelf edge (Carlson, 1989; Lagoe et al., 1993; Rea and Snoeckx, 1995). This glacial intensification is referred to as Glacial Interval C (Berger et al., 2008a). Since the onset of Glacial Interval C, a series of 100 kyr glacial-interglacial cycles characterize the late Pleistocene climate signal, with the Last Glacial Maximum estimated at ~10 ka in the Gulf of Alaska (Mann and Peteet, 1994). Recent high-resolution seismic reflection profiles in the Bering Trough image glacial erosion surfaces that extend to the shelf edge, likely correlating with widespread Pleistocene glacial advances associated with the onset of Glacial Interval C (Berger et al., 2008a).

Climatic influence on the width, structural style and distribution of deformation in mountain belts is well established through analog, numerical and analytical modeling studies based on critical wedge theory (Whipple, 2009). Generally, increase in erosional intensity through glacial or fluvial processes is predicted to accelerate rock uplift and decrease orogen width and relief (Roe et al., 2006; Whipple and Meade, 2004). Based on apatite (U-Th)/He thermochronometry, in conjunction with offshore seismic data and modeling results, Berger et al. (2008a) proposed that a structural reorganization of the St. Elias orogen occurred, associated with the onset of Glacial Interval C and the Mid-Pleistocene Transition. The proposed structural reorganization includes initiation of a large-scale backthrust onshore and deactivation of faults in the offshore frontal portion of the wedge (Figure 1.6). However, offshore faulting has remained active in the St. Elias, primarily associated with the Pamplona Zone deformation front (Bruns and Schwab, 1983; Chapman et al., 2008; Plafker et al., 1994). Investigating the details of the offshore response to climatic impact in the St. Elias orogen is one of the goals of this dissertation.

Recent modeling (Malavieille, 2010; Simpson, 2010) suggests that the extent of active faulting and folding in the frontal wedge is highly dependent on the details of mass redistribution by climate drivers and the magnitude of incoming sediment load.

1.1.4 Flat-Slab Subduction

The Yakutat segment is the only site along the Alaskan subduction zone experiencing active orogenesis, and is associated with a volcanic gap in the Aleutian system west of the Wrangell Mountains (Figure 1.1). The subducted area of the Yakutat terrane is known from seismic refraction (Brocher et al., 1994; Fuis et al., 2008), earthquake tomography (Eberhart-Phillips et al., 2006) and receiver function studies (Ferris et al., 2003) (Figure 1.2; Figure 1.7). Yakutat crust is imaged as an anomalous low-velocity unit up to ~15-20 km thick below Prince William Sound (Brocher et al., 1994) and at its northern subducted extent, ~150 km deep below the Alaska Range (Ferris et al., 2003). A recent tomographic study of the unsubducted Yakutat microplate offshore determines that Yakutat crustal thickness and seismic velocity structure are consistent with an oceanic plateau origin for the microplate (Christeson et al., 2010). These data taken together corroborate previous suggestions that the Yakutat terrane is an oceanic plateau (Bruhn et al., 2004; Eberhart-Phillips et al., 2006; Gulick et al., 2007; Pavlis et al., 2004).

A wide thrust zone, mountain building and absence of a volcanic arc are qualities shared with other flat-slab settings in which anomalously thick crust subducts along continental margins (von Huene and Ranero, 2009). Many of these flat-slab occurrences

are associated with an oceanic plateau (Gutscher et al., 2000). Several examples are well documented in the literature: the potential Inca Plateau under Peru (Gutscher et al., 2000); the Cocos Ridge below Costa Rica (Ranero et al., 2007; Walther, 2003); the Choco Block in northwest Columbia (Gutscher et al., 2000); and the Nazca Ridge off the Chilean coast (Ranero et al., 2006). Yakutat subduction, however, differs from these examples in three important ways. First, the Yakutat margin displays extremely high relief topography near the subduction front; the St. Elias mountains reach elevations > 5000 m within 25 km of the southern Alaska coast. Second, a broad accretionary complex has developed in the Gulf of Alaska margin, while the aforementioned examples are typified by erosive convergent settings (Gutscher et al., 2000; von Huene and Ranero, 2009). Third, the flat segment of Yakutat subduction maintains a shallow angle for more than ~500 km and may contribute to high relief of the Alaska Range at its inboard extent (Figure 1.7). In this way, Yakutat subduction and related tectonism may be analogous to Laramide style uplift in the western United States during the latest Cretaceous and early Cenozoic (i.e., Livaccari et al., 1981). The Gulf of Alaska margin, therefore, provides a unique opportunity to investigate geodynamic and orogenic processes related to oceanic plateau subduction in an accretionary margin and may serve as a modern example of Laramide-style orogeny.

1.1.5 Deformation and Orogenesis

Yakutat-North America convergence drives deformation at two spatial scales. At a regional scale, flat-slab subduction and collision of the Yakutat oceanic plateau is

responsible for high topography across parts of southern Alaska (Figure 1.8), as well as having possible far-field effects such as seismicity in the northern Canadian Cordillera foreland belt (Mazzotti and Hyndman, 2002), upper mantle flow towards northern Canada (Mazzotti et al., 2008) and Anatolian-style westward extrusion of Alaskan continental material toward the Bering Sea (Mackey et al., 1997; Redfield et al., 2007).

At a local scale, high relief of the St. Elias Mountains is superimposed on the broader, regional uplift. The highest topography and highest long-term exhumation rates in the St. Elias Mountains are concentrated north of the Malaspina Glacier, at the syntaxis formed by the corner geometry of the Fairweather and Chugach-St. Elias faults (Spotila and Berger, 2010) (Figure 1.9). This corner is also near the onshore extension of the Dangerous River Zone (DRZ), traditionally interpreted as a crustal boundary of the Yakutat microplate between oceanic plateau to the west and a continental fragment to the east (Plafker et al., 1994). In this interpretation, the Yakutat microplate acts as a micro-continental indentor attached to an oceanic plateau colliding with southern Alaska and creating the orogen. However, Yakutat crustal structure and thickness are virtually unconstrained east of the DRZ and across the offshore extent, so the details of collisional orogenesis remain unresolved.

1.2. DATA

A 2008 seismic reflection-refraction survey serves as the primary dataset to help accomplish the research objectives put forth. Supplementary datasets include additional

seismic reflection and refraction profiles across the margin and high-resolution bathymetric data of the continental shelf and slope.

1.2.1 2008 STEEP seismic survey

In 2008, ~1250 km of multi-channel seismic (MCS) reflection data and ~500 km of wide-angle seismic refraction data were acquired in the Gulf of Alaska as part of the St. Elias Erosion and Tectonics Project (Figure 1.10). For the purposes of this dissertation, the primary survey targets included the offshore Yakutat-North America deformation front, the offshore St. Elias orogenic wedge, known as the Pamplona Zone fold-thrust belt, and the DRZ. The survey also targeted the Transition Fault (results presented in Christeson et al., 2010) and the offshore zone of seismicity in the Pacific Plate known as the Gulf of Alaska Shear Zone (Gulick et al., 2007; preliminary STEEP results presented in Reece et al., 2009).

Acquisition parameters for the seismic reflection data included a seismic source of 36 Bolt airguns with a total volume of 6600 cubic inches fired every 50 m. Receivers were located in an 8 km long solid streamer at 12.5 m spacing. Common midpoint spacing was 6.25 m. Seismic data processing included trace regularization, normal move-out correction, bandpass filtering, muting, stacking and frequency-wave number migration using Paradigm Geophysical FOCUS software (Appendix B details the seismic data processing work flow). Vertical resolution at the seafloor for this dataset is ~30 m.

Wide-angle reflection and refraction data was recorded along two profiles: STEEP01 is oriented west-east, crossing the offshore Yakutat microplate from near the

Bering Glacier to east of the DRZ (Figure 1.10); STEEP02 is oriented north-south and crosses the Yakutat shelf, the Transition Fault and the adjacent Pacific Plate (Figure 1.8). For STEEP01, 25 ocean bottom seismometers (OBS) were deployed at ~15 km spacing across the profile. Data acquisition was simultaneous for the MCS and wide-angle data across STEEP01, with shot spacing of 50 m. Data was recovered from 21 instruments. Standard OBS data processing included corrections for clock drift during deployment and application of a Butterworth filter with bandwidth of 3-15 Hz. Processing and survey details for STEEP02 are presented in Christeson et al. (2010).

1.2.2 Supplementary seismic data

Locations of a 1975 USGS survey and a 1979 survey by Western Geophysical are shown in Figure 1.11. These seismic profiles provide ~30 m vertical resolution and reliably image up to 4 s (two way travel time) of the subsurface, ~3.5 km at 1750 m/s seismic velocity. These profiles image major faults, fault-related folds and unconformities, roughly illustrating stratigraphic and structural relationships along the margin (Bruns, 1983a, 1985; Bruns and Schwab, 1983; Lagoe et al., 1993; Zellers, 1995).

In 2004, a high-resolution reflection survey was collected as a site investigation for two IODP drilling proposals aboard the R/V *Maurice Ewing*. These profiles imaged the subsurface at ~5 m vertical resolution and reliably penetrate 1.5-1.75 s (~1.3 km). These data image a series of glacial erosion surfaces and depositional regimes associated with glacial-interglacial cycles from the Last Glacial Maximum to present (Gulick et al., 2004b).

1.2.3 High-resolution bathymetry

In 2004, more than 162,000 km^2 of high-resolution (~100 m^2) multibeam sonar data were collected along the base of the Yakutat slope in the Gulf of Alaska in support of the United Nations Law of the Sea extended continental shelf investigation. Data were collected aboard the R/V *Kilo Moana* and post-processed at the University of New Hampshire Center for Coastal Studies (Gardner et al., 2006). Vertical accuracy is ~0.3-0.5% of the water depth.

1.3. DISSERTATION DESIGN

The western Gulf of Alaska is an ideal candidate for the study of structural interactions, evolution of margin architecture and geodynamic processes in a glacially impacted orogen driven by flat-slab subduction and collision. These broad, overriding questions are addressed in this dissertation in three, self-contained studies detailed in Chapters 2, 3 and 4. Chapter 2 addresses current margin architecture and structural interactions by identifying the loci of deformation within the offshore YAK fold-thrust belt and developing an integrated tectonic model. Chapter 3 investigates the coupled structural and stratigraphic evolution of the margin by quantifying macro-scale strain histories in the context of variable tectonic-climatic influence. Chapter 4 focuses on deeper structural interactions within the margin and the possible influence of YAK-NA convergence on the development of the Chugach-St.Elias orogen by modeling crustal structure across the offshore Yakutat microplate.

Chapter 2: Localized deformation in the western YAK block; Implications for offshore tectonics. Chapter 2 (published as Worthington et al., 2008) investigates the extent that active deformation within the offshore Yakutat leading corner, the region from the Kayak Island fault zone (KIZ) to the Pamplona fold and thrust belt (PZ), accommodates YAK-NA convergence. High-resolution seismic reflection profiles imaging the Kayak Island fault zone, the Bering Trough, the Khitrov Ridge, and industry seismic profiles imaging the northeastern extent of the PZ were interpreted for signs of neotectonic deformation, including stratal offset due to faulting, the presence of growth strata on the forelimb or backlimb of folds, and stratal offset at or near the seafloor. These interpretations were compared with earthquake locations and topographic disruption due to active faulting observed on high-resolution bathymetry in order to predict interaction among active offshore structures within a regional tectonic context. The primary contribution of Chapter 2 is a new tectonic framework for active tectonics on the offshore Yakutat shelf.

Chapter 3: Quantification of deformation histories and effects of glacially-derived sediment loading within YAK-NA margin. Chapter 3 (in press as Worthington et al.) constrains the timing and amount of shortening that has occurred across structures offshore of the orogen and explores the extent to which glacial processes have caused temporal and spatial shifting of deformational patterns within the margin. The study includes three primary components:

(1) Interpretation of 2008 STEEP seismic profiles across the offshore Pamplona Zone and integration of this dataset with existing

supplementary seismic data. Key interpretation targets are derived from multiple sources and include: biostratigraphic analysis by Zellers (1995) for the contact between glacial and pre-glacial strata; major regional unconformities created by glacial advance-retreat cycles during Glacial Interval C (Berger et al., 2008a); and the sediment-basement contact, which had not been visible until the acquisition of deeper penetrating STEEP seismic data in 2008. Sediment thickness maps were created from these interpretations, providing insight into how offshore depositional patterns evolved during St. Elias glaciation.

(2) The STEEP seismic profiles across the offshore Yakutat-North America deformation front and the Bering Trough were also analyzed for growth strata. In addition, I determined fault geometries in order to create reconstructions across the profiles and determine shortening in the offshore orogenic wedge. Reconstructions were performed using 2-D Move software through a combination of forward and inverse modeling. The final reconstruction provided the best fit given geometric constraints by the seismic reflection data at depth.

The results of Chapter 3 provide vital constraints for understanding the margin's structural evolution in response to varying climatic and tectonic interactions. Calculations for total shortening across the offshore margin help describe how deformation within the St. Elias orogen is distributed during Yakutat-North America convergence. Changing

patterns of fault activity compared with depocenter locations during different glacial periods suggest a linked relationship between active faulting and focused deposition.

Chapter 4: Deep crustal structure of the Yakutat block and related geodynamic processes. Chapter 4 presents a seismic velocity model for the offshore Yakutat crust, overlying sedimentary cover, and the uppermost mantle. The study includes interpretation of seismic travel-time arrivals for 21 ocean bottom seismometers and four land-based broadband seismic stations. Coincident seismic reflection data provide additional travel-time constraints for the sediment-basement contact. These two datasets were included in a joint tomographic inversion to determining the geometry and composition of the offshore Yakutat microplate.

Chapter 4 presents the first tomographic profile across the offshore accretionary prism and the DRZ. The profile also images the updip extent of the Yakutat flat-slab subduction segment beneath Bering Glacier. The results from Chapter 4 lead to a new model for how Yakutat crustal structure and composition affects the evolution of orogenesis in the St. Elias margin, perspectives on the extent of accretion and subduction during Yakutat-North America convergence and constraints for the pre-collisional history of the Yakutat microplate.

1.4. PUBLISHED RESULTS

Chapters 2 and 3 have been previously published in peer-reviewed publications with co-authors S. Gulick and T. Pavlis. Each of the elements for these chapters is my own original work. My co-authors provided a portion of previously acquired data,

funding, software and software assistance and revisions to the manuscripts. For Chapter 2, I interpreted and integrated the multiple reflection seismic surveys, presented and developed a neotectonic model for deformation in offshore St. Elias Mountains in Alaska. For Chapter 3, I was involved in planning the survey geometry for acquisition of seismic reflection and refraction data. I participated in the acquisition cruise and processed all the profiles from this survey presented in Chapter 3 and in Appendix B. I traveled to El Paso to collaborate with T. Pavlis on restorations of depth-converted seismic sections using the 2D Move software. I performed forward and inverse modeling of these sections. The reconstructions and fault geometries presented in this dissertation are the result of multiple iterations that best fit the data.

1.5. SUMMARY

The purpose of this dissertation is to resolve major issues regarding evolution of oblique convergence in a glaciated orogenic margin. The study primarily focuses on the offshore tectonic and structural effects of convergence and mass redistribution by erosional and depositional processes. This work provides parameters for the geodynamics of glaciated mountain belts, compressive margin development in a climatically impacted region, and the evolution of flat-slab subduction and potential collision at the distal extent of an accretionary system.

Chapter 2 (Worthington et al., 2008) describes the loci of active deformation within the margin and provides the framework for quantifying total shortening and accommodation of plate motion that is a major objective of Chapter 3. Chapter 2 also

provides the motivation for understanding the tectonic and geodynamic effects of rapid sediment loading at the distal extent of the orogen, which is addressed observationally in Chapter 3 (Worthington et al., in press). Chapter 4 continues the study of accretionary vs. subduction processes within the margin, by determining the geometry and crustal structure of the offshore Yakutat slab. Chapter 4 also addresses large-scale geodynamic processes and the orogenic driver in the margin by describing Yakutat crustal composition and the geometry of the subducting plate using seismic refraction techniques.

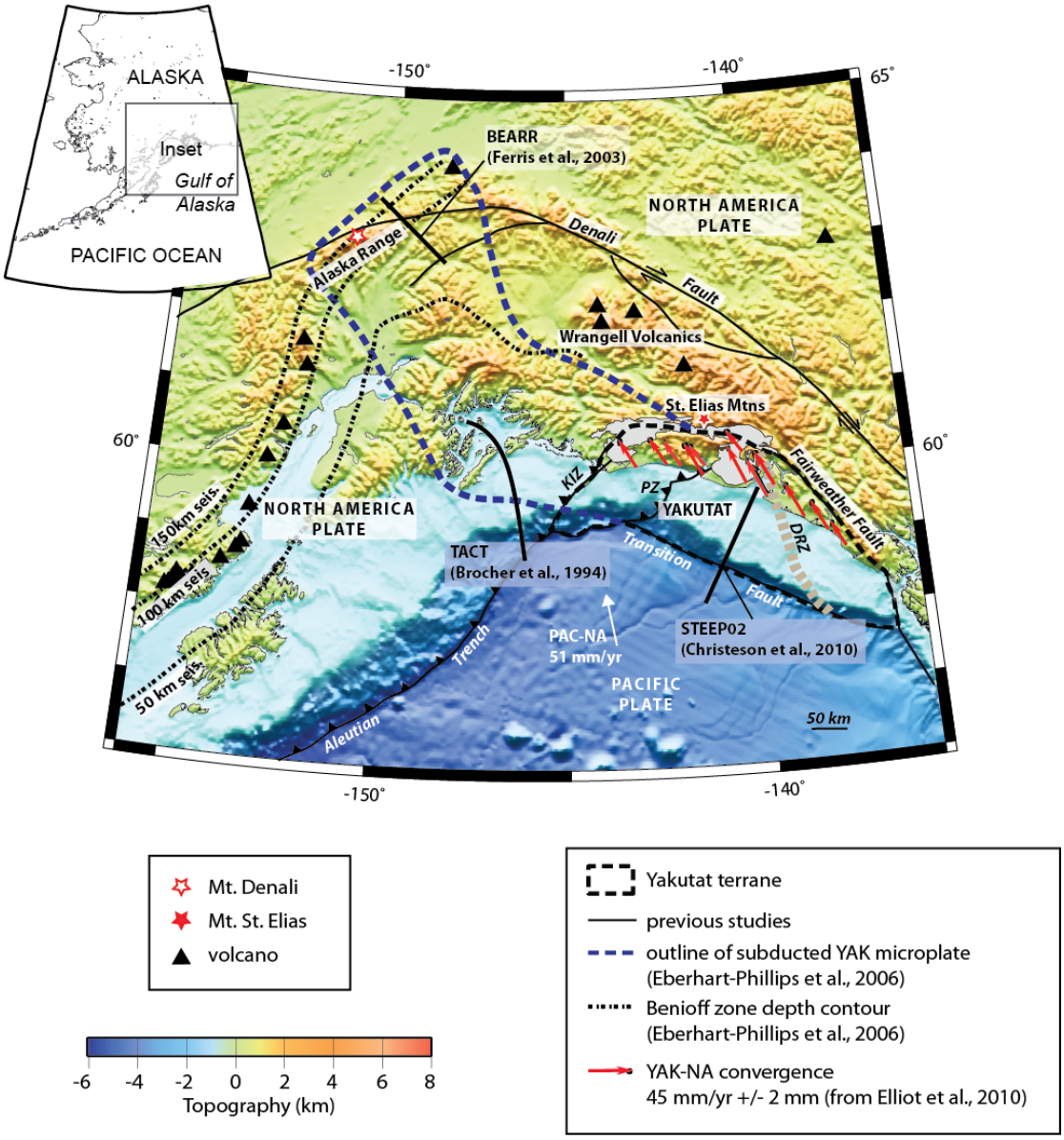

Figure 1.1. Regional tectonic map of southern Alaska showing major faults, topography and geographic landmarks. Pacific Plate velocity vector from Demets and Dixon (1999). Yakutat terrane velocity w.r.t. North America in red arrows (avg. 47 mm/yr from Elliot et al. (2010)). Blue dashed line shows extent of subducted Yakutat slab from Eberhart-Phillips et al., (2006). Black dashed outline shows currently defined Yakutat terrane. Benioff zone depth contours at 50, 100, and 150 km. KIZ = Kayak Island Zone; DRZ = Dangerous River Zone.

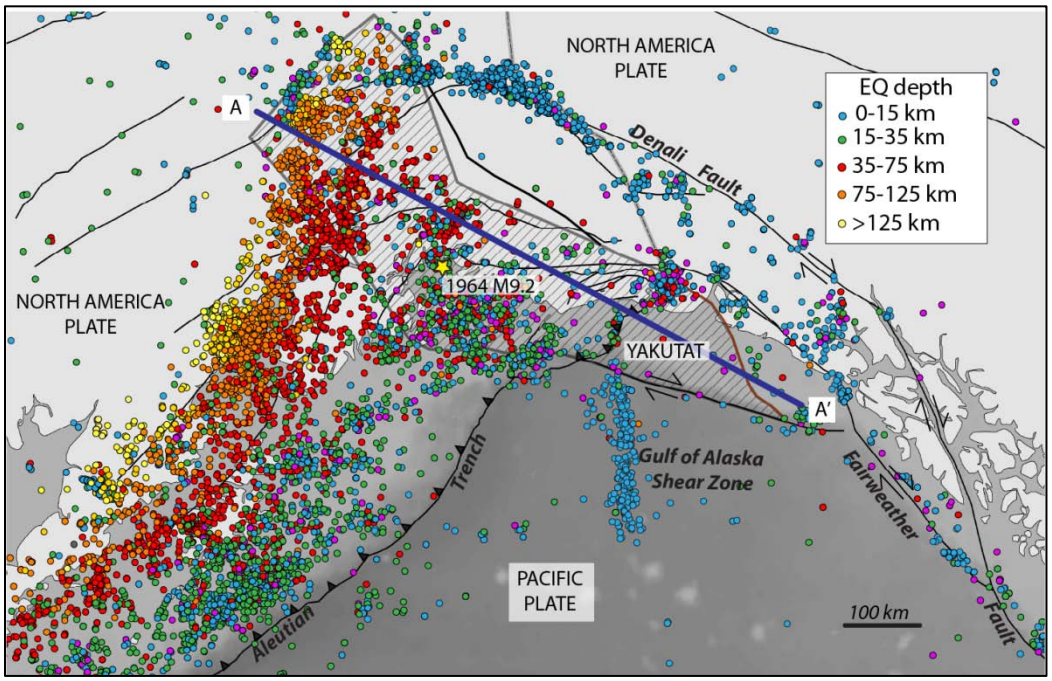

Figure 1.2. Seismicity map of southern Alaska with earthquakes color-coded with depth. Extent of Yakutat plate from Eberhart-Phillips et al. (2006). Epicenter of 1964 Alaska earthquake M9.2. Profile A-A' shown in Figure 1.7.

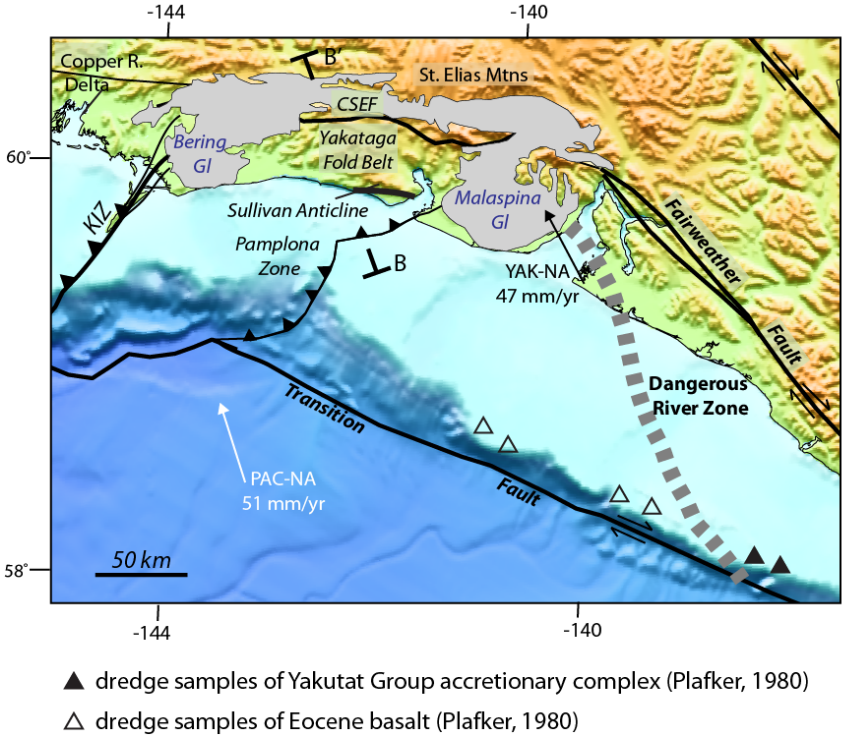

Figure 1.3. Study area basemap showing major faults, glaciers and dredge sample locations. Schematic cross-section B'-B shown in Figure 1.6. Yakutat-North American plate motion from Elliott et al. (2010). CSEF- Chugach-St. Elias Fault

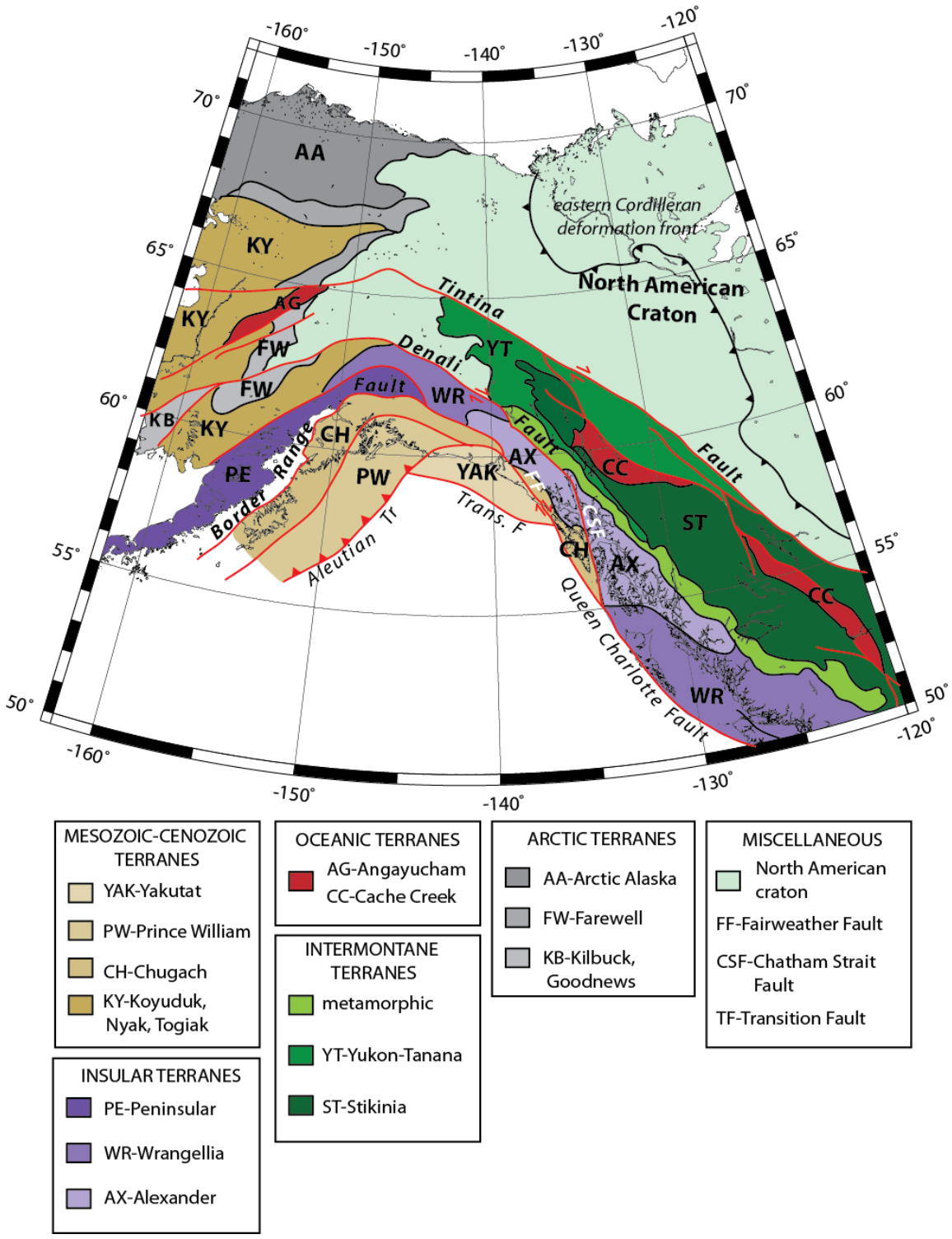

Figure 1.4. Terrane map of Alaska showing major tectono-stratigraphic terranes. Modified from Nokleburg (2001).

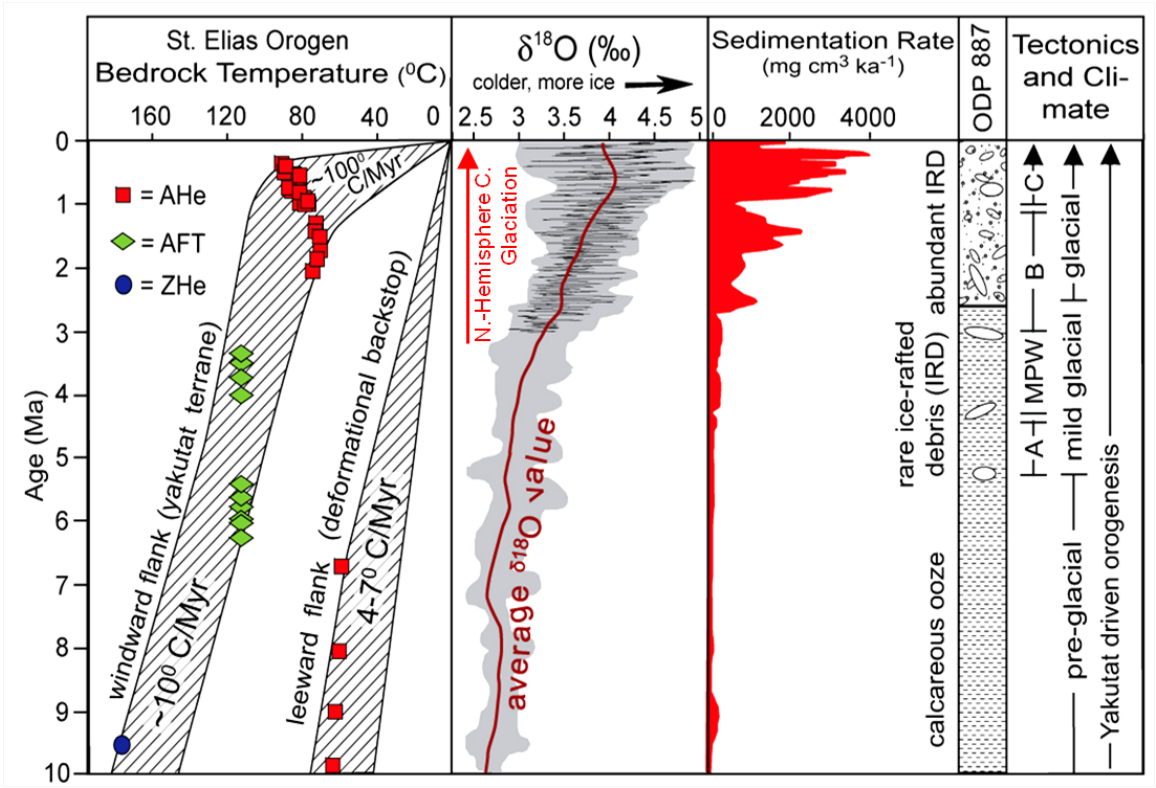

Figure 1.5. Summarized history of glaciations, bedrock cooling, sedimentation and orogenensis in the St. Elias orogen and offshore Gulf of Alaska. a) Bedrock temperature paths vs time. b) Global benthic oxygen isotope records as a proxy for global ice volume and temperature. c) Sediment accumulation rate derived from ODP site 887. d) Summary of sedimentary facies from ODP site 887. e) Synthesis of climate and tectonic events in the St. Elias orogen showing initiation and duration of glacial intervals A, B and C. Reproduced from Berger et al. (2008).

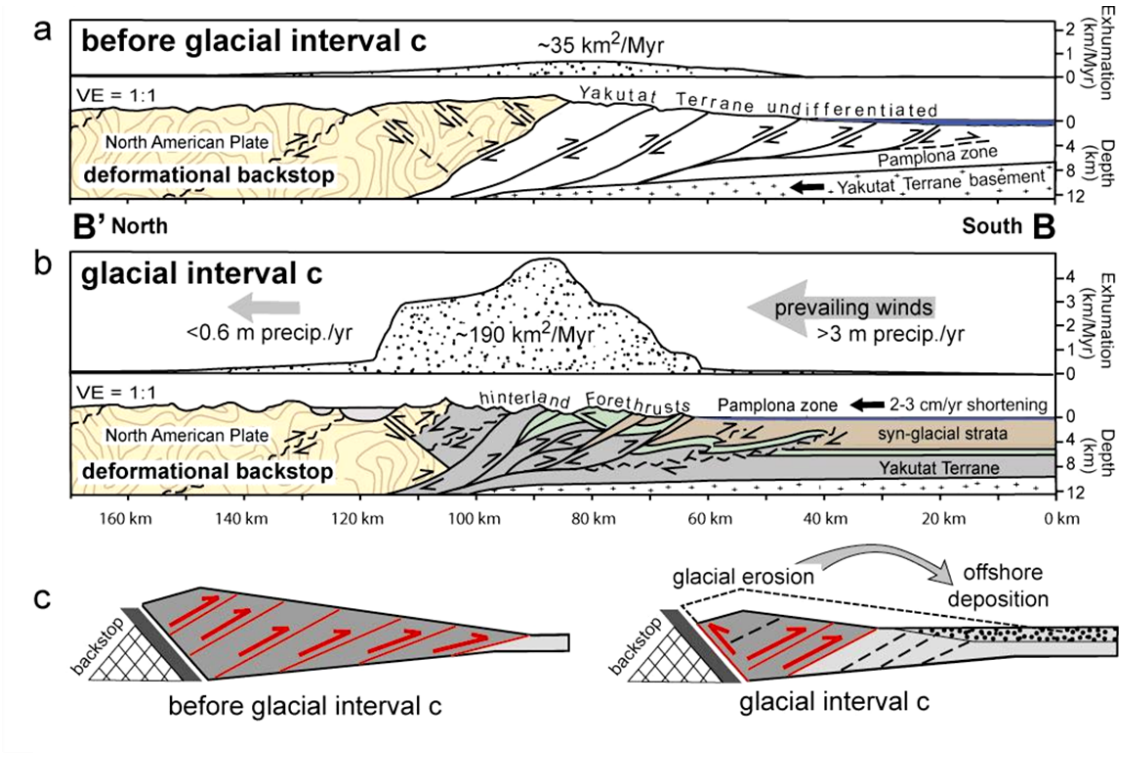

Figure 1.6. Schematic cross-sectional model showing predicted St. Elias orogen structural response to the onset of Glacial Interval C. a) Orogen before Glacial Interval C. b) Orogen after onset of Glacial Interval C. Orogen narrows, faulting concentrates within the back of the wedge, offshore faults in the frontal wedge are inactive. c) Cartoon of orogen before (left) and after (right) onset of Glacial Interval C. Location of cross-section shown in Figure 1.3.

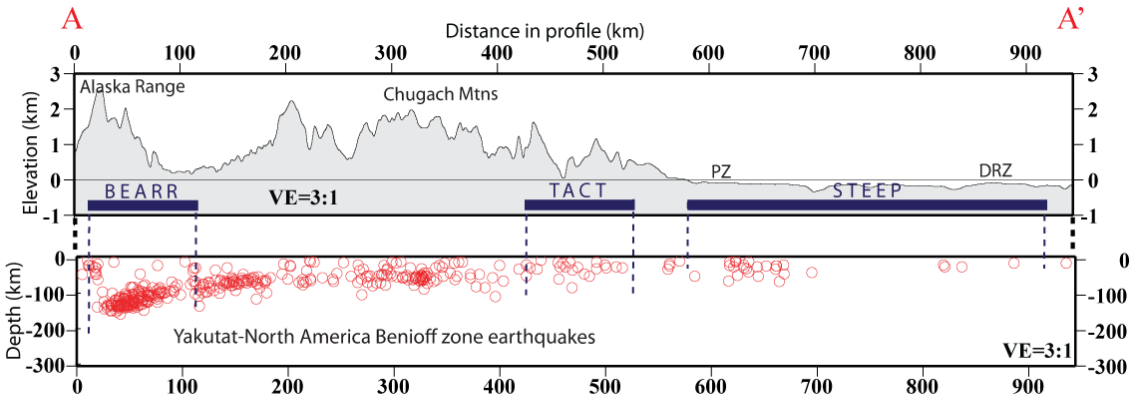

Figure 1.7.. Topography profile vs. Benioff zone earthquake depths showing Yakutat subduction beneath North America. Locations for A-A` shown in Figure 1.2. Earthquakes projected from a 100 km bin. Approximate projected locations of BEARR (Ferris et al., 2003) and TACT (Brocher et al., 1994) and STEEP surveys. PZ = Pamplona Zone; DRZ = Dangerous River Zone. Modified from Gulick et al., 2007.

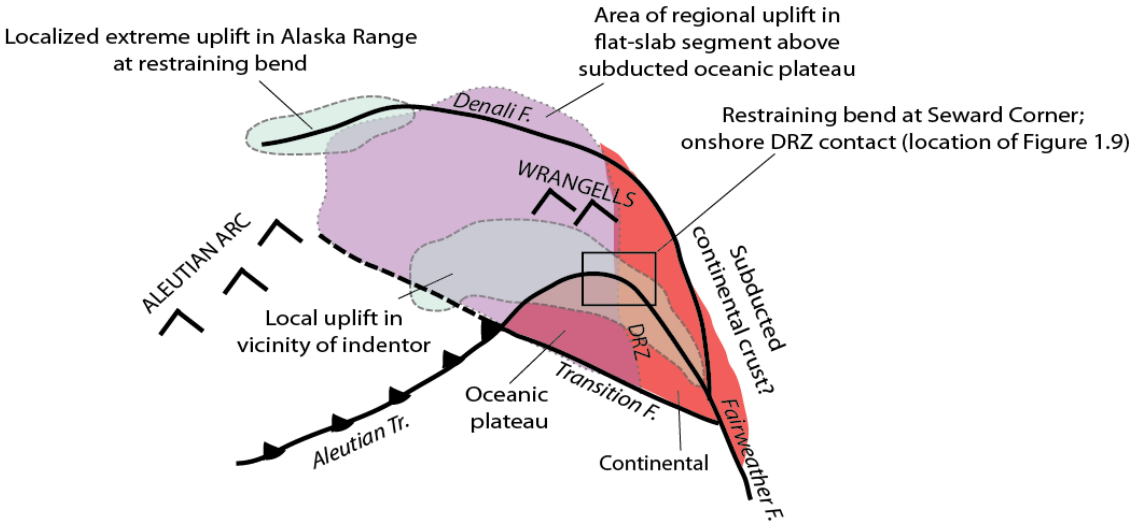

Figure 1.8. Schematic map of current model for Yakutat-North America convergence and St. Elias orogenesis in the Gulf of Alaska margin. High topography of southern Alaska results from regional uplift above a flat subducting oceanic plateau. St. Elias orogen is the result of localized deformation and focused exhumation within a broader zone of regional uplift. DRZ – Dangerous River Zone.

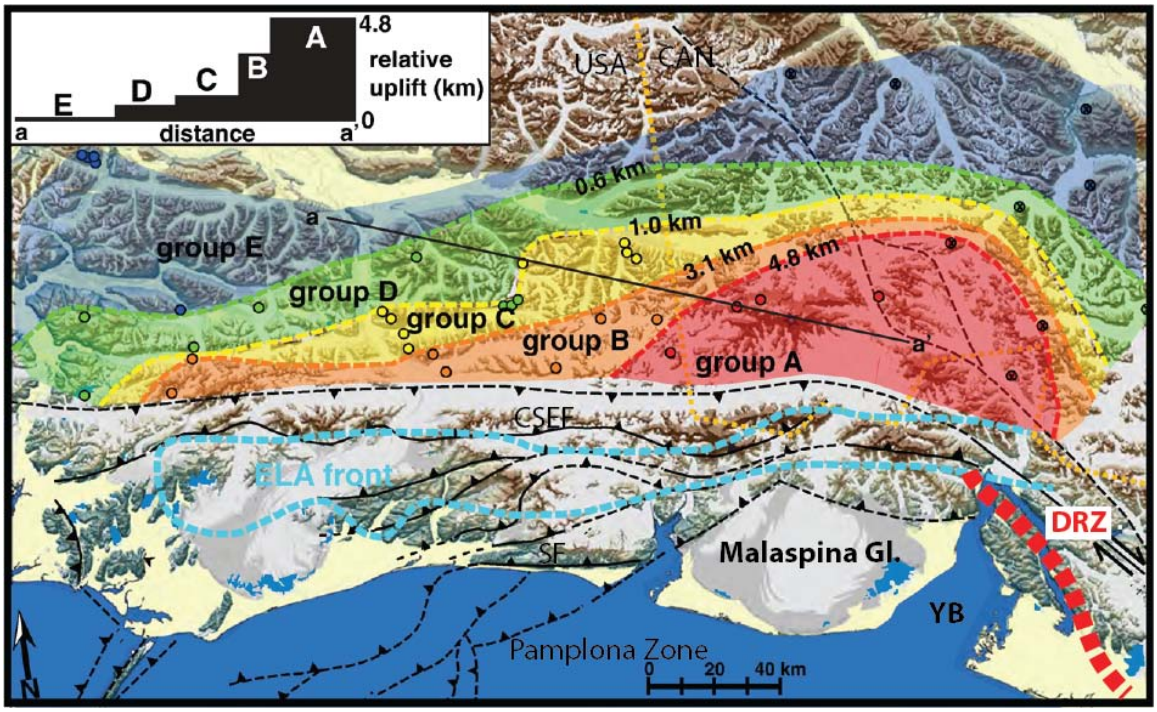

Figure 1.9. Map showing contours of long term (~16 Myr) rock uplift rates base on apatite (U-Th)/He thermochronology centered around the Seward Corner compared relative to background uplift rates from the Chugach terrane to the west. Group A experienced 4.8 km more uplift than the compared region, Group B 3.1 km more, etc. Mapped Dangerous River Zone contact from Plafker et al. (1994). YB = Yakutat Bay; DRZ = Dangerous River Zone. Location shown in Figure 1.8. Modified from Spotila and Berger, 2010.

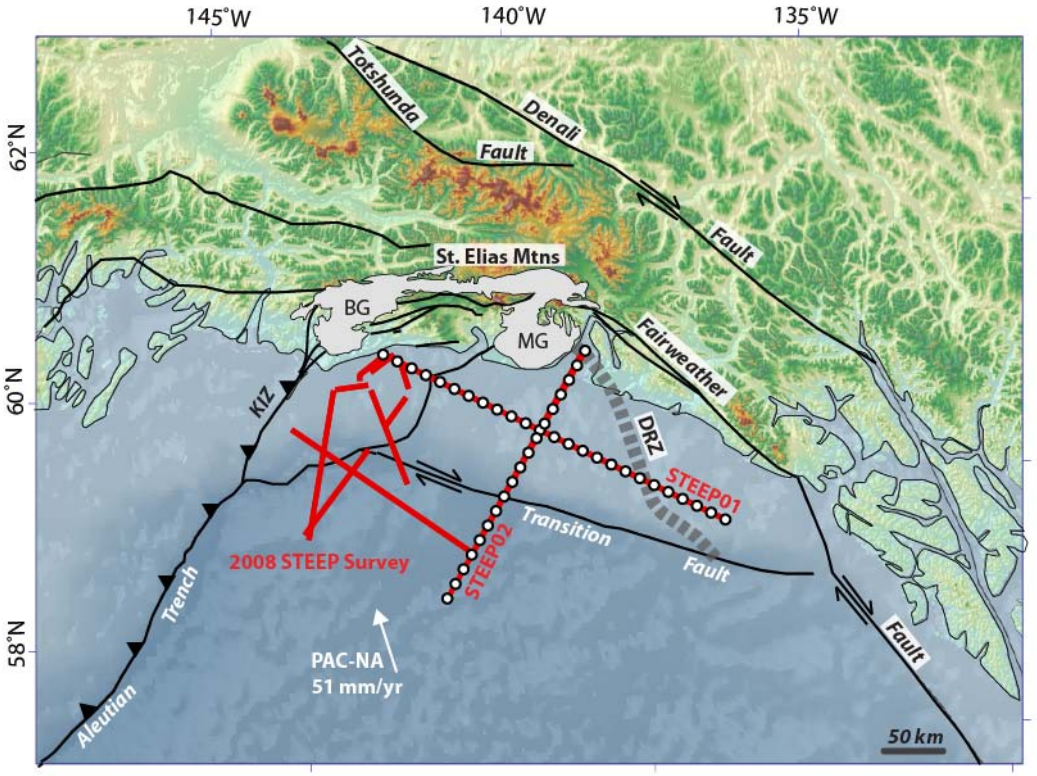

Figure 1.10. Map showing profile locations for the 2008 STEEP seismic survey. Red lines are seismic reflection profiles. White dots are ocean bottom seismometers. DRZ – Dangerous River Zone; KIZ – Kayak Island Zone; BG – Bering Glacier; MG – Malaspina Glacier.

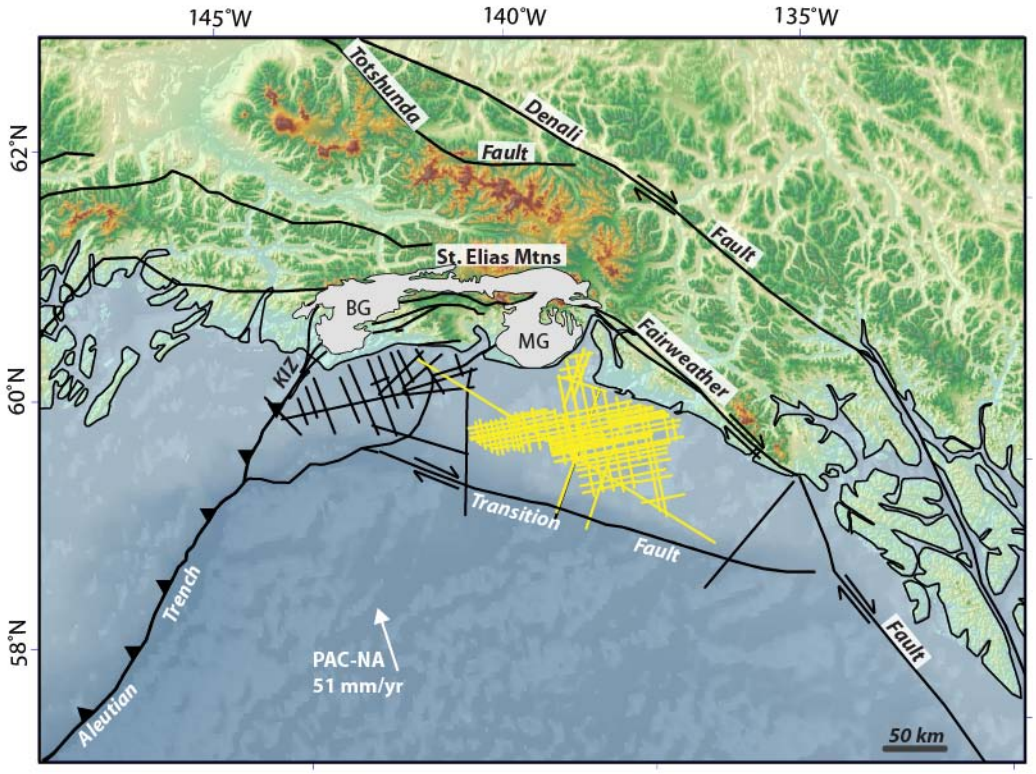

Figure 1.10. Map showing profile locations of supplementary seismic reflection data. Black lines are 1975 USGS seismic profiles. Yellow lines are 1979 Western Geophysical seismic profiles. KIZ = Kayak Island Zone; BG = Bering Glacier; MG = Malaspina Glacier

Chapter 2: Active structures in the Kayak Island and Pamplona Zones: Implications for offshore tectonics of the Yakutat microplate [*]

ABSTRACT

Within the northern Gulf of Alaska, the Yakutat (YAK) microplate obliquely converges with and subducts beneath the North American continent (NA) at near-Pacific plate velocities. I investigate the extent that thin-skinned deformation on offshore structures located within the western portion of the unsubducted YAK block accommodates YAK-NA convergence. I compare faulting and folding observed on high-resolution and basin-scale MCS seismic reflection data with earthquake locations and surface ruptures observed on high-resolution bathymetric data. Holocene sediments overlying the Kayak Island fault zone (KIZ), previously interpreted as a region of active contraction, are flat-lying, suggesting that active convergence within the KIZ is waning. Seismic reflection profiles east of KIZ show up to ~200 m of undisturbed sediments overlying older folds in the Bering Trough, indicating that this area has been tectonically inactive since at least the last ~1.3 Ma. Farther east, MCS profiles image active deformation in surface sediments along the eastern edge of the Pamplona Zone fold and thrust belt (PZ), that are collocated with a concentration of earthquake events that continues southwest to Khitrov Ridge and onshore through Icy Bay. These observations suggest that, during the late Quaternary, offshore shallow deformation style changed

[*] Large portions of this chapter have been published with co-authors S. Gulick and T. Pavlis in: *Active Tectonics and Seismic Potential of Alaska*, AGU Monograph 179, 2008

from distributed across the western Yakutat block to localized at the eastern edge of the PZ with escape of sediments southwest through the Khitrov Ridge area to the Aleutian Trench.

2.1. INTRODUCTION

Within the Gulf of Alaska, the Pacific plate subducts beneath North America along the Aleutian trench to the west, and translates along the Queen Charlotte-Fairweather right-lateral strike-slip fault system to the east. The margin is complicated by the 40-55mm/yr oblique convergence and flat-slab subduction of the Yakutat microplate beneath the North American continent that has resulted in the Chugach-St. Elias orogenic system. In recent years, a number of studies have investigated tectonic processes and associated deformation across the St. Elias orogen (e.g., Bruhn et al., 2004; Pavlis et al., 2004; Plafker, 1987). As a result, two primary models have emerged that describe current tectonic motions in the Gulf of Alaska margin. *Plafker et al.* (1994) propose a collision model in which the St. Elias Mountains are the result of YAK-NA collision. In this model, the Fairweather fault ends near Yakutat Bay and transfers slip into the thrust belt to the west. Offshore, *Plafker* (1987) describes the western segment of the Yakutat microplate, defined in this study as the Yakutat leading corner, as a continuous eastward verging fold and thrust belt bounded by the Pamplona Zone on the east and the Kayak Island Zone on the west (Figure 2.1). Evidence for this interpretation is given by *Bruns and Schwab* (1983) who mapped broad, northeast-trending synclines and anticlines

across the region. This model predicts a regional décollement at ~10 km depth (Plafker, 1987) that connects large-scale structures within the Yakutat block.

In contrast, *Bruhn et al.* (2004) and *Pavlis et al.* (2004) propose a transpressional model in which the YAK-NA boundary is slip-partitioned. Strike-slip motion in this model is accommodated by the Fairweather fault system that continues west past Yakutat Bay into the interior of the orogen, connecting with the Kayak Island fault zone and the Ragged Mountain thrust at its western extent. The contractional component in this model is distributed across the fold-thrust belt between the Chugach-St. Elias fault suture and the Pamplona Zone. *Pavlis et al.* (2004) propose that the current structure of the onshore fold-thrust belt west of the Malaspina Glacier and south of the Bagley Icefield has developed in response to contraction plus complications from oroclinal bending of the microplate during the past 0.5 Ma. In this interpretation, the Pamplona Zone is a recent, minor structure related to second-order tectonic effects as the Yakutat plate indents into the northwest corner of the southern Alaska margin, and does not accommodate a large component of YAK-NA convergence.

In both models, oblique convergence is absorbed through a combination of dextral strike-slip and thrust faulting across the orogen onshore, and across the Pamplona Zone fold and thrust belt and the Kayak Island fault zone offshore. Additionally, the Kayak Island zone is interpreted as a zone of contraction that links active structures in the extreme western extent of the orogen between the Bering Glacier and the Copper River delta to the Aleutian Trench.

These models and others (e.g., Bird, 1996; Fletcher and Freymueller, 1999, 2003) provide valuable constraints on the tectonic framework of southern Alaska. However, further study of thin-skinned offshore deformation patterns and strain accommodation is vital to understanding the tectonic evolution of the southern Alaskan margin as a whole, including the uplift history of the Chugach-St. Elias Mountains, the depositional history of the Gulf of Alaska continental shelf and slope and the stability of current margin geometry. My study seeks to contribute to the understanding of late Pliocene to Holocene offshore deformation in the orogen by interpreting high-resolution seismic and bathymetry datasets in a regional tectonic context.

In light of recently acquired high-resolution datasets, I investigate the extent that active thin-skinned deformation within the region from the Kayak Island fault zone to the Pamplona fold and thrust belt accommodates YAK-NA convergence. I propose a tectonic model in which deformation within the leading corner of the offshore Yakutat block is localized on structures on the northeastern edge of the Pamplona Zone. I further corroborate the prediction that this deformation is thin-skinned (Pavlis et al., 2004; Plafker, 1987) and suggest a shallower décollement in light of more recent constraints on offshore sedimentation that show total sediment thickness of ~4600 m (e.g., Jaeger et al., 1998). This décollement connects the waning KIZ, inactive Bering Trough and the active PZ. Additionally, I suggest that offscraped sediments are constricted west of the Pamplona Zone and escape through a developing Khitrov Ridge deformation zone.

2.2. DATA

Gulick et al. (2007) detail the acquisition methods and processing steps of the bathymetric and high-resolution seismic data used in this study. The high-resolution bathymetric data include more than 162,000 km^2 of 100 m^2 resolution multibeam sonar data that were collected in the summer of 2005 along the base of the continental slope in the Gulf of Alaska as part of a mapping project for the United Nations Convention on the Law of the Sea (Gardner, 2006). High-resolution seismic reflection profiles of the Yakutat Block and adjacent fjords were collected in 2004 as a site survey for two IODP drilling proposals. Additionally, I obtained a 1979 basin-scale seismic reflection survey by Western Geophysical via the USGS. Earthquake locations used in this study were gathered from the Harvard CMT catalogue and the Alaska Earthquake Information Center. Earthquake locations used to map deformation structures were georeferenced using ArcGIS to ensure proper data integration.

2.3. OBSERVATIONS AND INTERPRETATIONS

2.3.1 Kayak Island

High-resolution seismic profile GOA-3002 (Figure 2.2a) images the Kayak Island fault zone (KIZ), the geologic boundary between the Yakutat and Prince William terranes (Plafker, 1987). The ~5 m vertical resolution of this new data gives detailed insight into the behavior of strata near the sea floor, allowing interpretation of Quaternary deformation along this boundary. Below Horizon 1 (Figure 2.2a), bedding steepens but

does not thin toward the Kayak Island Fault Zone. Above Horizon 1 and below the subhorizontal fill within the Kayak Trough, the section shows a northwestward depocenter shift indicated by tilted horizons and northwestward migration of the thickest fill in each package. Above Horizon A, the section images ~200 m of flat-lying sediments within Kayak Trough and up to ~50 m of variably deformed sediment over the fault zone. Overall, deformation of stratal horizons over the fault zone decreases progressively upsection. The sedimentary package between Horizons A and B (Figure 2.2b) thins toward the southeast. The geometry of the strata above Horizon B (Figure 2.2b) appears to result as a combination of drape over previously existing sedimentary structures at the western extent of the fault zone and deformation by underlying structures toward the east. Specifically, the subhorizontal strata onlap Horizon B above the western most fault (Figure 2.2b). The strata steepen and become thinner to the east and are clearly deformed by the easternmost fault. The sea floor, however, is very minimally deformed.

These observations indicate that deposition of strata below Horizon 1 occurred prior to faulting. The observed depocenter shift above Horizon 1 suggests that deposition of these packages was contemporaneous with deformation due to faulting within the KIZ. The southeastward thinning package between Horizons A and B is an example of deposition synchronous with growth along the two southeastern faults. The minimally deformed sea floor suggests that movement on structures within the fault zone has recently diminished. Within the fault zone itself, the lack of reflectivity is likely due to vertical bedding as evidenced by the increasingly steep reflections from northwest to

southeast (Figure 2.2a). This trend is consistent with observations of vertical strata onshore on Kayak Island, directly north of the profile location (Plafker, 1974).

2.3.2 Bering Trough

High-resolution seismic profile GOA-2505 (Figure 2.4) images the Bering Trough between KIZ and PZ and the backlimb of an active slope structure associated with PZ (Figure 1). This profile is divided into two primary sedimentary packages separated by the erosional unconformity labeled Horizon A (Figure 2.4a). Two large-scale folds are visible within the lower package. The overlying ~200 m-thick package lies depositionally atop the bottom package and does not display major signs of deformation such as faulting or large-scale folding. Some of the sequences display subtle thinning and steepening towards the shelf break. The topmost strata do not display signs of deformation at the shelf break.

The two folds imaged below Horizon A provide evidence that sediments were syntectonically deposited on a deforming shelf and slope; thus, YAK-NA convergence was once at least partly accommodated within the Bering Trough region. The upper package depicts a series of minimally deformed glacial-interglacial sequences. These observations indicate that shallow deformation in the Bering Trough area of the Yakutat leading corner has become progressively less active over time. The thinning and steepening of some of the sequences toward the shelf break indicate syndepositional deformation on the southern fold, while limited deformation within the topmost strata indicate that deformation on this fold has since ceased. Taken together, the overall

geometries of the upper and lower sedimentary packages within the Bering Trough suggest a fundamental shift in margin architecture from primarily tectonically influenced to primary depositionally influenced.

2.3.3 Pamplona Zone and Khitrov Ridge

Industry basin-scale seismic profile FW-074 images the eastern edge of the Pamplona Zone, showing recently active east-verging thrust faults and their associated folds (Figure 2.5). Overlying strata are deformed up to the seafloor, with growth strata present on the forelimbs of both folds, indicating syndepositional deformation.

High-resolution bathymetry images the continental slope where active Pamplona Zone faulting and folding imaged on FW-074 (Figure 2.5) and GOA-2505 (Figure 2.4) can be traced to the shelf edge (Figure 2.6). An indentation in the shelf edge is imaged where PZ faulting links up with three structures: 1) the active western portion of the Transition fault (Gulick et al., 2007), 2) the right-lateral Pacific Plate zone of weakness defined by the earthquake lineation shown in Figure 2.3 (e.g., Pegler and Das, 1996), and 3) active Khitrov Ridge deformation (Figure 2.7).

Active Khitrov Ridge faulting is imaged in high-resolution seismic profile GOA-3101, showing surface deformation indicative of significant amounts of extension. The faults in this extensional array, however, merge toward a common position, suggesting an underlying transtensional flower structure (Figure 2.7). This faulting may indicate a recent shift in the mechanism of shallow deformation and sediment offscraping in which the strata above the Yakutat microplate are extruded west of the Pamplona Zone.

2.4. DISCUSSION

Observations that deformation on structures within the Kayak Island Zone is waning, combined with evidence of localized shallow deformation on the eastern edge of the Pamplona Zone and in the Khitrov Ridge area and quiescent conditions in the Bering Trough area, lead to my proposed model of thin-skinned deformation within the Yakutat leading corner (Figure 2.8).

2.4.1 Kayak Island Suture

Seismically imaged sediments overlying the Kayak Island fault zone (Figure 2.2) exhibit limited Holocene offset, which seemingly contradicts previous interpretations of this region as a zone of active contraction (e.g., Plafker, 1987). This observation suggests that shallow deformation in the Kayak Island zone is waning. Therefore, a significant portion of convergence within the Yakutat leading corner sedimentary cover must be accommodated on structures other than the KIZ.

One possible explanation for the apparent waning deformation on the Kayak Island zone proper is that the deformation has shifted westward onto the shelf, redeforming the rocks in this region. Although not visible in Figure 2.2, there are numerous young folds and thrusts in the region west of Kayak Island (e.g., Bruns and Schwab, 1983). Moreover, recent work onshore (Bruhn et al., 2006) indicates active deformation occurring northeastward along strike from this area, an observation which is consistent with deformation localizing both inboard and outboard of the locus of sediment accumulation within the Bering Trough.

The observed shallow structural behavior in the KIZ records the gradual abandonment of the KIZ as a zone of active contraction within the sedimentary cover. Additionally, the structures imaged in the Kayak Island Zone appear to be forming a suture that may be the offshore extension of the suture observed onshore at Ragged Mountain and Wingham Island (Plafker, 1974). The seismically opaque region which appears to be caused by vertical bedding (Figure 2.2) echoes that seen onshore Kayak Island where Yakutat terrane material is constricted against the Poul Creek formation and the basaltic Orca Group of the Prince William terrane (Plafker, 1974, 1987). In this case, offscraped sediments are constricted between the developing KIZ suture and active PZ.

2.4.2 Pamplona Zone Deformation Front

Industry, basin-scale MCS data show ongoing deformation and faulting along the northeastern extent of the Pamplona Zone fold and thrust belt (Figure 2.5). These structures are roughly collocated with a lineation of earthquakes concentrated along the eastern edge of the PZ (Figure 2.3). *Doser et al.* (1997) determined thrusting focal mechanisms for a series of these events from 1958-1970, with depths ranging from 7-13 km, with the exception of event at 20 km (Figure 2.3). The large scale folds observed in Figure 2.6 may be formed by a combination of shallow response to seismogenic thrusting at depth and of aseismic deformation as sediments are offscraped and constricted between the PZ and KIZ.

The PZ seismic lineation appears to continue northeast onshore to the Malaspina Fault through Icy Bay, given observed seismicity patterns (Figure 2.3). Offshore to the

southwest, the seismic lineation curves toward the Khitrov Ridge deformation zone and the Aleutian Trench. This seismic lineation appears to form a continuous deformation front extending from the PZ northeast onshore along the Malaspina Fault and southwest, farther offshore, to the Khitrov Ridge zone. This observation corroborates previous assertions that the PZ is the current deformation front for YAK-NA convergence (Plafker et al., 1994) and further indicates that this deformation front extends for approximately 250 km across the Yakutat block, forming the southern and eastern boundaries of the Yakutat leading corner.

My interpretation of the PZ as the primary deformation front is a departure from *Pavlis et al.'s* (2004) suggestion that the PZ is principally related to second-order tectonic processes as the Yakutat block has been forced into the subduction corner over the last 3 Ma (Pavlis et al., 2004). Here, I interpret the PZ as the deformation front of the fold and thrust belt, and infer that the localization of the deformation front is strongly controlled by relatively young sedimentation that has shifted the locus of active deformation. My observations are consistent with *Picornell's* (2001) conclusion that the amount of deformation on the active Pamplona Zone accounts for only a fraction of current YAK-NA convergence. That is, convergence across the zone is <1 km over a period of >200 kyr, which is less than 10% of the total plate motion.

This conclusion is tentative, however, because chronologies are poorly constrained. Industry well-tie data (i.e., Zellers, 1995) is insufficient in the shallow strata to provide reliable age constraints for the change in architecture in this part of the margin. Estimated Holocene sediment accumulation rates of >10 mm/yr (Jaeger et al., 1998) in

the margin suggest that the underlying structures have been inactive for a minimum of 20 ka, assuming that accumulation rates are constant and that a majority of shelf sediment has not been eroded by glacial advances. A maximum age of inactivity on the underlying structures can be estimated, assuming that 50% of the margin has been eroded by glacial advances and an average Pliocene sediment accumulation rate of 2 mm/yr (Jaeger et al., 1998). These assumptions give an estimated maximum age of ~1 Ma. Though further data is needed to understand the structural development of the Bering Trough, it is clear that these buried structures do not currently accommodate sedimentary deformation due to YAK-NA convergence.

Additionally, my observations are limited to the uppermost ~2 km of the section, thus, it is possible that a significant portion of differential YAK-NA plate motion occurs on a sub-horizontal detachment fault at depth. The superficial folds and faults observed on the available seismic reflection data may not necessarily record this motion at depth. However, active deformation and associated seismicity in the Pamplona Zone could indicate significant localized thin-skinned deformation, representing offscraping of the shelf sediments from the top of the subducting Yakutat plate, while the bulk of lithospheric-scale tectonic deformation has been transferred onshore [e.g. *Bruhn, et al.*, 2004].

2.4.3 Khitrov Ridge Deformation Zone

I interpret the Khitrov Ridge zone as a possible structural link between active structures within the offshore Yakutat block and the Aleutian Trench. In the Khitrov

Ridge area, where the PZ seismic lineation continues to the southeast, high-resolution seismic and bathymetry data show complex deformational patterns. Seismically imaged extensional features at the shelf break (Figure 2.7) indicate either transtensional strain, in the case of a flower structure, or slope failure processes such as slumping due to continued sediment accumulation and gravity slides. These extensional features may be related to mapped contractional features at the toe of the slope (Fisher et al., 2006), recording accommodation of a large-scale fold at depth.

Pamplona Zone faulting can be traced to the shelf edge in the bathymetry (Figure 2.6). Thus, this slope area appears to be a developing deformation zone that is bounded on three sides: 1) to the south, by oblique-slip thrust faults associated with the active western portion of the Transition Fault, 2) to the north, by oblique-slip normal faults associated with slope processes and lateral extrusion of offscraped material, and 3) to the east, by Pamplona Zone faulting (Figure 2.8). To the west, the deformation belt narrows as it enters the YAK-NA-PAC triple junction vicinity.

Lateral escape of offscraped material and counter-clockwise rotation due to oroclinal bending suggested by *Pavlis et al.* (2004) are possible mechanisms for the formation of this deformational response in the Khitrov Ridge zone. Seismic data coverage is currently insufficient to determine slip direction on the transtensional feature imaged in Figure 2.7. As such, both hypothesized mechanisms are viable since I cannot determine the direction of material transport. This deformation zone may be analogous to the area bounded by the Contact and Chugach-St. Elias Faults on the northern onshore

portion of the leading corner (Figure 2.8). Further study is needed both onshore and offshore to test this deformation zone hypothesis and confirm the mechanism.

2.4.4 Structural Interactions

Significant lithospheric-scale intraplate deformation of the Yakutat block is unlikely in light of recent evidence that the YAK microplate is an oceanic plateau, composed of anomalously thick, >15 km, oceanic crust (Eberhart-Phillips et al., 2006; Ferris et al., 2003; Gulick et al., 2007; Pavlis et al., 2004). Thus, interactions between major leading edge structures are best understood as a thin-skinned deformational response to YAK-NA convergence. I predict that the developing KIZ suture is connected to active PZ and buried Bering Trough structures through a sub-horizontal décollement that has developed within either the sediment pile sitting atop the Yakutat block or the weak, interbedded layers at the sediment-basement interface. My model proposes that deposits located above the décollement are partly offscraped and accreted to the North American continent and partly extruded through the Khitrov Ridge deformation zone. This interpretation is consistent with the prediction that the continental slope between Khitrov Ridge and KIZ consists of accreted sediment sequences (Plafker, 1987). The underlying thick, buoyant Yakutat crust below the décollement undergoes flat-slab subduction beneath North America (Eberhart-Phillips et al., 2006; Gulick et al., 2007). In addition, I propose that the décollement is the effective YAK-NA tectonic boundary.

In this context, overlying sediments located between the KIZ and PZ can be analyzed as an accretionary complex in which imbricate thrusts sole into the décollement.

In most accretionary complexes, deformation is concentrated at the distal extent of the complex (e.g., Gulick et al., 2004a); thus, highly localized deformation at the eastern edge of the Pamplona Zone is not surprising. An important distinction between the Pamplona thrust system and typical accretionary prisms, however, is that the deformation front is clearly absorbing only a fraction of the total plate convergence, and a major part of the deformation is localized behind the deformation front onshore, toward the suture. In addition, shallow deformation has shifted in time, as evidenced by the shutdown of structures and burial by flat lying sediments within the Bering Trough (Figure 2.4).

Thin-skinned structural interaction within the Yakutat leading corner may also be complicated by the structurally defined deformation zones that border the accretionary complex to the north and south; i.e. the Chugach-St. Elias and Contact fault bounded structure to the north and the Khitrov Ridge deformation zone to the south (Figure 2.8). The development of the Khitrov Ridge deformation zone is likely a recent structural response to inactivity elsewhere in the Yakutat leading corner. A broad zone of deformation no longer accommodates the influx of accreted material. This material is forced to deform and escape through the free surface of the block, i.e. the Khitrov Ridge zone, toward the Pacific Ocean basin and the Aleutian trench (Figure 2.8).

Buried, inactive structures observed within the Bering trough (Figure 2.4) likely sole into the predicted décollement. These faults and their associated folds could represent an abandoned deformation front similar to that currently observed in the PZ. Alternatively, these structures may have been a component of a broad fold-thrust belt over which deformation was dispersed in the YAK leading corner prior to the current

phase of deformation. Given high sedimentation rates in the Bering trough of 5-10 mm/yr (Jaeger et al., 1998; Sheaf et al., 2003; Spotila et al., 2004), sediment loading may have effectively dampened motion on these structures, rendered them inactive between 20 ka and 1 Ma, and deformation to localize elsewhere on the margin. This process may be the anti-corollary to observed strain localization that occurs in areas undergoing focused erosion (e.g., Pavlis et al., 2004). Indeed, these observations together are powerful evidence that the present deformation is transitional, and has temporally shifted in response to mass transfer in the orogenic wedge from onland erosion to rapid offshore deposition.

2.5. CONCLUSIONS

Analyses of high-resolution and basin-scale seismic sections in conjunction with high-resolution bathymetry and earthquake locations indicate that the Yakutat leading corner is undergoing significant intraplate thin-skinned deformation that is currently localized on the eastern edge of the Pamplona Zone and in the Khitrov Ridge area. I propose a décollement located near the base of the sediments deposited on top of the Yakutat block as the structural accommodation of the transitioning deformation front. The KIZ is interpreted as an incipient suture that acts as a partial backstop for material west of the PZ, causing constriction and extrusion of offscraped sediments through the Khitrov Ridge area to the YAK-NA-PAC triple junction. The shutdown of structures within the Bering Trough, associated shifting of deformation to the present deformation

front of the PZ, and active deformation onshore suggest that the orogen is undergoing a transient response to mass redistributions by erosion and sedimentation.

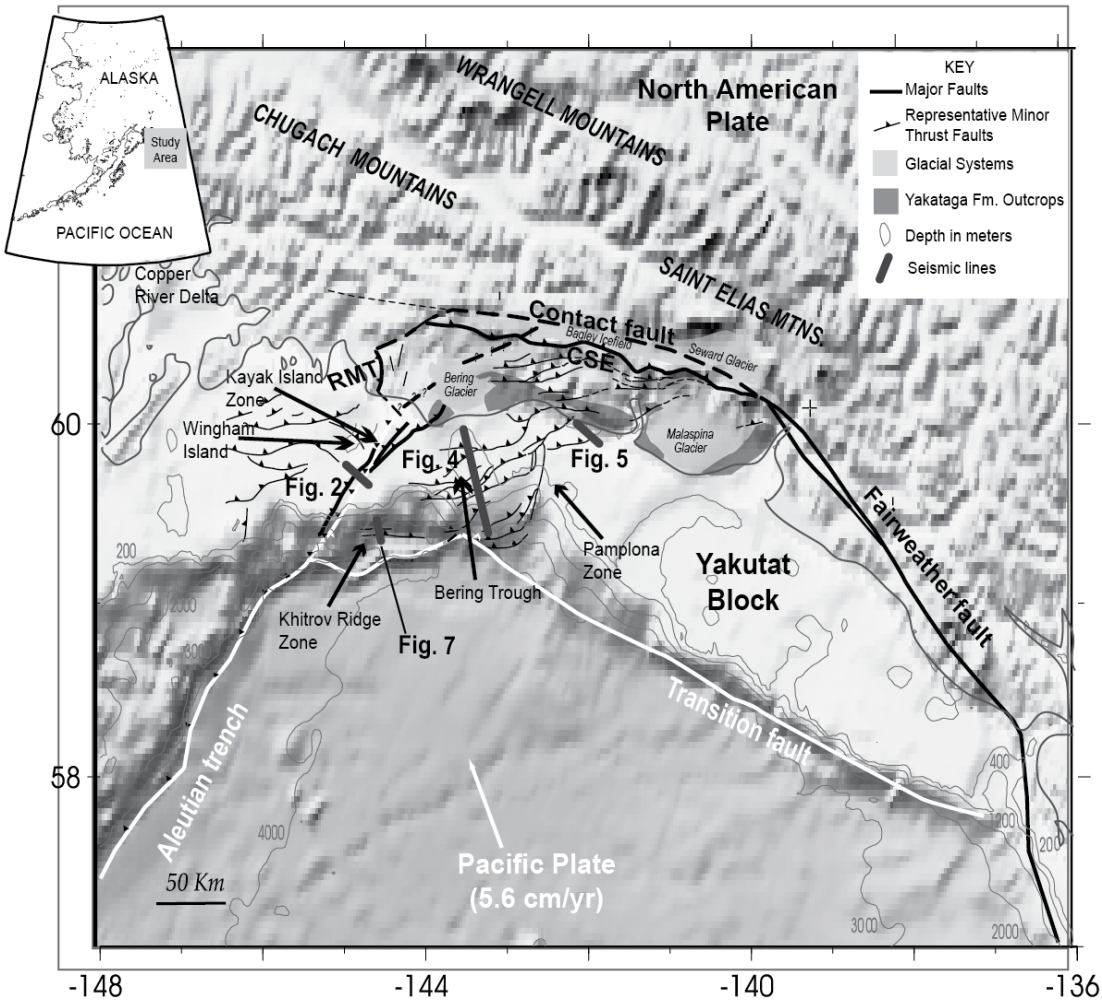

Figure 2.1. Regional map of southern Alaska showing the Yakutat microplate and major structures related to the collision of the Yakutat microplate with North America [after *Pavlis et al.*, 2004]. Mapped thrust faults within YAK leading corner after *Plafker* [1987]. Map includes locations of seismic profiles used in this study (Figures 2.2, 2.4, 2.5, and 2.7). (CSE = Chugach-St. Elias fault).

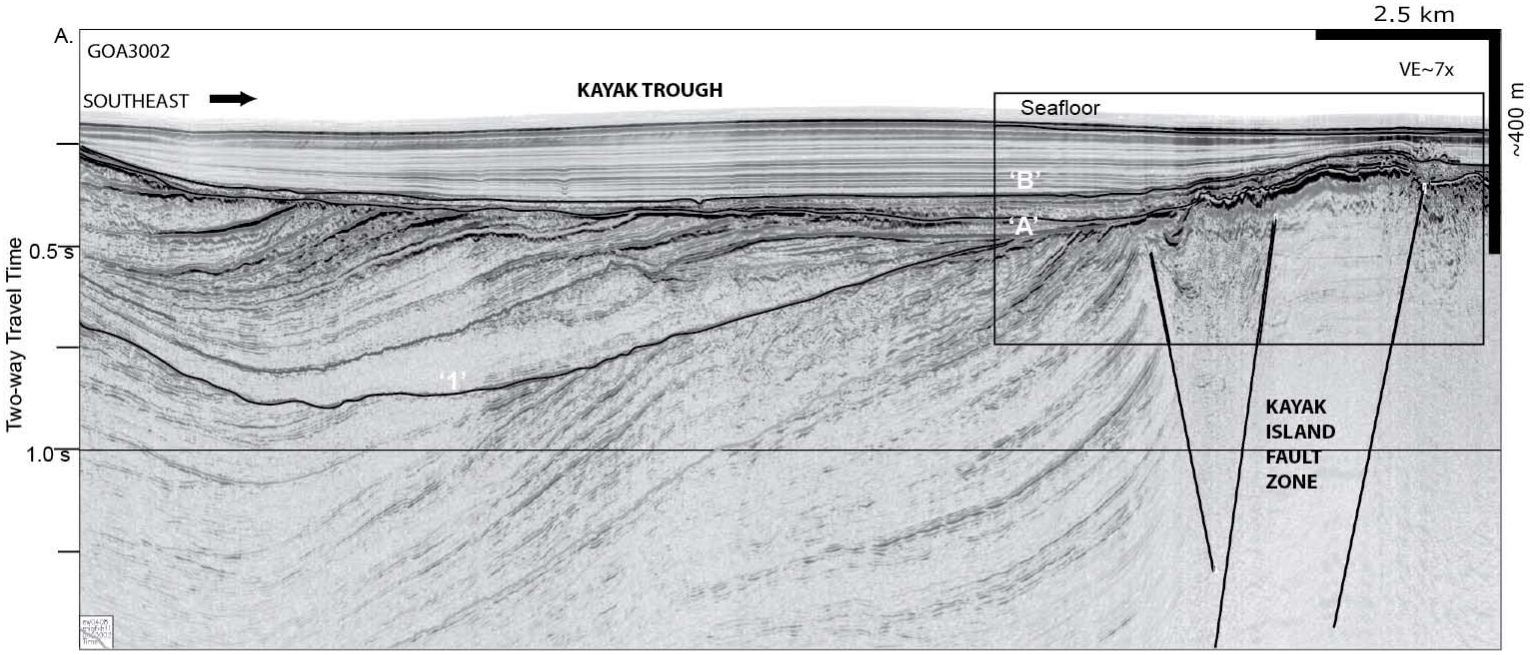

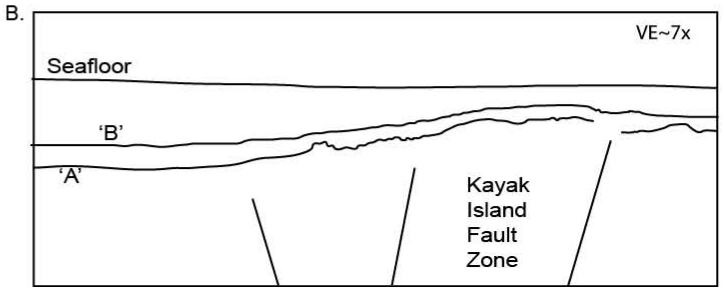

Figure 2.2. High-resolution seismic profile GOA-3002 imaging Kayak Trough and Kayak Island fault zone. a) Strata overlying fault zone is progressively less deformed to the sea floor. These strata display limited Holocene deformation. Opacity of seismic signal within fault zone due to

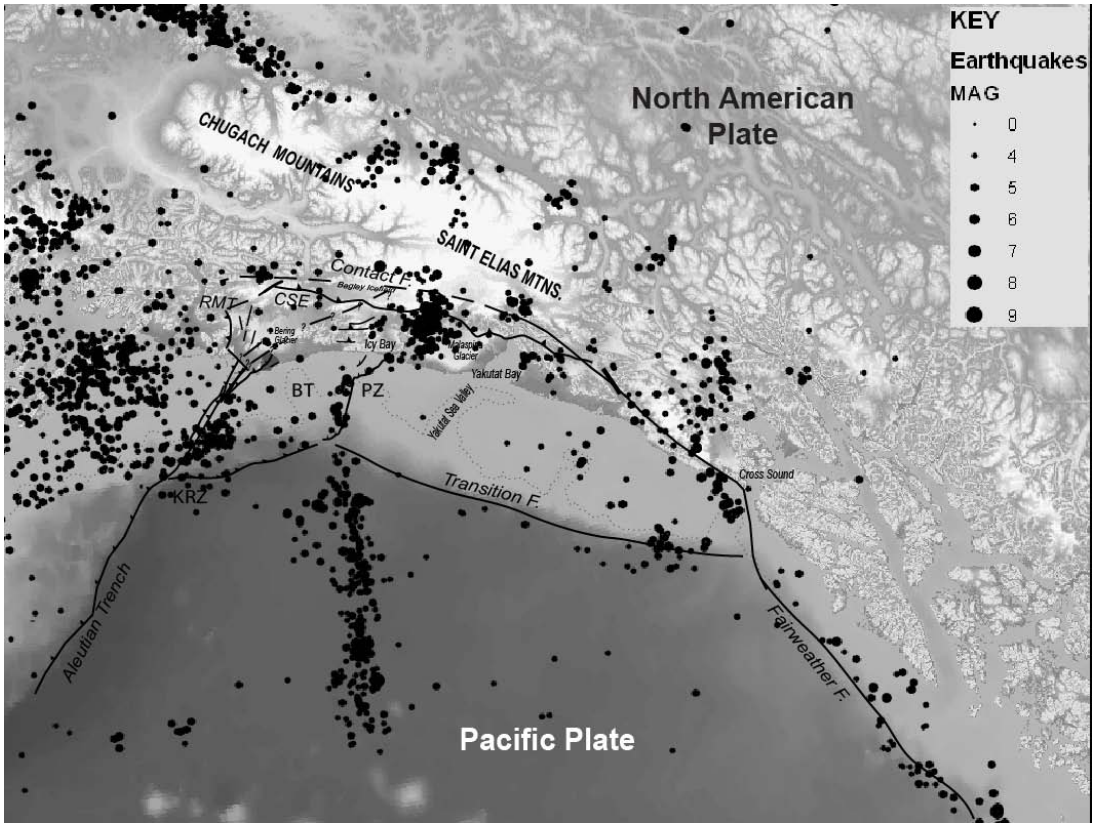

Figure 2.3. Earthquake location map of southern Alaska margin. Note seismic lineation along eastern edge of Pamplona Zone. Seismicity is also concentrated near Icy Bay and the in the Khitrov Ridge area. (BT = Bering Trough, CSE = Chugach-St. Elias Fault, KIZ = Kayak Island Zone, KRZ = Khitrov Ridge Deformation Zone, PZ = Pamplona Zone, RMT = Ragged Mountain Thrust)

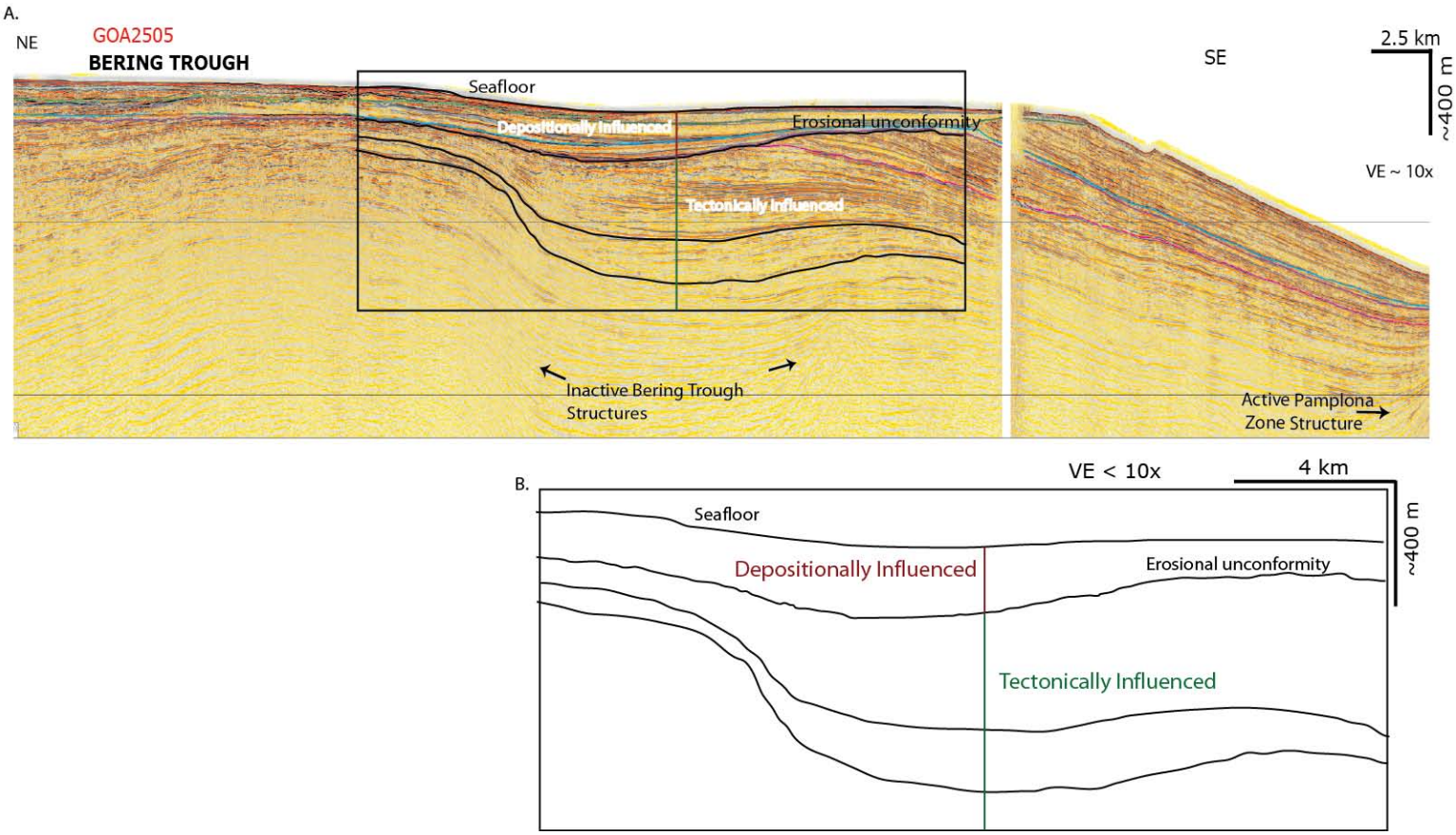

Figure 2.4. a) High-resolution seismic profile GOA-2505 imaging Bering Trough showing a distinct change in margin architecture from tectonically to depositionally influenced at the labeled erosional unconformity. b) Interpretations for seismic profile GOA-2505. Location of seismic profile shown in Figure 2.1.

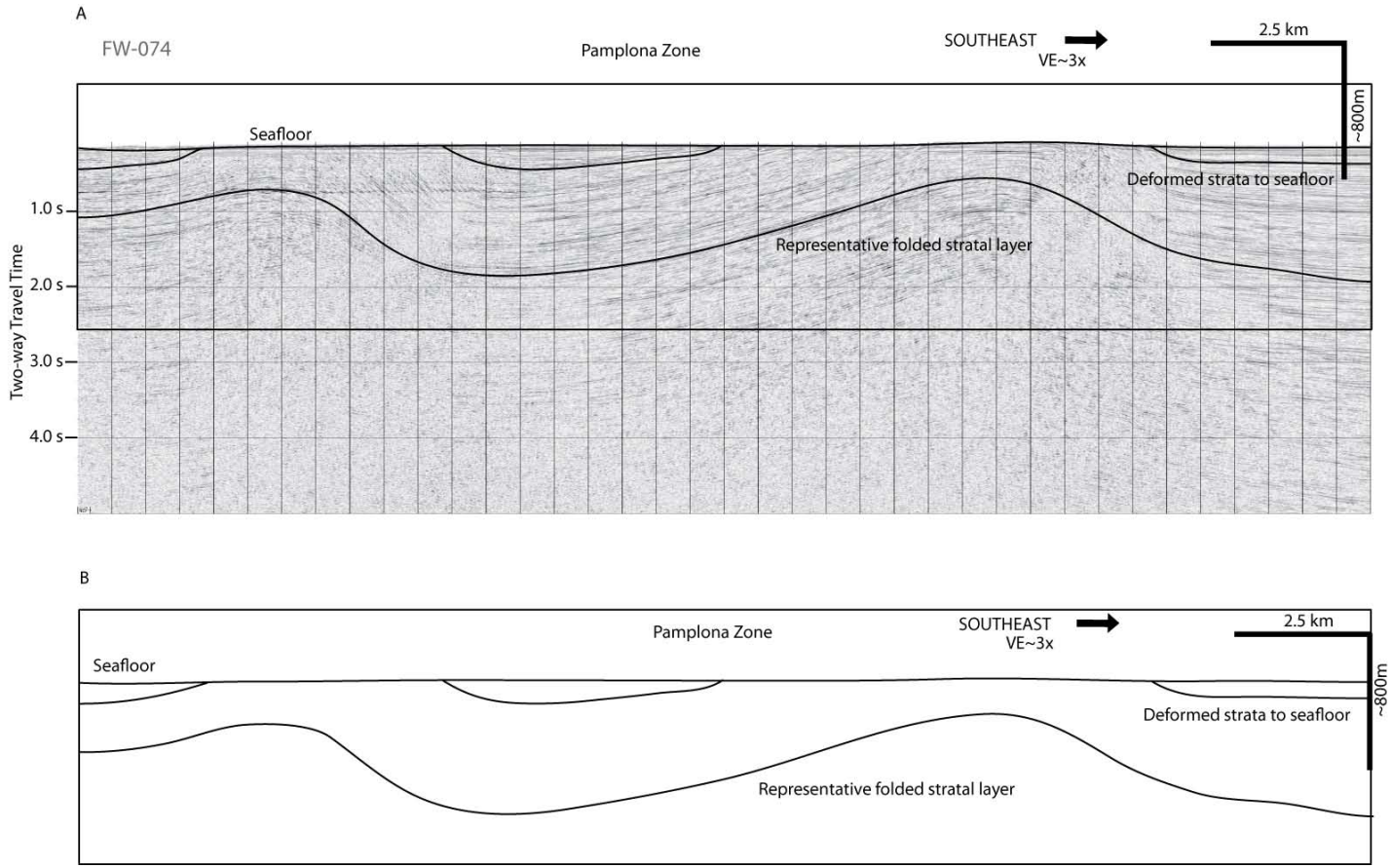

Figure 2.5. Basin-scale seismic profile FW-074 showing active Pamplona Zone folding. a) Growth strata are visible to seafloor on the forelimb of each fold. b) Interpretations for seismic profile FW-074. Location of seismic profile shown in Figure 2.1.

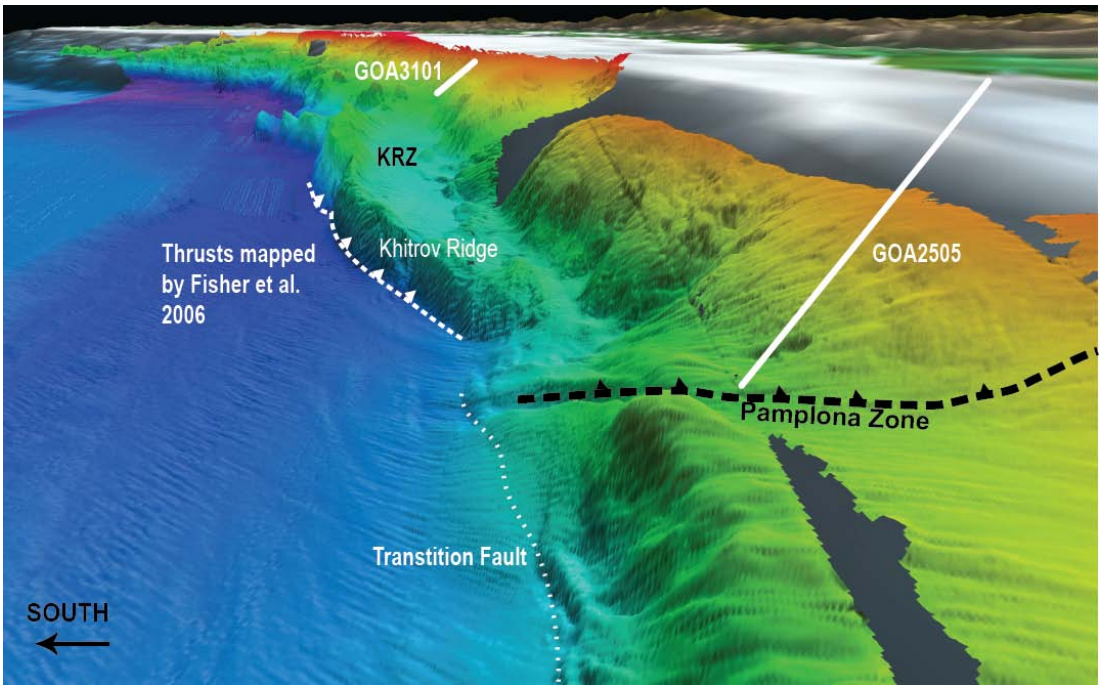

Figure 2.6. High-resolution bathymetry of Khitrov Ridge area. Active Pamplona Zone faulting is image to shelf edge. Thrust faults mapped at toe of slope after *Fisher et al.* [2006]. Note positions of seismic profiles GOA-3101 (Figure 2.7) and GOA-2505 (Figure 2.4).

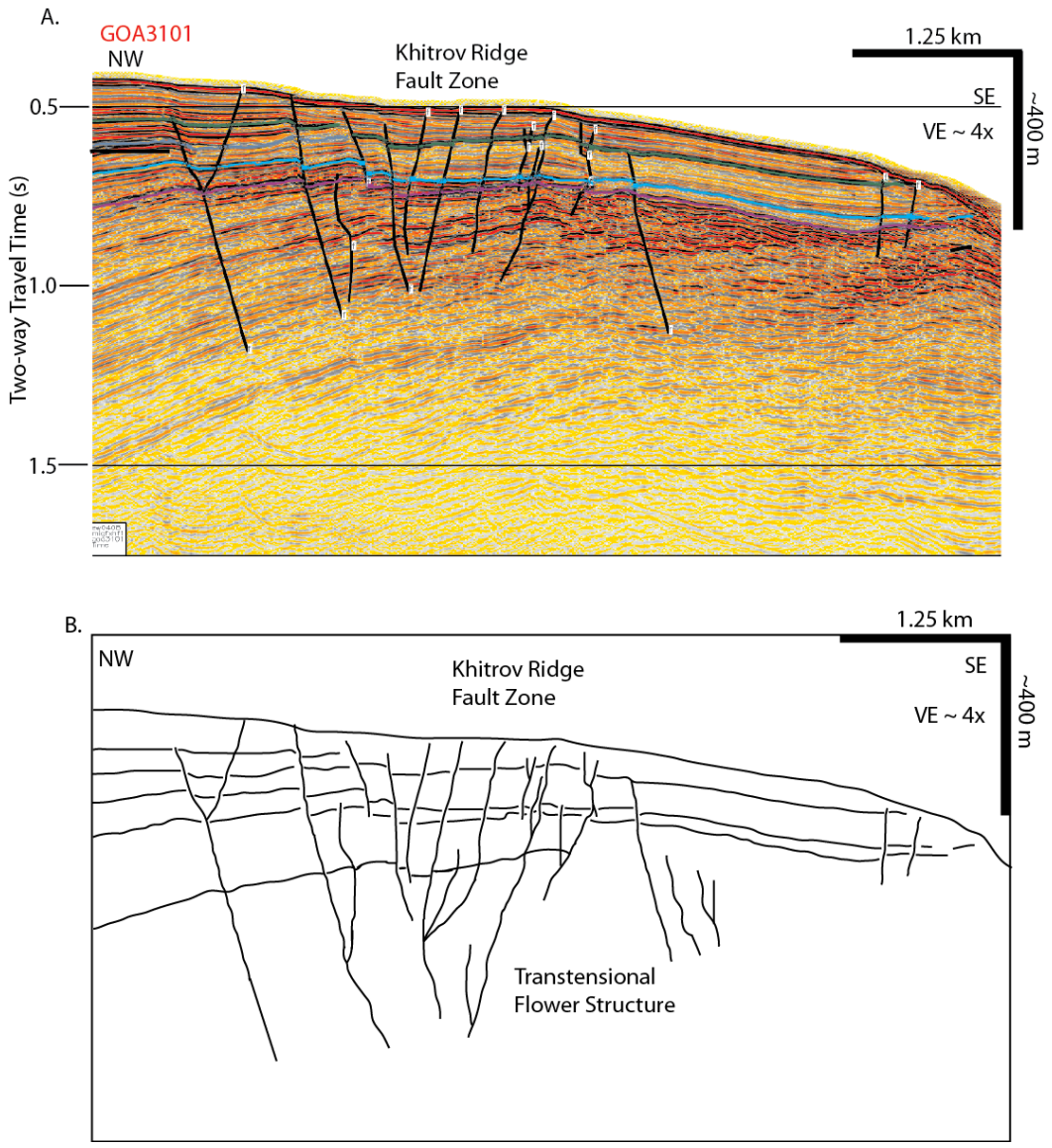

Figure 2.7. High-resolution seismic profile GOA-3101 imaging the shelf break at Khitrov Ridge. a) Active deformation and faulting at seafloor soles into a transtensional flower structure. Vertical distances estimated using a seismic velocity of 1500 m/s for the water column and 2000 m/s for unconsolidated sediment. Figure 2.7b. Interpretations for seismic profile GOA-3101. Location of seismic profile shown in Figure 2.1.

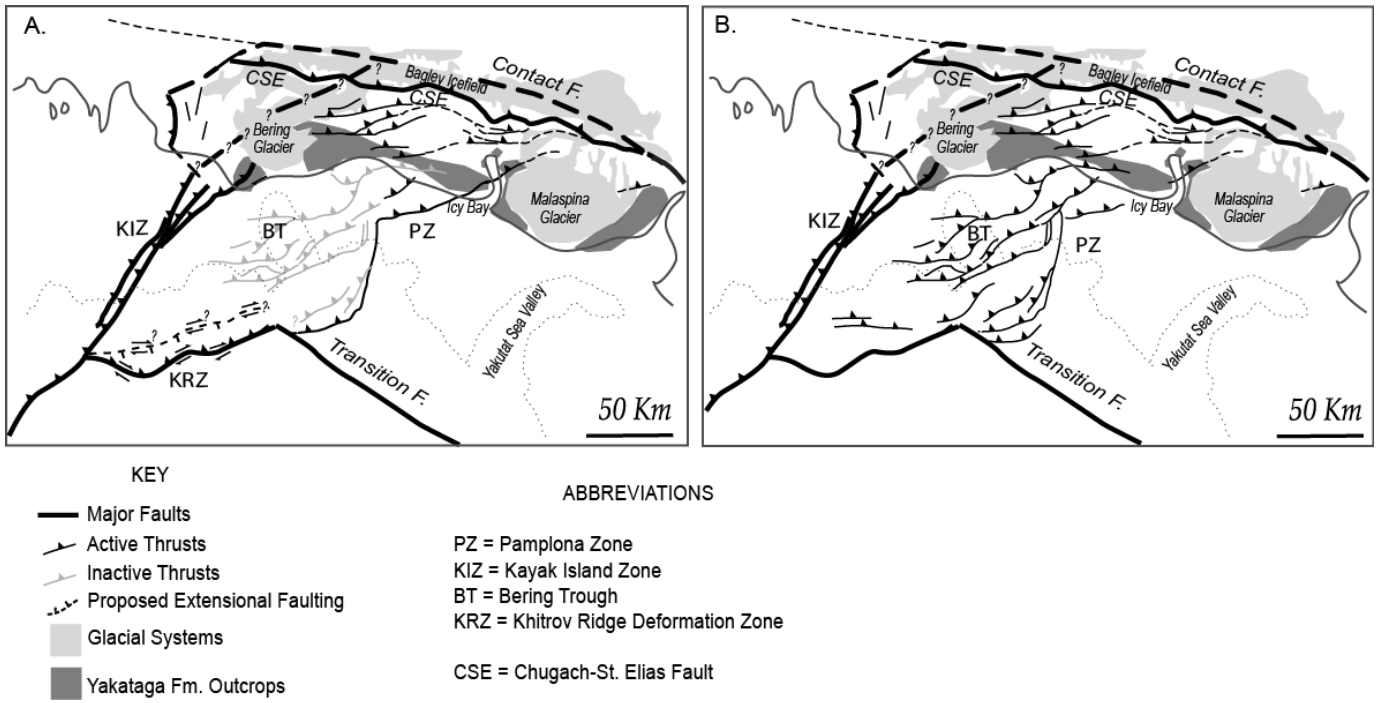

Figure 2.8. Tectonic map comparison of the proposed model (Figure 2.8a) and previous models (Figure 2.8b) [after *Pavlis et al.*, 2004]. Previously mapped active thrusts (black) within the PZ are mapped as inactive (gray) in proposed model. Figure 2.8a also defines the KRZ deformation zone near Khitrov Ridge as bounded by transtensional and transpressional structures. Active PZ faulting is connected onshore through Icy Bay. (BT = Bering Trough, CSE = Chugach-St. Elias Fault, KIZ = Kayak Island Zone, KRZ = Khitrov Ridge Deformation Zone, PZ = Pamplona Zone, RMT = Ragged Mountain Thrust)

Chapter 3: Coupled Stratigraphic and Structural Evolution of the offshore St. Elias Orogen, Alaska*

ABSTRACT

The St. Elias Orogen is the result of ~10 Myr of oblique collision and flat-slab subduction in the Gulf of Alaska between North America (NA) and the Yakutat microplate (YAK). Extensive glaciation and a complex tectonic environment make this region a unique case study in which to examine the details of terrane accretion and the possible coupled influence of climate and tectonics on the structural and topographic evolution of an orogenic wedge. Reflection seismic profiles across the offshore Pamplona Zone fold-thrust belt, the frontal St. Elias orogenic wedge, provide constraints for quantifying Pleistocene deformation recorded in the glaciomarine Yakataga formation. The Pleistocene shortening rate range from ~3 to ~5 mm/yr, compared to the current GPS-derived Yakutat-North America convergence rate across the St. Elias orogen of ~45 mm/yr. Growth strata and kinematic fold analysis allow comparison of relative timing of fault activity, which reveals temporal and spatial shifting of active deformation during the glacial period: faulting localized adjacent to the coastline and at the current submarine deformation front. The abandoned, currently inactive region is collocated with the major glacial depocenter in the region, the Bering Trough. These observations imply that glacial processes such as sediment loading and focused erosion during advance-retreat cycles have a direct effect on the evolution of individual faults within the Pamplona Zone and

* Large portions of this chapter are in press with co-authors S. Gulick and T. Pavlis in: *Tectonics*

the overall deformation pattern in the offshore St. Elias margin. This information provides key constraints for understanding how climatic shifts may have affected the evolution of margin architecture during Pleistocene glacial-interglacial periods.

3.1. INTRODUCTION

The Chugach-St. Elias mountain range and adjacent offshore fold-thrust belt in southern Alaska provides a unique natural laboratory in which to study the effects of surface processes on deformation and exhumation (Berger et al., 2008a; Chapman et al., 2008; Enkelmann et al., 2009; Meigs et al., 2008). Extensive glaciation of the orogen has occurred during three primary intervals since ~6 Ma (Berger et al., 2008a) each consisting of multiple glacial advance-retreat cycles. These cycles provide an efficient mechanism for mass redistribution, recognized as rapid erosion of the onshore orogen and associated deposition of glacially-derived terrigenous sediment to the offshore (Jaeger and Nittrouer, 1999; Stevenson and Embly, 1987). Recent thermochronologic studies in the area provide evidence for intensified exhumation and uplift in response to focused erosion by glaciers (Berger et al., 2008a; Enkelmann et al., 2009). Combined with the offshore sedimentary record, these data make a strong case for climatic influence on the evolving deformation of the orogen (e.g., Berger et al., 2008a; Worthington et al., 2008). Unlike other examples of eroding orogenic wedges (e.g., Roe et al., 2006; Whipple, 2009; Whipple and Meade, 2004; Whipple and Meade, 2006; Willett, 1999) the eroded material from the interior St. Elias remains partially within the system. These sediments are deposited in shelf basins located within the Pamplona Zone, the offshore

fold-thrust belt that forms the distal extent of the St. Elias orogenic wedge. As a result, I am able to examine the role of rapid deposition at the toe of a climatically-impacted glaciated wedge and determine if this process has an effect on the overall structural evolution and deformation pattern of the orogen.

Increased interest in the possible influence of climatic changes on the structural evolution of orogenic wedges (e.g., Roe et al., 2006; Whipple, 2009; Whipple and Meade, 2004; Willett, 2002) has motivated recent structural and thermochronologic studies of the Chugach-St. Elias (e.g., Berger et al., 2008a; Berger and Spotila, 2008; Berger et al., 2008b; Chapman et al., 2008; Enkelmann, 2008; Enkelmann et al., 2009; Meigs et al., 2008; Meigs and Sauber, 2000; Spotila and Meigs, 2004). The orogen provides a case study for examining this phenomenon given the strong climatic signal in the form of glacial advance/retreat cycles over the last ~6 Myr and continued accretion and uplift driven by YAK-NA convergence. However, fundamental questions regarding the quantification of shortening across the orogen and distribution of internal deformation within the wedge remain unanswered. These ambiguities limit understanding of how the orogen responds to climate forcing and the ability to measure potential structural reorganization due to mass redistribution by glacial erosion and deposition.

In this study, I investigate the structural and stratigraphic evolution of the Pamplona Zone within the context of a climatically impacted orogenic wedge. Constraints are provided by new seismic reflection profiles resulting in an updated fault map of the Pamplona Zone; restored offshore cross-sections documenting total shortening across key structures in different parts of the Pamplona Zone; and a model for the

structural evolution of the offshore margin at key time intervals showing temporal and spatial variations within the pattern of deformation. The results of this study provide the first detailed investigation of fault-fold kinematics and depositional trends in the offshore orogen and new insight into how the related processes of erosion, deposition and accretion influence deformation patterns within convergent margins.

3.2. THE ST. ELIAS OROGEN

3.2.1 Tectonic History

Orogenesis in the St. Elias region initiated at ~10 Ma at the onset of Yakutat-North America (YAK-NA) convergence (Rea and Snoeckx, 1995). In the last ~6 Myr, the Yakutat terrane has been lodged into the subduction corner, immediately east of the Copper River delta, constructing the present high topography and initiating extensive alpine and tidewater glaciation (Lagoe et al., 1993; Lagoe and Zellers, 1996; Rea et al., 1995; Rea and Snoeckx, 1995; Zellers, 1995). The modern Yakutat microplate is described by Pavlis et al. (2004) as the geologically defined Yakutat terrane plus segments of adjacent terranes that are undergoing active deformation between the Chugach-St. Elias fault and the Contact-Fairweather Fault lineation (Figure 3.1). The active offshore YAK-NA deformation front is located at the eastern extent of the Pamplona Zone fold and thrust belt (Plafker, 1987; Worthington et al., 2008). This geometry implies a wide, gently sloping thrust zone across the western third of the

Yakutat microplate, between the Chugach-St. Elias fault and the easternmost faults of the Pamplona Zone.

Current estimates of total shortening across the orogen are derived from restored onshore-offshore cross sections (Meigs et al., 2008; Wallace, 2008) and Euler pole modeling using current geodetic plate motions (Pavlis et al., 2004) (Table 3.1). Pavlis et al. (2004) assume that modern plate motion characterized by GPS data, 40-44 mm/yr (Elliott et al., 2010; Fletcher and Freymueller, 1999, 2003), were viable up to 0.5 Ma, resulting in a shortening estimate of ~20 km for the late Pleistocene which includes a rotational component. This and other fold kinematic studies (Chapman et al., 2008) conclude that the Pamplona Zone structures absorb only a small fraction of the total convergence, and are a second-order result of YAK rotation with respect to North America. Shortening across the offshore deformation front in these studies is estimated at ~5 km over 1 Ma, approximately 10% of total shortening across the orogen. These results suggest that the bulk of neotectonic deformation occurs farther towards the interior of the margin (Bruhn et al., 2004; Chapman et al., 2008; Pavlis et al., 2004).

Though they employ differing assumptions that result in variable shortening estimates, these studies (i.e., Chapman et al., 2008; Meigs et al., 2008; Pavlis et al., 2004; Wallace, 2008) are each predicated upon the synthesis of decades of onshore field studies and current campaigns that enhance the knowledge base regarding onshore structural relationships (detailed summaries of past work found in Plafker, 1987; Plafker et al., 1994; Risley et al., 1992). By comparison, knowledge of offshore structural relationships is limited. Until 2008, there had been no new regional offshore data available since the

1970's, with the most recent detailed mapping completed by Risley et al. (1992). This knowledge gap is especially problematic given that the St. Elias deformation front is located primarily offshore, continuing southwest via the Malaspina fault to the eastern extent of the Pamplona Zone fold-thrust belt (Chapman et al., 2008; Plafker, 1987; Worthington et al., 2008) (Figure 3.1). In hopes of addressing this problem, this study provides detailed fold analysis and shortening estimates across the major offshore structures of the St. Elias orogen. These results provide important constraints for future calculations of the total amount of shortening across the orogen and the distribution of internal deformation.

3.2.2 Glacial History

Glacial advance-retreat cycles provide the primary climate forcing that may affect structural evolution of the orogen. Alpine glaciation within the margin may have occurred as early as ~7 Ma (Lagoe et al., 1993) and was well underway by 5.5 Ma (Lagoe et al., 1993; Rea and Snoeckx, 1995; White et al., 1997), when elevation of the Chugach-St. Elias mountain belt was sufficient to trap precipitation from storms generated in the Gulf of Alaska. The margin's glacial period, continuing from ~5.5 Ma to present, can be divided into three distinct intervals. The first two intervals, early-Pliocene Glacial Interval A and mid-Pliocene Glacial Interval B are linked to the appearance of ice-rafted debris (IRD) within deep-sea records. These intervals are separated by reduction in glaciomarine sedimentation related to the ~4.5-2.8 Ma Mid-Pliocene Warm Period

(Krissek, 1995; Lagoe et al., 1993; Prueher, 1998; Rea et al., 1995; Rea and Snoeckx, 1995).

Berger et al. (2008a) identified the third interval, Glacial Interval C, as a series of widespread glacial advances throughout the middle to late Pleistocene in response to the transition to 100 kyr orbital cycles. This interval is recorded by a doubling of terrigenous sediment offshore and a regional unconformity that marks the initial glacial advance to the shelf edge (Berger et al., 2008a; Carlson, 1989). These glacial advances carved a series of U-shaped sea valleys that define glacial troughs that are re-occupied with each successive advance and are visible as seafloor depressions (Berger et al., 2008a; Carlson, 1989; Lagoe et al., 1993; Lagoe and Zellers, 1996; Rea and Snoeckx, 1995). The Last Glacial Maximum is estimated at ~14 ka in the Gulf of Alaska (Mann and Peteet, 1994).

3.2.3 Stratigraphic Framework

A thick sedimentary cover overlies Yakutat basement of Paleocene-lower Eocene oceanic basalt (Plafker, 1987) and can be divided into two primary packages: pre-glacial sedimentary rocks and syn-orogenic glaciomarine deposits. The offshore pre-glacial sedimentary sequence is formed by the Poul Creek and Kultieth Formations. The glacial sequence is known as the Yakataga Formation. Sandstone, siltstone, mudstone, and interbedded coal form the Kulthieth Formation, the oldest unit, dated by faunal and floral material to be early Eocene-early Oligocene in age (~55-28.5 Ma) (Plafker, 1987). Onshore thickness of the Kulthieth Formation has been measured up to ~3 km (Plafker, 1987; Trop and Ridgway, 2007). The younger Poul Creek Formation was deposited

conformably over the Kulthieth Formation. This unit is made up of Oligocene-Miocene marine mudstones interbedded with siltstones and sandstones, as well as localized intercalated tuffs and pillow lavas (Lagoe et al., 1993; Plafker, 1987).

The glacially-derived Yakataga Formation is the youngest unit and ranges in thickness from 0 km to >6 km. The Yakataga is not well dated, but is known to date from the onset of St. Elias glaciation in the late-Miocene (~5.5 Ma) to present (Lagoe et al., 1993; Rea and Snoeckx, 1995; White et al., 1997). For the purposes of this paper it is important to note that the Yakataga Formation is a generic term for a great variety of syn-orogenic strata that range from flat-lying sequences deposited conformably on older deposits to complex depositional sequences with numerous internal angular unconformities associated with deposition during fold-thrust activity (i.e., Plafker et al., 1994; Trop and Ridgway, 2007).

3.3. DATA

This study is based on interpretation, integration and remapping of multiple seismic reflection surveys and a high-resolution bathymetric survey (Figure 3.1b). In 2008, ~1250 km of multichannel seismic reflection profiles were collected aboard the R/V *Marcus Langseth* as part of the St. Elias Erosion and Tectonics Project (STEEP). The seismic source included 36 Bolt airguns with a total volume of 6600 cubic inches fired every 50 m. Receivers were located in an 8 km long solid streamer at 12.5 m spacing, leading to a common midpoint (CMP) spacing of 6.25 m. Processing included trace regularization, normal move-out correction, bandpass filtering, muting, stacking and

frequency-wave number migration using Paradigm Geophysical FOCUS software. Vertical resolution at the seafloor for this dataset is ~30 m. Gulick et al. [2007] details the acquisition methods and processing steps of high-resolution seismic data (vertical resolution ~5 m) collected in 2004 as a site survey for two IODP drilling proposals. I also interpret a 1975 basin-scale seismic reflection survey by the USGS (Bruns, 1983b; Bruns and Schwab, 1983) in the context of newer datasets. In addition, mapping on a 1979 Western Geophysical survey to the east of the Pamplona Zone provides a regional perspective of the sediment-basement contact and estimation of the total sediment volume on the Yakutat shelf for use in mass balance estimates. Locations of the high-resolution and basin-scale seismic profiles used in this study are given in Figure 3.1.

High-resolution bathymetric data include more than 162,000 km^2 of 100-m^2 resolution multibeam sonar data that were collected in the summer of 2005 along the base of the continental slope in the Gulf of Alaska as part of a mapping project for the United Nations Convention on the Law of the Sea (Gardner et al., 2006).

3.4. METHODS

3.4.1 Seismic Interpretation and Correlation

I mapped five horizons where possible throughout the seismic surveys to determine relative timing of observed structural and stratigraphic events (Table 3.2). The basis for horizon mapping and correlation is a combination of independent seismic facies and seismic stratigraphic analysis; application of previous biostratigraphic work and

interpretations (Lagoe and Zellers, 1996; Zellers, 1995); and integration of previous interpretations of the 1975 USGS survey (Bruns and Schwab, 1983; Zellers, 1995). The procedure for correlating previous interpretations to more recent surveys included uploading previous seismic SEGY data into the GeoFrame interpretation software and verifying geometry and survey relationships; digitizing interpretations and well correlations from the original paper seismic sections; and examining line-ties between and within each survey to compare seismic facies and correlate horizons.

The basement contact, Horizon 5, separates the Pamplona Zone sedimentary cover sequence from the Yakutat basement. The basement contact is characterized by bright, low frequency arrivals that are visible through noise and migration artifacts typical at depths greater than ~5 s two-way-travel time (twtt) on the STEEP survey profiles. The basement reflector is not readily observed on the 1975 G-1-75 USGS survey or the 2004 EW0408 high-resolution survey due to lack of penetration. However, in light of the full penetration provided by the STEEP data, I have partially correlated the basement reflector on some G-1-75 profiles where appropriate.

The contact between the Yakataga and Poul Creek Formations, Horizon 4, is mapped throughout the region based on Zellers' (1995) correlation of industry well data on a subset of G-1-75 USGS profiles. The data points at industry wells ARCO 07 and Exxon 80 (Figure 3.1b) sample the Yakataga/Poul Creek contact at ~2600 m and ~3500 m below sea level, respectively (Zellers, 1995). These data correlate to horizons at 2.2 s twtt and 2.6 s twtt on profiles from the 1975 USGS dataset (Zellers, 1995) (Figure 3.2b). I apply Zellers' (1995) interpretation to the 2008 STEEP survey by examining line

crossings within my interpretation software. This methodology is preferred to relying solely on seismic facies analysis, given the locally gradational Yakataga-Poul Creek transition.

Zellers (1995) biostratigraphic analysis and seismic interpretation provides the key parameter for mapping Horizon 3, the approximate Plio-Pleistocene transition, throughout the current seismic surveys. The Pliocene planktonic foraminifera *Neogloboquandrina asanoi* is last observed in offshore wells at a depth of ~2250 m (Texaco 46) and ~1400 m (Exxon 80) (Figure 3.1b) below sea level. These depths correlate to seismic horizons at ~1.8 s twtt and ~1.3 s twtt, respectively (Figure 3.2b). Absence of the *N. asanoi* fossil above these depths indicates that younger sedimentary packages and associated mapped reflectors and unconformities are Pleistocene in age (Zellers, 1995). Horizon 3 is essentially equivalent to the "Yellow/Orange" transition from Zellers (1995), but has been remapped where high-resolution data from EW0408 provides better imaging and reveals errors in the original interpretation. This comparison and remapping is particularly helpful where strong water bottom multiples in the G-1-75 survey eclipse the near-surface trends of the seismic strata.

Horizon 2 (H2), is interpreted throughout the three seismic surveys as a time-marker for understanding the structural evolution of specific faults and folds across different profiles. An early Pleistocene age assignment is derived from the horizon's location within the seismic strata between the Plio-Pleistocene transition (H3) and a proposed mid-Pleistocene unconformity (Horizon 1) from Worthington et al. (2008) and Berger et al. (2008a).

Horizon 1 (H1) is defined on the EW0408 profiles (Figure 3.1) as an angular unconformity that correlates with the ~1 Ma onset of Glacial Interval C as described in Berger et al. [2008a] (Table 3.2). Berger et al. (2008a) define the start of Glacial Interval C as the first glacial advance beyond the inner shelf to the shelf edge. This and subsequent glacial advances to the shelf edge are thought to be coeval with an order-of-magnitude increase in exhumation rates onshore (Berger et al., 2008a). Worthington et al. (2008) describe this unconformity as a fundamental transition of the stratal architecture within the Bering Trough. Below H1, underlying strata are deformed by shortening on underlying faults. Above H1, strata do not display major signs of deformation such as faulting or large-scale folding (Worthington et al., 2008).

3.4.2 Depth Conversion and Structural Analysis

I calculate velocity-depth conversions for structural analysis and estimations of sediment thickness and volume using velocities models derived from two wide-angle seismic refraction profiles acquired as part of the 2008 STEEP survey (Figure 3.1a). Figure 3.2 shows the calculated velocity model that is used for depth conversion of post-stack seismic profiles. To evaluate the validity of my seismic interpretations and relate these observations to deformation rates, I used the software package 2D Move to restore depth sections prepared for two of the seismic lines. Structural analysis and shortening calculations were performed through a series of forward and inverse modeling of various fault geometries.

3.5. RESULTS

3.5.1 Structural Contours and Depositional History

The sediment-basement contact, Horizon 5, is observed at depths up to 7.57 s twtt on the 2008 STEEP survey. The structural contour map (Figure 3.3a) of the basement horizon reflects a regional NW basement dip of ~5.7° over a horizontal distance of 150 km from a basement high where the basement surface is at the seafloor to a low of ~15 km at the western extent of 2008 STEEP profile STEEP01a (A-A', Figure 3.3a). The basement also dips along B-B' at ~3° (orthogonally to A-A') from a high of ~9 km at the shelf edge to ~15 km near the Alaskan coast (Figure 3.3a).

A time-thickness map of the seafloor-basement interval illustrates the overall sediment thickness (in twtt) and depositional patterns on the Yakutat shelf from near Yakutat Bay across the Pamplona Zone to Kayak Island (Figure 3.3b). Sediment thickness increases in the direction of basement dip creating a large wedge of sediment that is composed of offscraped and accreted material in addition to sediment deposited through the process of exhumation and erosion of the St. Elias Mountains. Based on my coincident refraction data, the maximum sediment thickness is ~15 km, which is thicker than reported by previous authors (e.g., 10 km in *Plafker et al.*, 1987).

The thickest sedimentary cover is a composite effect of structural thickening and sedimentation that varies over time, located near the coast covering the interior Pamplona Zone thrust belt. The estimated total sediment volume within the Pamplona Zone, which is essentially an accretionary prism created by the subduction of the Yakutat block

beneath North America, is ~32 x10^3 km^3. The total sediment volume across the Yakutat shelf can be estimated at ~110 x10^3 km^3.

The Yakataga-Poul Creek contact, Horizon 4, divides the total sediment volume into two distinct packages: pre-glacial sediments and glaciomarine sediments deposited after the onset of glaciation at ~5.5 Ma. This horizon is observable on profiles within both the STEEP and G-1-75 surveys at depths between ~1.2-11.7 km (0.74-4.63 s twtt). A time-thickness map of the pre-glacial Yakutat shelf formations, the interval between the basement contact and Horizon 4, is shown in Figure 3.4a. Thickness increases near Cape Yakataga and decreases gradually away from the current coastline, reaching a minimum in the modern Bering Trough region. Thickness gradually increases again to the west, where deposition may have been influenced by the Copper River system. These apparent thickness variations are a combined product of pre-glacial depositional patterns and thickening of the section along stacked thrust faults, folds, or both in the deeper, poorly imaged part of the seismic sections. Overall, offshore thickness of pre-Yakataga deposits on the Yakutat shelf range from ~2.4 km to ~10 km (~1.38-5.20 s twtt).

Total thickness of glaciomarine sediments, the interval between Horizon 4 and the seafloor is depicted in Figure 3.4b. The thickest sediments are located in the modern Bering Trough and near the depocenter associated with advance of the Malaspina/Icy Bay glacier system, whereas sediment thickness decreases away from these modern depocenters. This observation indicates that, though troughs are typically defined as erosional features, sediment infill during retreat cycles also makes them primary depocenters. Comparing sediment thickness of pre-glacial and glaciomarine sediments

reveals a shift in the position of total sequence thickness from shelf proximal to more evenly distributed across the shelf. The shifting depositional patterns also highlight the development of the Bering Trough as the modern shelf depocenter after the onset of glaciation in the orogen.

Horizons 1, 2 and 3 further divide the offshore, glacially derived Yakataga Formation. The Plio-Pleistocene transition, Horizon 3 (H3), is observed on the STEEP, G175 and EW0408 surveys between depths of ~0.20 an ~7.7 km (~0.136-3.454 s twtt). Horizon 2 is fairly continuous throughout the Pamplona Zone, occasionally truncated by Horizon 3 and is observed at depths of ~0.18-5.4 km (0.120-2.647 s twtt). H1 is mapped on adjacent STEEP and G-1-75 profiles within the Bering Trough and to the northwest near the Pamplona Zone deformation front at depths ranging from ~0.20 to ~3.8 km (~0.136-1.984 s twtt).

A time-thickness plot of the Mio-Pliocene Yakataga interval (Figure 3.4c; H4-H3 Interval) reveals two primary active depocenters. One depocenter formed directly offshore from the modern Bering Glacier, infilling a proto-Bering Trough on the inner shelf. The other depocenter is isolated from the proto-Bering Trough and from the coastline, though it is partially collocated with the primary active pre-glacial depocenter identified in Figure 3.4a (H5-H4 Interval). The isolation of this feature away from major sediment sources onshore or associated with the Bering Trough suggests that this interval illustrates a transition in deposition pattern on the shelf as the Bering Glacier became the dominant sediment source. In addition, uplift on structures near the Cape Yakataga region

initiated during this time, as indicated by the thinning of the section directly adjacent to the isolated depocenter.

Figure 3.4d depicts sediment thickness during the interval between the Plio-Pleistocene transition and the 1 Ma unconformity (H3-H1 Isopach). Here, I observe further concentration of deposition near the Bering Trough. Deposition during Glacial Interval C (Figure 3.4e) shows concentration of sediments towards the outer shelf. This pattern is consistent with observed glacial advance-retreat cycles in the current Bering Trough strata. As glaciers advance to the shelf edge, previous deposits are eroded and subsequently deposited off the shelf towards the slope and abyssal plain.

Sediment time-thickness of the interval between the Mid-Pleistocene Transition and the seafloor reflects the extent of shelfal erosion that occurred at the onset of Glacial Interval C (Figure 3.4e). The thickest portions of sediment on the shelf are collocated with the modern Bering Trough, as expected. Further, erosion during this interval was not limited to the immediate Bering Trough locale, indicating that the Bering Glacier and its associated arms advanced to the east of the modern trough. In addition, I have interpreted the horizon to the edge of the shelf and onto the slope at the distal extent of the Bering Trough, confirming glacial advance across the entire width of the modern Yakutat shelf.

3.5.2 Analysis of Fault Activity

3.5.2.1 Cape Yakataga-Icy Bay Region

Profile STEEP01a (Figure 3.5) images the northeastern Pamplona Zone fold-thrust belt near Icy Bay, from the eastern deformation front to the interior of the currently active fold-thrust belt. The profile crosses three faults and their associated folds (A1, A2, A3; Table 3.3) that deform a sedimentary sequence ~14 km thick from the basement reflector to the seafloor. East of F1, strata lie relatively flat, with a gentle westward dip observed on H4 and H5 and a slight thinning of the Pliocene Yakataga deposits, defined by H3 and H4 (Figure 3.5). Strata are abruptly deformed at F1 and are folded and faulted on multiple structures west of F1. Thus, F1 forms the easternmost fault of the Pamplona Zone and the modern Yakutat-North America deformation front.

Structural relief of A1 is gentle at the seafloor, where Horizon 2 has been eroded and truncated. Growth strata are present above Horizon 2, but not observed below Horizon 2 (Figure 3.5). This observation, combined with relatively constant stratal thickness across the structure and minimal vertical offset indicates that deformation of A1 initiated in the early-mid Pleistocene, after the deposition of Horizon 2. Deformation on F1 appears continuous since its early-mid Pleistocene initiation given constant growth strata angle on the backlimb of A1. Vertical relief at the seafloor across Anticline A2 is approximately 100 ms, or ~75 m using a water column velocity of 1500 m/s (Figure 3.5; Figure 3.6). Vertical relief associated with deformation on F2 and growth of A2 increases with depth until the Plio-Pleistocene transition, marked by H3. Vertical offset across the

fault on Horizons 2 and 3 are ~500 ms and >1000 ms, respectively. Potential errors in these estimations arise due to erosion at the seafloor and imaging problems. Vertical offset on Horizon 4 is ~1200 ms.

Deformation history observed on A2 since initiation appears to have occurred in two stages. Truncations observed below Horizon 3, within the Pliocene Yakataga sediments, as well as a change in thickness of this package across A2, indicate that deformation initiated prior to the Plio-Pleistocene transition and define Growth Stage 1 (Figure 3.6; Table 3.3). In addition, the fold displays a significant footwall syncline suggestive of early fold growth followed by fault propagation. Imaging problems prevent exact delineation of this deformation stage; however, strata return to parallel above H2.This observation indicates that growth across this fold slowed or ceased in the early-mid Pleistocene. A second stage of deformation across A2, Growth Stage 2, initiated during the mid-Pleistocene and is possibly related to fault propagation continuing growth of A2.

Figure 3.7 defines two growth stratal packages between folds A2 and A3 above Horizon 3. On the forelimb of A3, the dark gray stratal package thins as growth strata are truncated during deposition, onlapping onto the forelimb, while retaining constant thickness on the backlimb of A2. These observations indicate that, though deformation was initiated on A2 before the Plio-Pleistocene transition, growth subsequent to the deposition of Horizon 3 shut down for a period while deformation initiated across A3. A2 has since reactivated to deform the seafloor and initiate growth strata near the surface on the forelimb and backlimb of A2.

Anticline A3 exhibits a box-fold shape with a shallow dipping backlimb, a relatively flat top and a steeply dipping forelimb (Figure 3.5). Deformation initiated subsequent to the Plio-Pleistocene transition, given lack of fault-adjacent growth strata observed at depths below Horizon 3. Depositional packages on the backlimb of A3 appear to be thickening above H3 before truncating at the erosive surface defined by H1. Strata on the forelimb are parallel above H3 and thin above Horizon 2.

Profile STEEP16 (Figure 3.8) images two folds, A3 (also described in Figure 3.5) and A2. The eastern fold, A2, was largely inactive after the Plio-Pleistocene transition, Horizon 3. Using Horizon A as a time marker, I deduce that initial deformation of A2 predates that of A3, given placement of growth strata below Horizon A on A2 and above Horizon A on A3. Thinning of sedimentary packages on the forelimb of A3 is most pronounced just below and above Horizon 3, suggesting that deformation of A3 was most rapid during the Plio-Pleistocene transition. The presence of deformed strata at the seafloor suggests that A3 is currently active, though deformation appears to be waning above Horizon 3. Horizon 1 is interpreted near the seafloor on the profile, suggesting that the erosional unconformity related to the mid-Pleistocene transition and the onset of the glacial interval C (Berger et al., 2008a) is regional and not only limited to the Bering Trough locale.

STEEP17 (Figure 3.9) images the flank of A4, which may be the offshore continuation of the Sullivan fault (Figure 3.1). Between Horizon A and Horizon 3, strata are not well imaged, though the thicknesses of individual layers appear constant across the profile, indicating that movement on this fault initiated well after the Plio-Pleistocene

transition. Above Horizon A, Horizon 2 and overlying strata downlap and pinch out onto the flank of the anticline. Though subtle, topography across the top of the structure suggests that the fold is currently deforming. As in STEEP16, the mid-Pleistocene transition (Horizon 1) can be mapped near the seafloor, as well as multiple erosion events prior to and subsequent to the ~1 Ma erosional unconformity.

3.5.2.2 Bering Trough Region

Seismic section STEEP09 (Figure 3.10a) images the continental shelf below the current Bering Trough and adjacent slope. The profile crosses two abandoned structures beneath the current shelf (BT3 and BT4) and two currently active slope-toe faults (BT1, BT2).

Faults BT3 and BT4 are currently buried by ~1500 ms of undeformed sediments and have gradually been rendered inactive since before the early Pleistocene deposition of Horizon 2. Thinning and truncated strata are observed on the forelimb of BT4 (Table 3.4) both above and below Horizon 3. This geometry indicates that deformation on BT4 pre-dates the Plio-Pleistocene transition and continues for a short time into the early-Pleistocene.

Above Horizon A, which marks the cessation of thrusting on BT3, sediments are relatively flat-lying and slightly seaward dipping indicating an increase in accommodation space, possibly by subsidence, during the time period defined by Horizons 2 and 3. Seaward thickening of stratal packages defined by marker Horizons B, C and D also indicate progradation of the shelf edge during this time period.

The series of erosive surfaces including and above Horizon 1 are the signature of glacial advance-retreat cycles as outlined in Berger et al. (2008a) and Worthington et al. (2008). Horizon 1 marks the first glacial advance to the edge of the modern continental shelf, eroding the top of the previous shelf and depositing much of the current slope sediments. Subsequent glacial cycles have continued the erosion of the top of the shelf and deposition of slope sediments.

At the southeastern end of the seismic profile, two currently active faults and associated anticlines are positioned towards the toe of the continental slope. Scarps ~750 m and ~300 m high associated with these folds are visible on high-resolution bathymetry of the continental slope (Worthington et al., 2008) (Figure 3.10b). Given high sediment rates in this portion of the study area, the presence of well-defined seafloor escarpments provides additional evidence that these structures are currently active. These observations strengthen conclusions from previous structural (Worthington et al., 2008) and earthquake (Doser et al., 1997) studies that indicate current activity on these structures.

BT2 initiated after the Plio-Pleistocene transition, given lack of growth strata observed below Horizon 3 (Figure 3.10a). Discontinuity observed in the seismic strata below Horizon 3 and between Horizons 2 and 3 is most likely due to slope sediment processes such as slumping and minor, non-glacier related channelization. During the early Pleistocene, the time period bounded by Horizons 2 and 3, BT2 appears to have undergone two stages of deformation. The first stage is defined by Horizons 3 and F, characterized by minor thinning of the sediment package on the backlimb of the fold. These sediments follow the fold's structure to the top of the forelimb where they downlap

on Horizon E, indicating sediment failure and deposition into the small basin between BT2 and BT1. The second stage of deformation is defined by Horizons F and 3. This stratal package thins rapidly and truncates at the top of the forelimb on the downlap surface provided by Horizon F. The remaining sediment is presumably deposited in the basin formed between BT1 and BT2.

The presence of these two distinct sedimentary packages is indicative of either a decrease in slope sedimentation during the early Pleistocene or an increase in deformation rate across BT2. Between Horizons 1 and 2, the angle of the observed growth strata becomes less pronounced, indicating a gradual decrease in fault growth rate during the early-mid-Pleistocene. Above Horizon 1, sediments are truncated by the anticline and are very slightly tilted towards the shelf, indicating minimal deformation on BT2 from ~1Ma to the present.

Like BT2, BT1 also appears to have undergone distinct stages of deformation. Within the mini-basin formed on the backlimb of the anticline associated with BT1, I define three sedimentary packages above Horizon E associated with three stages of deformation. The lowermost package exhibits the most dramatic thinning, while the uppermost package is relatively flat-lying, with some truncation of strata at the seafloor. This overall pattern indicates that either the deformation rate across this structure has decreased or the sedimentation rate has increased since inception. The chaotic nature of the strata below Horizon E and secondary, minor faulting increases the difficulty of constraining the relative timing of fault initiation compared to BT2. Given the placement of Horizon E with respect to the Plio-Pleistocene transition marked by Horizon 3, and the

slight thinning of strata below Horizon 3 towards the top of the fold, I infer that deformation on BT1 was initiated at the same time as, or slightly before, BT2.

Seismic section GOA2505 (Figure 3.11) provides a high-resolution image of the Bering Trough above ~2000 ms, partially collocated with profile STEEP09. The profile can be divided into two distinct sedimentary packages defined by Horizon 1. Two large-scale folds, BT4 and BT5, are imaged below Horizon 1. Near BT4, growth strata above Horizons 2 and 3 indicate that deformation on this structure occurred throughout the early Pleistocene. Deformation appears to have ceased before the mid-Pleistocene transition demarcated by Horizon 1. As observed on profile STEEP09 (Figure 3.10) deformation on BT4 predated the Plio-Pleistocene transition and ceased in the early-Pleistocene. Above Horizon 1, the overlying ~200 m-thick package depicts a series of minimally deformed glacial-interglacial sequences. Lack of significant deformation in these upper sequences indicates that the underlying faults have been abandoned prior to the mid-Pleistocene transition.

Seismic section GOA2507 (Figure 3.12) images the Bering Trough region west of GOA2505 and is collocated with the current bathymetric expression of the Trough. The portion of the profile imaged here is located on the inner shelf, with respect to GOA 2505 and depicts glacial advance sequences prior to the regional Mid-Pleistocene erosional event H1. Below H2, on the forelimb of fold BT5, shelf-break facies are present between 1.0-1.5 s twtt, suggesting a previous depositional shelf break at this location subsequent to the Plio-Pleistocene transition. Thus, it appears that the formation of BT5 is partially controlled by glacial depositional processes that dominate the inner shelf. Truncations of

seismic strata, the presence of growth stratal packages on the backlimb and overall geometry of BT5 provide evidence that this structure accommodated YAK-NA convergence as a growth fold in addition to acting as the former shelf edge. The overall architecture of BT5 is thus the product of coupled depositional and tectonic processes.

Toplapping of strata below Horizon A indicates that, in this portion of the shelf, Horizon A initially beveled the top of the BT5 fold. The flatter dip angle of sediments above Horizon A and the more continuous nature of the strata define glacial advance-retreat cycles, which have increased in frequency subsequent to the Mid-Pleistocene Transition. Strata above Horizon A are minimally deformed, suggesting that active convergence on BT5 had ceased by the early-mid Pleistocene.

3.5.3 Synthesis of Pamplona Zone fault activity

Examination of the relative timing and extent of deformation on faults imaged by the seismic data reveals two overall trends in structural evolution of the Pamplona Zone since the Pliocene. First, fault initiation is asynchronous and discontinuous: frontal faults can initiate prior to internal structures (e.g., Anticlines A2 and A3; Figure 3.5) and distinct, multiple stages of growth can occur on individual faults (e.g., Anticline A2; Figures 3.5, 3.6, 3.7). Second, faults underlying the modern Bering Trough (BT3, BT4, BT5) have been gradually abandoned (Figures 3.10, 3.11, 3.12), while deformation has localized on the easternmost PZ structures (BT1, BT2, A1, A2; Figures 3.5, 3.10) and on faults to the northwest, near the core of the orogen (A3, A4; Figures 3.5, 3.8, 3.9).

Comparison of fault activity across the margin at specific time increments reveals these trends in structural evolution (Figure 3.13). During the Mio-Pliocene glacial period (Figure 3.13a), at ~6–1.8 Ma, deformation occurred on two primary structures that cut through the Bering Trough region, across the shelf in the strike direction. During this interval, the deformation front was located west of the current deformation front and deposition was primarily concentrated near the coastline. This observation is consistent with a narrow depositional shelf in which the distal extent is demarcated by the deformation front (Chapman et al., 2008).

In the early Pleistocene, the time interval subsequent to the Plio-Pleistocene transition and prior to the arbitrary time marker represented by Horizon 2 (Figure 3.13b), deformation was distributed across multiple structures mapped throughout the PZ. Faults BT1 and BT2 were activated on the slope, representing the outboard migration of the YAK-NA deformation front. Deformation continued on A2 and initiated on A4. This period also marks an overall widening of the Pamplona Zone as material continued to accrete.

From the early to mid-Pleistocene, the time interval demarcated by the arbitrary time marker Horizon 2 and the Mid-Pleistocene Transition (Horizon 1), previously active structures within the interior of the PZ and near the current Bering Trough, were abandoned while the current deformation front initiated (Figure 3.13c). Bimodal fault localization occurred, with deformation migrating westward towards the inner St. Elias orogen, and farther offshore towards the distal extent of the wedge. The current offshore

deformation front most likely continues onshore through Icy Bay to link up with the Malaspina Fault (Chapman et al., 2008; Worthington et al., 2008).

From the mid-Pleistocene to Recent, the time period that encompasses Glacial Interval 'C' (Berger et al., 2008a) faulting has further localized adjacent to the coastline and at the current submarine deformation front (Figure 3.13d). By this time, fault activity within the Bering Trough had been entirely abandoned, and the Bering Trough has developed as the primary glacial depocenter (Figure 3.4d).

3.5.4 Shortening Estimates

Figure 3.14 shows a converted depth section of STEEP01 and two possible reconstructions. In the first reconstruction, near surface dip-slip on Fault F2 is restored before the remainder of the line is restored by simple flexural slip unfolding (Figure 3.14a). This reconstruction is more conservative than the second and yields a total shortening across STEEP01 of ~3600-3900 m. Although this model provides a general reconstruction of the growth strata and the pre-growth strata, the geometry of the décollement in unconstrained and would require accommodation of the motion within the poorly imaged, deeper part of the section.

In the second reconstruction scheme, dip-slip on F2 is restored as in Figure 3.14a. For the next reconstruction steps, A3 was modeled as a tri-shear fault propagation fold (e.g., Zapata and Allmendinger, 1996). This model is appropriate given the apparent convergence of the fold axes at depth toward an interpreted fault tip (Figure 3.14b, c; 3.15). The broad fold width and shallow back limb was accommodated by an interpreted

flat and gentle ramp of the Pamplona Zone detachment at depth (Figure 3.15). Further, the reconstruction of A3 was split into two steps which allows for fault propagation and a slight change in geometry of F3 with time, more accurately accommodating the complicated fold geometry of A3. In this way, I was also able to consider fault tilt and propagation during deformation. The remainder of the profile was reconstructed by simple flexural slip unfolding of A1 and A2 as well as restoration of minor residual dip on A3. This last restoration step avoids the details of the formation of A1 and the early phase of A2, but produces a reasonable restoration for evaluation of the total shortening in the system. This model yields a total shortening across the profile of ~6 km.

Figure 3.16 shows a converted depth section of STEEP09 and my best-fit model reconstruction developed through a combination of seismic profile interpretation and forward modeling of various fault-fold scenarios. This model is consistent with both the seismic data and limited well control. Fault-bend fold modeling (e.g., Suppe, 1997; Suppe et al., 1992) of BT1 and BT2 reveal a combined ~8 km shortening, resulting in a Pleistocene deformation rate of ~4.4 mm/yr. Approximately 200 m of shortening on BT3 is restored using a trishear model with a trishear angle of 60 degrees (apex = 60) (e.g., Zapata and Allmendinger, 1996). Restoration of BT4 and the auxiliary fault BT4a begins with 400 m on a flat segment at the seaward extent of BT4. Next, three increments of slip were restored on BT4a, the blind flat fault that branches off the main BT4 thrust. This was modeled as fault propagation with 200 m slip increments and 1000 m fault propagation increments. The total shortening restored on this structure is 600 m. Finally,

fault-bend fold modeling of the main fault BT4 reveals an additional 4 km of shortening. Total shortening across the STEEP09 is ~13.2 km.

3.6. DISCUSSION

3.6.1 Implications for orogen-scale evolution

Analysis of Pamplona Zone faulting at multiple time intervals reveals bimodal progression of active deformation: faulting steps both westward, towards the rear of the St. Elias orogen, and eastward, towards the advancing deformation front with time (Figure 3.13). The westward progression is exemplified by activation of coastal faults A3 (Figures 3.5, 3.7, 3.8, 3.15) and A4 (Figure 3.9) since the Plio-Pleistocene transition (Figures 3.13). Structural reorganization in response to onshore glacial erosion, as proposed by Berger et al. (2008a) and others (Berger et al., 2008b; Chapman et al., 2008; Worthington et al., 2008), likely controls activation of these proximal faults. The proposed structural reorganization is based on investigations of critical wedge response to climate forcing in the form of erosion, in which orogens respond to changes in material flux through redistribution of internal deformation (e.g., Tomkin and Roe, 2007; Whipple and Meade, 2006). Multiple studies have shown that glacial intensification in the St. Elias and the related increase in erosion are directly related to accelerated exhumation rates in the onshore portion of the wedge (Berger et al., 2008a; Berger and Spotila, 2008; Berger et al., 2008b; Spotila and Meigs, 2004). This exhumation is accomplished by initiation, acceleration and reactivation of out-of-sequence thrusts within the hinterland and an

overall narrowing of the wedge (Berger et al., 2008a). Similarly, I propose that activation of coastal faults within the Pamplona Zone may be related to predicted localization of deformation in the hinterland.

Eastward progression of the active deformation front at the toe of the wedge (Figure 3.13) appears to conflict with models (e.g., Berger et al., 2008a) for the orogen in which deformation is localized towards the hinterland as a means of achieving critical taper in response to intensified glacial erosion. In fact, the activation of these distal faults during the late Pliocene suggests a widening of the wedge as the deformation front steps eastward during the same period in which these models predict an overall narrowing of the wedge. I propose that continued frontal accretion of YAK shelf material above the predicted décollement leads to initiation and persistence of these active faults irrespective of glacial processes farther back in the wedge. Recent modeling results by Simpson (2010) support this proposal by showing that sediment influx at a wedge front is accommodated by accretion and faulting at the trench, even while most deformation is concentrated at the back of a wedge. In the case of the Pamplona Zone, sediment thickness across the deformation front is ~8 km and incoming sediment volume is substantial (Figures 3.4, 3.5). Additionally, the predicted décollement depth on the shelf is near the sediment-basement contact (Figure 3.5). It follows that a sizable portion of incoming sediment is incorporated into the wedge by continued frontal accretion as YAK-NA convergence progresses. Long-term growth of the orogen, therefore, is partly influenced by this frontal accretion which I predict is accommodated by further eastward advance of faulting at deformation front.

Structural evolution of the Pamplona Zone during St. Elias glaciation is also characterized by abandonment of structures within the Bering Trough, BT3, BT4 and BT5 (Figures 3.10, 3.11, 3.12, 3.13), which is the primary glacial depocenter on the shelf (Figures 3.4d, 3.17). I suggest that the simultaneous development of the Bering Trough depocenter and abandonment of these faults is not coincidental. Recent numerical modeling by Simpson (2010) supports this suggestion by showing that interior thrusts in a critical wedge can be buried by a constant sediment influx from the adjacent hinterland, while frontal thrusts remain active. Worthington et al. (2008) propose that these linked depositional and structural patterns are the result of rapid sedimentation suppressing internal deformation by increasing normal stress on buried faults. This focused deposition increases the load on structures within the depocenter and may cause strain localization elsewhere in the margin, i.e., near Cape Yakataga, at the easternmost Pamplona Zone, and in the onshore fold-thrust belt. This phenomenon could be the corollary process to what is occurring onshore, where focused erosion localizes strain in its vicinity.

Taken as a whole, climate drivers of tectonic evolution of the St. Elias wedge include multiple cycles of glacial erosion in the onshore hinterland (i.e., Berger et al., 2008a; Berger and Spotila, 2008; Meigs and Sauber, 2000; Spotila and Meigs, 2004) and rapid sedimentation in the offshore middle wedge (Berger et al., 2008a; Worthington et al., 2008) (Figures 3.10, 3.11). Various numerical models (e.g., Malavieille, 2010; Roe et al., 2006; Simpson, 2010; Tomkin and Roe, 2007; Whipple and Meade, 2006; Willett, 1999) predict that these related processes lower the taper angle of orogenic wedge. In these models, the system responds by structural reorganization to initiate and reactivate

faulting towards the rear of the wedge in an attempt to achieve critical taper. In the St. Elias system the large sediment influx due to offscraping at the front of the wedge appears to combine with erosion in the hinterland and deposition in the foreland to maintain a subcritical taper angle over the long term (Figure 3.18).

Continued localization of deformation and uplift at the back of the wedge is the predicted orogen response to a sub-critical taper angle (i.e., Davis et al., 1983). However, this response is likely to contribute to continued high erosion and exhumation rates (e.g., Tomkin and Roe, 2007) which, in turn, act to lower the wedge taper angle. The potential result of this feedback is a long-term sub-critical orogenic wedge always "playing catch up" in an attempt to achieve steady state. Based on observations in this study and potential applications to wedge theory, it is likely that the St. Elias orogen provides an example of a highly erosive wedge in a long-term sub-critical state. Continued study of fault evolution in the onshore St. Elias (after Chapman et al., 2008; Meigs et al., 2008) and possible modeling with these constraints in mind is needed to further understand the evolution of the orogen in this context and apply these concepts to other eroding wedges.

3.6.2 Distribution of deformation in the St. Elias orogenic wedge

A key element to furthering understanding of tectonic evolution under glacial conditions is constraining how internal deformation is distributed across the St. Elias orogen. Thus, quantifying shortening in the offshore wedge provides a vital test of the proposed models and constraints for both future neotectonic models of the St. Elias and future explorations of critical wedge dynamics in glaciated margins.

Based on modern GPS velocities (Elliott et al., 2010; Fletcher and Freymueller, 1999, 2003) and plate/microplate reconstructions (Pavlis et al., 2004), the fold-thrust belt of the St. Elias orogen has absorbed between 240 and 300 km of convergence during the last 6 Myr. Attempts to restore the shortening from surface geology and offshore seismic available prior to this study yielded shortening estimates for the last 6 Myr of as little as 36 km (Wallace, 2008) to as much as 82 km (Meigs et al., 2008). Both of these estimates determined from onshore mapping and reconstructions fall far short of the known convergence. As such, significant shortening remains unaccounted for.

Structural analysis and profile reconstruction reveal a Pleistocene deformation rate of ~5 mm/yr across the Bering Trough and a maximum offshore shortening estimate of ~12 km. My restorations of the structures across the Bering Trough (Figure 3.16) are well constrained by growth strata developed on fault-related folds, and the deposition of the thick package of sediments atop older folds in the Bering Trough provide a clear record of the deformational history. Specifically, my restorations show that the shortening across STEEP 09 is ~13 km, with ~60% of the deformation occurring post-H3 and a significant amount of the shortening occurring post H2. In the 1.8 Myr since H3, the total Yakutat convergence is ~70 km based on the present GPS velocities, and thus, the Pamplona Zone has absorbed, at most, ~17% of the total Pleistocene convergence. Stated as rates, the Pamplona zone has accommodated ~6 mm/yr of the ~40 mm/yr convergence of the entire Yakutat convergence. Similarly, the projection of the Pamplona Zone onto the shelf that is imaged in STEEP01, records ~6 km of convergence over

essentially the same time interval, which represents an even smaller fraction of the convergence, both in terms of total shortening and rates (Table 3.5).

This analysis indicates that it is highly unlikely that the slip discrepancy between reconstructions and known convergence is taken up by Pamplona Zone thrusts. It is possible that fault BT1 at the leading edge of the Pamplona Zone has a large hidden slip component that is not well imaged, but the footwall cutoffs are well imaged in the upper part of the section implying large-scale underthrusting of a footwall flat is highly unlikely. Similarly, STEEP01 provides a very clear image of the structures on the shelf and it is difficult to envision any interpretation of these data that would lead to even a doubling of the net convergence for this section.

I conclude that the bulk of YAK-NA convergence must be accommodated outside the offshore Pamplona Zone, through some combination of onshore deformation within the wedge and motion along the décollement at the base of the wedge. Previous Euler pole models for plate motions (Pavlis et al., 2004), fold kinematic studies (Chapman et al., 2008) and modeling based on critical wedge mechanics (i.e., Berger et al., 2008a) similarly concluded that the bulk of neotectonic convergence is accommodated within the onshore hinterland of the St. Elias orogen. Work in progress tying the onshore and offshore data also supports this conclusion with several reasonable structural scenarios yielding shortening estimates over 200 km on onshore structures. However, the onshore structure is clearly three-dimensional and any restoration requires assumptions regarding subsurface relationships. Nonetheless, onshore data generally supports Chapman et al.'s

[2008] inference that a series of northeast-trending *en echelon* structures are taking up most of the young convergence.

In addition to onshore faulting and deformation, movement on the décollement at depth during large earthquakes likely accommodates a significant percentage of YAK-NA convergence. Eberhart-Phillips (2006) indicate that the great 1964 (M9.2) in Prince William Sound, to the west of the study area, was caused in part by movement on the YAK-NA plate interface. Paleoseismic studies by Shennan (2009) and Shennan et al. (2009) provide evidence for recurring seismic events (~1500 yrs BP and ~900 yrs BP) with asperities covering the St. Elias margin from Yakutat Bay to Prince William Sound. These events may have been greater in magnitude than the 1964 event and indicate potential for great events in the future (Shennan et al., 2009).

3.7. CONCLUSIONS

This study presents an observational approach to critical wedge dynamics in a glaciated margin and determines that an erosive wedge with high sediment influx in the foreland may be in a long-term subcritical state. Quantification of the coupled depositional and shortening history across the Pamplona Zone fold-thrust belt reveals a bimodal localization of faulting away from the primary glacial depocenter. This coupled evolution provides a possible link between the tectonic evolution of the margin and glacial processes. Faulting near the Bering Trough has gradually ceased during the glacial period, while faulting has initiated westward towards the hinterland and eastward towards the deformation front. My observations imply that glacial processes have direct effect on

the structural evolution of the St. Elias orogen, a conclusion strengthened by recent modeling results.

I determine that the offshore deformation front accommodates <17% of total Yakutat-North American Pleistocene convergence. The bulk of Pleistocene convergence must therefore be accommodated within the onshore St. Elias orogen or on the plate interface at depth. This result provides the tectonic driver for past and future great earthquakes along the Yakutat-North America plate boundary megathrust.

Further contributions of this study include an updated fault map of the offshore St. Elias orogen that may be important for future studies of neotectonics, geodesy modeling and earthquake hazard. This study also provides the first regional mapping of the offshore Yakutat basement, leading to an estimate of total current sediment volume of ~110 $x10^3$ km^3 on the Yakutat shelf. This estimate is a fundamental constraint for exhumation studies of the orogen, providing a minimum estimate of total eroded and exhumed material derived from the southern Alaska margin during ~10 Myr of orogenesis.

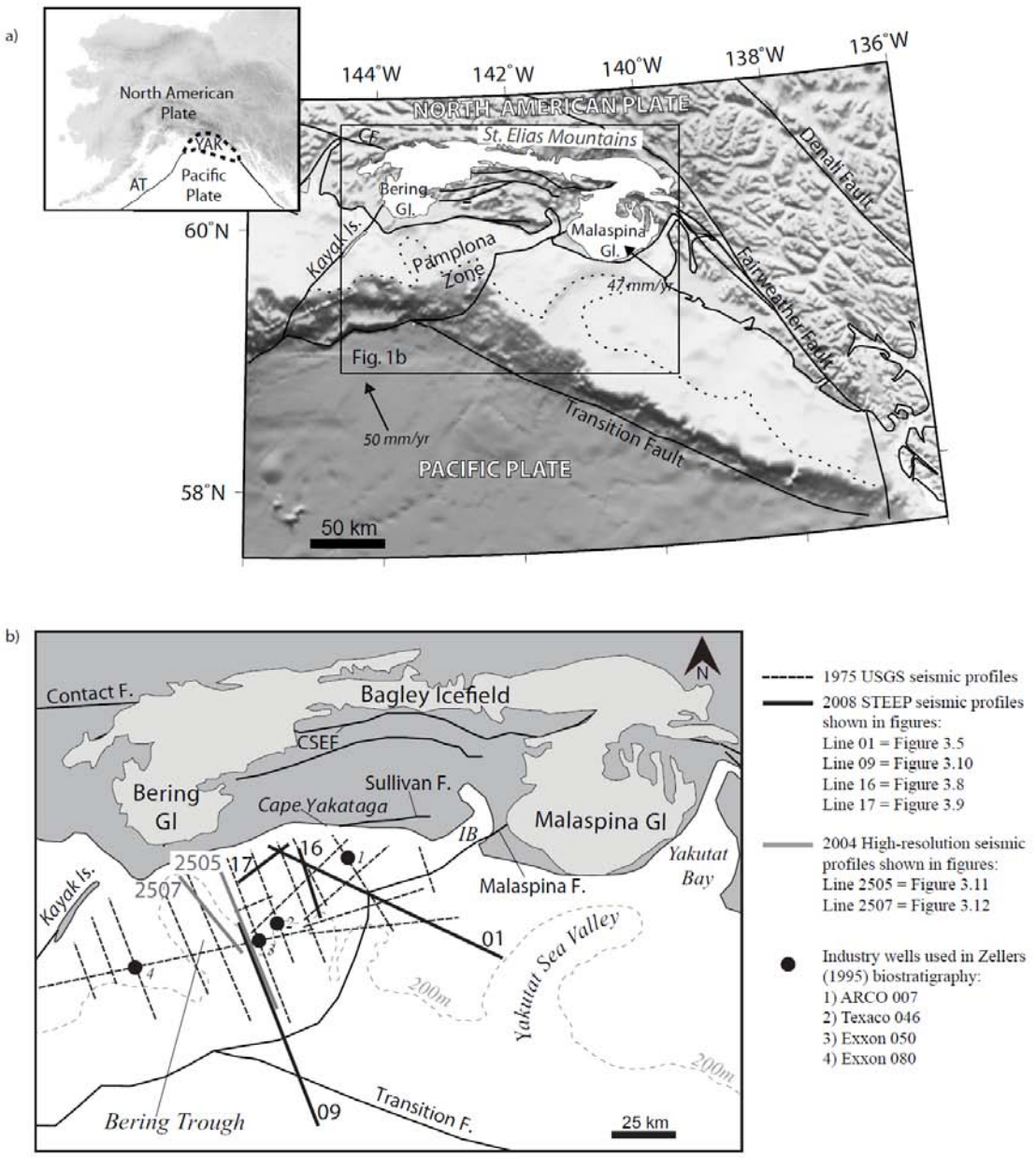

Figure 3.1. Basemap for Pamplona Zone study area. a) Digital elevation model of study area includes relative plate motion and YAK-NA convergence estimates based on GPS constraints (Elliott, in press). CF = Contact Fault; black dotted line = 200m bathymetric contour. Inset: YAK = Yakutat microplate; AT = Aleutian Trench. b) Inset of Pamplona Zone study area, showing seismic profiles used in this study and industry wells used by Zellers (1995). IB = Icy Bay; CSEF = Chugach-St. Elias fault.

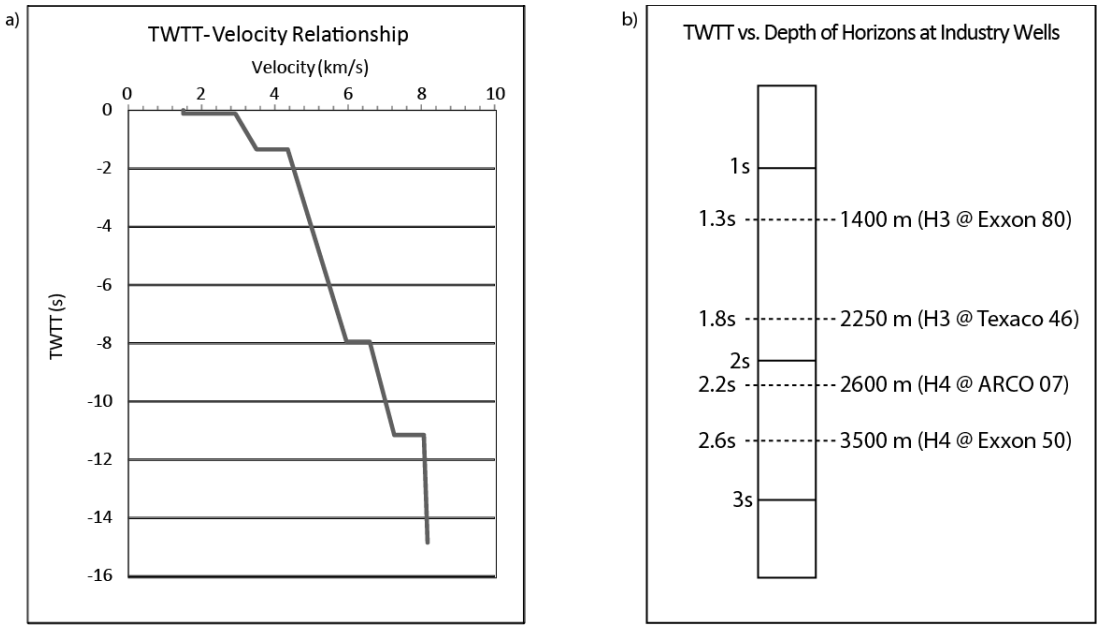

Figure 3.2. Velocity and depth relationship. a) One-dimensional velocity model showing velocities used for depth conversion. Velocity model derived from coincident refraction data. b) Comparison of two-way travel time vs. depth for Horizons 3 and 4 at industry wells, from Zellers (1995).

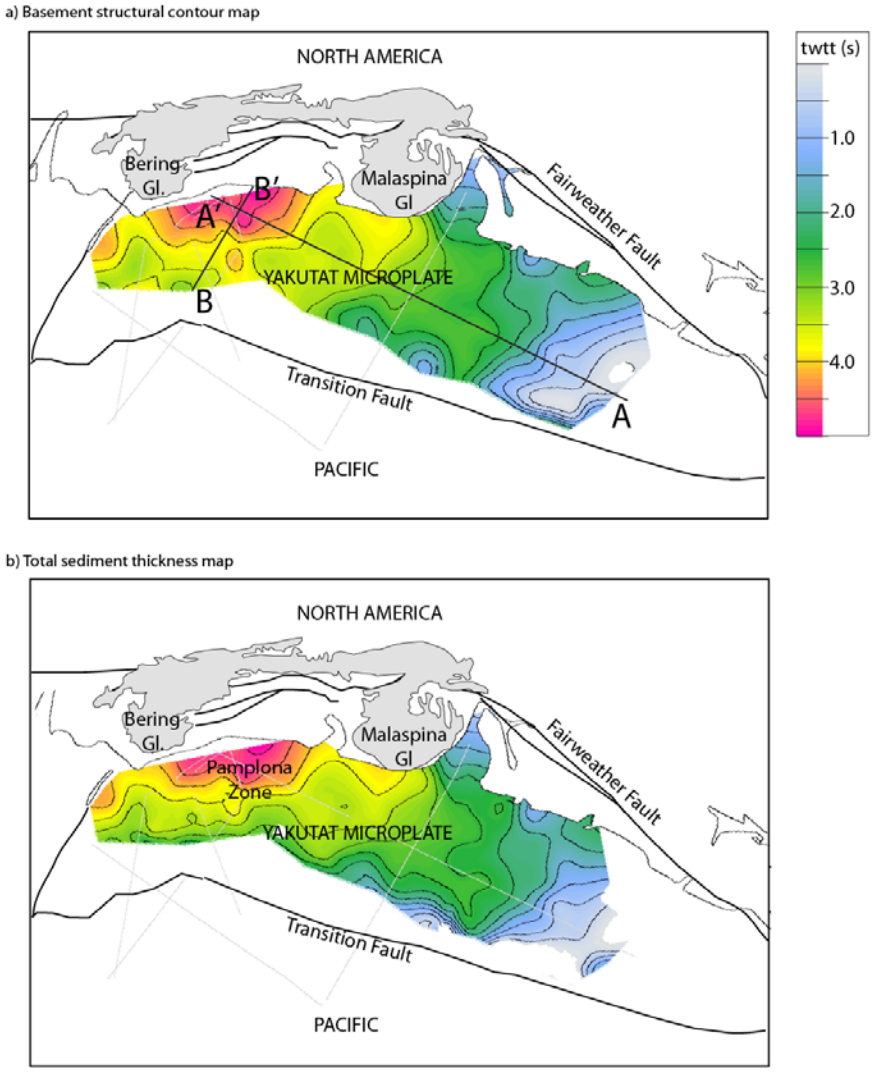

Figure 3.3. Contour maps for Yakutat basement and sediment thickness. a) Structural contour map of Yakutat basement reflector in two-way travel time. Contour intervals every 250 ms. BG = Bering Glacier; MG = Malaspina Glacier. b) Map showing total thickness of Yakutat shelf sediments in two-way travel time. Contour intervals every 250 ms.

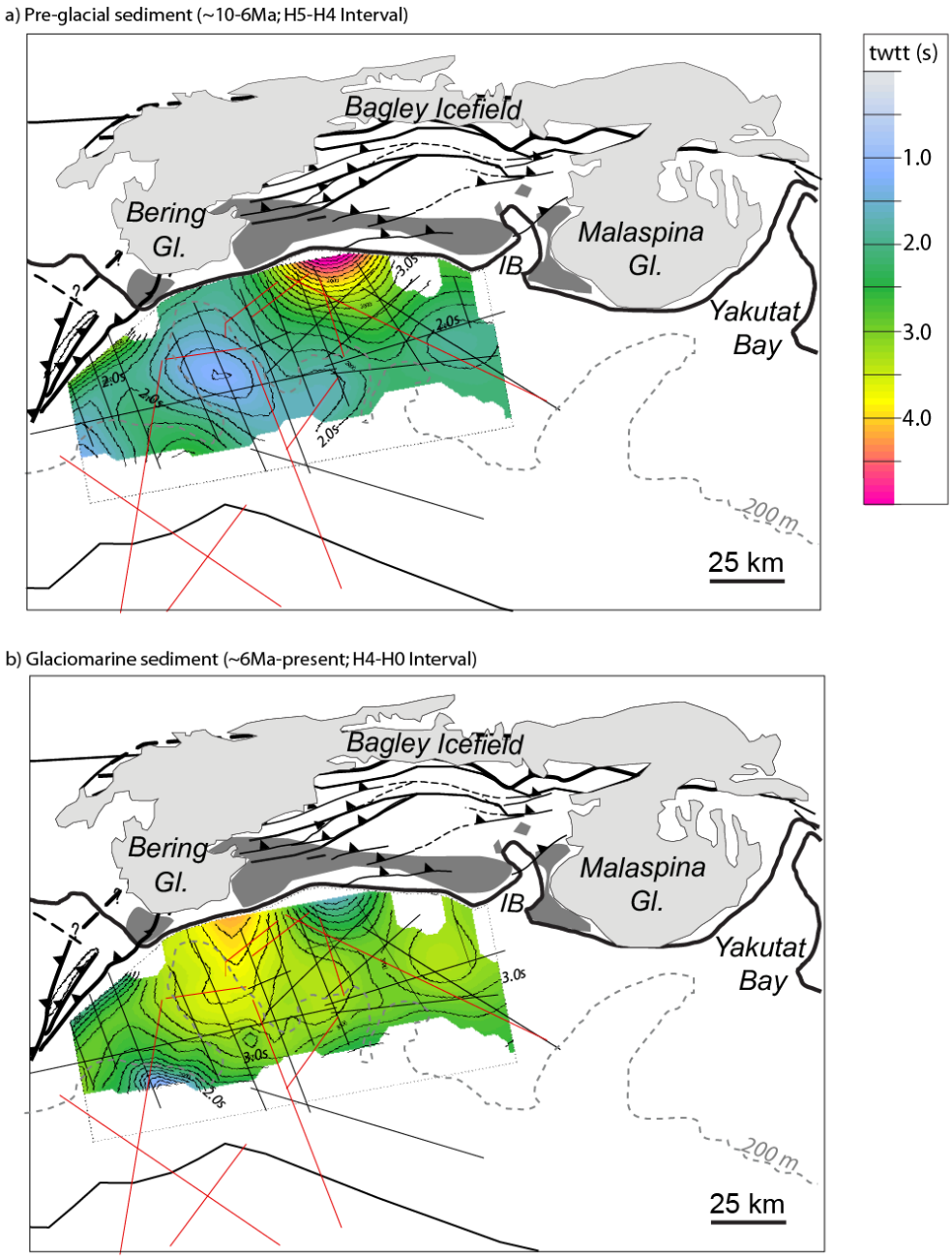

Figure 3.4. Sediment thickness maps. a) Sediment thickness in two-way travel time of pre-glacial sedimentary sequence on Yakutat shelf. Contour interval = 200 ms. b) Sediment thickness in two-way travel time of glaciomarine sedimentary sequence on Yakutat shelf. Contour interval = 200 ms. c) Sediment thickness in two-way travel time of Mio-Pliocene glaciomarine sedimentary sequence on Yakutat shelf. Contour interval = 200 ms.

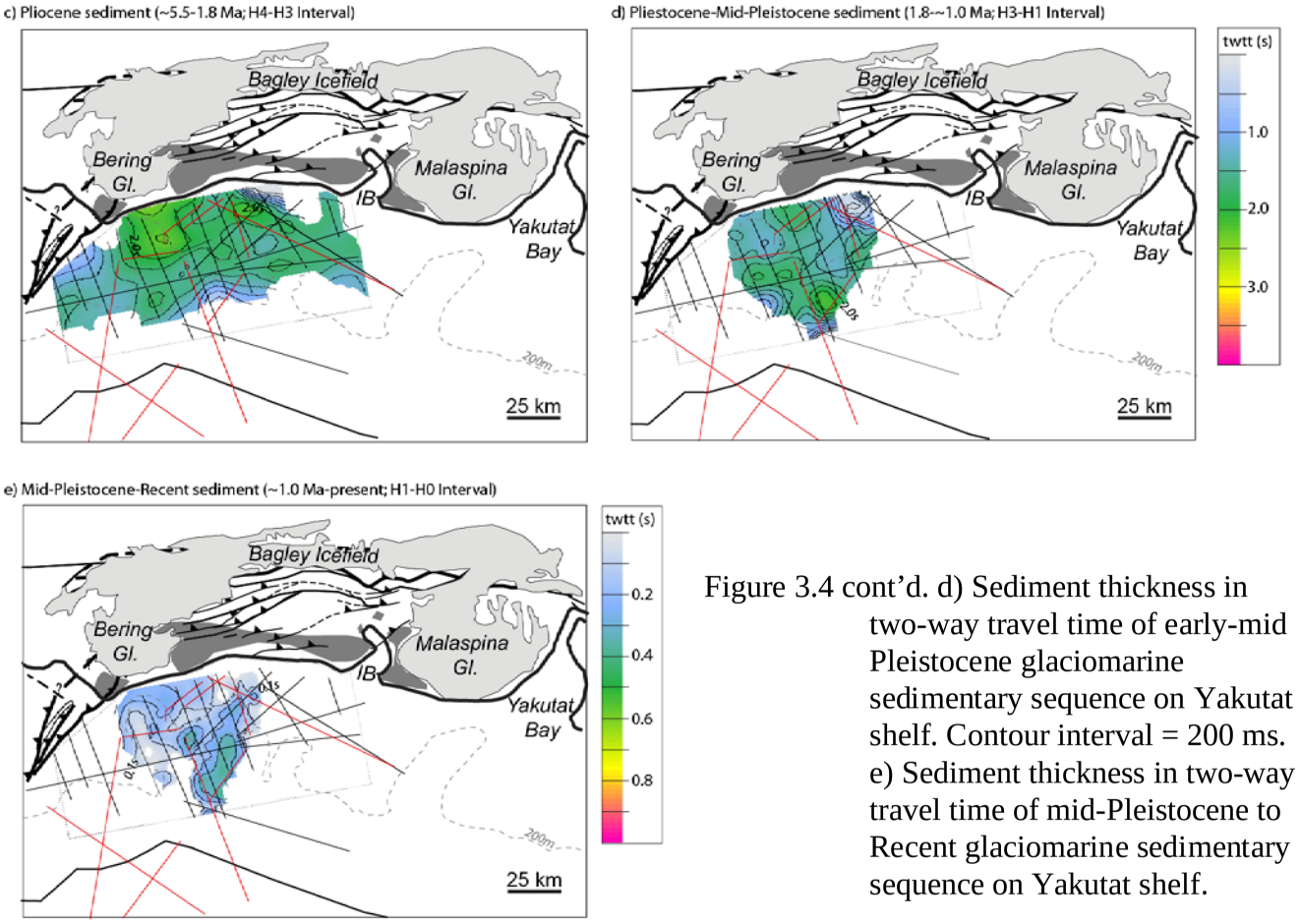

Figure 3.4 cont'd. d) Sediment thickness in two-way travel time of early-mid Pleistocene glaciomarine sedimentary sequence on Yakutat shelf. Contour interval = 200 ms. e) Sediment thickness in two-way travel time of mid-Pleistocene to Recent glaciomarine sedimentary sequence on Yakutat shelf.

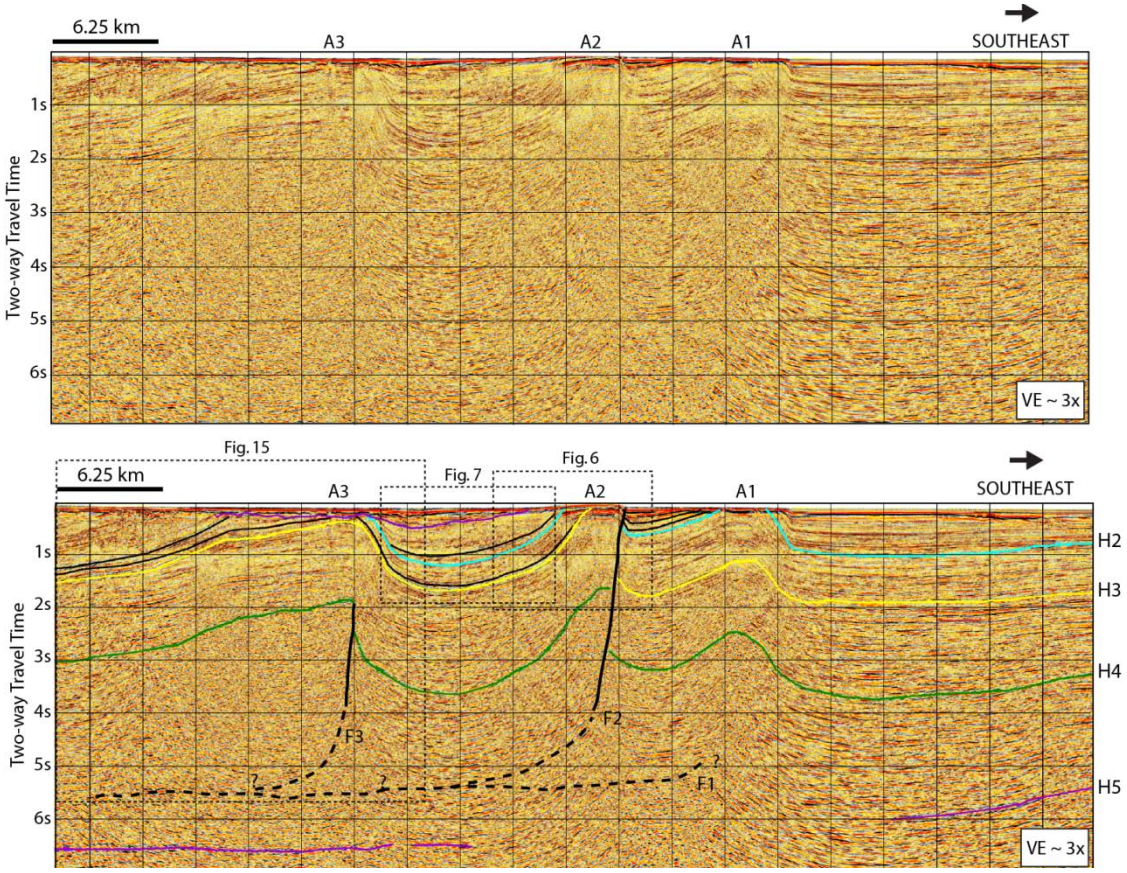

Figure 3.5. STEEP01 seismic section, uninterpreted (top) and interpreted (bottom). Interpreted section shows structures A1, A2, A3, F1, F2, F3, locations of subsequent figures, and key horizons. Colored horizons are regional horizons interpreted throughout the study area. Black horizons are interpreted locally to define growth strata packages on fold limbs. See Figure 3.1 for location.

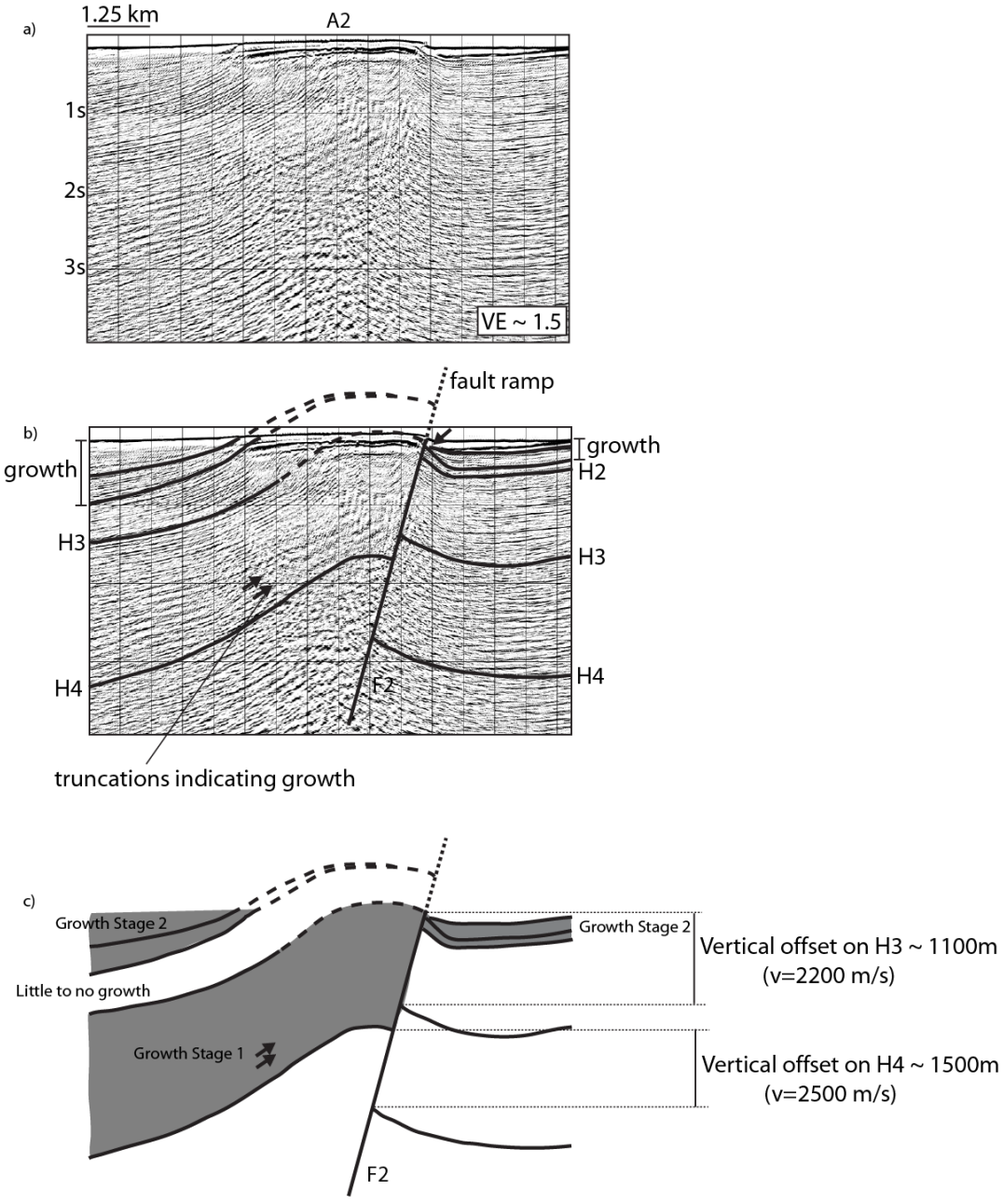

Figure 3.6. Anticline A2. a) Anticline A2 uninterpreted. b) A2 interpreted. c) Line model of A2 showing growth stages. See Figure 3.5 for location.

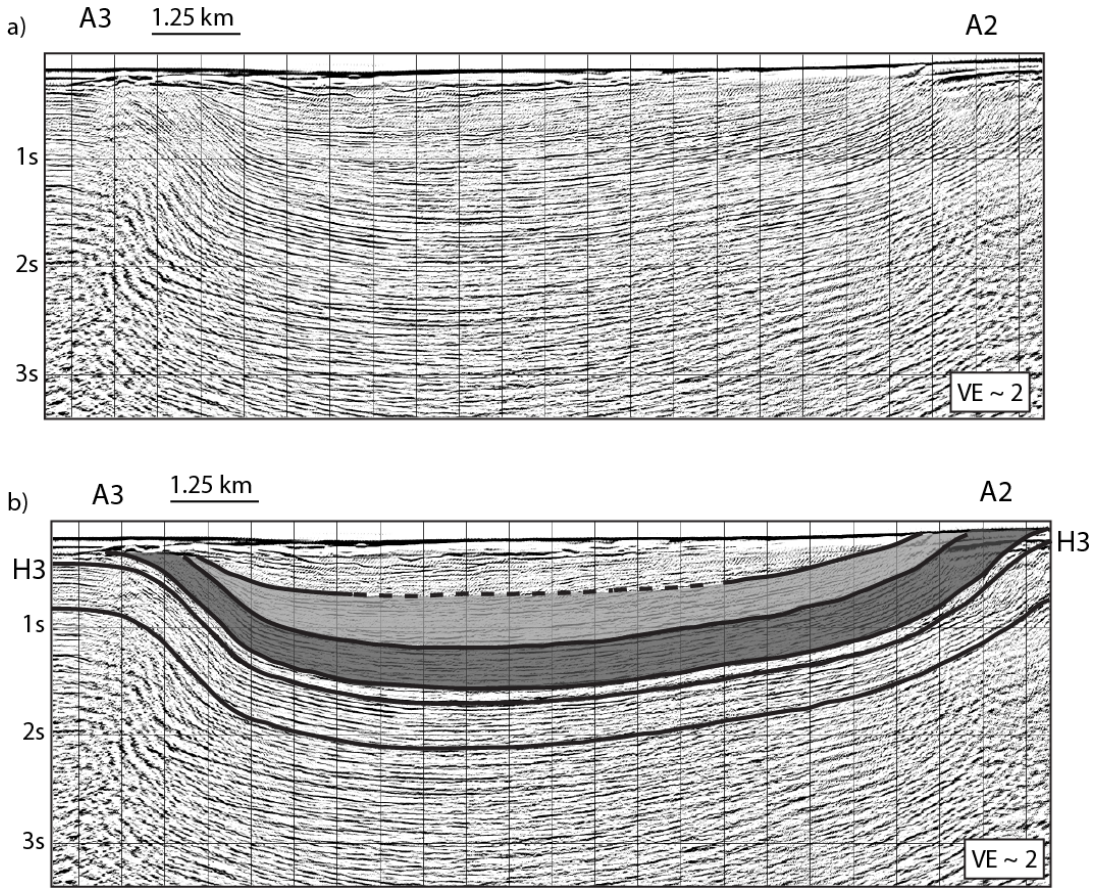

Figure 3.7. Anticlines A2 and A3. a) Strata between anticlines A2 and A3, uninterpreted. b) Strata between A2 and A3, showing different growth stages across folds. A3 is growing during deposition of both the light gray and dark gray stratal packages. Deformation on A2 does not initiate until deposition of the light gray stratal packages. See Figure 3.5 for location.

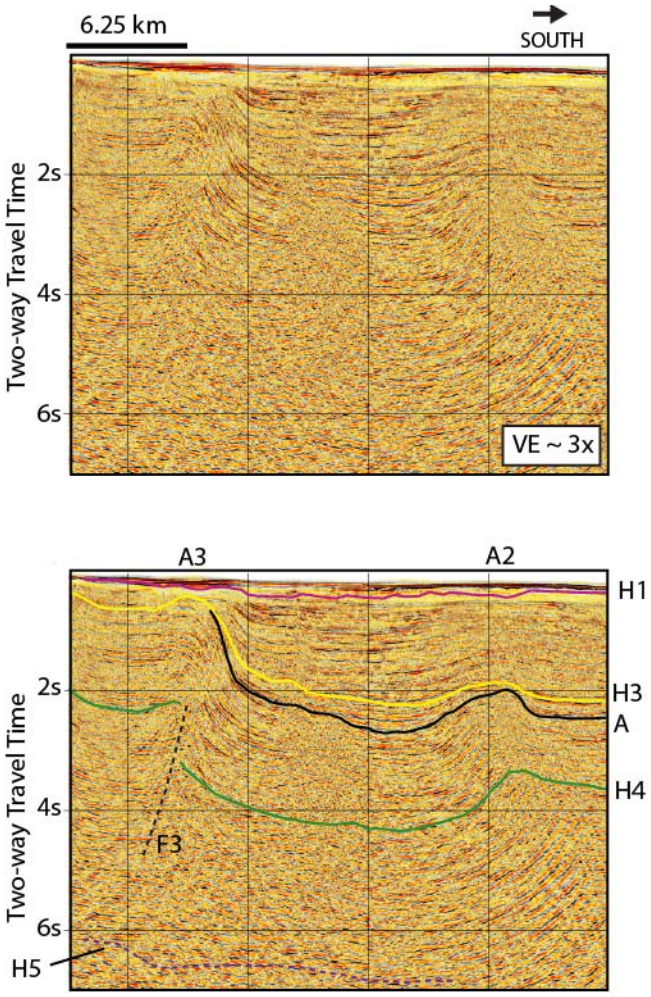

Figure 3.8. STEEP16 seismic section, uninterpreted (top) and interpreted (bottom). Interpreted section shows structures A2 and A3, and key horizons. Colored horizons are regional horizons interpreted throughout the study area. Horizon A (black) is interpreted locally to define growth strata packages on fold limbs. See Figure 3.1 for location

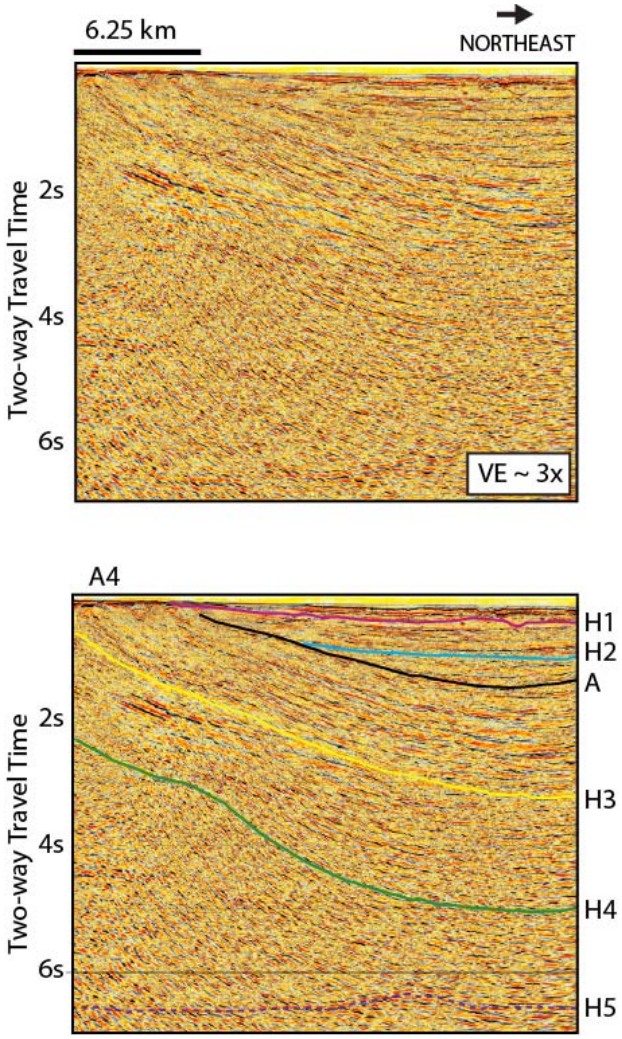

Figure 3.9. STEEP17 seismic section, uninterpreted (top) and interpreted (bottom). Interpreted section shows structure A4, and key horizons. Colored horizons are regional horizons interpreted throughout the study area. Horizon A (black) is interpreted locally to define growth strata packages on fold limbs. See Figure 3.1 for location.

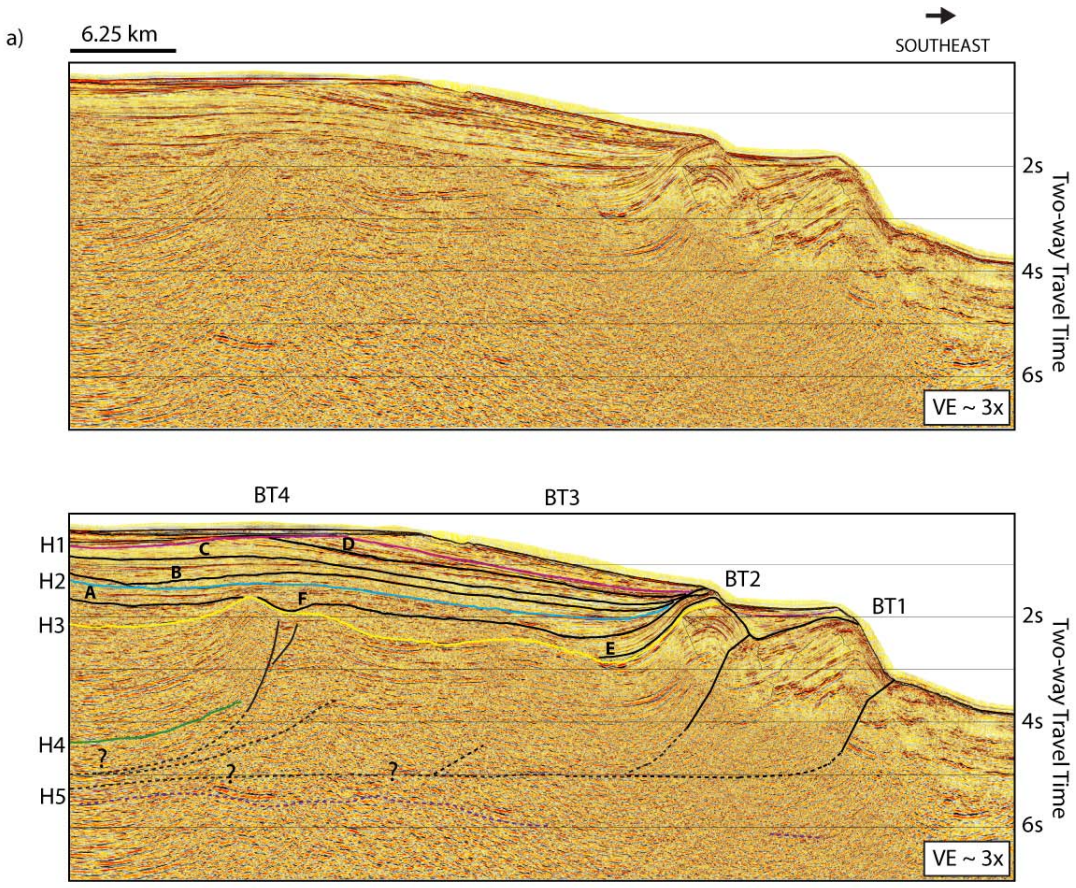

Figure 3.10. STEEP09 seismic section. a) STEEP09 seismic section, uninterpreted (top) and interpreted (bottom). Interpreted section shows structures BT1, BT2, BT3, BT4 and key horizons. Colored horizons are regional horizons interpreted throughout the study area. Horizons A-F (black) are interpreted locally to define growth strata packages on fold limbs and glacial depositional sequences in the upper 2 seconds of the record.

b)

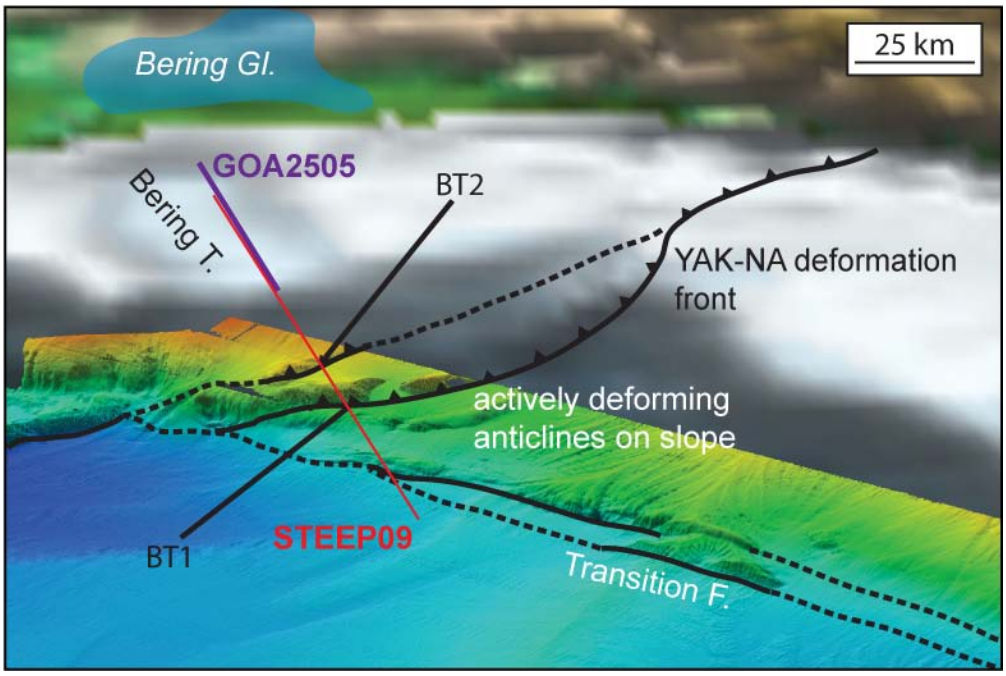

Figure 3.10 cont'd. b) High-resolution (100^2 m) bathymetry shows escarpments on Yakutat slope associated with BT1 and BT2. Locations of seismic profiles STEEP09 (red) and GOA2505 (purple).

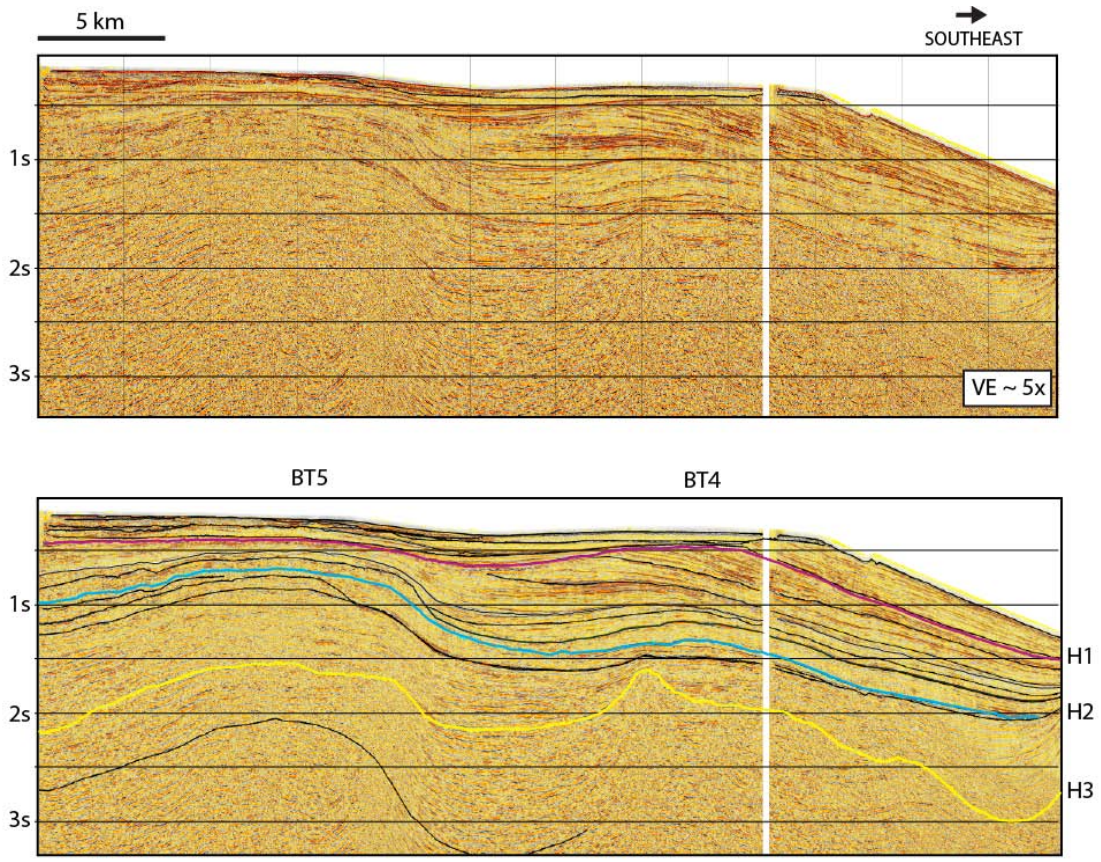

Figure 3.11. GOA2505 seismic section, uninterpreted (top) and interpreted (bottom). Interpreted section shows structures BT4, BT5 and key horizons. Colored horizons are regional horizons interpreted throughout the study area. Black horizons are interpreted locally to define glacial depositional sequences in the upper 2 seconds of the record.

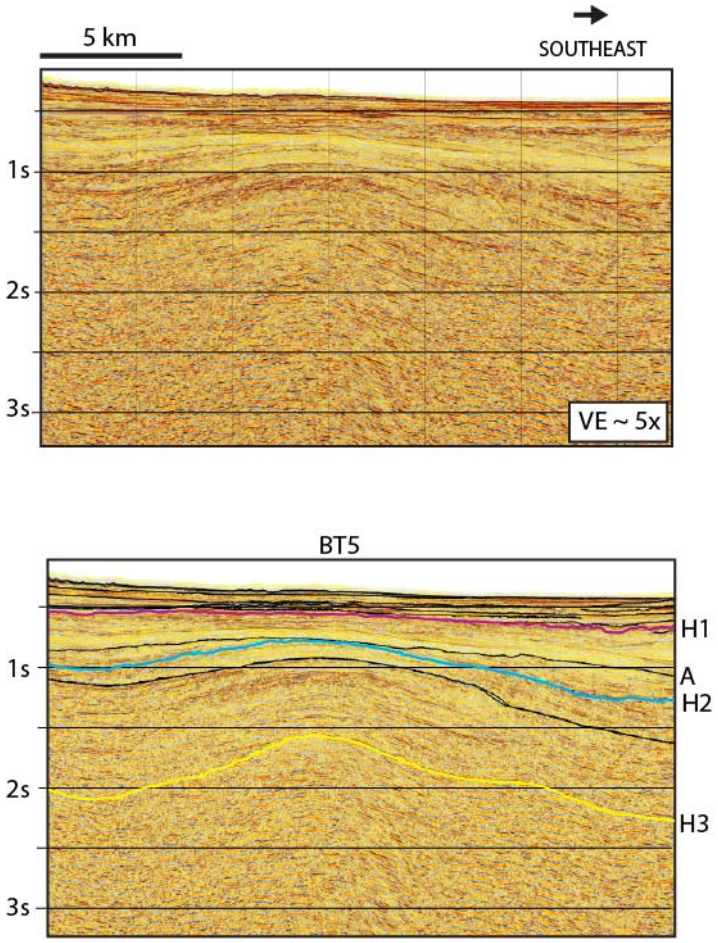

Figure 3.12. GOA2507 seismic section, uninterpreted (top) and interpreted (bottom). Interpreted section shows BT5 and key horizons. Colored horizons are regional horizons interpreted throughout the study area. Black horizons and Horizon A are interpreted locally to define glacial depositional sequences in the upper 2 seconds of the record.

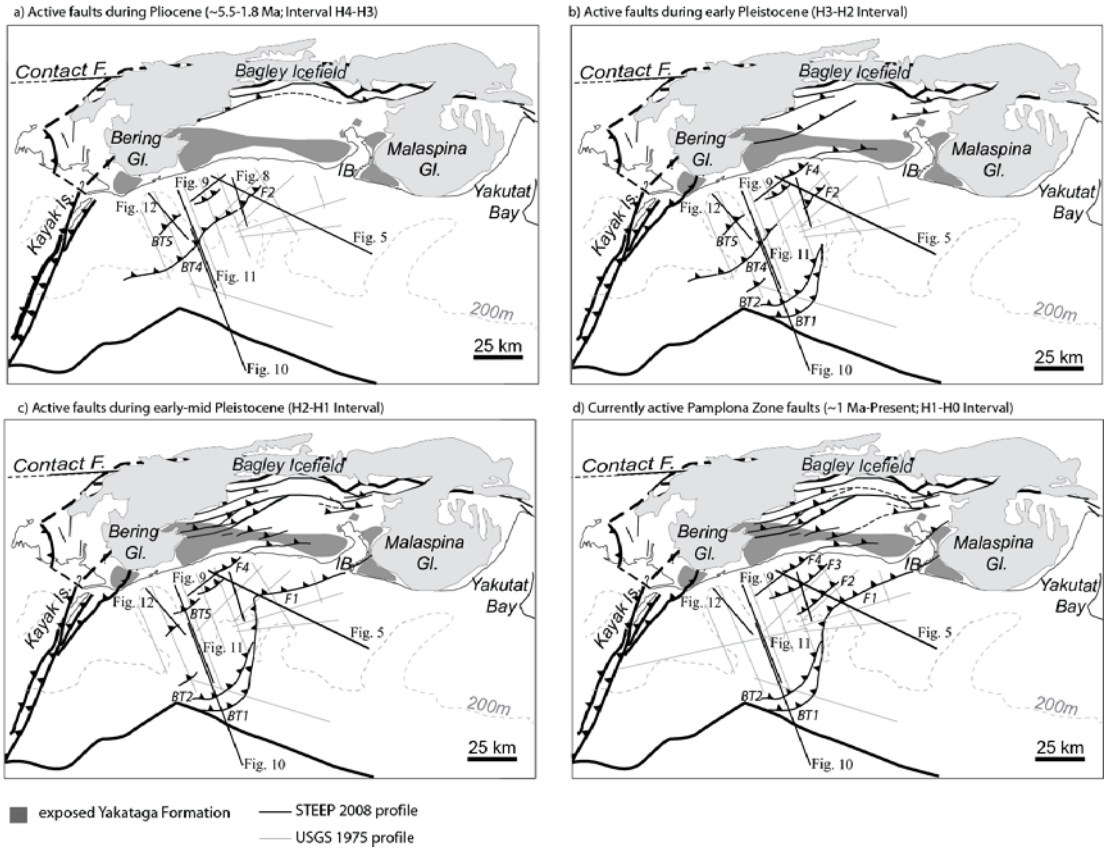

Figure 3.13. Summary of temporal and spatial evolution of Pamplona Zone faulting during glacial period. IB = Icy Bay. Evolution of onshore faulting represented schematically, based on previous work by Meigs et al. (2008) and Berger et al. (2008a). a) Faults active during the interval between Horizon 4 and Horizon 3. b) Faults active during the interval between Horizon 3 and Horizon 2. c) Faults active during the interval between Horizon 2 and Horizon 1. d) Currently active Pamplona Zone faults. Onshore faulting after Plafker (1987) and Bruhn et al. (2004).

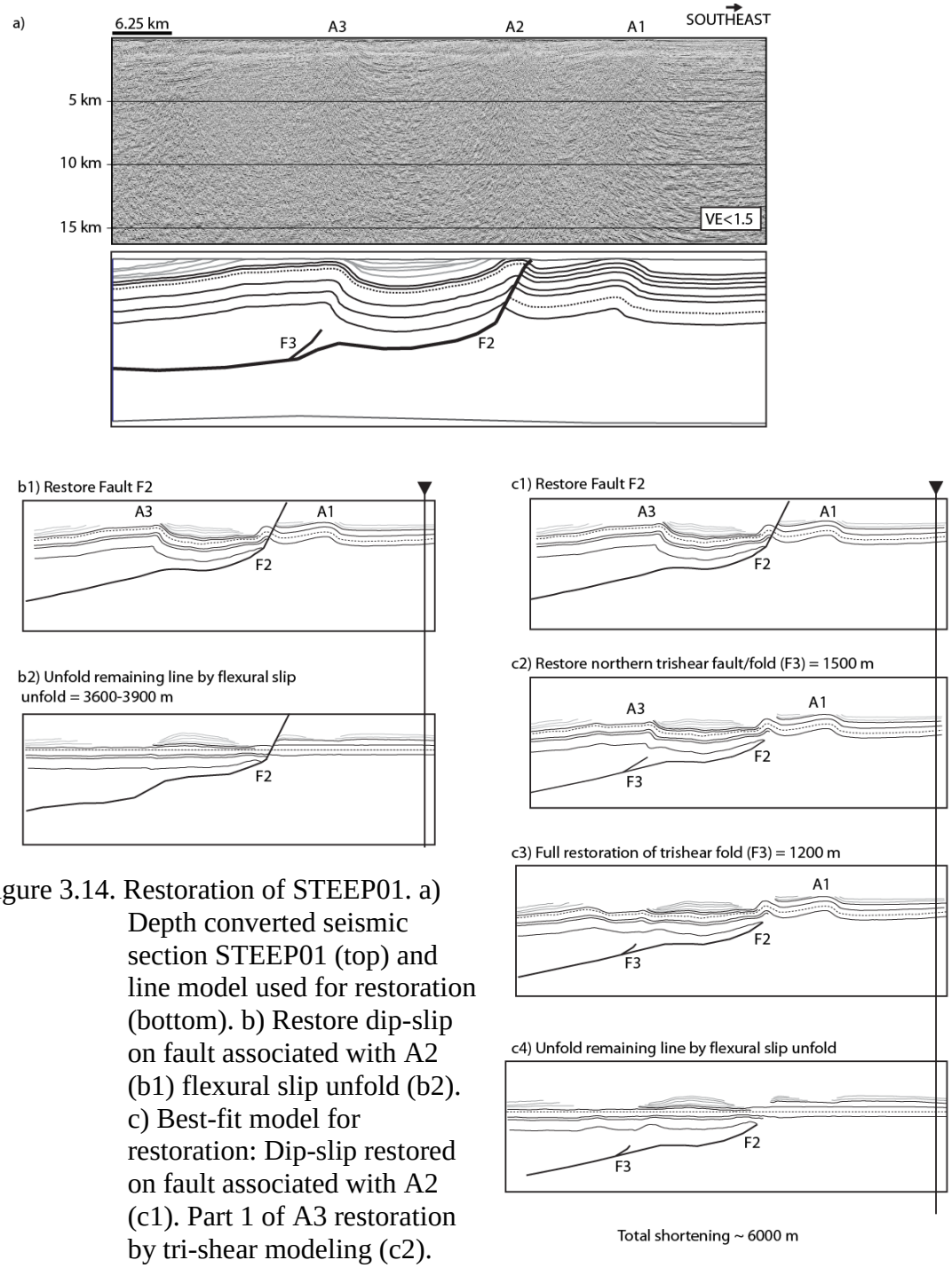

Figure 3.14. Restoration of STEEP01. a) Depth converted seismic section STEEP01 (top) and line model used for restoration (bottom). b) Restore dip-slip on fault associated with A2 (b1) flexural slip unfold (b2). c) Best-fit model for restoration: Dip-slip restored on fault associated with A2 (c1). Part 1 of A3 restoration by tri-shear modeling (c2). Finish restoration of A3 by trishear modeling (c3). Unfold remaining line by flexural slip unfold (c4).

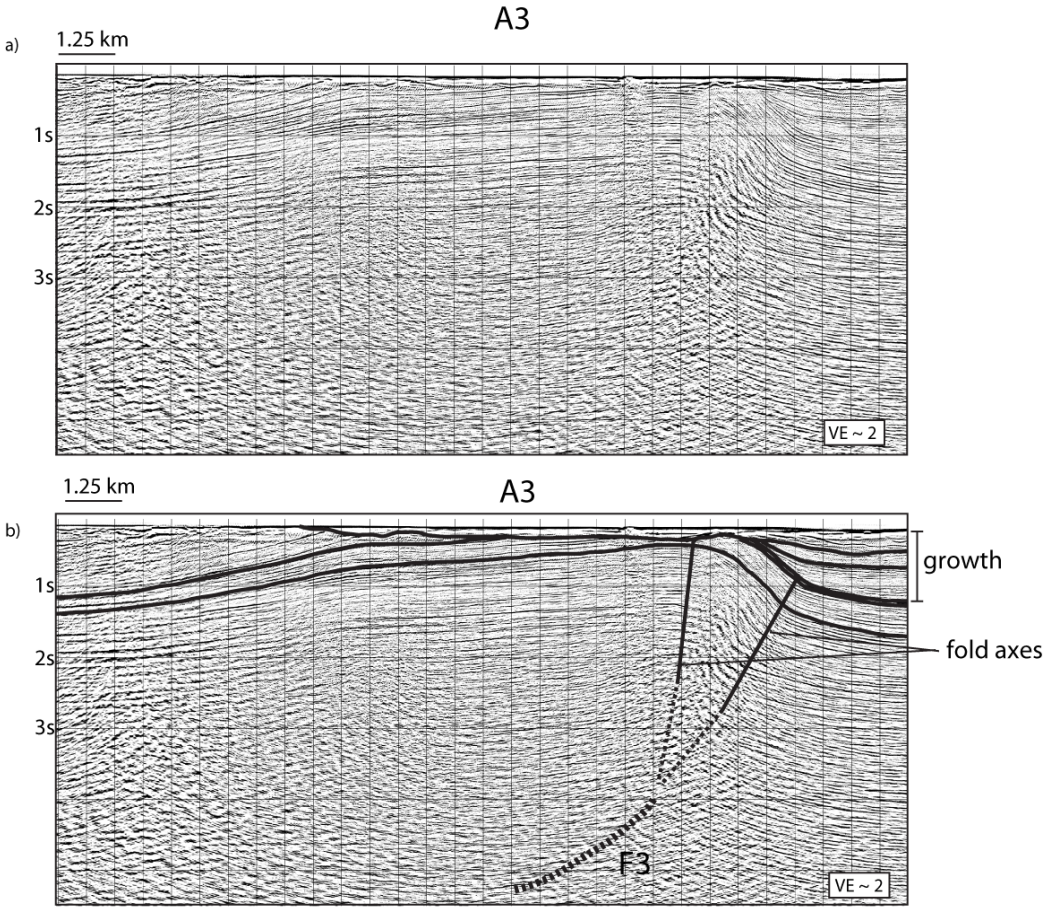

Figure 3.15. Anticline A3. a) Anticline A3 uninterpreted. b) A3 with interpreted fold axes.

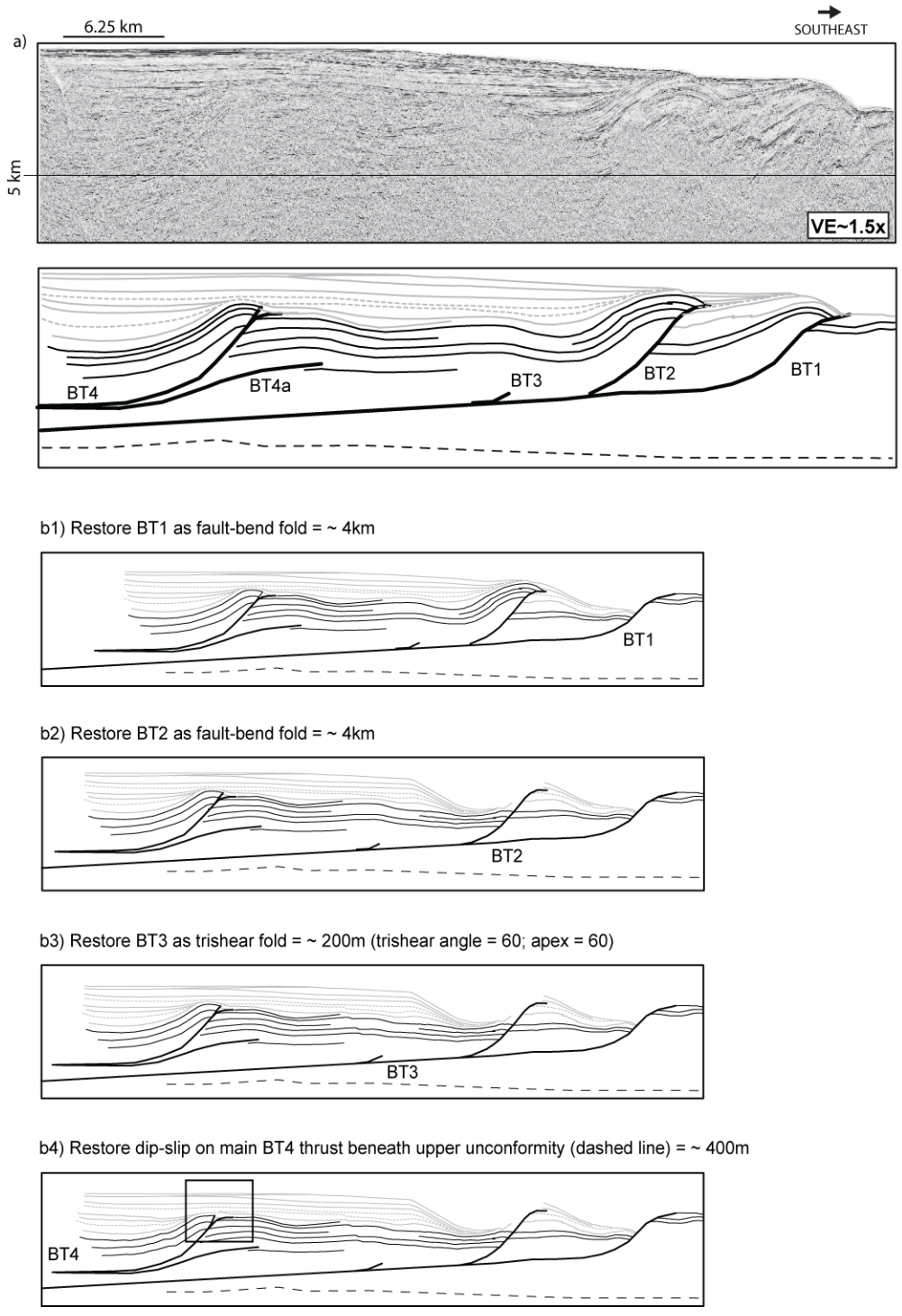

Figure 3.16. Restoration of STEEP09. a) Depth converted seismic section STEEP09 (top) and line model used for restoration (bottom).

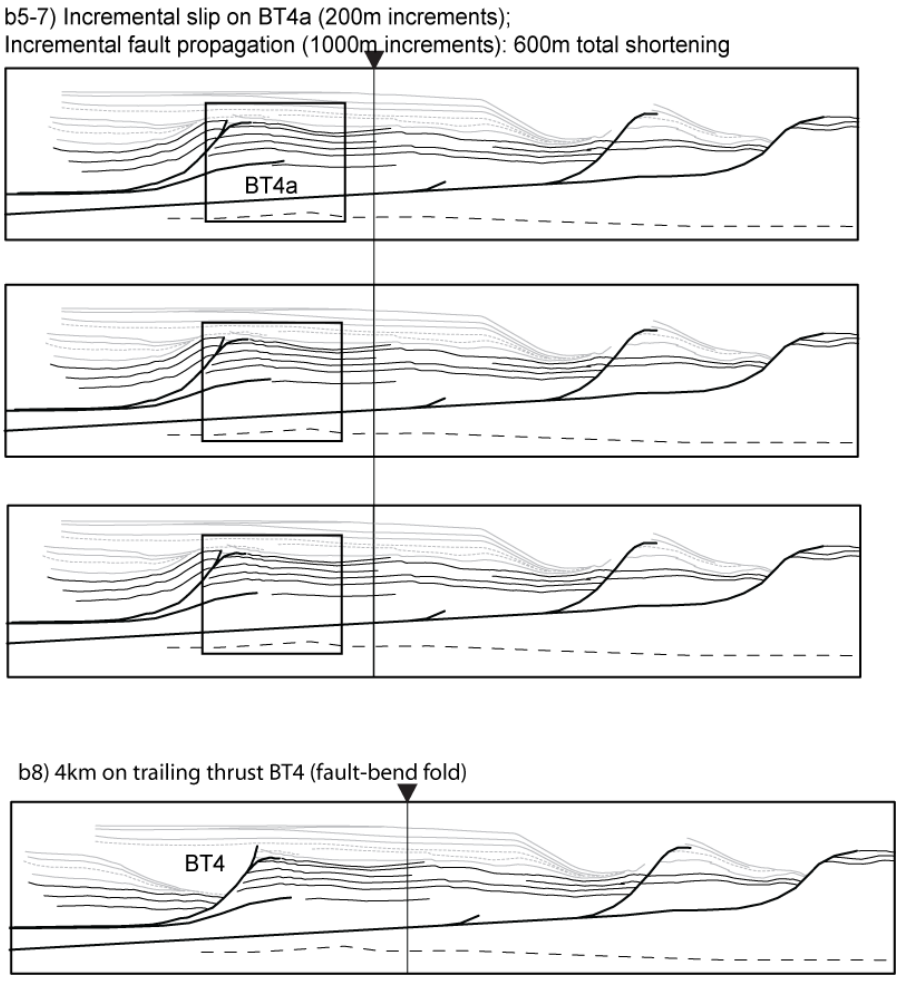

Figure 3.16 cont'd. Gray lines are growth strata. Black lines are pre-growth strata. Heavy black lines are faults. Dotted gray lines are angular unconformities. b) Staged reconstruction of STEEP09. BT1 restored as a fault-bend fold (b1). BT2 restored as fault-bend fold (b2). BT3 restored using a trishear model (b3). 400m of dip-slip restored on BT4 (b4). Begin incremental slip and propagation on BT4a in three stages for a total of 600m of restored slip; pin line shown (b5). The main fault BT4 restored by trishear modeling (b8).

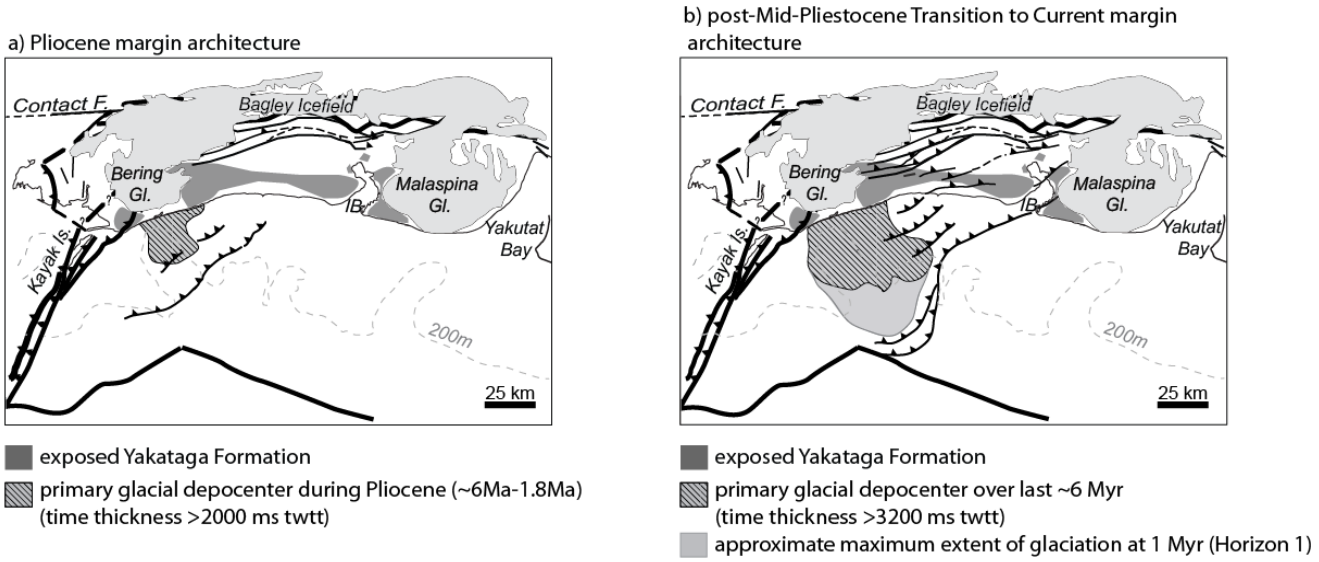

Figure 3.17. Combined depositional and structural patterns in the St. Elias margin (a) before the Plio-Pleistocene transition and (b) after the Mid-Pleistocene Transition. Schematic onshore faults in (a) after Figure 13; onshore faults in (b) after Plafker (1987) and Bruhn et al. (2004).

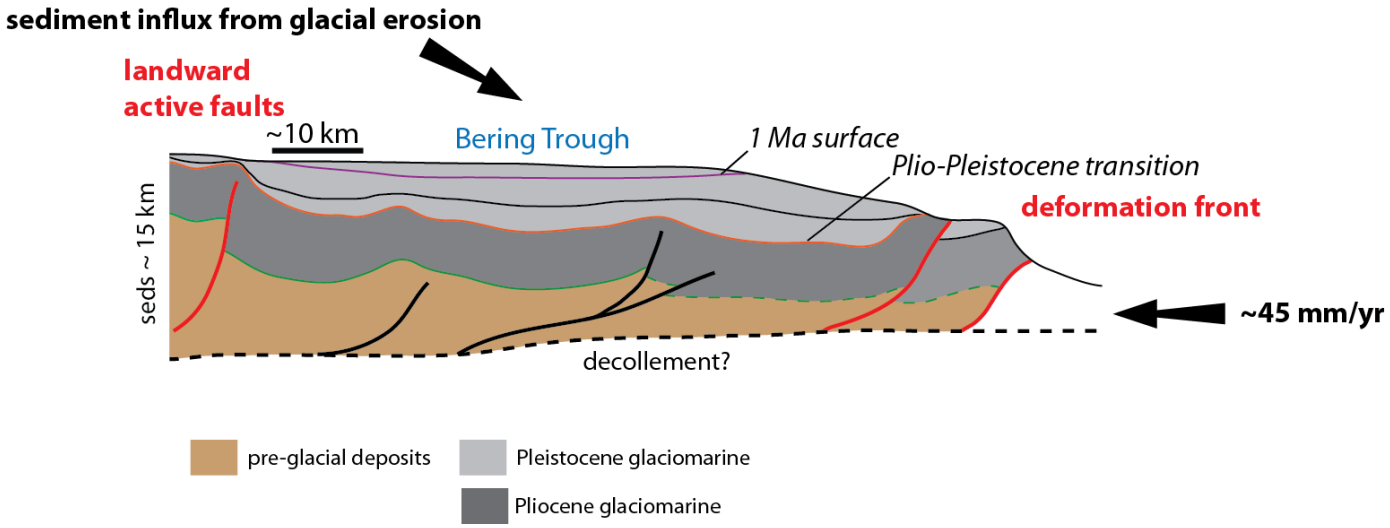

Figure 3.18 Schematic cross-section across frontal St. Elias wedge.

TABLE 3.1. Summary of previous shortening estimates and reconstructions

Author	Total Shortening Across Orogen	Estimated Offshore Shortening	Long Term Deformation Rate	Pleistocene Deformation Rate	1 Ma Deformation Rate	Method
Pavlis et al., 2004	20 km over 0.5 Ma; 120 km over 3Ma	5 km over 1 Ma;	40 mm/yr (3Ma)	40 mm/yr	40 mm/yr	Euler pole plate reconstruction using current plate YAK-NA relative plate motion of 40-44 mm/yr (Fletcher and Freymueller, 2003)
Meigs et al., 2008	82 km over 5.9 Ma	~1900 m total; ~500 on A1, ~1400 on A2	14mm/yr	Not Specified	Not Specified	line length and area balancing: top and bottom of YAK and PC formations; three principal thrust sheets
Wallace, 2008	36 km over 5.9 Ma	Not Specified	6.1 mm/yr	Not Specified	Not Specified	area balanced restoration

TABLE 3.2. Interpreted horizons on seismic profiles

Horizon	Age	Definition	Color	References
H1	~1 Ma	Mid-Pleistocene Transition (MPT)--local angular erosional unconformity created by shelfal glacial advance	Purple	Worthington et al. (2008); Berger et al. (2008)
H2	~1.8-1 Ma	arbitrary time marker	Blue	---
H3	1.8 Ma	Plio-Pleistocene transition	Yellow	Zellers (1995)
H4	~5.9 Ma	Yakataga-Poul Creek contact; generally defines onset of glaciation	Green	Zellers (1995)
H5		acoustic basement; contact between shelf sediment and Yakutat basement crust	Purple	---

TABLE 3.3. Mapped structures in Icy Bay-Cape Yakataga Region

Profile	Anticline		Timing of Initiation	Last Observed Fault Activity
STEEP01	A1		Early-Mid Pleistocene	Present
	A2	Growth stage 1	Pliocene	Early-Mid Pleistocene
		Growth stage 2	Mid-Pliocene	Present
	A3		Early-Mid Pleistocene	Present
STEEP16	A2	Growth stage 1	Pliocene	Early-Mid Pleistocene
	A3		Pliocene, after initiation of A2 growth stage 1	Present
STEEP17	A4		Pleistocene	Present

TABLE 3.4. Mapped structures in Bering Trough Region

Profile	Anticline	Timing of Initiation	Last Observed Fault Activity
STEEP09	BT1	Early-Mid Pleistocene	Present
	BT2	Early-Mid Pleistocene	Present
	BT3	Pliocene	Early-Mid Pleistocene
	BT4	Pliocene	Early-Mid Pleistocene
GOA2505	BT4	Pliocene	Early-Mid Pleistocene
	BT5	Pliocene	Early-Mid Pleistocene
GOA2507	BT5	Pliocene	Early-Mid Pleistocene

TABLE 3.5. Comparison of Pleistocene offshore deformation rates

Region	Profile	Pleistocene Shortening	Pleistocene Deformation Rate	% of Total Pleistocene convergence (based current GPS rates from Fletcher and Freymueller, 2003; and plate reconstructions by Pavlis et al., 2004)
Icy Bay	STEEP01	~6 km	~3.3 mm/yr	~8%
Bering Trough	STEEP09	~8 km	~4.4 mm/yr	~12%

Chapter 4: Crustal Structure of the Yakutat Microplate: New Constraints for Understanding the Evolution of Subduction and Collision in southern Alaska

ABSTRACT

An onshore-offshore wide-angle refraction profile shows Yakutat crustal thickness ranging from ~15 km near the Bering Glacier to ~30 km east of the Dangerous River Zone (DRZ), with calculated lower crustal velocities potentially >7 km/s. Crustal velocity and structure are continuous across the DRZ on the YAK shelf, which is historically described as a vertical boundary between continental crust on the east and oceanic basement on the west. Instead, I observe a gradual shallowing of elevated crustal velocities associated with a basement high observed on coincident marine reflection data near the DRZ. Crustal velocity and thicknesses are comparable to the Kerguelen oceanic plateau in the Indian Ocean and the Siletz terrane of eastern Oregon, thus supporting the oceanic plateau theory for the origin of the YAK microplate.

The observed variable crustal thickness indicates that the YAK slab may be slightly doorstop-shaped, thinning in the direction of convergence. The thickest portion of the offshore YAK crust is entering the orogen near the eastern corner of the St. Elias orogen, where the Fairweather fault system encounters a restraining bend as its orientation changes from north-south to east-west. It follows that observations of elevated exhumation rates and concentrated seismicity in the vicinity of the syntaxis may not be

the exclusive result of this corner geometry. Instead, we must consider that underlying crustal structure of the YAK indentor partially determines the large-scale patterns of mountain building in southern Alaska. These observations also imply that uplift and deformation have intensified through time, particularly in the St. Elias syntaxis, as thicker, more buoyant YAK crust attempts to subduct.

4.1. INTRODUCTION

Flat-slab subduction and collision of the Yakutat microplate in southern Alaska characterizes the latest iteration of terrane accretion that forms the tectonic assemblage of the Canada-Alaska Cordillera (Figure 4.1) (Plafker et al., 1994; von Huene and Ranero, 2009). Over the last ~10 Myr, the Yakutat slab has subducted ~500 km at a dip of ~6° (Eberhart-Phillips et al., 2006; Gulick et al., 2007), has driven orogenesis of the Chugach-St. Elias mountain belt (e.g., Bruhn et al., 2004; Pavlis et al., 2004) and has characterized seismicity in the area (e.g., Doser et al., 1997; Doser et al., 2007; Lahr and Plafker, 1980; Pegler and Das, 1996). Beyond local uplift and seismicity, the Yakutat-North American convergence has initiated far-field tectonic effects including mantle flow towards Arctic Canada (Mazzotti and Hyndman, 2002) and possible Anatolian-style counterclockwise extrusion of Alaskan crustal blocks westward toward the Bering Sea (Redfield et al., 2007).

The flat-slab segment of the Yakutat microplate is defined by a distinct bend in Wadati-Benioff zone depth contours near the northeastern extension of the Aleutian subduction system and occupies a gap in the Aleutian magmatic arc (Figure 4.1). The

shallow subduction of the Yakutat slab is the result of its anomalous buoyancy, partly related to its thickness. Regional tomographic (Eberhart-Phillips et al., 2006) and receiver function studies (Ferris et al., 2003) image subducting YAK crust as a ~15-20 km-thick low-velocity zone ~150 km below the Alaska Range (Figure 4.1). These results are consistent with interpretations of the Yakutat microplate as an oceanic plateau mostly comprised of anomalously thick, buoyant oceanic crust (e.g., Bruhn et al., 2004; Christeson et al., 2010; Gulick et al., 2007; Pavlis et al., 2004).

The Yakutat convergence zone provides a case study for understanding orogenic processes in a flat-slab setting as the plate interface transitions from subduction to collision near the St. Elias orogen. Yakutat-North America convergence drives uplift of the St. Elias Mountains, where exhumation rates exceed 192 km^2/yr (Berger and Spotila, 2008). Farther afield, uplift of the Alaska Range is coincident with Yakutat collision at the Gulf of Alaska margin (Preece and Hart, 2004). Significant upper plate deformation (von Huene and Ranero, 2009) and possible reorganization of the plate boundary system (Gulick et al., 2007) are also symptoms of Yakutat convergence in southern Alaska.

In this chapter, I present a 2-D seismic velocity model of the Yakutat microplate based on joint inversion of coincident marine seismic reflection and refraction data. These new constraints on Yakutat crustal thickness and geometry lead to a new model for how Yakutat-North America convergence has influenced orogenesis of the St. Elias Mountains. New details regarding crustal composition across the Yakutat basement further support the oceanic plateau hypothesis for the origin of the YAK block.

Additionally, I propose new constraints on the microplate's pre-collisional history based on the newly modeled velocity structure east of the Dangerous River Zone (DRZ).

4.2. TECTONIC SETTING

The unsubducted Yakutat microplate lies offshore in the northern Gulf of Alaska, where it converges with North America at near Pacific Plate (PAC) velocities (Elliott et al., 2010). The St. Elias Mountains and associated fold-thrust belt accommodate the bulk of YAK-NA convergence. The microplate is bounded on the west by a combination of structures that define the northeastern extension of the Aleutian Trench through the Kayak Island zone, although the details of how deformation is partitioned remains poorly resolved (Bruhn et al., 2004; Worthington et al., 2008). To the east and north, the Yakutat terrane boundary with North America is defined by the right-lateral strike-slip Fairweather Fault and the Chugach-St. Elias fault, respectively. The present microplate boundary, however, extends beyond the suture and involves deformation northward beneath the Bagley Icefield (Figure 4.1) in the core of the St. Elias mountains (e.g., Berger et al., 2008a; Pavlis et al., 2004). The strike-slip Transition Fault forms the Yakutat-Pacific Plate boundary on the south (Bruns, 1983a; Christeson et al., 2010; Gulick et al., 2007).

In the northern Gulf of Alaska, the Yakutat microplate converges with North America forming the high-relief coastal St. Elias orogen (Plafker, 1987). The St. Elias Mountains exhibit their highest relief at the onshore extension of a subsurface structure that Plafker (1987) named the DRZ. Christeson et al. (2010) calculated a Yakutat crustal

thickness west of the DRZ between 25-30 km and a velocity structure that suggests a mafic composition. East of the offshore DRZ, Yakutat crustal composition and seismic velocity structure are less well-defined and crustal thickness is almost entirely unconstrained. Based on outcrop observations and offshore dredging near the Fairweather Ground, Plafker (1987) and Plafker et al. (1994) suggested that Yakutat basement east of the DRZ may be an offset fragment of the adjacent Chugach terrane, characterized by metamorphosed flysch and mélange intruded by granitoids. Previous offshore seismic studies and comparison of onshore and offshore well-data indicate that the DRZ marks an abrupt thinning of Yakutat sedimentary cover from west to east (Plafker et al., 1994).

4.3. DATA

In 2008 seismic profile STEEP01 was collected aboard the R/V *Marcus Langseth* as part of the St. Elias Erosion and Tectonics Project (STEEP) (Figure 4.1). The profile includes ~340 km of coincident marine multichannel seismic (MCS) and ocean-bottom seismometer (OBS) data. The profile crosses the offshore Yakutat microplate from the Bering Glacier to east of the DRZ (Figure 4.2), aligned in the approximate orientation of Yakutat-North America convergence. An array of 36 Bolt airguns with a total volume of 6600 cubic inches comprised the seismic source which was fired at 50 m spacing.

For reflection data acquisition, shots were recorded by receivers spaced every 12.5 m within an 8 km solid streamer, resulting in common midpoint spacing (CMP) of 6.25 m. The reflection profile was processed as two lines, STEEP01a and STEEP01b, separated by a ~ 20 km data gap near the Yakutat Sea Valley (Figure 4.2) caused by

temporary air compressor failure (Figure 4.3). The western profile section, crossing the Pamplona Zone deformation front is STEEP01a; the eastern profile section crossing the DRZ is STEEP01b (Figure 4.3). Data processing using Paradigm Geophysical FOCUS software included trace regularization, normal move-out correction, bandpass filtering, muting, stacking and frequency-wave number migration. The final stack for STEEP01b also included a time-varying filter to help mitigate the effect of strong water-bottom multiples. Vertical resolution at the seafloor is ~30 m and maximum energy penetration across the profile is ~7 seconds two-way travel time (twtt) at the western end of STEEP01a.

The top of Yakutat basement can be interpreted across the STEEP01 seismic reflection profile as a high-amplitude, low-frequency reflector (Figure 4.3b). At the western extent of STEEP01a, near the Bering Glacier, the reflector is visible at ~6.5 seconds twtt, despite some noise and migration artifacts. The basement reflector gradually shallows from west to east, visible at ~4 seconds two-way travel time (twtt) beneath the Yakutat Sea Valley at the western end of STEEP01b, until the reflector reaches the seafloor near the mapped DRZ (Figure 4.1; Figure 4.3). Strong seafloor multiples and the decrease in energy penetration east of the mapped DRZ are the result of strong reflections off the shallow Yakutat basement. My joint tomographic inversion uses 406 travel-time picks, spaced at ~1 km intervals, of Yakutat basement depth interpreted across the offshore MCS profile. I visually assigned a constant uncertainty of 80 ms to the reflection travel-time picks.

Twenty-five UTIG OBS's were deployed at 15 km spacing along the STEEP01 profile (Figure 4.2). Two instruments were flooded during deployment and did not record data. Data recordings for two of the recovered instruments were corrupted by noisy channels. Thus, 21 OBS records were available for the tomographic inversion. Phase arrival times were determined from vertical component and hydrophone data for 6376 airgun shots. A marine mammal sighting and temporary compressor failure caused two breaks in data acquisition leading to data gaps of ~5 km and ~20 km, respectively, in the OBS receiver gathers (Figures 4.4-4.6).

Figures 4.4-4.6 show representative OBS record sections for the western, central and eastern portion of the profile, respectively, with interpreted arrivals for several phases. OBS 105 is located at the western end of the profile, ~ 60 km from the coast line near Bering Glacier (Figure 4.4). Turning waves from the sedimentary cover sequence (Ps) are the first arrivals at offsets up to ~50 km. Crustal turning waves (Pg) are observed at offsets greater than ~40 km. I also detect wide-angle basement reflections (PgP) and, at offsets greater than ~100km, mantle reflections (PmP). OBS 115 is located ~150 km from the western end of the profile (Figure 4.5). Phase arrivals that sample Yakutat crust (Pg) arrive earlier on this record compared to OBS105, at offsets less than ~20 km. The PmP phase is also observed at closer offsets, between ~50 km and ~150 km. OBS 123 is near the eastern end of the line, ~ 30 km from the termination of the profile (Figure 4.6). Unlike records from the western and central portions of the profile, the change in slope of the first arrivals is gradual. Mantle reflections are observed at offsets between ~70 km and ~120 km. Instruments at the eastern portion of the profile also recorded mantle

refractions (Pn) at far offsets, >170 km in Figure 4.6. For stations in the central (Figure 4.5) and eastern (Figure 4.6) portions of the profile, it is impossible to distinguish between Ps and Pg arrivals. I identify a first-arriving phase, Po, which represents a wave that turns in the sediments or the crustal layer. The inversion does not constrain the depth at which the corresponding raypaths turn in order to limit bias in the inversion.

I visually assigned uncertainties for the travel-time picks based on signal-to-noise ratio. Figure 4.7 shows the distribution of assigned uncertainties for 4109 OBS travel time picks; picks were picked at ~1.5 km intervals. Generally, the uncertainty was larger with increased receiver offset, and negative offsets had higher uncertainties than positive offsets (Figure 4.7). This discrepancy occurs because picks at the eastern end of the profile included the farthest offset picks, which are inherently more affected by noise and energy attenuation.

Four broadband seismometers, deployed onshore as part of the STEEP passive seismic experiment, lie roughly in line with the offshore profile and recorded the marine shots. To incorporate these data into a 2-D model, I extended the offshore profile westward by 115 km (Figure 4.2). I applied travel-time corrections to account for the difference between three-dimensional ray paths for the observed arrivals and their two-dimensional projected ray paths in my profile. For each of these stations, the inline offset was much greater than the distance from the station and the extended profile, so the correction for each travel time pick was less than 0.3% of the observed travel time. In addition, uncertainties for the onshore picks, 120 ms for crustal arrivals and 200 ms for

mantle arrivals, were assigned so that the travel time correction was well within the uncertainty.

Figure 4.8 shows an example of a land-based record section from station BGLC. Arrivals associated with crustal turning waves (Pg) are visible at offsets greater than ~40 km. Reflections from the crust-mantle boundary are observed at ~60 km to ~90 km offsets.

The combined OBS and broadband dataset contributes 4489 travel-time picks to the inversion. The majority of these arrivals are attributed to crustal turning waves in the Yakutat basement, while mantle reflection arrivals and sedimentary layer arrivals are also well sampled across the profile.

4.4. TOMOGRAPHY

I present a seismic velocity model for the STEEP01 profile (Figure 4.9) constructed through a series of linearized tomographic inversions of travel time data derived from the MCS stack (Figure 4.3), OBS shot gathers (Figures 4.4-4.6), and onshore station records (Figure 4.8). For each iteration, I trace rays in the current velocity model to develop a set of calculated travel times. I invert for an update to the current velocity model using the difference between picked and calculated travel times. After each linear inversion, the updated velocity model becomes the starting model for the next iteration of ray-tracing and inversion. Data fit is assessed using the normalized data misfit, χ^2, between calculated and picked travel times for each new model. The two-step

process of ray-tracing and inversion continues until a good data fit, i.e., $\chi^2 \sim 1$, is achieved.

The model parameterization assumes smooth velocity variations within each layer and a velocity discontinuity at each layer boundary. Seismic refractions and reflections within each layer and at each layer boundary should correspond to phases assigned in the observed data (Ps, PgP, Pg, PmP, and Pn). First-arriving phases (Po) can turn in any layer of the model. All travel times are inverted to constrain velocities and boundary layer depths of the sedimentary cover layer, Yakutat crust and mantle in the STEEP01 model.

Raytracing for STEEP01 uses the shortest path method (SPM) (Moser, 1991; Nakanishi and Yamaguchi, 1986b) and ray-bending (van Avendonk et al., 2001) to compute seismic ray paths through the model from each receiver to each source. In the SPM, rays travel through the model on a network of randomly positioned nodes, choosing a path that travels the shortest distance between each node. SPM finds the approximate ray paths, even in complex velocity models, but travel times may be over-estimated (van Avendonk et al., 2001). After SPM, ray bending is applied, which results in a smoother ray path and smaller travel time. Raytracing for the first arriving phases (Po) is accomplished in one step of SPM. Raytracing for the remaining phases occurs in two steps: first, I calculate raypaths and travel times from an instrument to a layer boundary in the model-space (i.e., sediment-crust interface or Moho); next, I calculate raypaths and traveltimes back to the surface using the boundary layer as a time-varying source.

I constructed a three-layer starting velocity model with boundaries at the sedimentary cover-Yakutat crust interface and at the crust-mantle boundary. Starting velocities and layer boundary depths were based on the MCS stack and crustal and mantle velocities from Christeson et al. (2010). For raytracing, I used an average grid-spacing of 200 m. During inversion, horizontal grid-spacing was defined as 1.5 km, and vertical grid-spacing increased from 250 m near the top of the model to 500 m at depth. Horizontal and vertical regularization were 16 km and 6 km, respectively.

To obtain a velocity model with minimum structure, I applied damping, flattening (minimum first derivatives) and smoothness (minimum second derivatives) constraints during each linearized inversion step (after van Avendonk et al., 2004b). The flattening parameter controls the amplitude of velocity anomalies within each model layer. The smoothing parameter controls model roughness. In the final inversion, my smoothing parameter is double the flattening parameter. This setup allows greater velocity anomalies, but limits model roughness. The damping constraint controls how large a model perturbation is allowed between the current and updated models. A lower damping parameter allows larger perturbations. In the final inversion, I apply very little damping in order to limit bias toward the starting model. All model regularization is tuned for my preferred data misfit in order to invert for a model that has discernable structure, but does not overfit the data and result in unrealistic anomalies.

4.5. DATA FIT AND MODEL ASSESSMENT

Figure 4.9 shows the final model and calculated raypaths for the STEEP01 profile. The model has an average RMS travel-time residual of 119 ms and a normalized data misfit, χ^2, of 0.998. Figure 4.10 compares calculated travel times through the final model with picked travel times for ten OBS record sections. In general, data misfit increases with source-receiver offset, a trend that was expected given the greater uncertainties assigned to larger offset picks (Figure 4.7). Figure 4.11 shows travel time fits and corresponding raypaths for first arriving phases (Po), crustal turning waves (Pg), Moho reflections (PmP) and mantle refractions (Pn).

I can assess the quality of the final velocity model by inspecting the ray density with the calculated derivative weight sum (DWS) (Figure 4.12). The derivative weight sum is the summation of the column of the Frechet matrix used in inversion (Toomey and Foulger, 1989). The DWS shows the coverage of the data set for each model parameter: velocity and layer boundary depth. Generally, ray coverage is low in the western onshore portion of the profile and highest within the sedimentary cover layer and the upper crust in the offshore profile. The sediment-basement boundary layer is well constrained at all offsets in the offshore and more sparsely controlled beneath the onshore stations. Ray coverage in the lower crust is less dense than in the upper crust, but is fairly evenly sampled across the offshore profile. The crust-mantle boundary is well constrained at positive offsets across the profile.

An important question for my preferred model is how well does the model resolve variations in seismic velocity and boundary layer depth. To test the model resolution, I construct the resolution matrix from the generalized inverse that created the final seismic velocity model (see Appendix C). The resolution matrix can be used to predict how any seismic velocity structure will be mapped into the final model (van Avendonk et al., 2004b). First, I define a theoretical input model feature of a specified size that acts as a sliding window across the model. The size of test anomalies can be adjusted to test the limits of model resolution. In Figure 4.13, I determine the model resolution for windows of varying length scales. Resolution values are non-dimensional and range from zero (not resolved) to one (fully resolved). Resolution values > 0.5 are achieved for a feature 20 km x 10 km (horizontal x vertical) in the upper ~15-20 km of the model at positive offsets (Figure 4.13b). For features 50 km x 20 km, model resolution is ~0.6-1.0 at all depths in the eastern third of the profile, across most of the crustal layer and within the entire sedimentary layer.

4.6. RESULTS

I present a model for crustal thickness and seismic velocity structure of the Yakutat microplate from west of the Bering Glacier onshore to east of the DRZ offshore (Figure 4.9). The velocity model includes three layers: the top layer represents the Yakutat sedimentary cover; the middle layer represents Yakutat crust; the lowest layer represents the top of lithospheric mantle. Overall crustal thickness across the profile (our model, minus the sedimentary cover) increases from ~17 km thick at the western end of

the profile to ~30 km thick east of the DRZ. The thickness change is accompanied by west-to-east shallowing of the sediment-basement interface from ~13 km depth below the Bering Glacier to emerging at the ocean floor near the mapped DRZ, while the Moho maintains a relatively constant depth between ~29.5-31.5 km across the profile.

Velocities in the sedimentary layer range from ~2 km/s to greater than ~4 km/s, generally increasing towards the western profile. Towards the offshore DRZ, upper crustal velocities decrease to ~4.2-5.2 km/s as the basement surface gradually shallows before cropping out at the seafloor (Figure 4.9). These low crustal velocities are limited to a slightly wedge-shaped low-velocity cap that occupies the upper 5-7 km of Yakutat crust in the eastern ~100 km of the profile (Figure 4.9). Yakutat crust underlying this low velocity cap appears laterally continuous across the profile with velocities ranging from ~6.5 km/s to ~7.2 km/s. Figure 4.14 compares one-dimensional velocity profiles of the Yakutat block east and west of the DRZ. In Figure 4.14b, I remove the low velocity cap for the profile east of the DRZ and compare the resulting velocity profile to the crustal velocity profile, with sediments removed, west of the DRZ. This comparison shows that Yakutat lower-crustal velocities differ by <0.3km/s down to the crust-mantle boundary. The two profiles follow similar trajectories down to the crust-mantle boundary, at ~25 km on either side of the DRZ (Figure 4.14 b). Mantle velocities are ~8.2 km/s.

4.7. DISCUSSION

4.7.1 The Yakutat oceanic plateau

Yakutat crust west of the DRZ has been established as an oceanic plateau based on crustal thickness and velocity structure (Christeson et al., 2010). In the STEEP01 profile, crustal thickness ranges from ~17-30 km, compared to 5.0-8.5 km for normal oceanic crust (Figure 4.9;Figure 4.15) (White et al., 1992). This thickness is within the range of established thicknesses of other known oceanic plateaus: e.g., 18-22 km for the Kerguelen Plateau in the southern Indian Ocean (Charvis et al., 1995; Operto and Charvis, 1996); and 31 km for Ontong-Java in the western Pacific (Miura et al., 2004). Slightly extended continental crust displays similar average thickness of 30.5 +/- 5.3 km (Figure 4.12) (Christensen and Mooney, 1995; Christeson et al., 2010), but Yakutat crustal velocities are consistently 0.5-1.0 km/s faster than those established for extended continental crust (Figure 4.15) (Christeson et al., 2010).

East of the DRZ, Yakutat crust has been interpreted as continental in origin, possibly a fragment of Chugach terrane material that was excised from the Canadian Cordillera during transport of the Yakutat microplate northward to its current position (Bruhn et al., 2004; Bruns, 1983a; Plafker, 1987; Plafker et al., 1994). In this interpretation, the DRZ is a remnant crustal-scale strike-slip fault that juxtaposes oceanic and continental material (Plafker et al., 1994). However, my velocity model along profile STEEP01 is inconsistent with a steeply dipping crustal scale boundary. Instead, Yakutat velocity structure appears laterally continuous in the lower ~20 km of the crustal section

(Figure 4.9). Comparison of velocity-with-depth profiles taken west and east of the DRZ shows similar structure in the mid- to lower crust (Figure 4.14b). This observation suggests that the offshore Yakutat terrane is not two distinct crustal types separated by a vertical boundary, rather the lower crustal section is continuous beneath the DRZ.

Figure 4.15 shows comparison of Yakutat crustal velocity structure with several oceanic plateaus, continental crust and the Chugach terrane. Following Christeson et al. (2010), I compare only crystalline basement and upper mantle velocities beneath the sedimentary cover and the low-velocity upper crustal wedge below basement east of the DRZ. The upper crustal velocities west of the DRZ are ~6.5 km/s in the upper 5 km of Yakutat crust, faster than the ~5.0 km/s of the upper Ontong-Java Plateau (Miura et al., 2004), the ~5.5-5.7 km/s of the upper Siletz terrane (Gerdom et al., 2000) and the ~5.8-6.2 km/s of the upper Kerguelen Plateau (Operto and Charvis, 1996). This discrepancy may be attributable to differences in overlying sediment thickness, as suggested by Christeson et al. (2010). The 6-7 km-thick sedimentary sequence overlying the Yakutat crust may mask the velocity decreasing effect of surface fractures that characterize the upper crust of comparable oceanic plateaus (e.g., Miura et al., 2004). By contrast, the Kerguelen and Ontong-Java sedimentary cover sequences are between ~1 and ~2 km thick (Miura et al., 2004; Operto and Charvis, 1996), so the upper crustal velocity of these oceanic plateaus may be lower even if the lithology is the same. Mid- to lower crustal velocities west of the DRZ increase from ~6.5 km/s near 5 km depth to ~7.2 km/s at the crust-mantle boundary. Though specifics of the gradients differ, this velocity range compares to mid- to lower crustal velocities for the Ontong-Java plateau of ~6.4 km/s to

~7.4 km/s between ~10 km depth and the crust-mantle boundary (Miura et al., 2004). Similarly, the Kerguelen plateau ranges from ~6.2 km/s at 5 km depth to >7.5 km/s near the crust mantle boundary (Operto and Charvis, 1996).

Yakutat crustal velocities east of the DRZ, underlying the low-velocity wedge, range between ~5.5-6.2 km/s in the upper ~10 km of the profile (Figure 4.15). These velocities are less than the ~6.5 km/s measured in the upper part of the crustal section west of the DRZ, but are within range of upper crustal velocities measured for the Kerguelen and Ontong-Java Plateaus (~5.8-6.4 km/s and ~4.8-6.4 km/s, respectively) (Miura et al., 2004; Operto and Charvis, 1996). Below 10 km, Yakutat crustal velocities east and west of the DRZ differ by <0.3 km/s down to the crust-mantle boundary. Depth to mantle on each of these profiles is nearly identical, measuring ~25 km on either side of the DRZ. Therefore, based on velocity structure and crustal thickness below the low-velocity cap at the eastern end of the profile, the Yakutat microplate is an oceanic plateau across its entire offshore extent.

4.7.2 Origin of the eastern low-velocity cap

Constraints for the origin of the low-velocity cap at the eastern end of the offshore Yakutat microplate can be derived from previously observed onshore relationships. Onshore, the DRZ is defined by the contact between the Neogene sedimentary cover on the west and the Yakutat Group accretionary complex on the east (Plafker, 1987; Plafker et al., 1994). The Yakutat Group is interpreted as a metamorphosed, remnant accretionary prism consisting of both coherent greywacke-argillite assemblages and mélange of

greywacke, argillite, marble, and metachert (Plafker, 1987; Plafker et al., 1994). Average seismic velocities for similar lithologies range from ~3.8-4.6 km/s from ~0-3 km depth and ~4.6-6.2 km/s from ~3-8 km depth (Mooney and Luetgert, 1982). Along STEEP01, velocities for the upper basement southeast of the DRZ range from ~4.2-4.5 km/s in the upper ~3km and increase to ~5.2 km/s at ~5 km depth. Based on the nature of the onshore contact and the seismic velocity range, I interpret the low velocity cap as part of the Yakutat Group. This interpretation agrees with offshore dredging results that produced rocks with similar affinities to the Yakutat Group from locations near Fairweather Ground (Figure 4.1) (Plafker, 1987; Plafker et al., 1994).

Low upper crustal velocities, ~4.2-5 km/s, on the eastern end of the profile coincide with increased basement roughness and sub-basement reflectivity observed in the STEEP01b seismic reflection image (Figure 4.3; Figure 4.16). This observation may be indicative of chaotic bedding relationships or the presence of large blocks within the low-velocity cap. This type of internal structure is consistent with observations of numerous intact exotic blocks within the Yakutat Group mélange (Plafker, 1987; Plafker et al., 1994). In contrast, oceanic basement to the west of the low-velocity section does not display internal structure due to lack of seismic energy penetration.

Seismic reflection data image the subsurface near the mapped offshore DRZ showing an increase basement roughness and sub-basement reflectivity below the Alsek Sea Valley (Figure 4.16). However, there are no obvious sub-basement truncations indicative of a major structural boundary. The basement reflector gradually shallows toward the mapped DRZ and does not display abrupt offset that might be expected at a

primary crustal boundary separating crust of two very different compositions and densities (Figure 4.3; Figure 4.16). Onlap of flat-lying sediment packages onto the shallowing basement reflector indicates sediment infilling onto a previously existing basement high rather than a tectonically active boundary (Figure 4.16). Elsewhere, the overlying sedimentary sequence is not well-imaged at depth and lacks cohesive stratal relationships, making it difficult to discern any possible tilt or depositional patterns. It is possible that this portion of the sedimentary cover is fairly unconsolidated, an interpretation which agrees with calculated seismic velocities of ~2.0-2.5 km/s in the western portion of the sedimentary layer (Figure 4.9).

Based on seismic velocity range and potential onshore Yakutat Group equivalent, I suggest that the low-velocity cap at the eastern end of the STEEP01 profile represents a remnant accretionary prism that was attached to the underlying Yakutat oceanic plateau. In this interpretation, the mapped DRZ marks a basement high where the surface of the low-velocity crustal cap reaches the seafloor. The presence of Yakutat Group mélange overlying Yakutat oceanic crust implies that the Yakutat terrane must have been adjacent to the North American continent at some point during its pre-collisional history. This interpretation is consistent with tectonic models of Plafker (1994) and Bruns (Bruns, 1983a), which propose that the Yakutat microplate previously collided with North American near the American Pacific Northwest or southern British Columbia, respectively. The sub-horizontal contact between the Mesozoic Yakutat group mélange and the Eocene oceanic plateau implies that the remnant accretionary prism was underthrust by the Yakutat oceanic plateau, perhaps during this collision. Subsequently,

the Yakutat oceanic plateau plus the low-velocity cap was transported via strike-slip motion on the Queen Charlotte-Fairweather and Transition faults to its current position in the northern Gulf of Alaska (Christeson et al., 2010; Plafker, 1987; Plafker et al., 1994).

Previous work uses the DRZ as a piercing point (Plafker, 1987; Plafker et al., 1994), forcing a paleogeography where the Yakutat terrane was plucked from the margin in what is now southeast Alaska. The results of this study contradict that piercing point, and so other options must be considered. Basic crustal structure of the Yakutat terrane compares favorably with that of the Canadian Cordillera off Vancouver Island (Zelt and White, 1995) which includes North American basement and Pacific Rim accretionary complex (similar to the Yakutat Group) structurally overlying accreted high-velocity material of the Siletz-Crescent assemblage (Figure 4.15). This similarity suggests a possible southern Canadian origin for the Yakutat terrane, although more work is needed to test this hypothesis.

4.7.3 Subduction dynamics

Offshore Yakutat crust tapers in the direction of subduction from ~30 km thick east of the DRZ to ~17 km thick near Bering Glacier. After the initial taper offshore, Yakutat crustal thickness may be relatively constant, given observations of a subducted ~15-20 km thick-slab as far inboard as the Alaska Range (Figure 4.1) (Ferris et al., 2003). It follows that the flat-slab segment of the Alaskan subduction zone is caused by the continued subduction of the anomalously thick Yakutat crust and underlying Yakutat mantle lithosphere.

This conclusion is a departure from slab models predicted by the 1988 Tran-Alaska Crustal Transect (TACT) (Brocher et al., 1994; Eberhart-Phillips et al., 2006; Fuis et al., 2008). These models predict that anomalously thick subducted crust observed in the Prince William Sound region west of the Bering Glacier is indicative of overlapping Yakutat and Pacific plates at depth. My results indicate that Yakutat thickness alone in this region is ~15-20 km. If the Yakutat and Pacific plates were overlapped near Prince William Sound, we would expect observed slab thickness to exceed ~25-30 km (~15-20 km Yakutat crust plus ~8-10 km-thick Pacific crust). Additionally, Christeson et al. (2010) determined that there is no evidence for Pacific crust underthrusting Yakutat crust at the offshore Transition fault along profile STEEP02 (Figure 1), given abrupt changes in crustal thickness across the structure.

The thickness of the Yakutat crust leads to buoyancy conditions that favor flat-slab subduction beneath North America. The leading edge of subducting Yakutat crust is observed at ~100 km depths ~800 km inboard from the offshore deformation front (Eberhart-Phillips et al., 2006; Ferris et al., 2003). However, long-term subduction of the Yakutat terrane may be geodynamically unstable. Buoyancy analysis (Cloos, 1993) and numerical modeling (van Hunen, 2002) results indicate that subduction of basaltic crust >18 km is dynamically unfavorable. Given these parameters, the subducted Yakutat crust may be at the upper limit of subductibility. Indeed, Gulick et al. (2007) attributed movement on the Transition Fault and seismicity on the Pacific Plate at the Gulf of Alaska Shear Zone (GASZ) to incipient plate reorganization as the Yakutat terrane resists subduction. The Pacific Plate is the weakest lithosperic member of the North America-

Yakutat-Pacific Plate subduction corner and the Transition Fault is a long-lived structural boundary (Christeson et al., 2010), so deformation is localized on these structures (Gulick et al., 2007).

Offshore, Yakutat crust increases in thickness to ~30 km and is likely unable to continue subduction. Convergence of this thickened Yakutat crust with North America near the DRZ may be driving orogenesis of the St. Elias Mountains in an evolving collision. As Yakutat-North American convergence continues, it is possible that subduction will ultimately fail and the plate interface will jump seaward (Gulick et al., 2007; von Huene and Ranero, 2009). In this scenario, the offshore accretionary prism would dock onto the underlying Yakutat crust and the unsubducted Yakutat crust would become part of the North American continent. Following accretion of Yakutat crust, the region may be affected by a combination of slab break-off of the subducting Yakutat lithosphere and underplating closer to the plate interface. The hypothesized presence of the Yakutat Group accretionary prism overlying the Yakutat plateau on the east may be evidence of previously failed Yakutat subduction prior to emplacement at the Gulf of Alaska margin.

4.7.4 Yakutat sedimentary cover sequence and accretionary prism

The sedimentary cover layer overlying Yakutat crust exhibits seismic velocities ranging from ~2.0-4.5 km/s (Figure 4.9). Velocities generally increase from east-to-west towards the Yakutat-North America deformation front and the onshore-offshore fold-thrust belt that forms the St. Elias foreland. The cover sequence is primarily composed of

the glacially-derived Yakataga Formation composed of marine mudstones and interbedded sandstones and siltstones (Plafker, 1987; Trop and Ridgway, 2007). The Yakataga Formation ranges in thickness up to ~10 km (Worthington et al., in press) and overlies the pre-glacial Poul Creek and Kultieth Formations (Plafker et al., 1994; Trop and Ridgway, 2007). These sedimentary units are not differentiated by the velocity model. I interpret the increase in velocity from east to within the sedimentary cover as a result of increased deformation and related compaction and dewatering due to Yakutat-North American convergence. This phenomenon is documented in other accretionary settings such as near the Barbados Ridge, in the Makran accretionary prism, and the southern Cascadia subduction zone (Gulick et al., 1998; Kopp et al., 2000; Westbrook et al., 1988).

Higher velocity zones within the sedimentary cover layer ~20-60 km east of the coastline coincide spatially with the Pamplona Zone fold-thrust belt (Figure 4.17). The Pamplona Zone essentially forms the outer accretionary prism created by subduction of the Yakutat microplate beneath North America (Worthington et al., 2008; Worthington et al., in press). The reflection seismic profile does not clearly image the Yakutat-North America décollement; however, I argue that the décollement must be at or near the sediment basement contact based on interpretation and fold analysis by Worthington et al. (Worthington et al., in press). The position of the décollement near the Yakutat basement suggests that most, if not all, of Yakutat sedimentary cover is accreting to the North American continent.

The current presence of an accretionary margin in a region of flat-slab subduction is somewhat of an anomaly. Subduction erosion dominates the flat-slab segments in South America and is thought to have characterized the Gulf of Alaska margin in the past (von Huene, 1999; von Huene and Ranero, 2009). However, the current Yakutat region is unique in that it is directly adjacent to an extensively glaciated orogen, which creates a steady sediment supply that is partially deposited in basins located on the Yakutat shelf (Worthington et al., in press). This eroded material that remains within the system is reworked into the offshore foreland that forms the accretionary wedge (Worthington et al., in press).

4.7.5 St. Elias orogenesis

The St. Elias orogen displays its highest relief and highest long-term exhumation rates near the St. Elias massif north of the Malaspina Glacier in an area termed the Seward Corner (Enkelmann et al., 2010; Spotila and Berger, 2010) (Figure 4.1). Relative Yakutat-North American plate motions transition in this area from strike-slip on the Fairweather fault to convergence on the Malaspina fault and other thrusts (Bruhn et al., 2004; Elliott et al., 2010; Pavlis et al., 2004; Spotila and Berger, 2010). The shift in orientation of the major faults from north-northwest to northeast trending creates an orogenic corner comparable to Himalayan syntaxes, producing high uplift and deformation rates (Enkelmann et al., 2010; Koons et al., 2010; Spotila and Berger, 2010).

The Seward Corner lies near the mapped onshore DRZ. Existing orogenic models for the St. Elias make use of previous definitions of the Yakutat microplate as a

composite oceanic-continental terrane in which the continental fragment east of the DRZ acts as a local indentor (Bruhn et al., 2004; Pavlis et al., 2004). My velocity model provides no evidence that Yakutat crustal composition changes across the offshore DRZ (Figure 4.10; Figure 4.13). However, the wedge shape of the offshore Yakutat microplate and the onshore continuation of the mapped DRZ basement high indicate that the thickest Yakutat crust enters the orogen at this corner. Additionally, the ~5 km thick Yakutat Group metasediments that overlie the thickest Yakutat crust provide additional mass being transported into the Seward Corner.

I propose a new "door-stop model" for the orogenic driver of the St. Elias Mountains in which thicker Yakutat crust with its cap of metasediments near the DRZ acts as a pseudo-indentor in the corner. Accelerating uplift and increasing deformation occur as the plate boundary attempts to accommodate convergence of increasingly thick Yakutat crust. In this model, localized uplift in the Seward Corner is the combined result of lateral changes in the thickness of the incoming Yakutat slab and the orogenic corner geometry observed at the surface. Exhumation at this corner is likely enhanced by glacial erosion (Enkelmann et al., 2010), but I propose that the overall topographic signature is primarily controlled by structural interactions at depth.

4.8. CONCLUSIONS

1. Yakutat crustal thickness and seismic velocities at depth are consistent with an oceanic plateau origin across the entire offshore profile, on either side of the DRZ.

2. The offshore DRZ is a basement high associated with a ~100 km-wide, ~5 km-thick, low-velocity crustal cap overlying the Yakutat oceanic plateau in the eastern quarter of the profile.
3. The offshore Yakutat block is wedge-shaped: Yakutat crust tapers in the direction of subduction from ~30 km thick east of the DRZ to ~17 km thick near Bering Glacier. After the initial taper observed offshore, subducted Yakutat thickness remains relatively constant, resulting in observed flat-slab subduction and anomalously thick low-velocity zones beneath Prince William Sound and as far inboard as the Alaska Range.
4. The thickest Yakutat crust enters the St. Elias orogen near the St. Elias massif north of Malaspina Glacier, where the orogen displays its highest relief and highest long-term exhumation rates. Uplift patterns and present-day St. Elias topography are likely controlled by the interplay of lateral variations in the Yakutat slab "door stop" geometry at depth and the restraining-bend geometry of surface faults.
5. I provide new constraints for the pre-collisional history of the Yakutat microplate. The presence of overlying remnant accretionary prism, the Yakutat Group, near the DRZ implies that the Yakutat block previously collided with the North America cordillera before transport to the Gulf of Alaska. The Yakutat microplate seismic velocity structure is similar to the Siletz terrane in southern Oregon, indicating that these terranes may share common ancestry or were previously juxtaposed.

6. Given proposed limits on subductibility of thickened oceanic lithosphere, I suggest that Yakutat microplate subduction in southern Alaska will eventually cease. It is likely that the Transition fault will become the major transform plate boundary between North America and the Pacific Plate in the northern Gulf of Alaska and some portion of the subducted Yakutat microplate will underplate North America while the unsubducted Yakutat microplate material will become part of the North American continent.

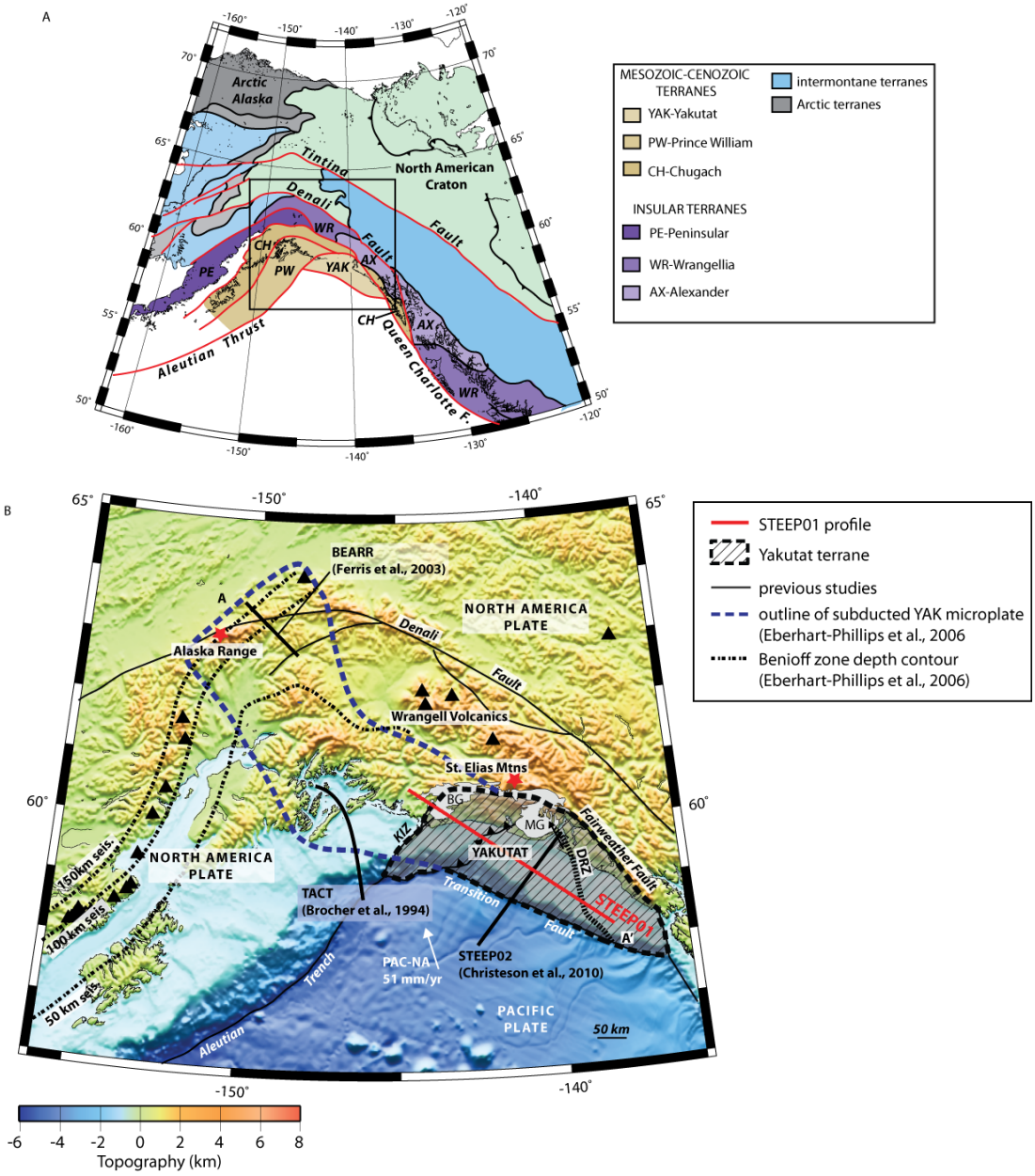

Figure 4.1. Tectonic setting and regional basemap of southern Alaska. a) Generalized terrane map after Nokleberg et al. (2000) and Plafker et al. (1994). b) Map of southern Alaska showing major faults, mountain belts and geographic landmarks. Pacific Plate velocity vector from Demets and Dixon (1999). Yakutat block velocity vector (black arrow) 47 mm/yr from Elliot et al. (in press). Blue dashed line shows extent of subducted Yakutat slab from Eberhart-Phillips et al., (2006)

Figure 4.1 cont'd. Black dashed outline shows currently defined Yakutat terrane. Red star in Alaska Range is Mt. Denali; red star in St. Elias Mountains is Mt. St. Elias. Black lines show previous studies. Red line shows STEEP01 profile. Black triangles are volcanoes. Benioff zone depth contours at 50, 100, and 150 km. KIZ = Kayak Island Zone; DRZ = Dangerous River Zone; BG = Bering Glacier; MG = Malaspina Glacier.

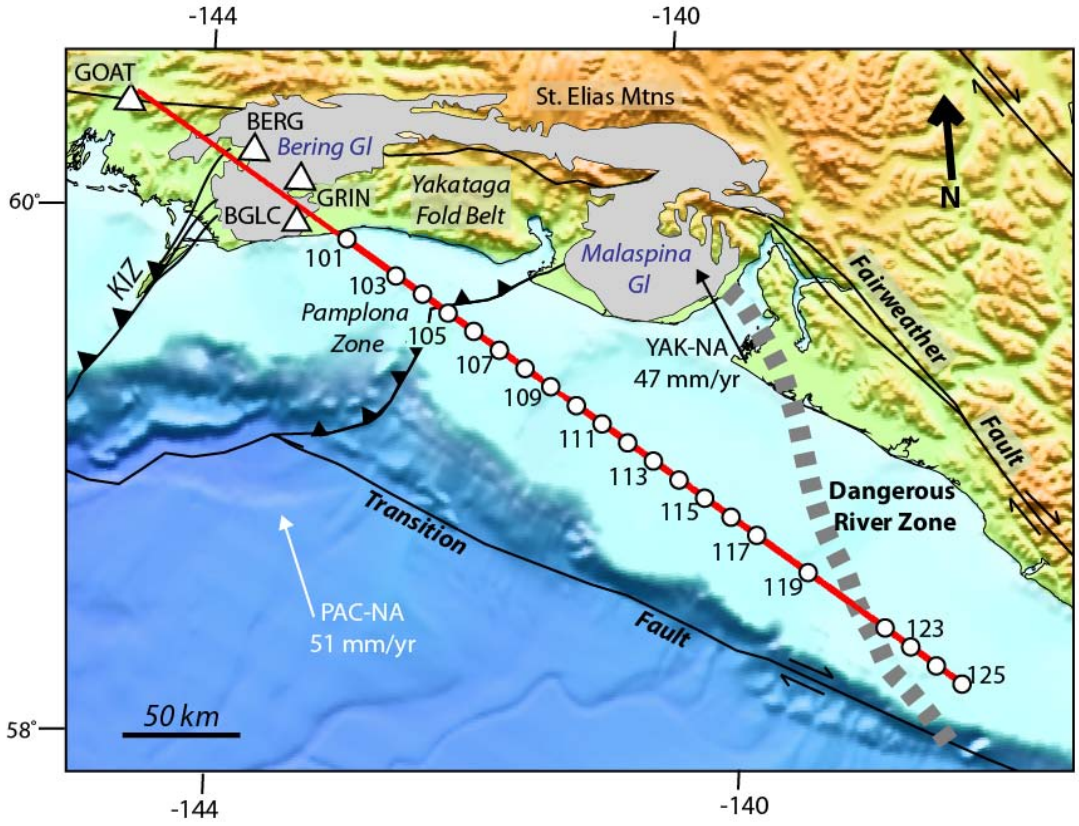

Figure 4.2. Map of study area. Red line is STEEP01 profile. White triangles are broadband stations. White circles are ocean bottom seismometers. Yakutat terrane velocity vector from Elliot et al. (2010). KIZ = Kayak Island Zone. Mapped Dangerous River Zone from Plafker et al. (1994).

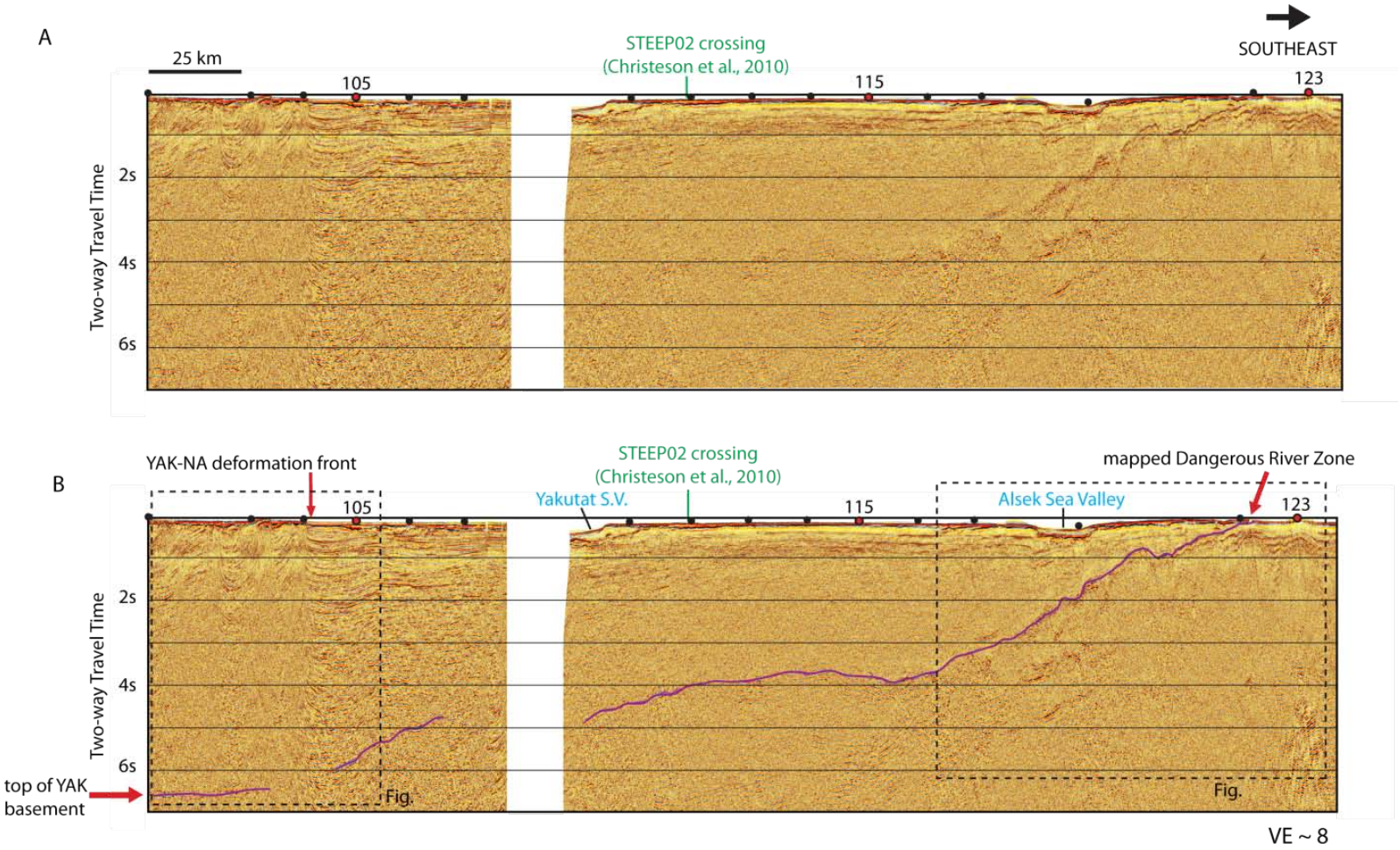

Figure 4.3. STEEP01 marine multichannel seismic reflection data uninterpreted (a) and interpreted (b). Black circles are ocean bottom seismometers (OBS). OBS 105, OBS 115, OBS 123 are red circles, data records shown in Figures 4.4-4.6. b) Top of Yakutat basement interpreted. Mapped Yakutat-North

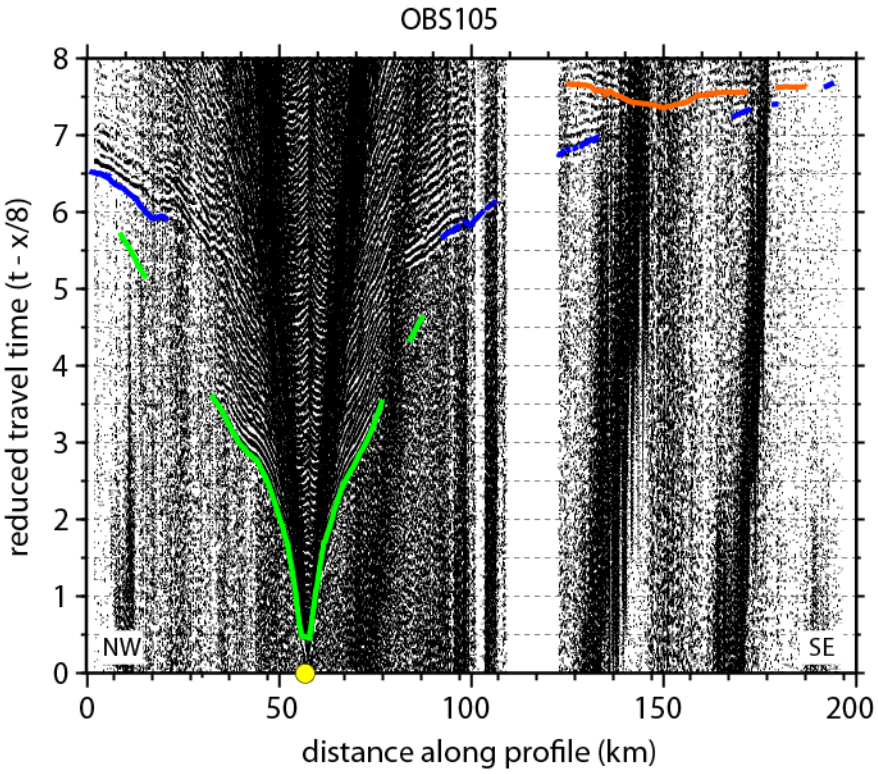

Figure 4.4. Data record from OBS 105 (location shown in Figure 3) shown with a reduction velocity of 8 km/s. Picked travel time arrivals shown for Psed (green), Pg (blue) and PmP (orange).

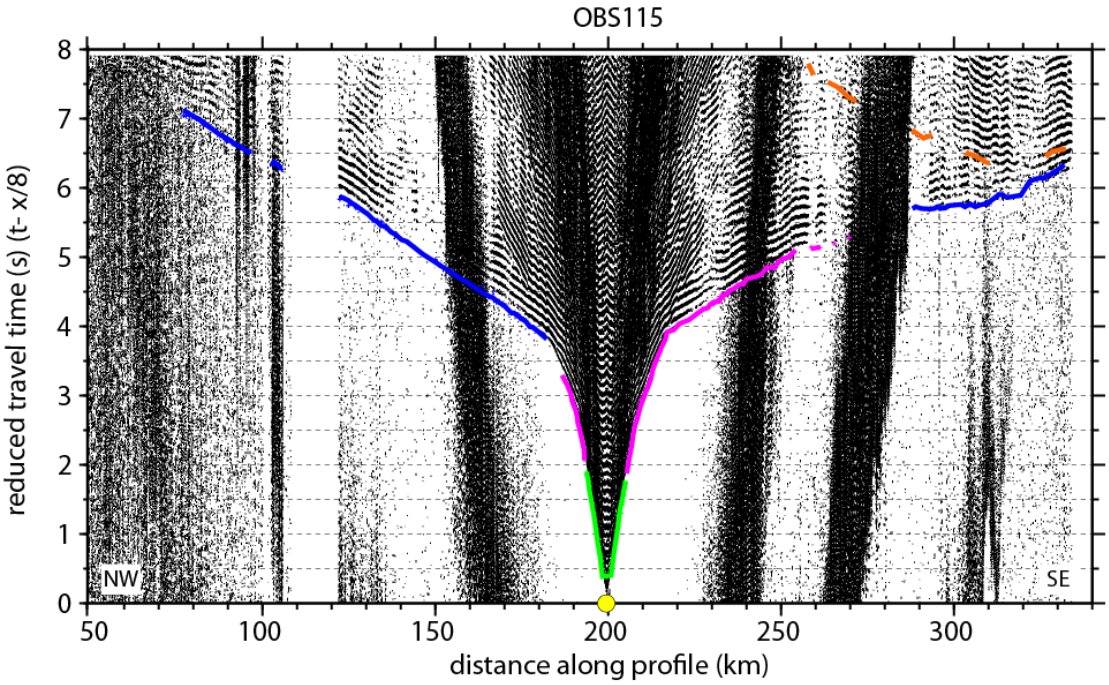

Figure 4.5. Data record from OBS 115 (location shown in Figure 3) shown with a reduction velocity of 8 km/s. Picked travel time arrivals shown for Psed (green), Po (magenta), Pg (blue) and PmP (orange).

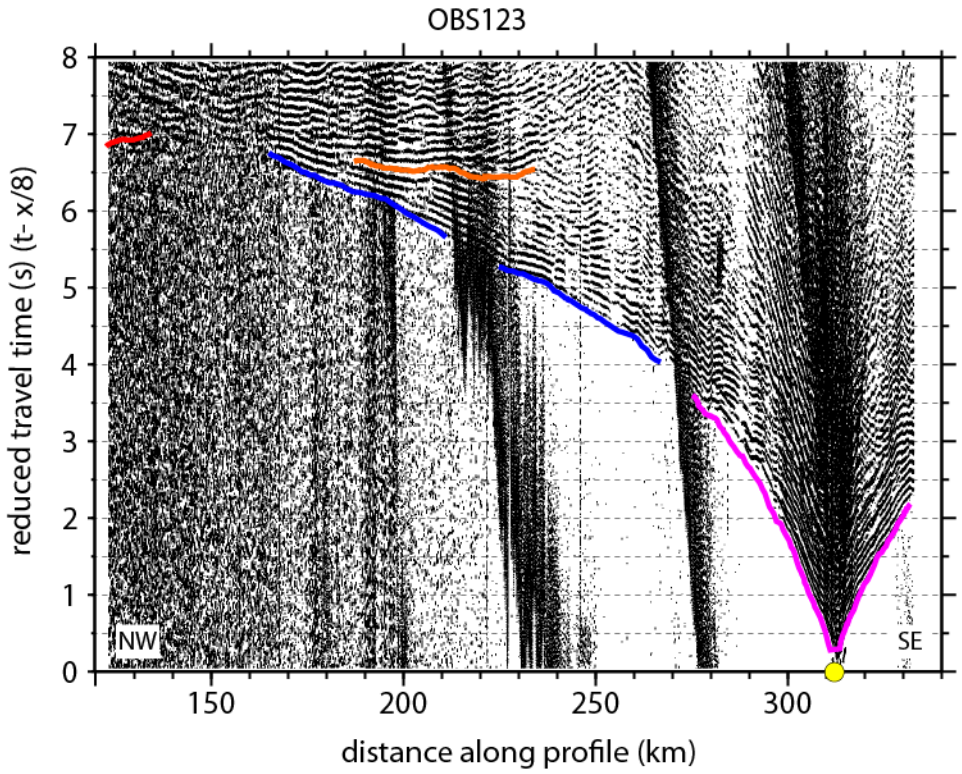

Figure 4.6. Data record from OBS 123 (location shown in Figure 3) shown with a reduction velocity of 8 km/s. Picked travel time arrivals shown for Po (magenta), Pg (blue), PmP (orange), and Pn (red).

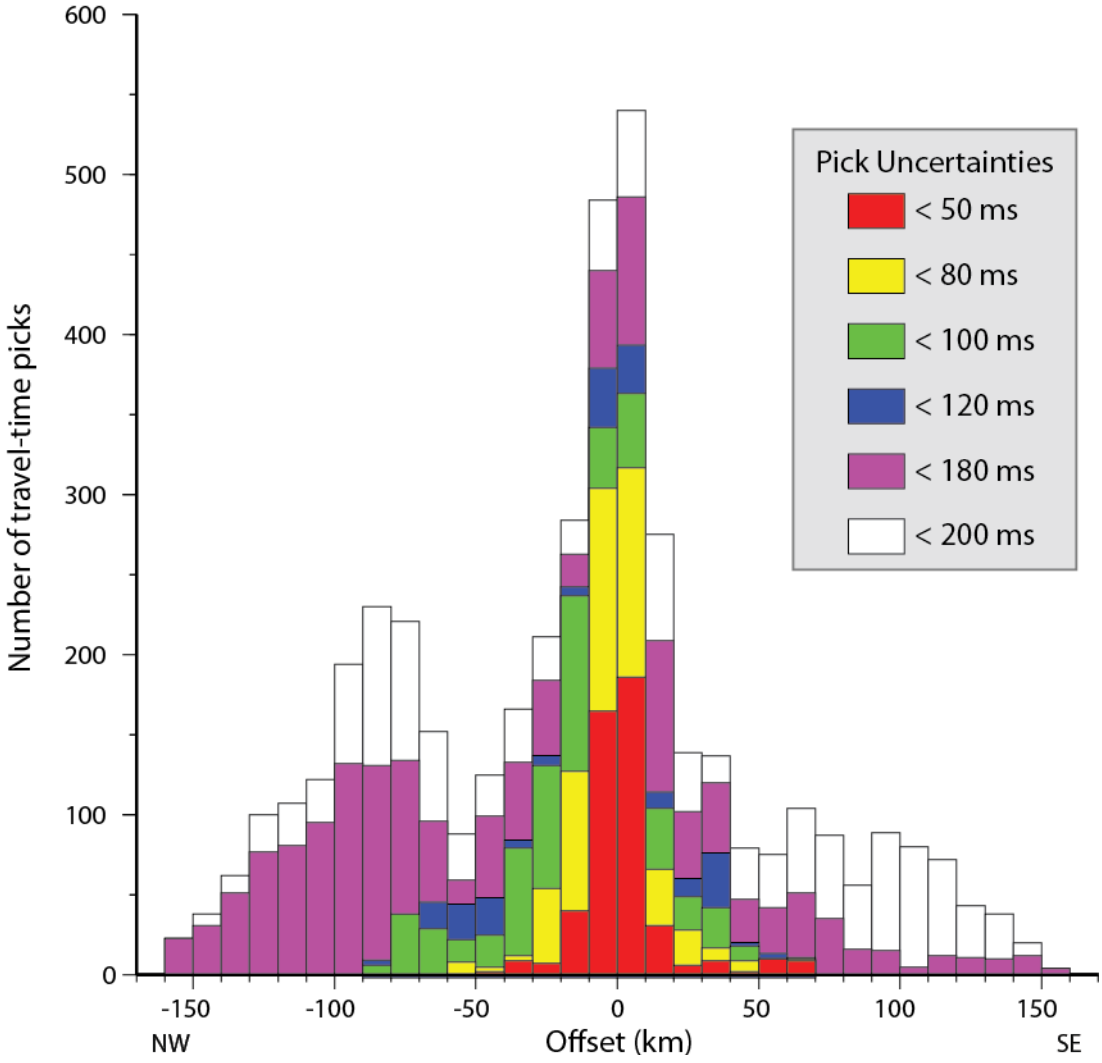

Figure 4.7. Distribution of pick uncertainties versus source-receiver offset.

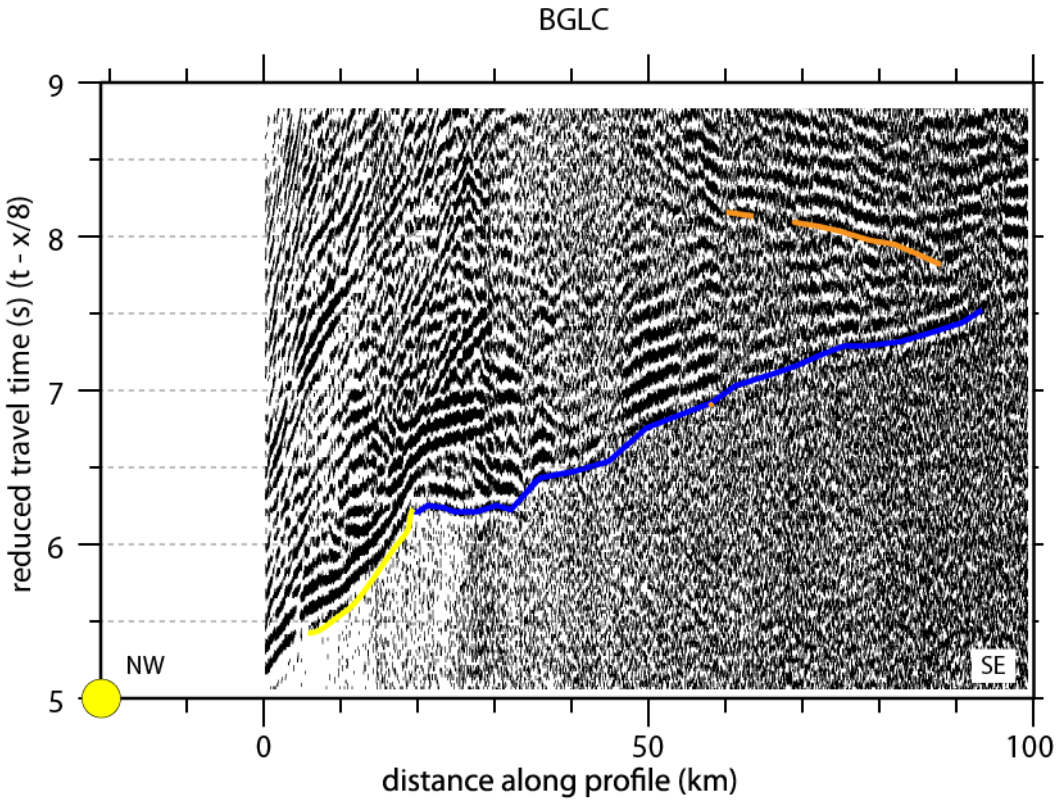

Figure 4.8. Data record from broadband station BGLC (location shown in Figure 3) shown with a reduction velocity of 8 km/s. Picked travel time arrivals shown for PgP (yellow), Pg (blue), and PmP (orange).

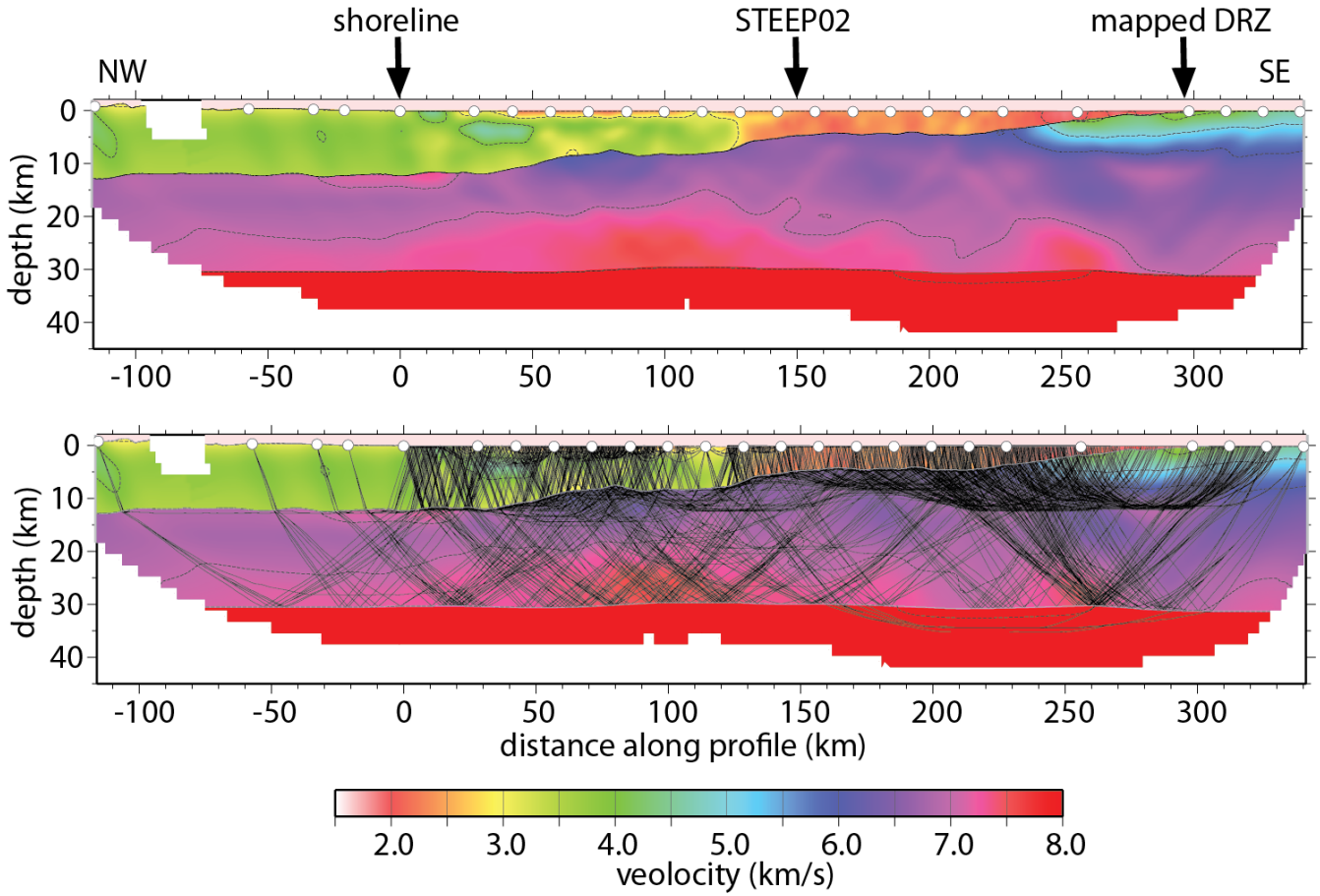

Figure 4.9. a) The final velocity model. b) The final velocity model with calculated raypaths. Vertical exaggeration = 2:1

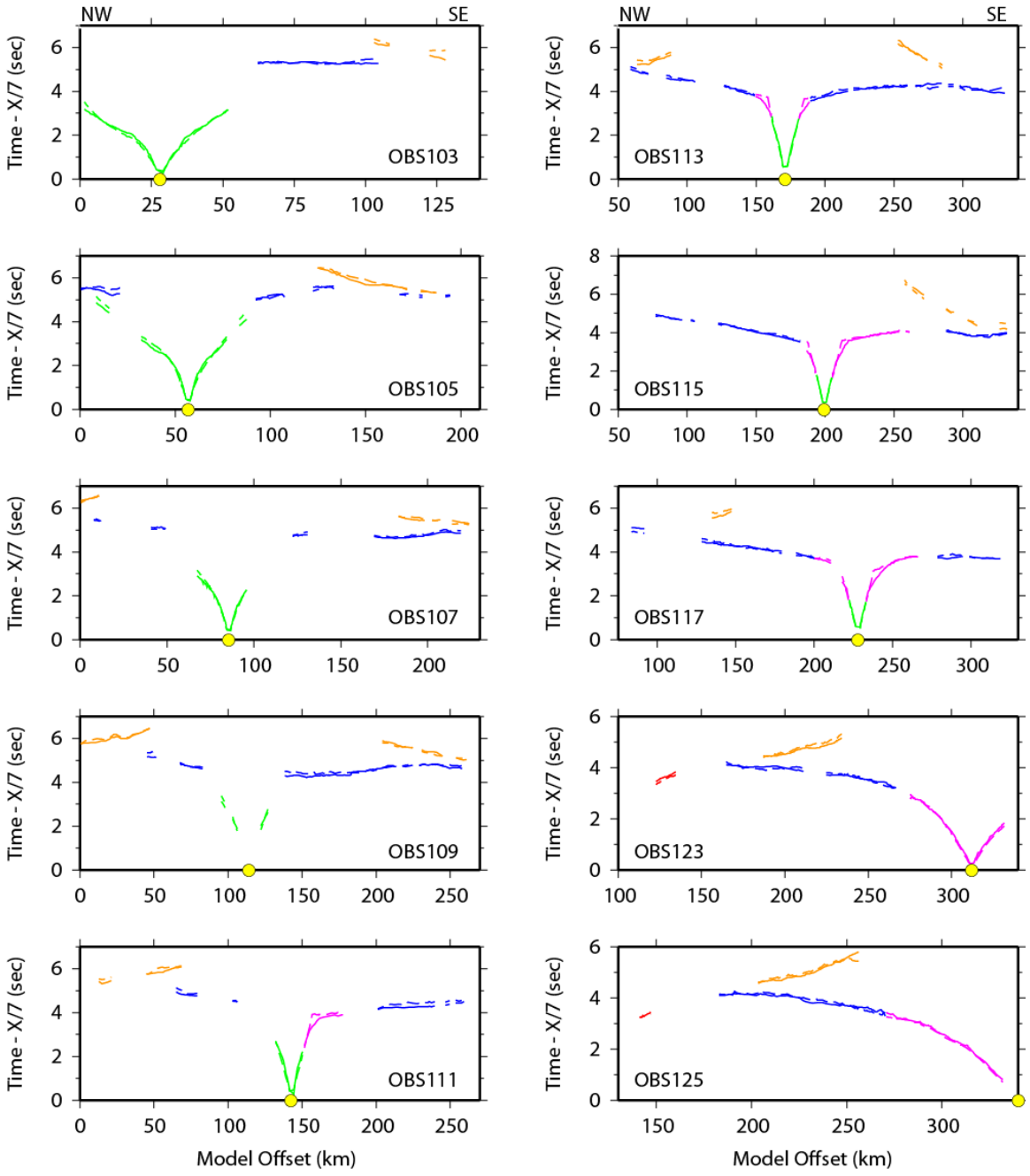

Figure 4.10. Travel time curves for representative ocean bottom seismometers. Picked travel times are solid lines, calculated travel times for the final model in Figure 4.9 represented by dashed lines.

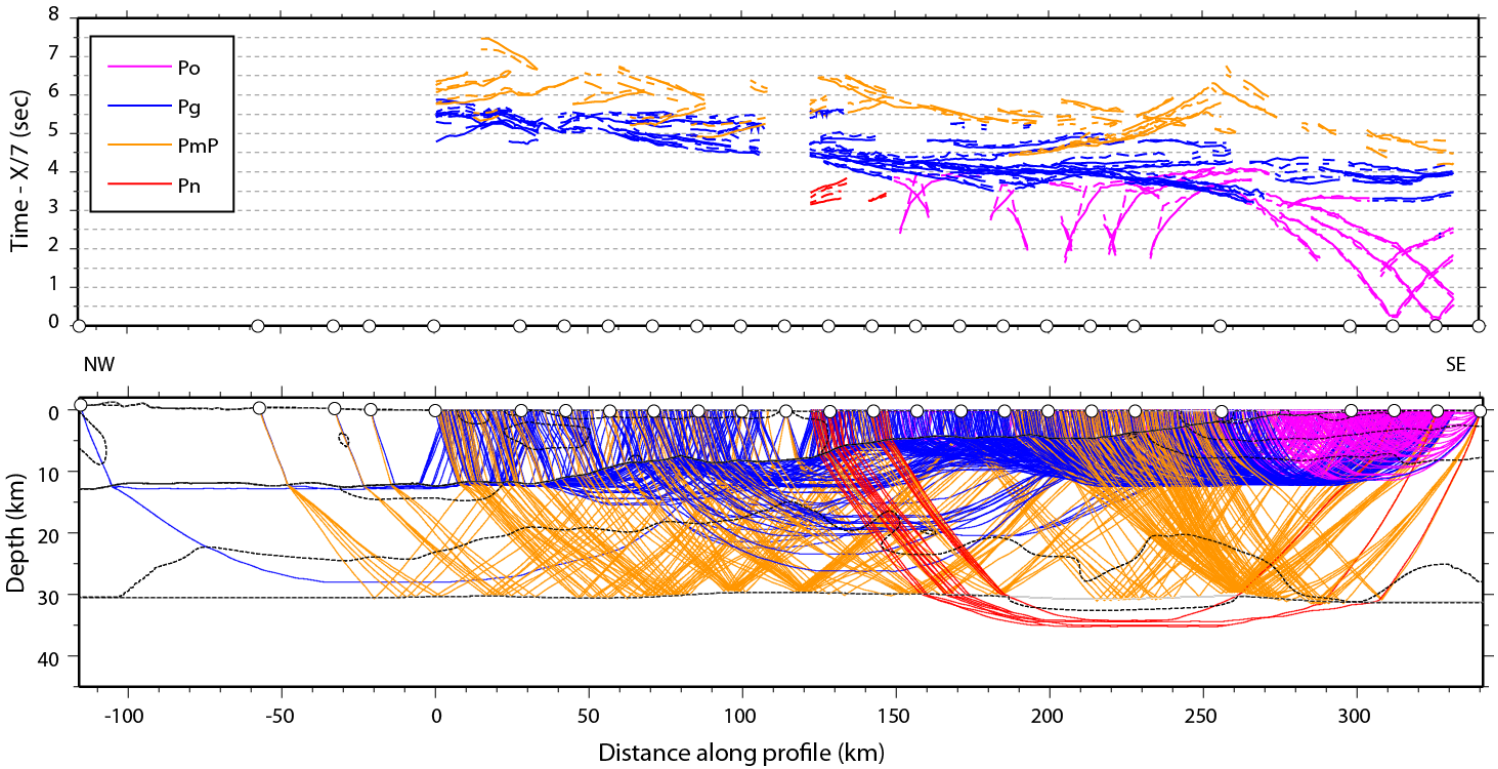

Figure 4.11. Data fit (a) and raypaths (b) for all instruments and phases Po, Pg, PmP, and Pn. a) Travel time picks are solid lines, model predictions are dashed lines. b) Corresponding raypaths traced through the final model. Vertical exaggeration = 2:1

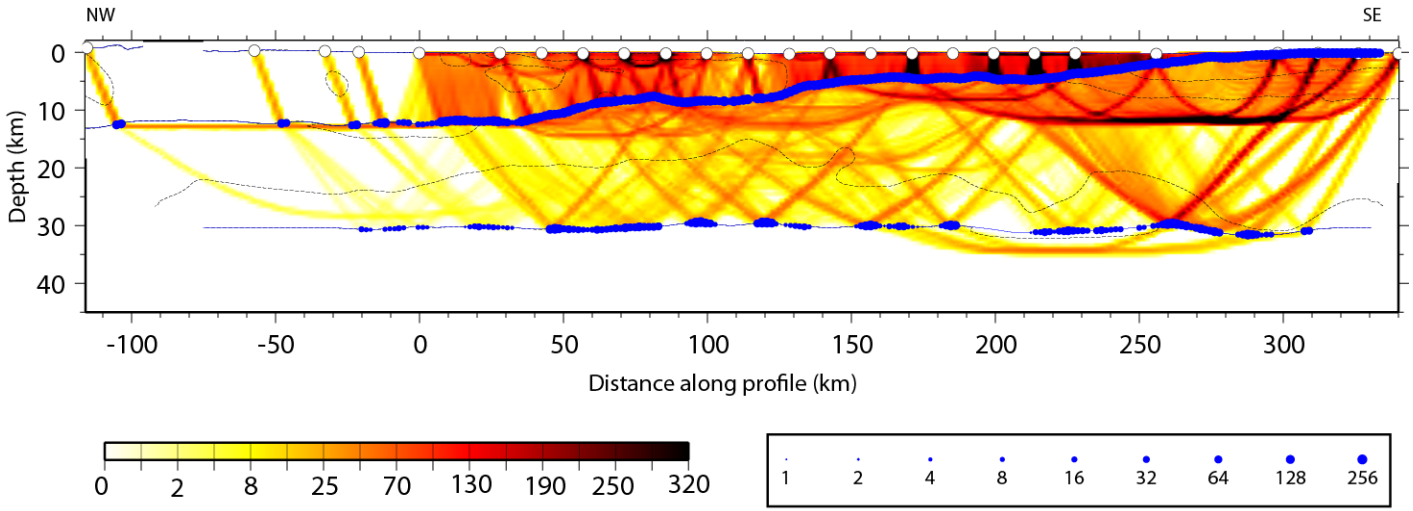

Figure 4.12. The derivative weight sum (DWS) showing ray coverage across the profile. The DWS is a non-dimensional value used as a proxy for ray density. Vertical exaggeration = 2:1

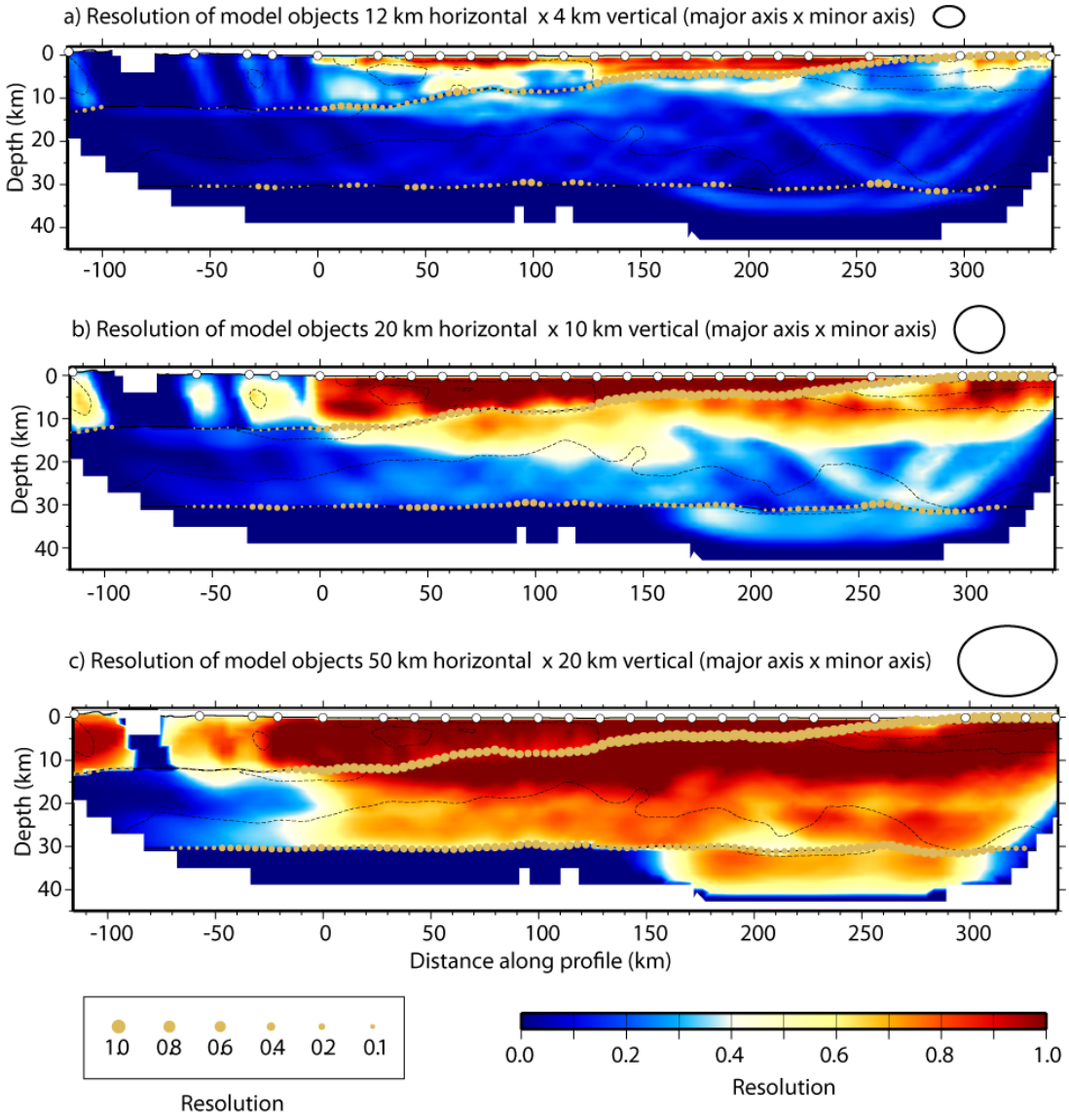

Figure 4.13. Resolution of seismic velocity variations and layer boundary depth at varying scales. a) Elliptical model features 12 km x 4 km, are well resolved is some portions of the sedimentary layer and in the upper crust at the eastern end of the profile. b) Resolution of objects 20 km x 10 km is > 0.5 in the upper ~15-20 km of the model at positive offsets; these objects are not well resolved at the western extent of the profile or within the lower crust. c) The model is well resolved (resolution value ~0.6-1.0) for a 50 km x 20 km window throughout the model extent, except at crustal depths in the onshore portion of the profile.

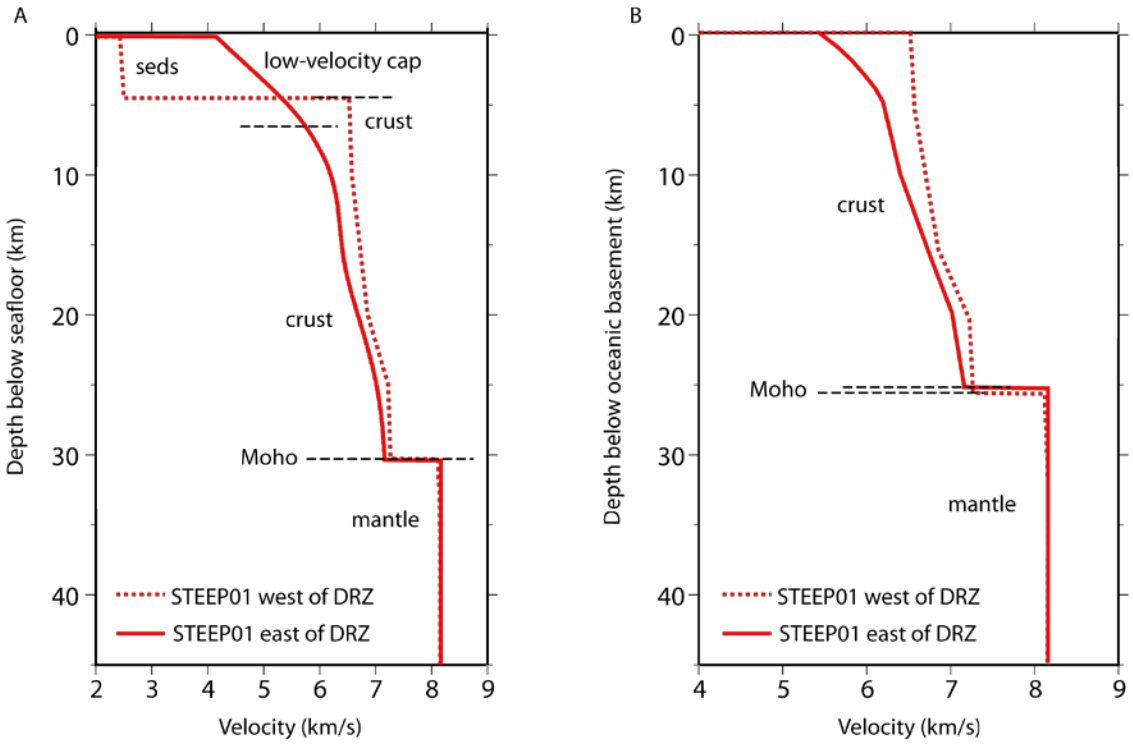

Figure 4.14. One-dimensional velocity profiles of taken from the STEEP01 model west and east of the Dangerous River Zone at 175 km and 325 km model offset, respectively. a) Velocity profile sampling full model depth. b) Comparison of crustal velocities. Sedimentary cover removed from the profile at 175 km. Low-velocity upper-crust removed from profile at 325 km.

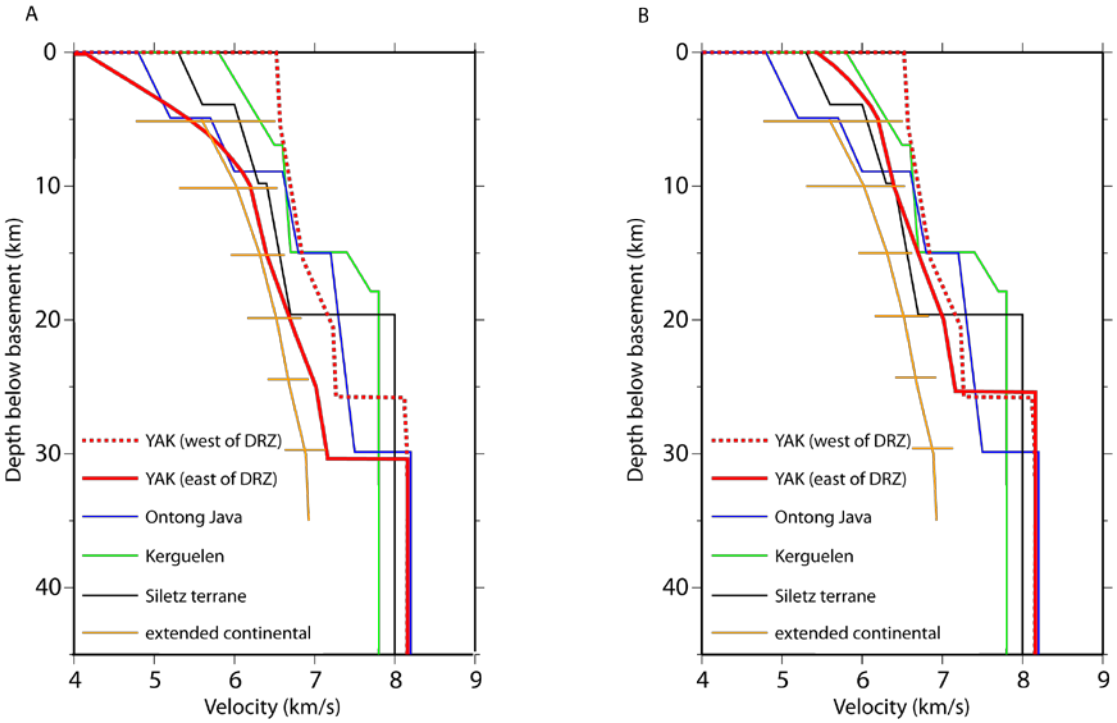

Figure 4.15. Velocity profiles with depth for Yakutat crust west and east of the Dangerous River Zone compared with velocities from the southern Kerguelen Plateau (Operto and Charvis, 1996), Ontong-Java Plateau (Miura et al., 2004), the Siletz terrane (Gerdom et al., 2003), extended continental crust (Christenson and Mooney, 1995). Modified from Christeson et al. (2010).

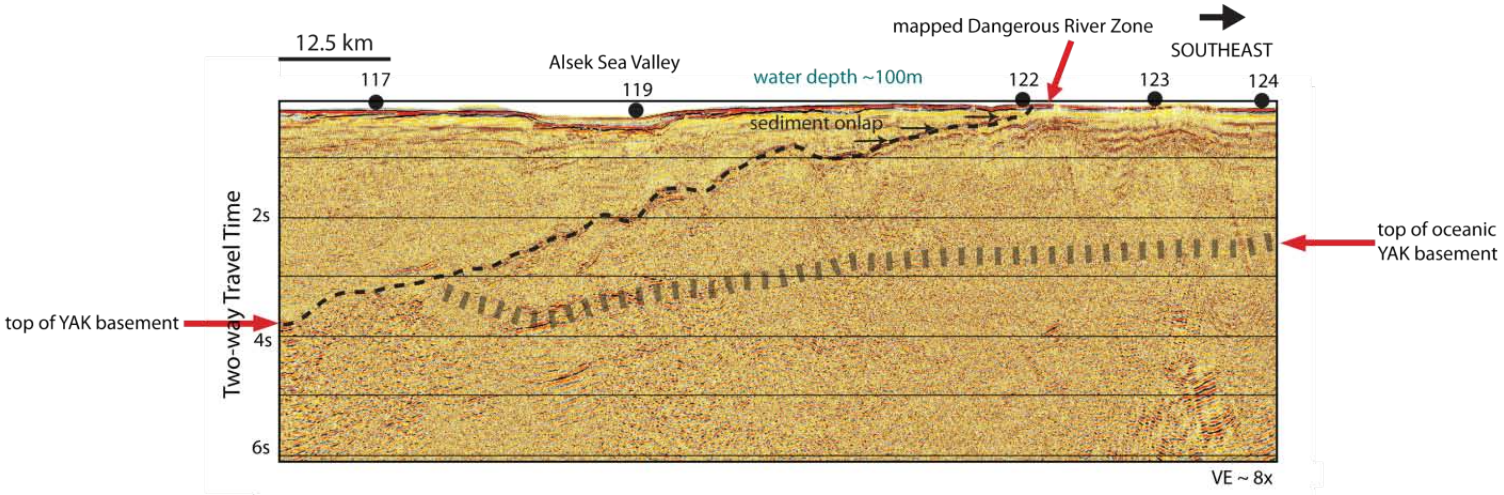

Figure 4.16. Segment of STEEP01b seismic section imaging the subsurface near the mapped Dangerous River Zone. Interpreted top of Yakutat basement and schematic top of Yakutat oceanic basement shown by dashed lines. Black circles are ocean bottom seismometers.

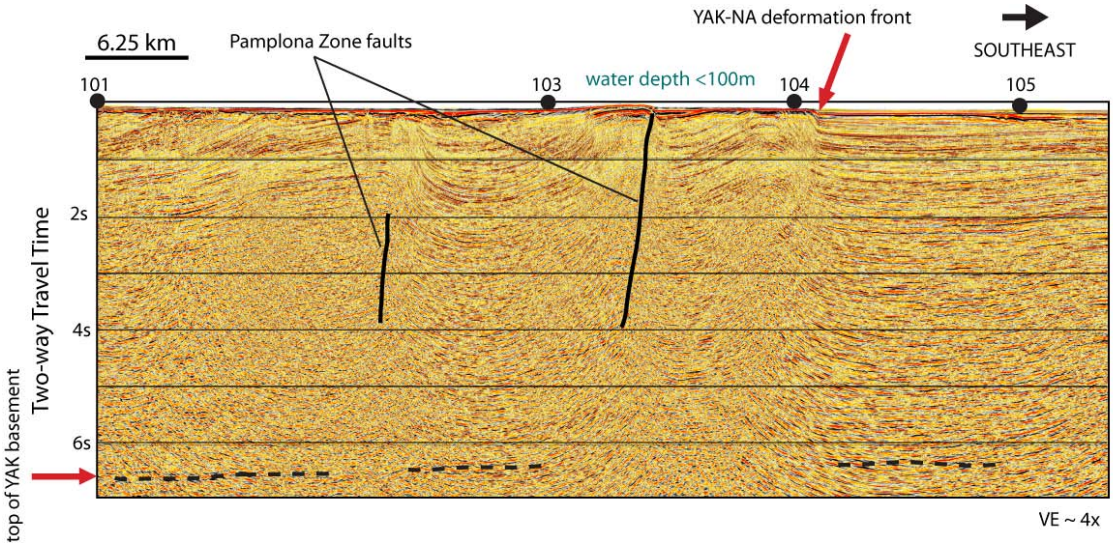

Figure 4.17. Segment of STEEP01a seismic section imaging the Pamplona Zone deformation front, faults associated with the accretionary prism and interpreted top of Yakutat basement.

Chapter 5: Summary and Conclusions

In Chapter 2, analyses of high-resolution and basin-scale seismic sections, in conjunction with high-resolution bathymetry and earthquake locations, indicate that the Yakutat leading corner is undergoing significant intraplate thin-skinned deformation that is currently localized on the eastern edge of the Pamplona Zone (PZ) and in the Khitrov Ridge area. This model differs from the traditional view of the Yakutat leading corner as a zone of distributed deformation across a broad, fold-thrust belt. A décollement is likely located within ~5 km of surface sediments, connecting the waning Kayak Island Zone (KIZ), inactive Bering Trough and the active PZ, and acting as the structural accommodation of the transitioning deformation front. The KIZ is interpreted as an incipient suture that acts as a partial backstop for material west of the PZ, causing constriction and extrusion of offscraped sediments through the Khitrov Ridge area to the Yakutat-North America-Pacific triple junction. The shutdown of structures within the Bering Trough, associated shifting of deformation to the present deformation front of the PZ, and active deformation onshore suggest that the orogen is undergoing a transient response to mass redistributions by erosion and deposition.

In Chapter 3, analysis of the evolution of fault activity and shortening in the offshore St. Elias provides an observable approach to understanding critical wedge mechanics under climate influence. Localization of fault activity away from the primary glacial depocenters during the Late Pleistocene indicates a causal relationship between rapid deposition and structural evolution. Eastward migration of the deformation front in

conjunction with deposition in the mid-wedge maintain a sub-critical wedge taper for the orogen, perhaps driving fault initiation on the onshore hinterland. These observations, along with shortening estimates showing that the bulk of Yakutat-North American convergence is accommodated away from the active offshore structures, agree with recent modeling results that investigate critical wedge evolution in which the sediment source and sink are integral to the development of the orogenic system.

Chapter 4 presents a velocity model for the offshore Yakutat microplate that shows increasing crustal thickness towards the eastern syntaxis, where the orogen displays the highest topography and relief. This observation motivates a new model for orogenesis of the St. Elias Mountains, the wedge model, in which the thickened Yakutat crust causes focused uplift in its vicinity. The model also shows that Yakutat terrane crust is a continuous oceanic plateau beneath the Dangerous River Zone (DRZ), with a low-velocity cap of remnant accretionary prism comprising the upper basement east of the DRZ. Prior to emplacement at the Gulf of Alaska margin, it's possible that the Yakutat terrane underwent partial subduction, which ultimately failed, at the Canadian Cordilleran coast and was subsequently transported to its current position.

Appendix A. Summary of multi-channel seismic survey

Survey dates: September 10- October 6, 2008

Survey location: Gulf of Alaska

Research vessel: R/V *Marcus G. Langseth*

Multi-channel seismic data were collected using the Lamont-Doherty Earth Observatory solid streamer, 8 km in length. 636 receivers in the streamer were spaced at 12.5 m intervals; common depth point spacing for the survey is half the receiver spacing, 6.26 m. For the seismic source, 40 Bolt airguns (36 + 4 spares) were deployed in four linear arrays. The full source was 36 guns shooting a total of 6600 cubic inches. Data was acquired in demultiplexed SEGD format in 16 second record lengths at 2 ms sample rate. Survey shot spacing was 50 m. The total survey totaled ~1250 km of seismic reflection data. Summary of survey geometry and parameters (also see Figure A1):

Table A1. Survey geometry.

Channels	636
Near offset	164 meters
Shot spacing	50 meters
Receiver spacing	12.5 meters
Common midpoint spacing	6.25 meters

Table A2 summarizes the 14 MCS profiles collected as part of the STEEP survey. The table includes that line name, total shots, total CMP's and total line length.

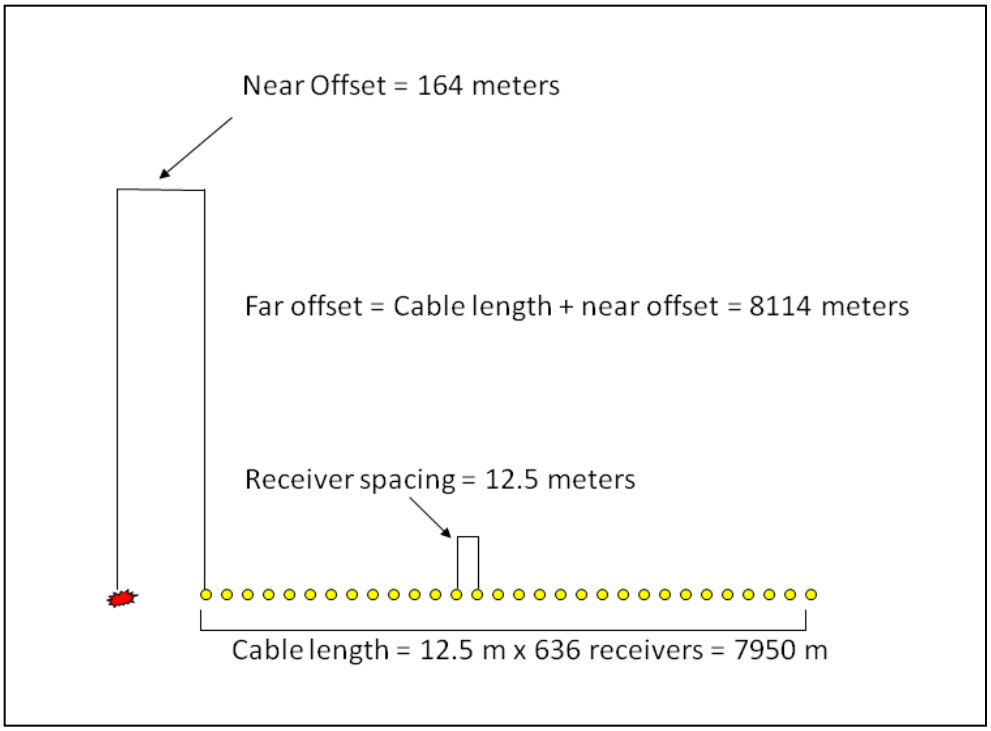

Figure A1. Survey geometry.

Table A2. MCS acquisition table.

STEEP MCS Acquisition Table

Line Number				
STEEP09	Start/End Tape Number	First Shot Point	Last Shot Point	Total Shots
	S: 1, E: 2	711	2510	1799
	First CMP	Last CMP	Total Line Length	
	652	15647	93.71875	
STEEP13	Start/End Tape Number	First Shot Point	Last Shot Point	Total Shots
	S: 4, E: 6	1007	3727	2720
	First CMP	Last CMP	Total Line Length	
	652	23047	139.96875	
STEEP15	Start/End Tape Number	First Shot Point	Last Shot Point	Total Shots
	S: 3, E: 3	996	1585	589
	First CMP	Last CMP	Total Line Length	
	652	5999	33.41875	
STEEP07	Start/End Tape Number	First Shot Point	Last Shot Point	Total Shots
	S: 7, E: 9	922	2830	1908
	First CMP	Last CMP	Total Line Length	
	652	16543	99.31875	
STEEP07a	Start/End Tape Number	First Shot Point	Last Shot Point	Total Shots
	S: 10, E: 10	2690	2726	36
	First CMP	Last CMP	Total Line Length	
	na	na		
STEEP07b	Start/End Tape Number	First Shot Point	Last Shot Point	Total Shots
	S: 11, E: 11	3338	3990	652
	First CMP	Last CMP	Total Line Length	
	652	6503	36.56875	
STEEP16	Start/End Tape Number	First Shot Point	Last Shot Point	Total Shots
	S: 12, E: 12	1042	1645	603
	First CMP	Last CMP	Total Line Length	
	652	6103	34.06875	
STEEP19	Start/End Tape Number	First Shot Point	Last Shot Point	Total Shots
	S: 14, E: 14	990	1088	98
	First CMP	Last CMP	Total Line Length	
	652	2071	8.86875	
STEEP17	Start/End Tape Number	First Shot Point	Last Shot Point	Total Shots
	S: 13, E: 13	1036	1561	525
	First CMP	Last CMP	Total Line Length	
	652	5471	30.11875	
STEEP18	Start/End Tape Number	First Shot Point	Last Shot Point	Total Shots
	S: 15, E: 15	996	1484	488
	First CMP	Last CMP	Total Line Length	
	652	5199	28.41875	
STEEP01a	Start/End Tape Number	First Shot Point	Last Shot Point	Total Shots
	S: 16, E: 18	1031	3176	2145
	First CMP	Last CMP	Total Line Length	
	652	18447	111.21875	
STEEP01b	Start/End Tape Number	First Shot Point	Last Shot Point	Total Shots
	S: 19, E: 23	3448	7679	4231
	First CMP	Last CMP	Total Line Length	
	660	35143	215.51875	
STEEP02	Start/End Tape Number	First Shot Point	Last Shot Point	Total Shots
	S: 24, E: 28	953	5152	4199
	First CMP	Last CMP	Total Line Length	
	660	34767	213.16875	
STEEP11	Start/End Tape Number	First Shot Point	Last Shot Point	Total Shots
	S: 29, E: 32	361	4305	3944
	First CMP	Last CMP	Total Line Length	
	652	32823	201.06875	
			Total All Lines	
			1245.44375	

Appendix B. Summary of multi-channel seismic processing sequence

This appendix shows the processing steps and representative examples of each step used to convert the seismic data into the final stacked and migrated sections for interpretation. These interpretations are used for analysis Chapters 3 and 4. Processing for all the STEEP seismic data followed the same basic processing flow. All figures shown here are from processing profile STEEP09. Processing was performed using FOCUS software by Paradigm Geophysical. Processing based on methods and theories described in Yilmaz (2001).

Processing flow:

1. Trace editing and filtering
2. Correct for spherical divergence
3. Deconvolution
4. Sort to common depth point (CDP)
5. Normal moveout (NMO) correction
6. Mute
7. Stacking
8. Frequency-time migration

B1. NOISE REDUCTION: TRACE EDIT AND BROADBAND FILTER

The primary objective in trace editing and the application of a broadband filter is to eliminate as much random noise as possible without disturbing the signal. For trace-editing, individual noisy traces are removed from the shot gathers before filtering. Figure B1 shows an unfiltered shot gather from profile STEEP09.

Before assigning a filter, the frequency content of the data was examined. Time-frequency and spectral analysis plots (Figures B2 and B3) can be generated to show the frequency distribution and energy amplitude in each shot gather. These plots help determine at what frequencies the bulk of the signal energy is located. In Figure B2, the bulk of the energy below the seafloor is recorded at frequencies between ~20-75 Hz, up to ~6500 ms two-way travel time (twtt). Low frequency noise is present in the water column and throughout the record at ~0-10 Hz. Figure B3 shows how the energy amplitude is distributed over frequencies from 0-125 Hz. At the low end of the frequency spectrum, the amplitudes shows two spikes between 0-3 Hz, likely representing the direct wave. Amplitudes increase at frequencies greater than ~10 Hz before peaking at ~42 Hz. Amplitudes decrease to near zero at frequencies greater than ~80 Hz. Based on these diagnostics, I chose a noise reduction filter that would pass most of the energy between 10 Hz and 60 Hz. The final filter is a trapezoidal bandpass filter with corner frequencies at 3, 8, 60 and 80 Hz.

Figure B4 shows a filtered shot gather from profile STEEP09. The low frequency noise has been removed and the energy arrival is clear at far offsets.

B2. CORRECT FOR SPHERICAL DIVERGENCE

As the input energy from the shot source travels farther away from the source, amplitudes suffer from attenuation. Amplitude attenuation reduces signal clarity for deeper reflectors, hindering velocity picking and decreasing signal to noise ratio within each trace and, eventually, within the stacked section. In order to recover some of this lost energy, a gain recovery function is applied to the data which helps correct amplitude changes due to geometrical spreading and spherical divergence (Eq 1).

For the STEEP survey, amplitudes have been corrected using a t^2 scaling function that is offset independent (Eq 2). Scalar input parameter, A, is set to 1. The velocity power value, B, is set to 0. The time power value, C, is set to 2. Rootp-mean-square velocity at time zero is V_o, which is 1500 m/s for this approximation. Figure B5 shows a filtered shot gather after the spherical divergence correction.

$$At = (V_{RMS}(t)^B \times t^C)/(V_o \times 1/A)$$

Equation 1. Scaling for offset independent spherical divergence.

$$t = t^2/V_o$$

Equation 2. Spherical divergence parameters used in STEEP processing

B3. DECONVOLUTION

Predictive deconvolution was applied to the filtered shot gathers in order to compress the seismic wavelet. This processing step is based on the convolutional model for data processing. As expressed in Equation 3, this model assumes that the seismic

trace recorded in the field is the result of the convolution of the source wavelet with the earth response time series plus random noise.

$$X(t) = w(t) * e(t) + n(t)$$ **Equation 3. Convolutional model.**

Obtaining the earth response series, *e(t)*, is the primary goal of all seismic data processing steps.

After trace editing and broadband filtering (Section B1) to remove random noise, Equation 4 becomes:

$$X(t) = w(t) * e(t)$$ **Equation 4. After removing random noise.**

The earth structure series can now be extracted by performing deconvolution on the traces with noise removed. Ideally, the wavelet, *w(t)*, is an impulse function in which amplitude changes occur over zero time. In practice, the wavelet is an energy pulse that occurs over a discrete time interval. As the wavelet reflects off of impedance contrasts in the earth, a periodic, repeating event is embedded in the trace, *X(t)*. Deconvolution removes the effect of this source wavelet so that the recorded trace becomes the impulse response of the earth structure series. From times series analysis rules, the impulse response of a time series describes the time series itself.

$$X(t) = IR(e(t)) = e(t)$$ **Equation 5. Signal trace is equal to impulse response of e(t) after deconvolution.**

I applied a predictive deconvolution to the shot gathers with a filter length of 96 traces and an operator length of 40 ms. To test the efficacy of the deconvolution parameters, I compared the autocorrelation function before and after deconvolution

(Figure B6). The auto-correlation function after deconvolution removes, reduces and compresses many of the amplitude spikes.

Figure B7 shows a shot gather after deconvolution. Figure B8 shows a wiggle plot comparing the shot gather before and after deconvolution. Reflection arrivals are enhanced after deconvolution.

B4. GEOMETRY AND COMMON DEPTHPOINT SORT

Data acquisition and all previous processing steps are performed with the data in shot-receiver coordinates. Further data processing steps are performed in common depth point (CDP)-offset coordinates. In order to continue the processing using these coordinates, the survey geometry information given in Appendix A must be added to the trace headers. After adding the survey geometry headers to each trace, the traces can be reorganized into common depth points (Figure B9).

CDP gathers are described in terms of fold, which is a measure of the number of data points available for each CDP. The fold is a function of shot and receiver spacing and the number of recording channels used in acquisition. Equation 6 gives the fold calculation.

$$n_f = n_g \Delta g / 2 \Delta s$$

Equation 6. CDP fold, where n_f is fold, n_g is number of receivers, Δg is receiver spacing, Δs is shot spacing

The STEEP survey is 80 fold. Common depth point 13580 for profile STEEP09 is shown in Figure B10, shot numbers included in this CDP range from 2282-2360.

B5. VELOCITY ANALYSIS AND NORMAL MOVEOUT CORRECTION

After CMP sorting, velocity analysis is performed in order to more accurately correct for normal moveout (NMO) (Eq 7). The NMO correction is based on the assumption that reflection travel times in a CDP gather follow hyperbolic trajectories that are a function of distance. Basically, the NMO correction corrects for this hyperbolic moveout by stretching traces to mimic zero offset. NMO corrections flatten reflectors and undercorrect multiples, so it is also a useful tool for identifying multiples.

$$T_x^2 = T_o^2 + x^2/v^2_{rms}$$

Equation 7. Normal moveout equation, where x is distance from offset, v_{rms} is average interval velocity, T_o is two-way travel time at 0

Accurate velocity analysis is essential for determining the appropriate root-mean-square velocities for NMO correction. For line STEEP09, velocity analysis was performed for every 250 CDP gathers and interpolated for CDPs located between the picks (Figure B11). Velocity analysis results in a velocity profile that changes with time and offset (Figure B12). An example of a CDP gather corrected for NMO is shown in Figure B13.

B6. MUTE

After NMO, a mute must be applied in order to remove distortion at high offsets and in shallow reflectors. This mute is an outside mute that removes refraction and NMO artifacts. These distortions manifest as smeared traces at the left of the diagram (Figure

B13). For STEEP09, I hand-picked the mute during velocity analysis. A muted section is shown in Figure B14. In some instances, an inside mute was also applied in order to mitigate water bottom multiples.

B7. STACKING

Figure B15 shows the CDP stack for profile STEEP09.

B8. MIGRATION

While stacking improves temporal (vertical) resolution of the seismic section, migration improves spatial (horizontal) resolution within the stack by moving dipping reflectors to their true subsurface positions and by collapsing diffractions. I chose a time-frequency migration that uses the velocity profile (Figure B12) computed during velocity analysis for the migration. The minimum and maximum frequencies used in the migration were 3 Hz and 65 Hz, respectively. I assigned lateral smoothing of 5000m and vertical smoothing on 500 ms. The migrated section for STEEP09 is shown in Figure B16. Figure B17 is a zoom plot of the migrated section compared to the stacked section showing how diffractions are collapsed after migration.

B9. POST-MIGRATION DISPLAY

For display purposes, I assigned an automatic gain control with a gate length of 1000 ms. In addition to boosting amplitudes of deeper subsurface reflectors, noise in the water column is also amplified. In order to mitigate these effects and improve cosmetic

effect, a time/spatial varying filter is applied below the sea floor and a mute is applied above the sea floor in the migrated section.

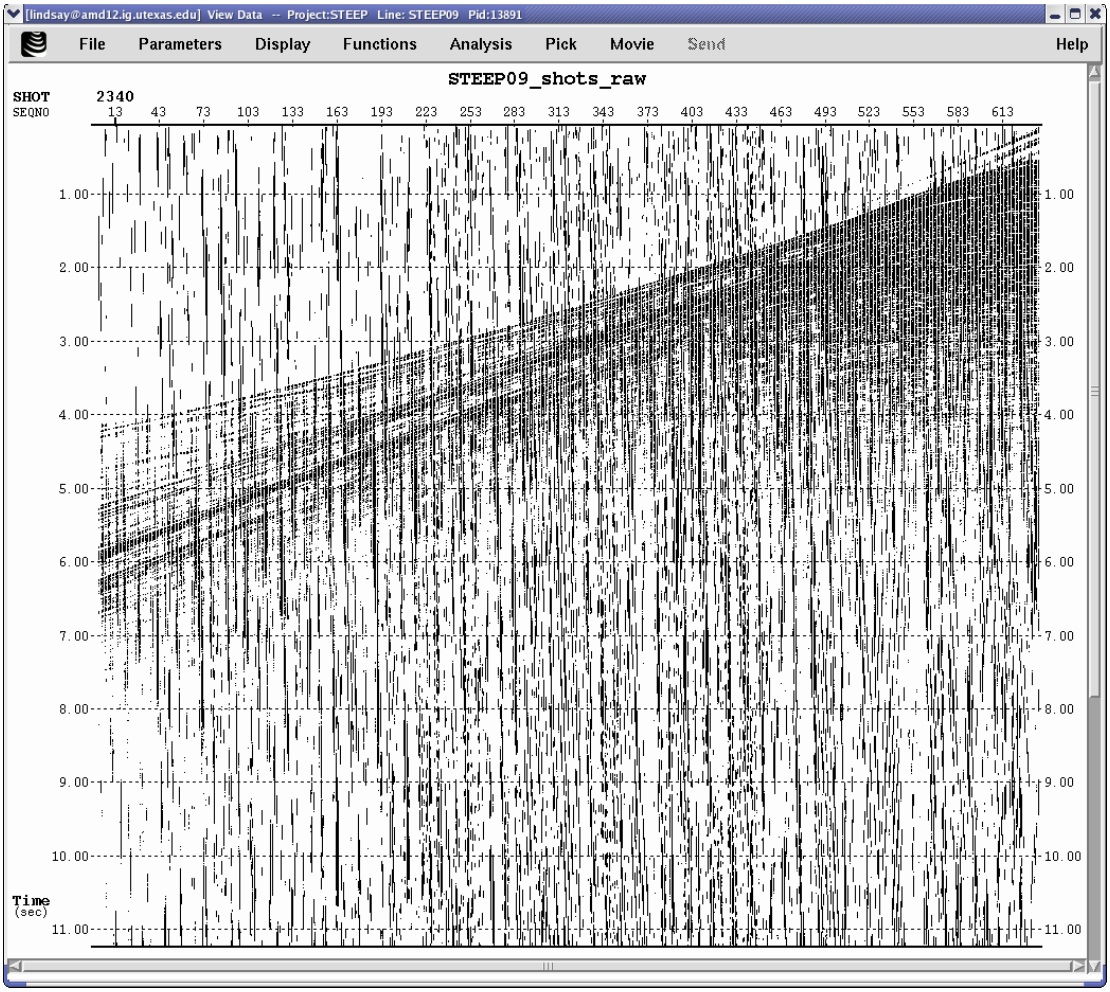

Figure B1. Shot gather 2340 from profile STEEP09, unfiltered

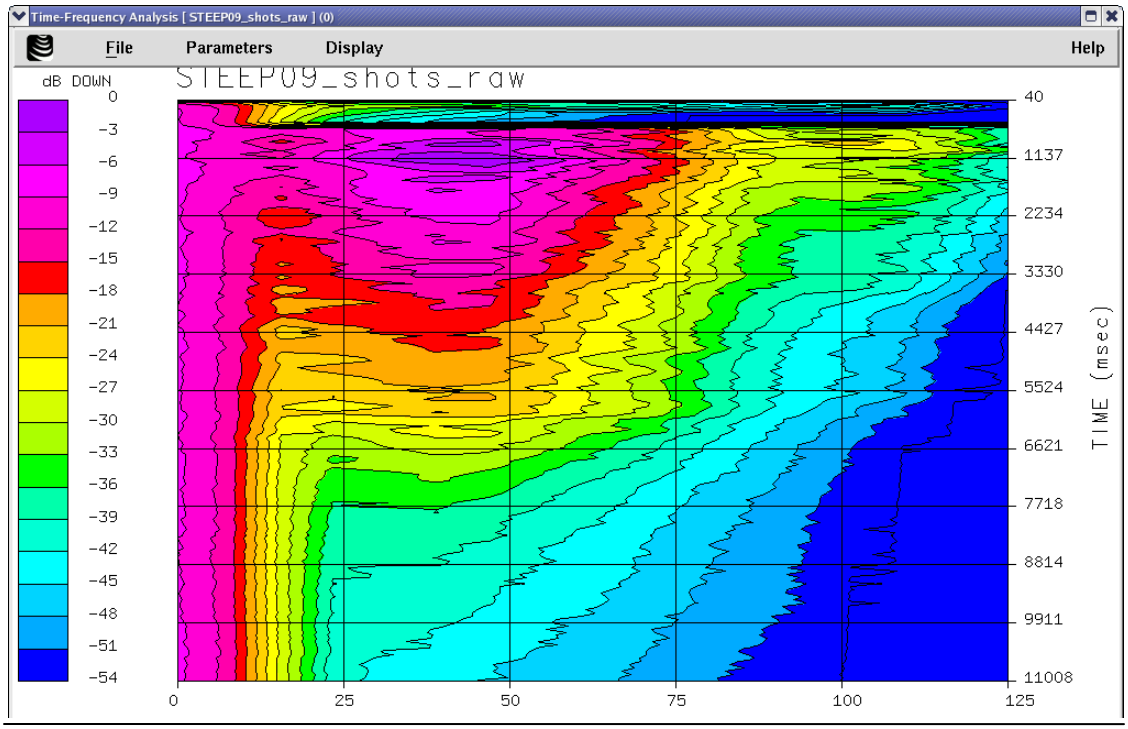

Figure B2. Time-frequency analysis for shot 2340. Top plot shows how energy (in dBs) is distributed with depth vs frequency.

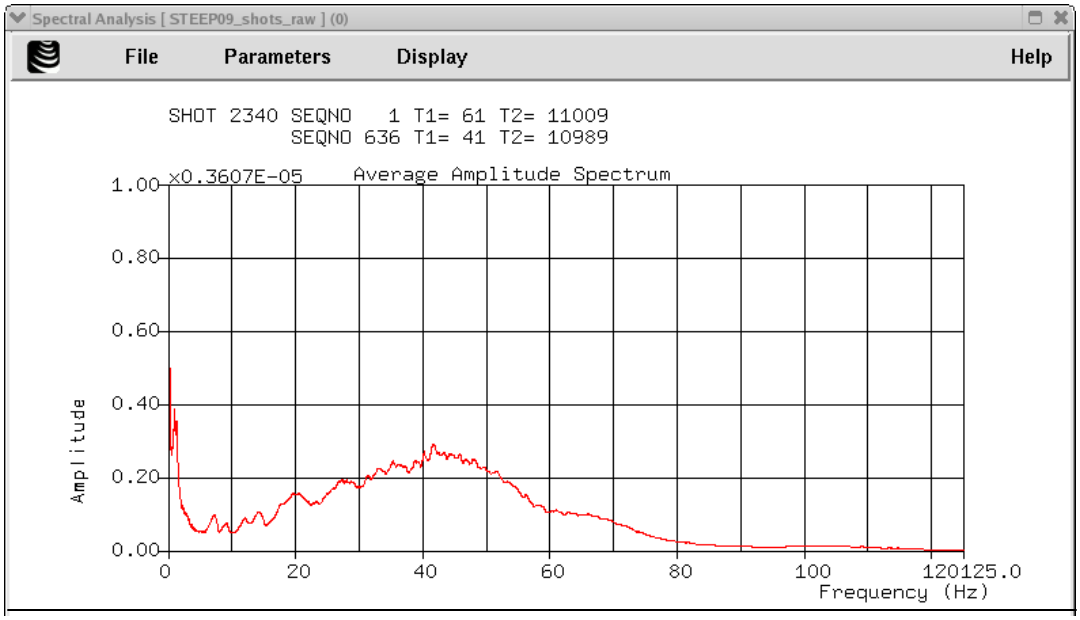

Figure B3. Spectral analysis for shot 2340. Top plot shows amplitude vs. frequency. The amplitude is shown as a percentage of maximum.

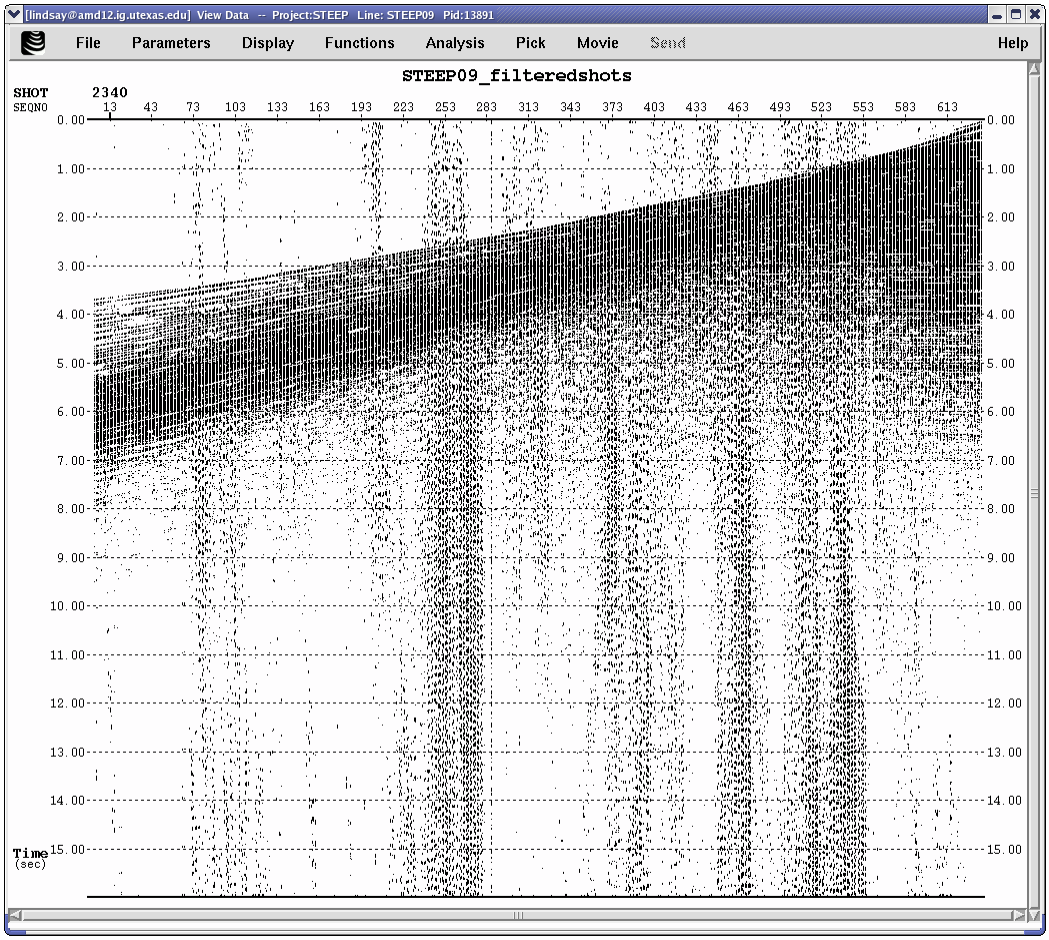

Figure B4. Shot gather 2340 after filtering.

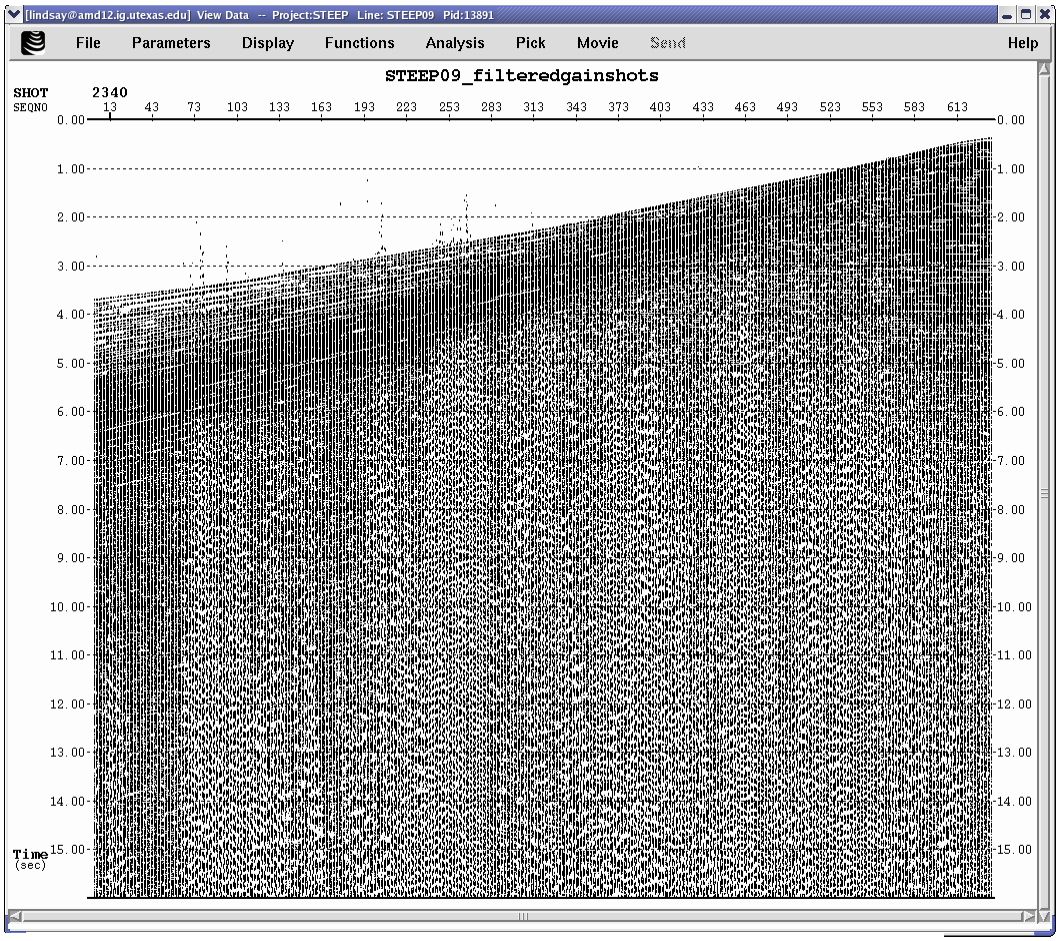

Figure B5. Shot gather 2340 after correction for spherical divergence.

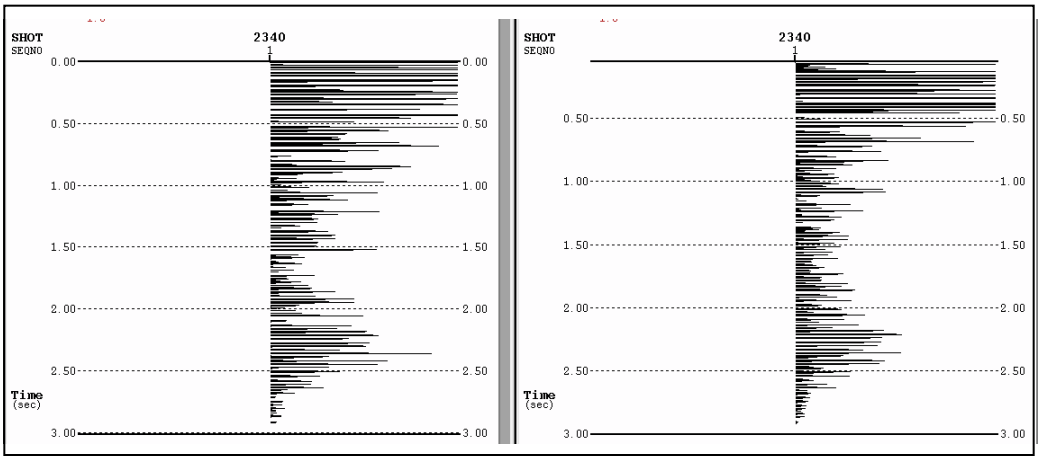

Figure B6. Auto-correlation function before (left) and after (right) deconvolution.

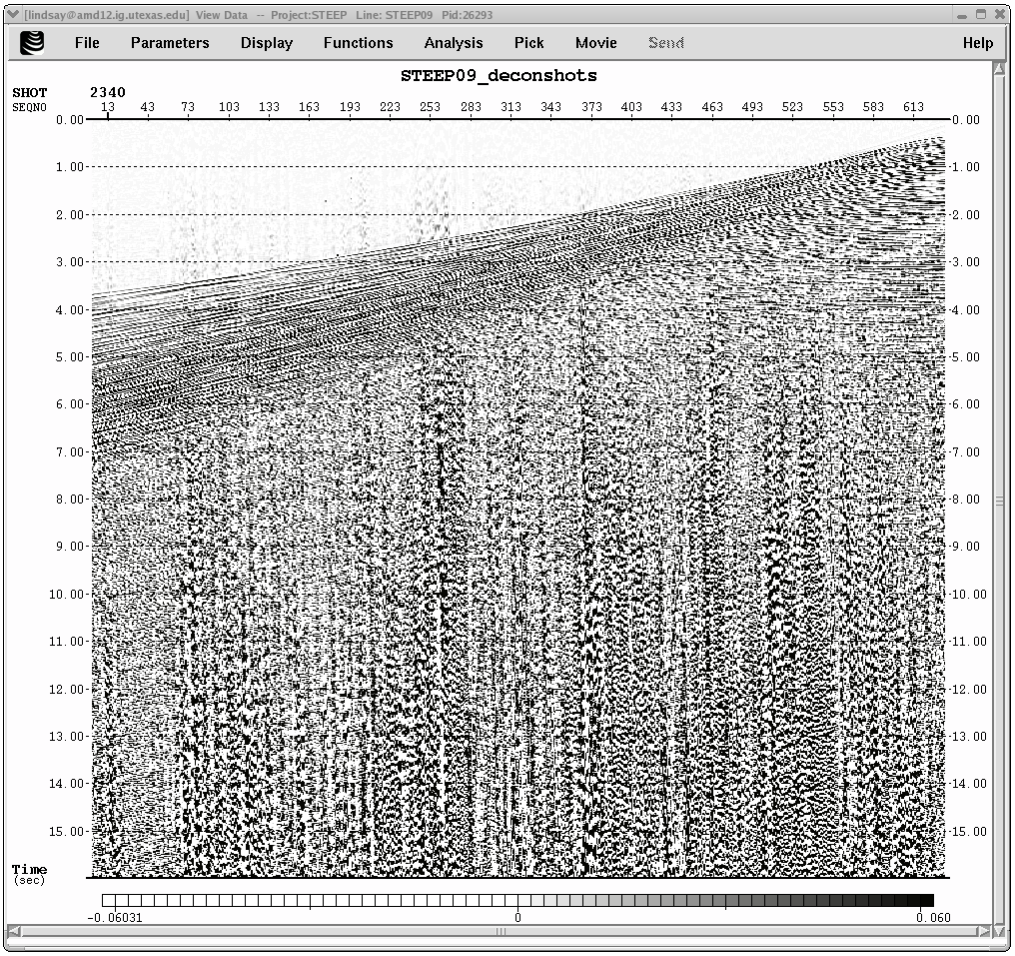

Figure B7. Shot gather 2340 after deconvolution.

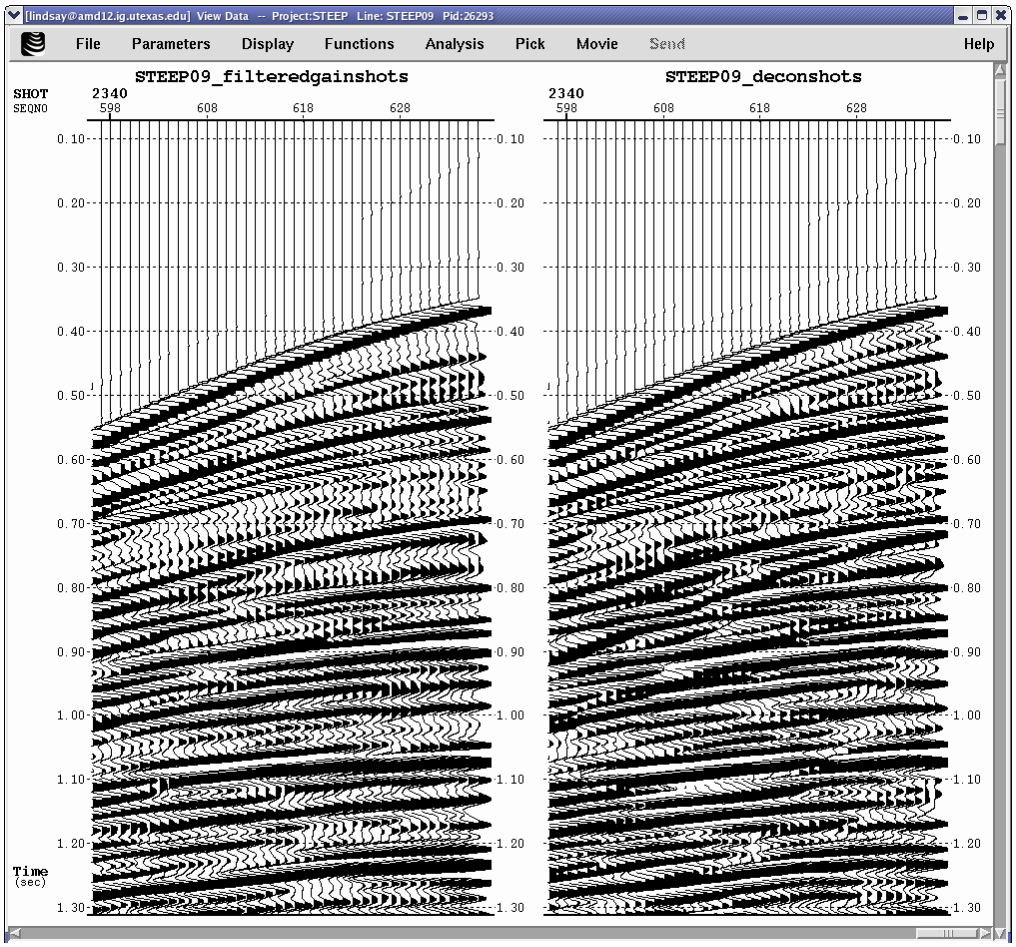

Figure B8. Zoom view of shot 2340 before (left) and after (right) deconvolution.

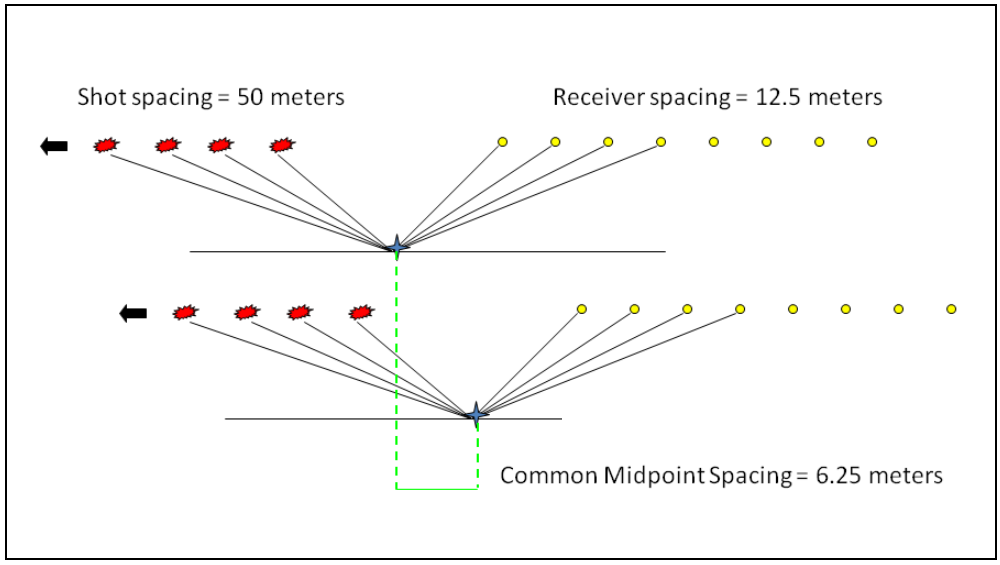

Figure B9. Schematic of geometry for common depth point sorting.
Common depth point spacing = 6.25m

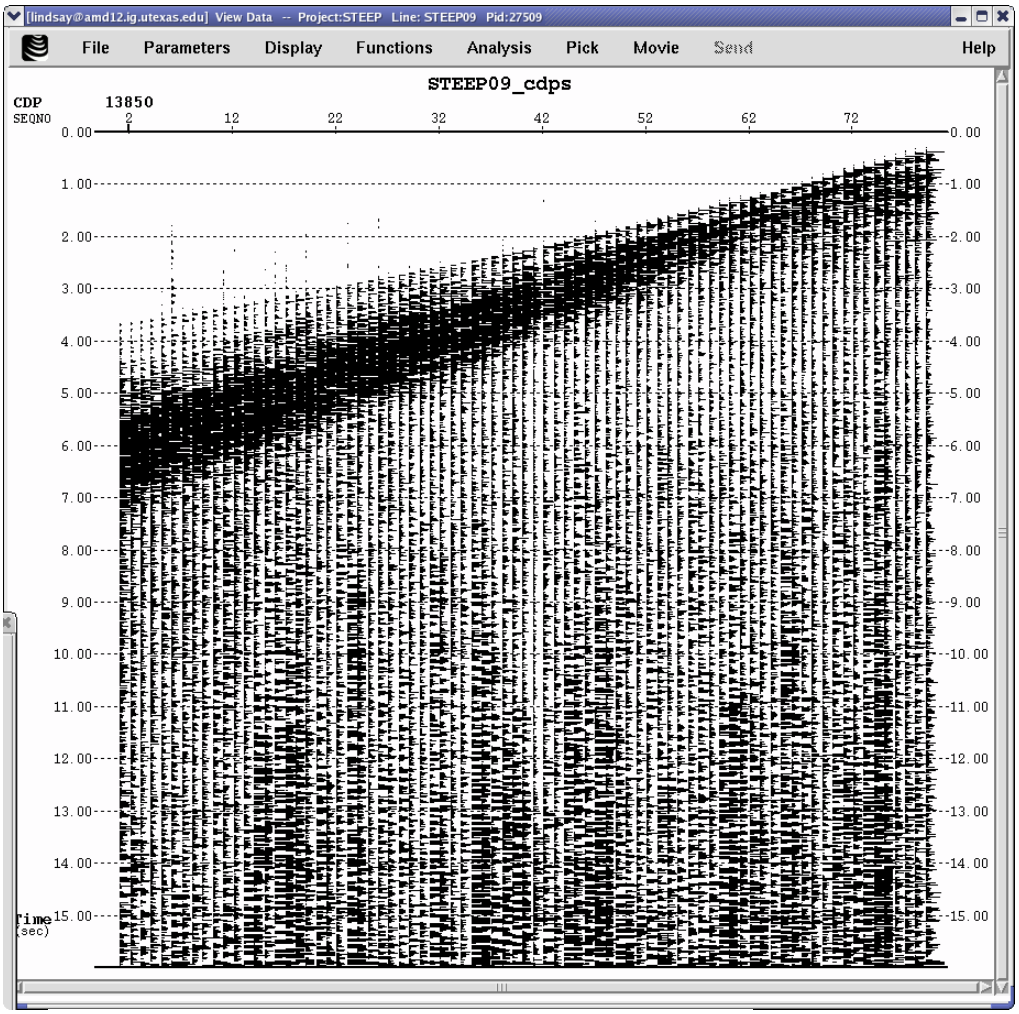

Figure B10. Example CDP plot from STEEP09.

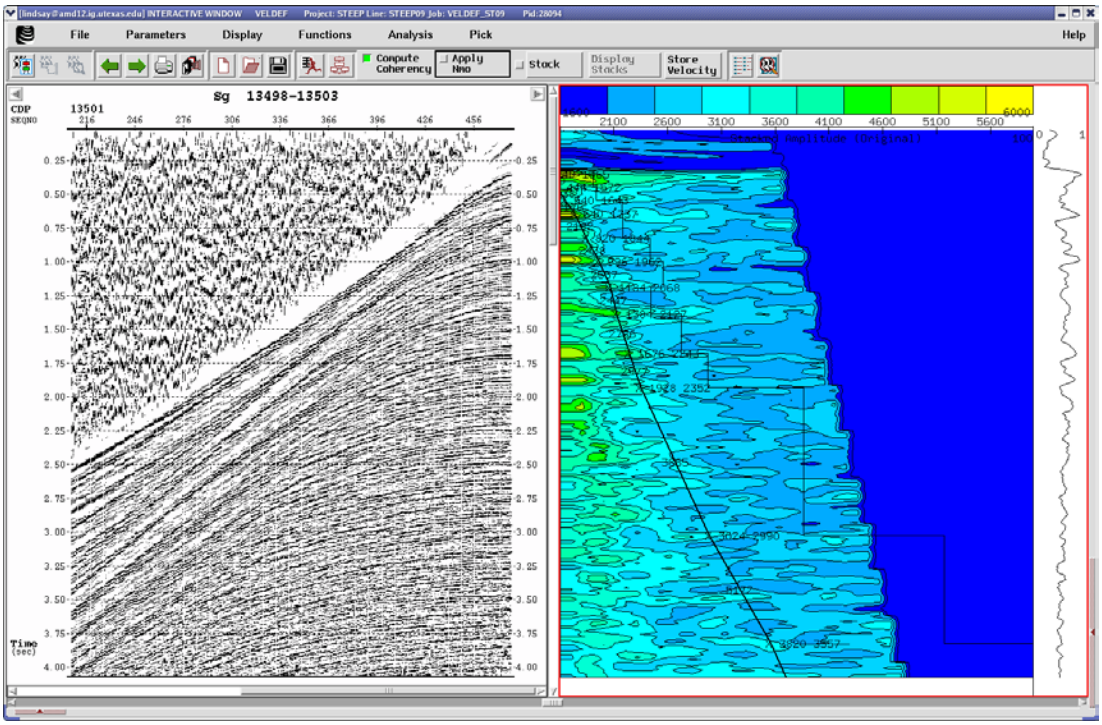

Figure B11. Velocity analysis window in FOCUS software by Paradigm Geophysical. Left side is a CDP supergather of six stacked CDP sections. Right side is a coherency plot showing how seismic energy is distributed with depth.

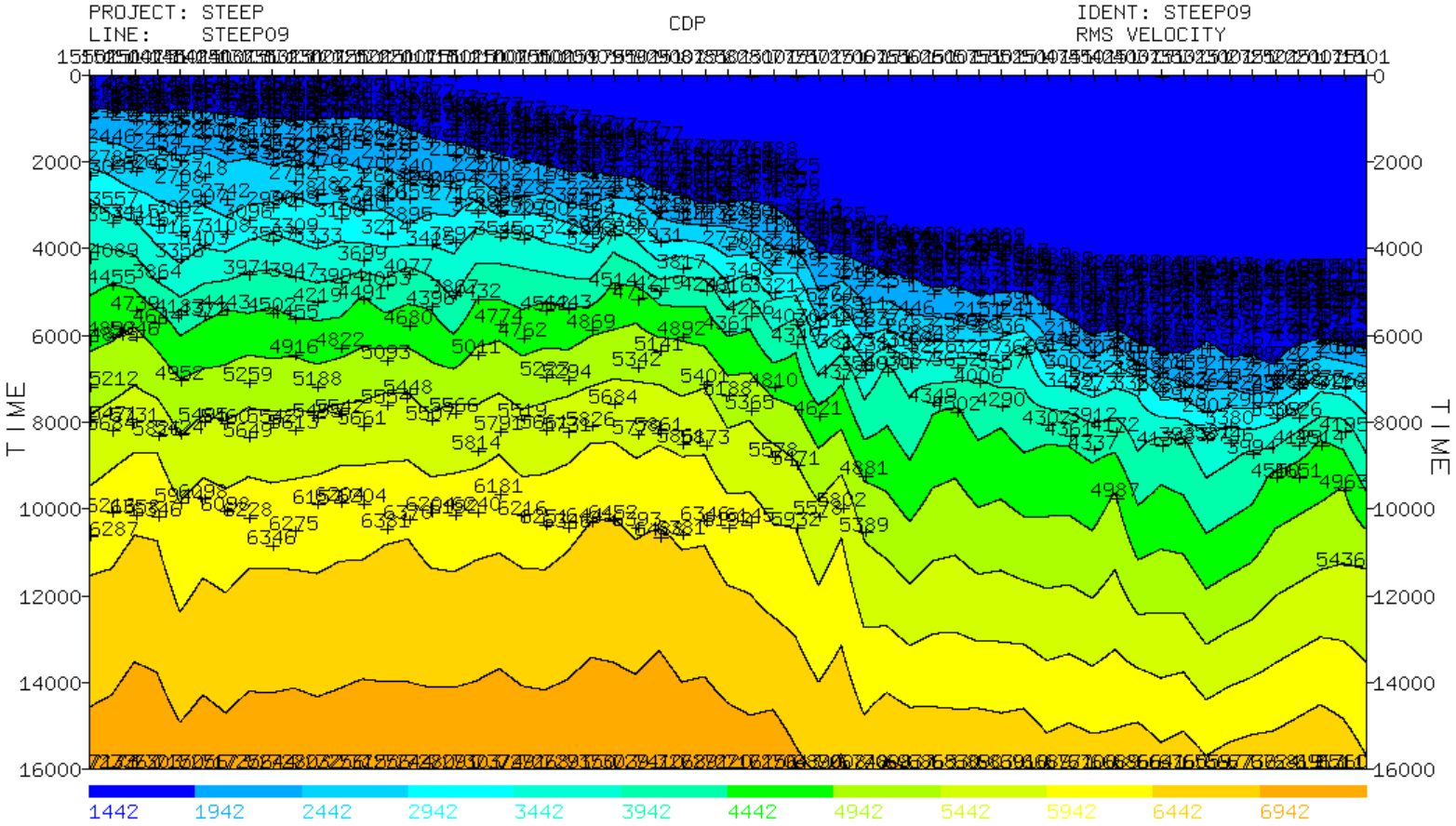

Figure B12. RMS velocity model of STEEP09 used for NMO correction.

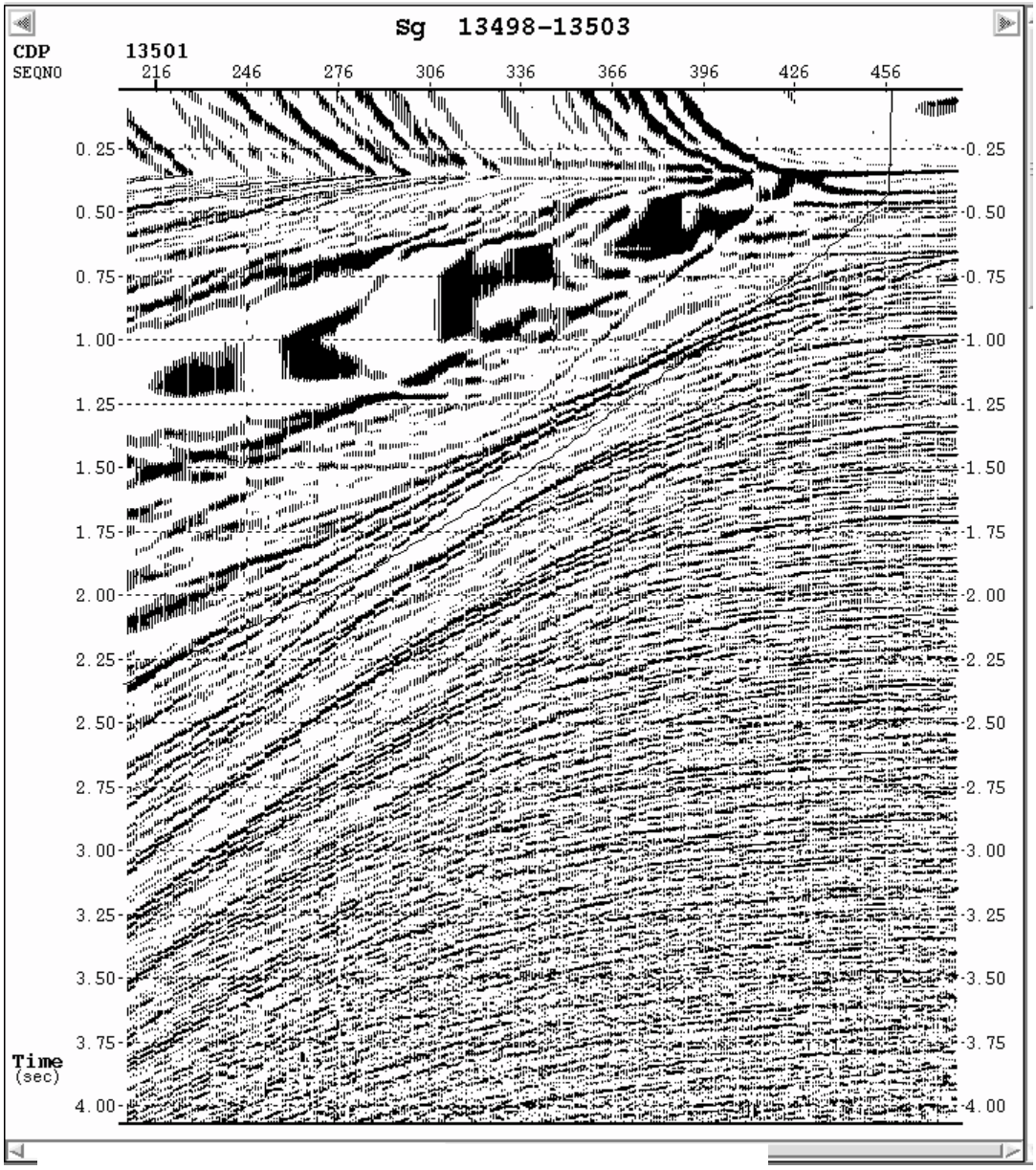

Figure B13. CDP supergather with NMO correction.

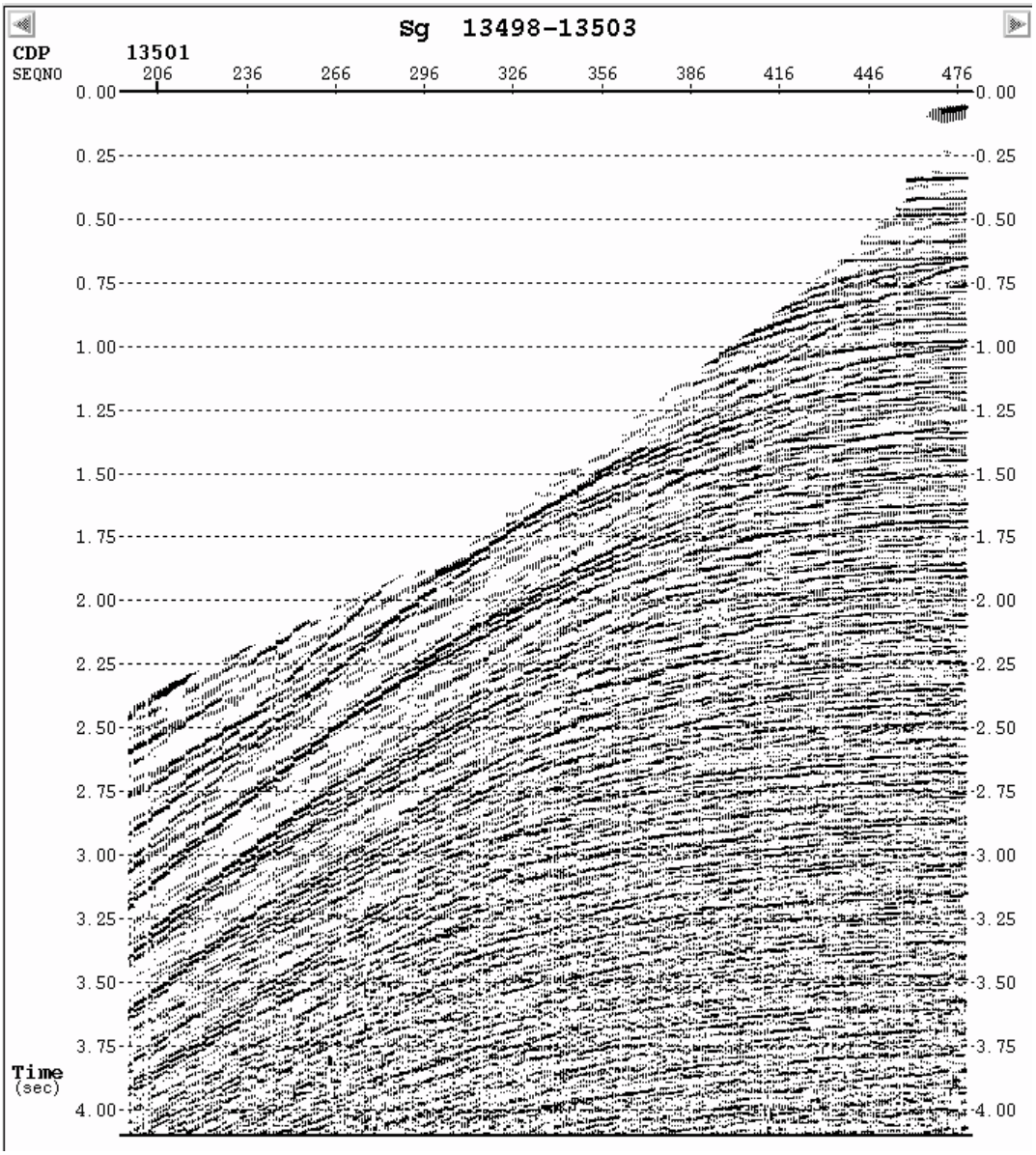

Figure B14. CDP supergather with mute.

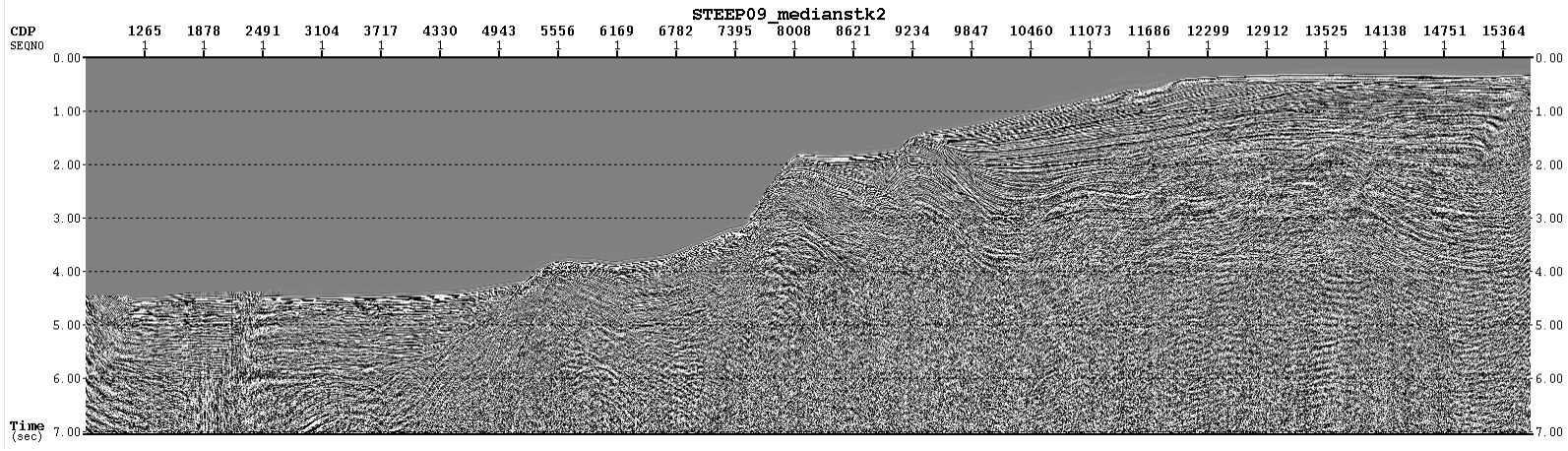

Figure B15. Filtered, deconvoluted, NMO-corrected CDP stack for profile STEEP09.

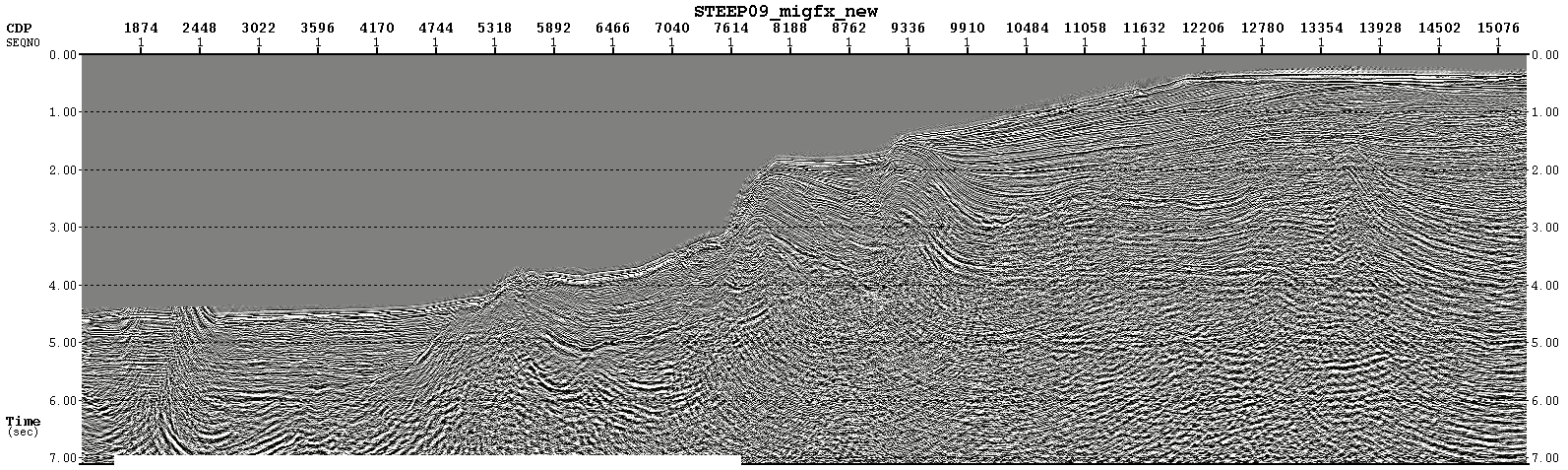

Figure B16. Profile STEEP09 after migration.

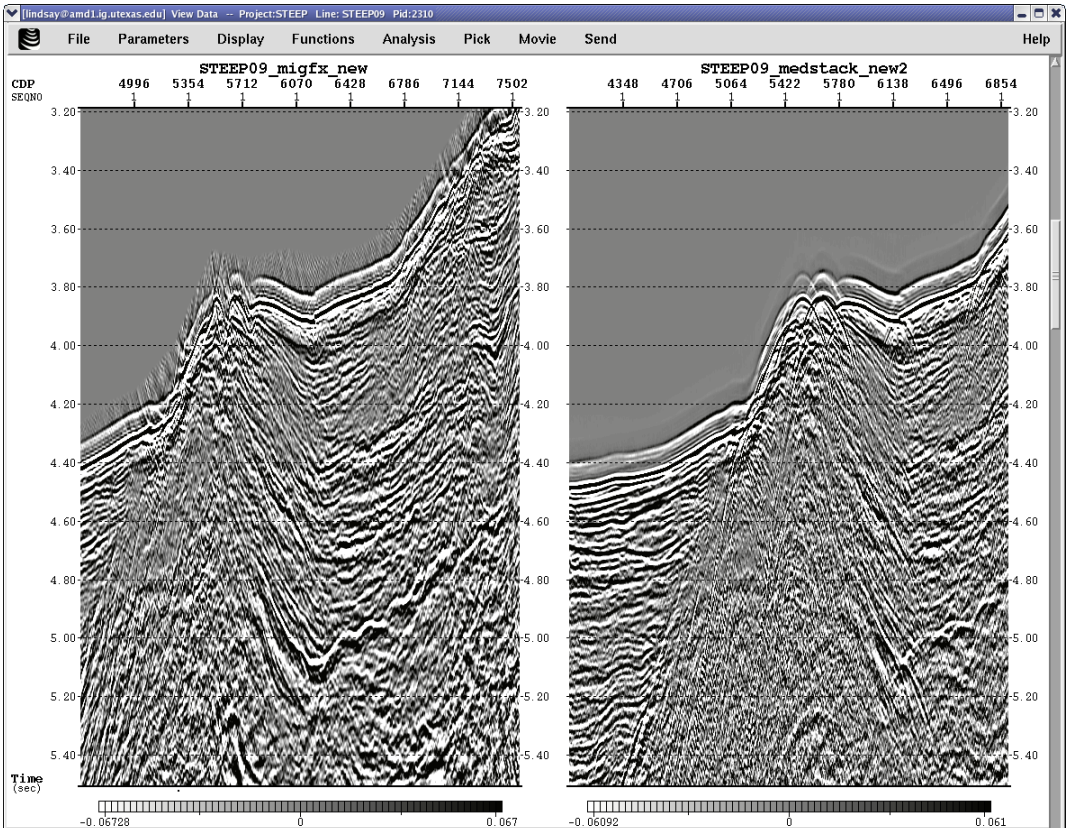

Figure B17. Zoom view of migrated (left) and unmigrated (right) stacked section of profile STEEP09. In the migrated section, diffractions are collapsed, especially at the seafloor. Migration also enhances some signals below the seafloor.

Appendix C. Seismic Travel-Time Tomography and Inversion Methods

This appendix shows the calculations and inversion steps for the inversion of active source ocean-bottom seismometer data in order to determine velocity structure for the offshore Yakutat microplate. In the following sections I describe the theory and equations behind the following tomography steps:

1. Determine starting model
2. Raytracing
3. Raybending
4. Inversion
5. Model Evaluation

C1. DETERMINE THE STARTING MODEL

Modeling and interpretation of refraction datasets can be performed in a variety of ways depending on the dataset, geologic structure and the goals of the study. In practice, analysis usually involves multiple iterations of forward modeling and inversions before a satisfactory data fit is achieved. *Zelt et al.* (2003) describe two basic modeling strategies: 1) a hypothesis-driven method in which a layered model is constructed based on previous knowledge of the study area and observed seismic arrivals. These arrivals may be grouped in a few different phases that are assigned to specific layers; 2) a tomographic approach in which minimum-structure crustal velocity models are constructed using observed first arrivals, and, if available, prominent Moho reflections. For the STEEP dataset, I started with a layered model based on previous work. The starting model (Figure 1) features velocities and thickness for Yakutat crust determined by

Christeson et al. (2010). Sediment velocities and the depth to the sediment-basement transition were determined using the MCS reflection data results.

C2. RAYTRACING

Raytracing results in a set of calculated travel times as a seismic wave travels through the given model from a source to a receiver. The raytracing used in Chapter 4 follows the shortest path method (SPM) (Nakanishi and Yamaguchi, 1986a). For raytracing, the model space is discretized with randomly spaced nodes (Figure 2). The average node-spacing (DRP) for the raytracing used in Chapter 4 is 200 m. The raypath travels in straight lines from node to node such that the total travel time for the raypath is minimized (Figure 2a). The raytracing method ultilizes a forward star (Moser et al., 1992) that defines the search radius for possible raypaths at each node (Figure 2b). For the raytracing scheme in Chapter 4, the forward star is three times DRP.

The total raypath, L_{tot}, is the sum of each length, L_i, between nodes (Figure 2b). Defining L_i in terms of model parameters, x_i, and, z_i, gives Equation 1 (Figure 2c). Defining a velocity, v_i, for each raypath segment leads to the solution for travel time, T, (Equation 2).

$$L_{tot} = \sum_{i=1}^{N} L_i = \sum_{i=1}^{N} \sqrt{(dx^2 + dz^2)}$$

Equation 1.

$$T = \sum_{i=1}^{N} \frac{\sqrt{(dx^2 + dz^2)}}{\frac{1}{2}(v_{i+1} + v_i)}$$

Equation 2.

C3. RAYBENDING

Travel times calculated by the SPM of raytracing have systematic errors because the paths are force to zigzag from node to node. To minimize these errors, the paths can be smoothed by raybending (Figure 3). In the raybending scheme, the preliminary raypath is resampled at ~10x the density of DRP. At each resampled position, the travel time and the travel time gradient are computed locally. The raypath is adjusted up or down in the model in order to minimize the travel time gradient (Figure 3b). The calculation loops until the path is stationary.

C4. INVERSION

The tomographic inversion follows a similar method to *van Avendonk et al.* (2004a), except we employ a linearized relationship between travel time residual and perturbations in velocity and boundary layer depth, instead of solving for slowness. Travel time residuals, δt, the difference between the picked source-receiver travel times and the calculated travel times can be expressed as a function of velocity perturbations, δv, and changes in boundary layer depths, δz (Equation 3). To formulate these relationships we assume that perturbations in the model are small, raypaths in the updated velocity model are parallel to those in the starting model (Figure 4).

$$\delta t \sim \int_{path} -(v^{-2}\delta v)ds + \sum_{reflect} 2v_1^{-1}\cos\varphi\cos\alpha\,\delta z + \sum_{pierce}\left(v_1^{-1}\cos\varphi_1 - v_2^{-1}\cos\varphi_2\right)\cos\alpha\,\delta z$$

Equation 3.

The first term integrates over seismic velocity perturbations within each of the model layers (Nolet, 1993). The second term adds the contribution in the case of a reflection (Bishop et al., 1985). The third term accommodates the addition of δz in the case that a raypath transverses a layer boundary (Hole, 1992).

The first step towards inversion is scaling the data and model parameters. Travel time residuals, δt, are scaled by pick uncertainties, so that more accurate picks carry more weight than noisy picks. Velocity and layer boundary depth perturbations, δv and δz, are scaled with a constant velocity and depth appropriate for the model.

Travel time constraints can be cast in matrix form (Equation 4) and are evaluated using a least-squares inversion with additional model constraints.

$$\mathbf{d} = \mathbf{G}\delta\mathbf{m}$$ **Equation 4.**

In equation 4, the data vector **d** contains the travel time residuals, δ**m** is the model perturbation vector that includes δz and δv, **G** is the Frechet matrix.

Model regularization reduces inaccuracies and accommodates non-uniqueness in the inverse problem. These additional model constraints for damping, smoothness and flattening

(Van Avendonk et al., 2004a) tune the inversion so that there is a realistic tradeoff between data fit and model fidelity. The inversion minimizes a penalty function:

$$F(\delta \mathbf{m}) = \left| \mathbf{G}\delta\mathbf{m} - \mathbf{d} \right|^2$$

$$\lambda \mathbf{D}(\mathbf{m} + \delta \mathbf{m}) \qquad \textbf{Equation 5.}$$

We can find a model update, $\delta\mathbf{m}$, by using sparse matrix solver such as LSQR (Paige and Saunders, 1982). The tradeoff between model structure and data misfit is controlled by the parameter λ, which we choose such that the normalized data misfit χ^2 is close to 1.0 (Van Avendonk et al., 2004a). Once we have updated the reference model $\mathbf{m}$ with the perturbation $\delta\mathbf{m}$, we can trace new ray paths and start a next iteration of the linearized inversion.

C5. MODEL EVALUTION

To obtain a quantitative measure of the model fidelity we calculate the *a posteriori* model covariance matrix, $\mathbf{C}_m$, and resolution matrix $\mathbf{R}$ (Menke, 1984). If the model regularization, $\lambda\mathbf{D}$, represents our *a priori* information of the model space, then we assume

$$\mathbf{C}_m = (\mathbf{G}^T\mathbf{G} + \lambda\mathbf{D}^T\mathbf{D})^{-1} \qquad \textbf{Equation 6.}$$

We compute, $\mathbf{C}_m$, with a regular singular value decomposition (Press et al., 1986) of the argument, $\mathbf{G}^T\mathbf{G} + \lambda\mathbf{D}^T\mathbf{D}$, in Equation 6. After scaling the elements of, $\mathbf{C}_m$, with the velocity, v_0, and depth, z_0, we can assess the tradeoffs between model coverage and data fit. The covariance gives us an estimation of ray density across the model.

We can assess the resolution of the model using by calculating the resolution matrix

$$\mathbf{R} = (\mathbf{A}^T\mathbf{A})^{-1}\mathbf{G}^T\mathbf{G} \qquad \textbf{Equation 7.}$$

Then, we determine resolution by applying a sliding window in model space (Equation 8), multiplying by the resolution matrix and testing the resolution of different sized windows.

$$\mathbf{R}_w(x,z) = \mathbf{w}(x,z) \cdot \mathbf{R} \cdot \mathbf{w}(x,z) \qquad \textbf{Equation 8.}$$

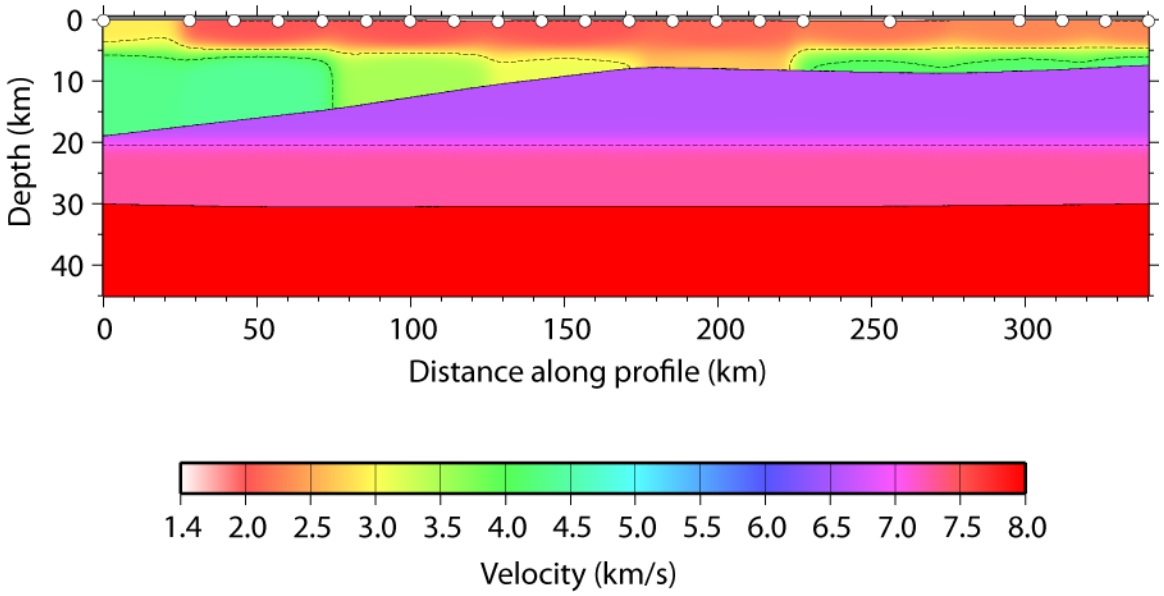

Figure C1. Starting velocity model for STEEP01.

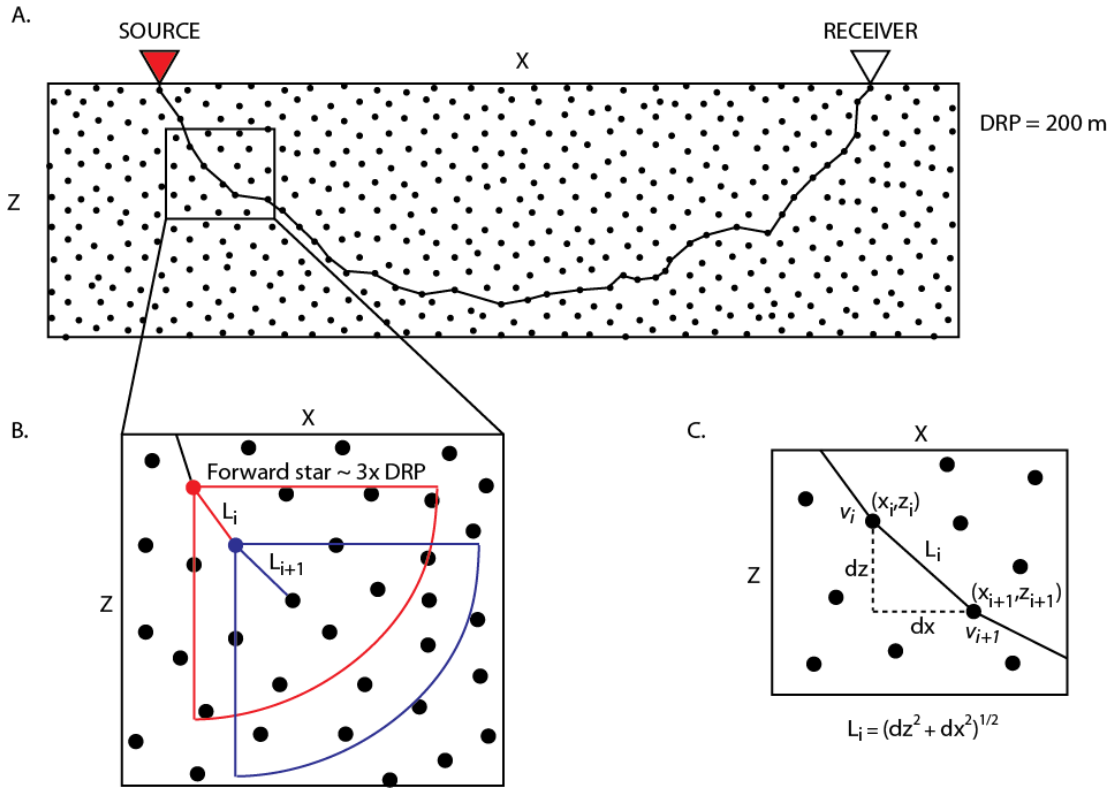

Figure C2. Schematic diagram of raytracing. A) Full raypath. B) Schematic of forward star search radius. C) Definition of portion of raypath in terms of model parameters, x, v, and z.

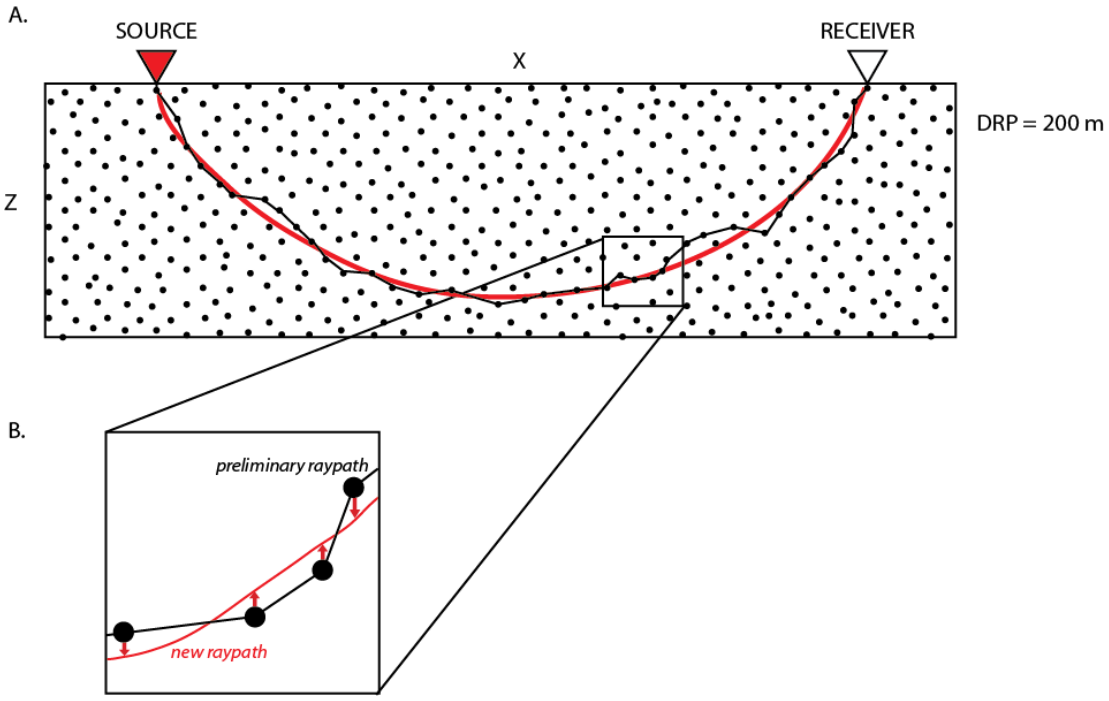

Figure C3. Schematic diagram of raybending. A) Full raypath. B) Small perturbations in raypath.

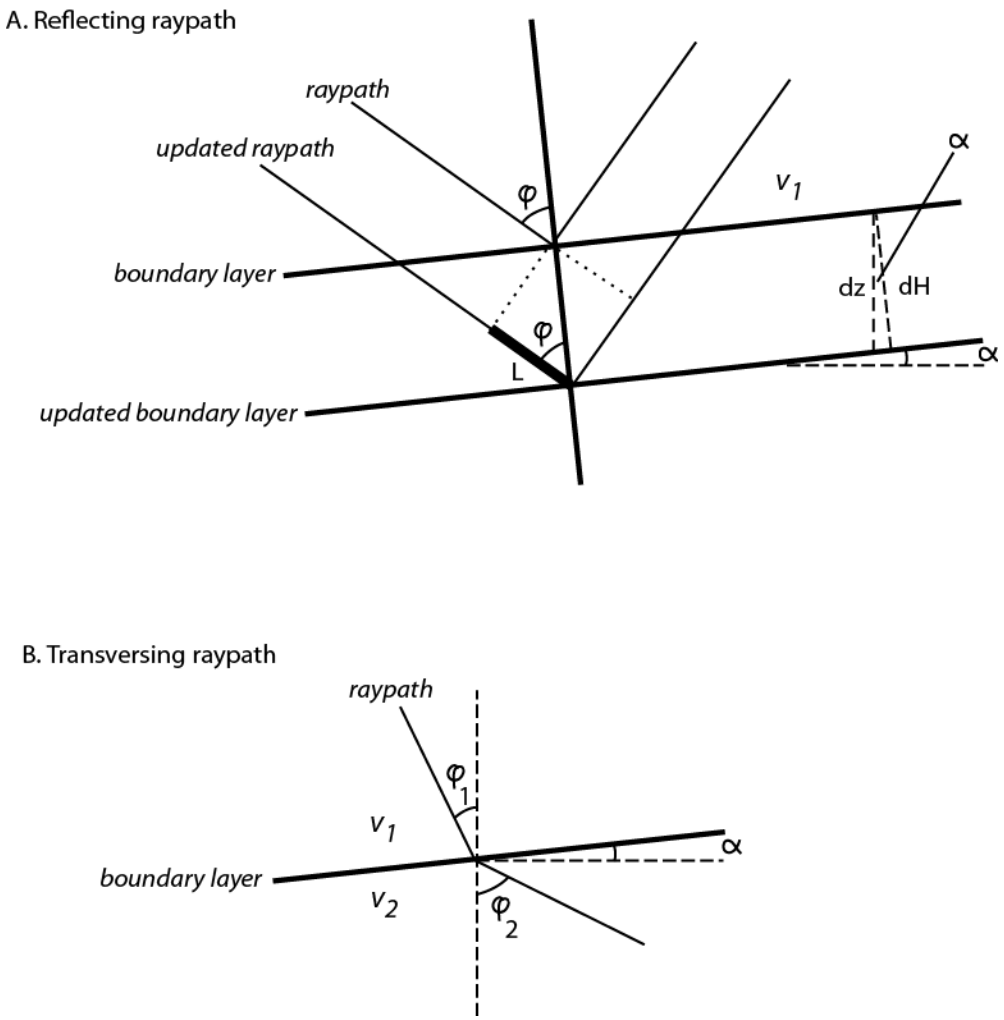

Figure C4. Variable definitions for Equation 3. A) For reflections. B) For refracting raypaths across layer boundaries.

Appendix D: Wide Angle Reflection and Refraction Data

The following pages show data, picked phase arrivals, calculated phase arrivals and corresponding raypaths through the velocity model for record used in the tomographic inversion described in Chapter 4. In the upper portion of each figure, the picked phase arrivals are shown in the dashed lines, calculated phase arrivals are the solid lines. Magenta = Po, Green = Ps, Blue = Pg, Yellow = PgP, Orange = PmP, Red = Pn.

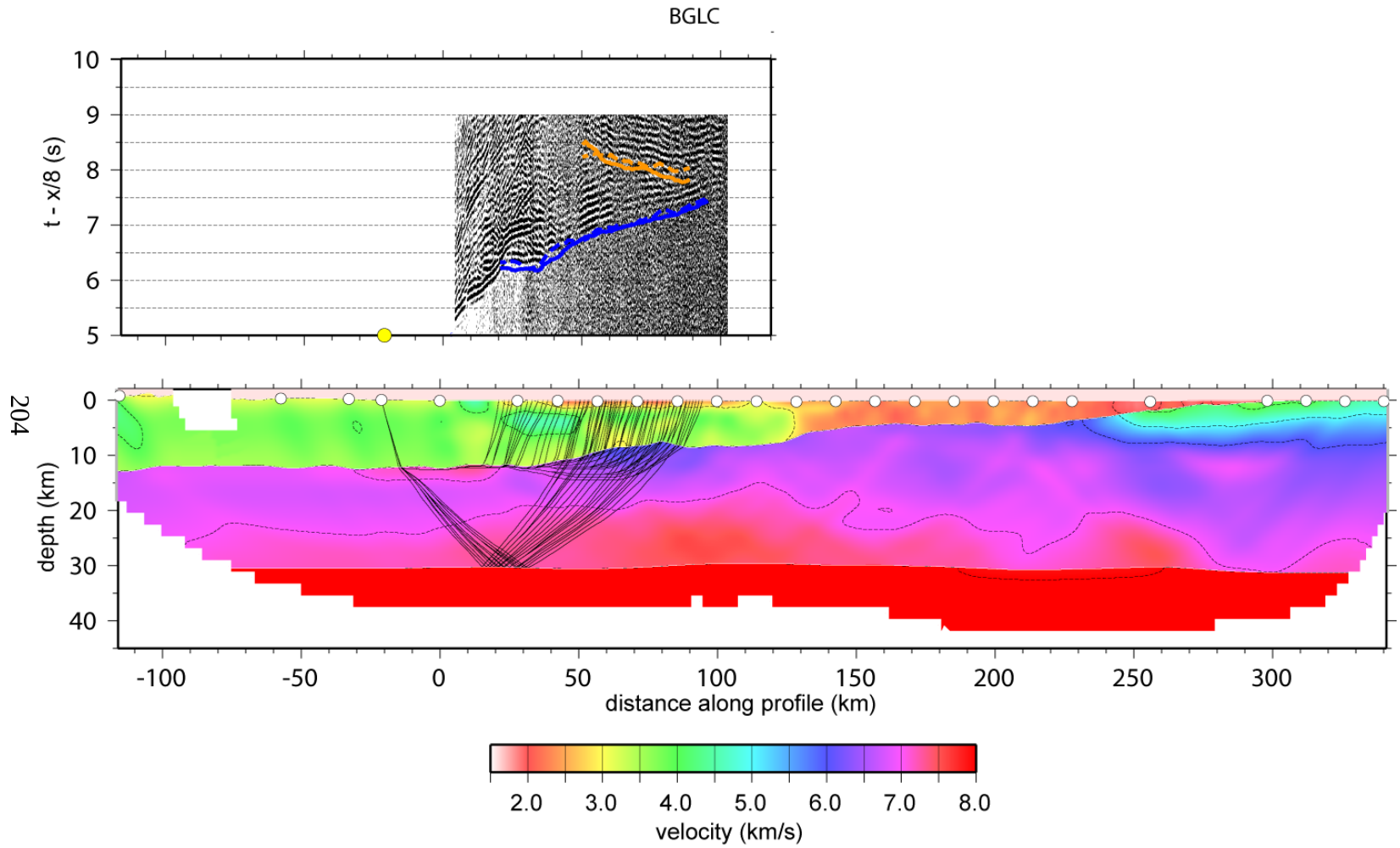
BGLC
t - x/8 (s)
10
9
8
7
6
5
204
depth (km)
0
10
20
30
40
-100
-50
0
50
100
150
200
250
300
distance along profile (km)
2.0
3.0
4.0
5.0
6.0
7.0
8.0
velocity (km/s)

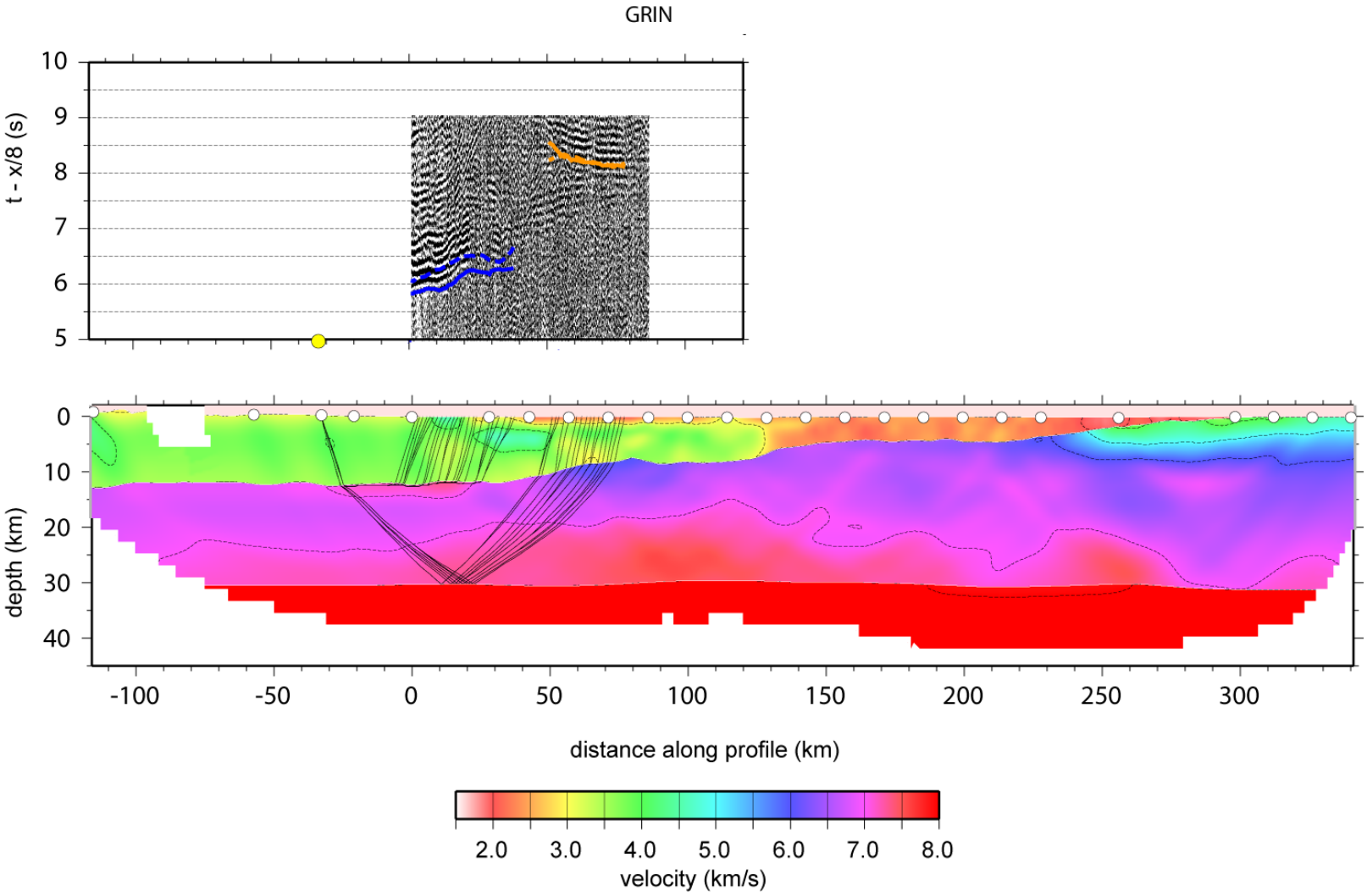
GRIN
t - x/8 (s)
10
9
8
7
6
5
depth (km)
0
10
20
30
40
-100
-50
0
50
100
150
200
250
300
distance along profile (km)
2.0
3.0
4.0
5.0
6.0
7.0
8.0
velocity (km/s)

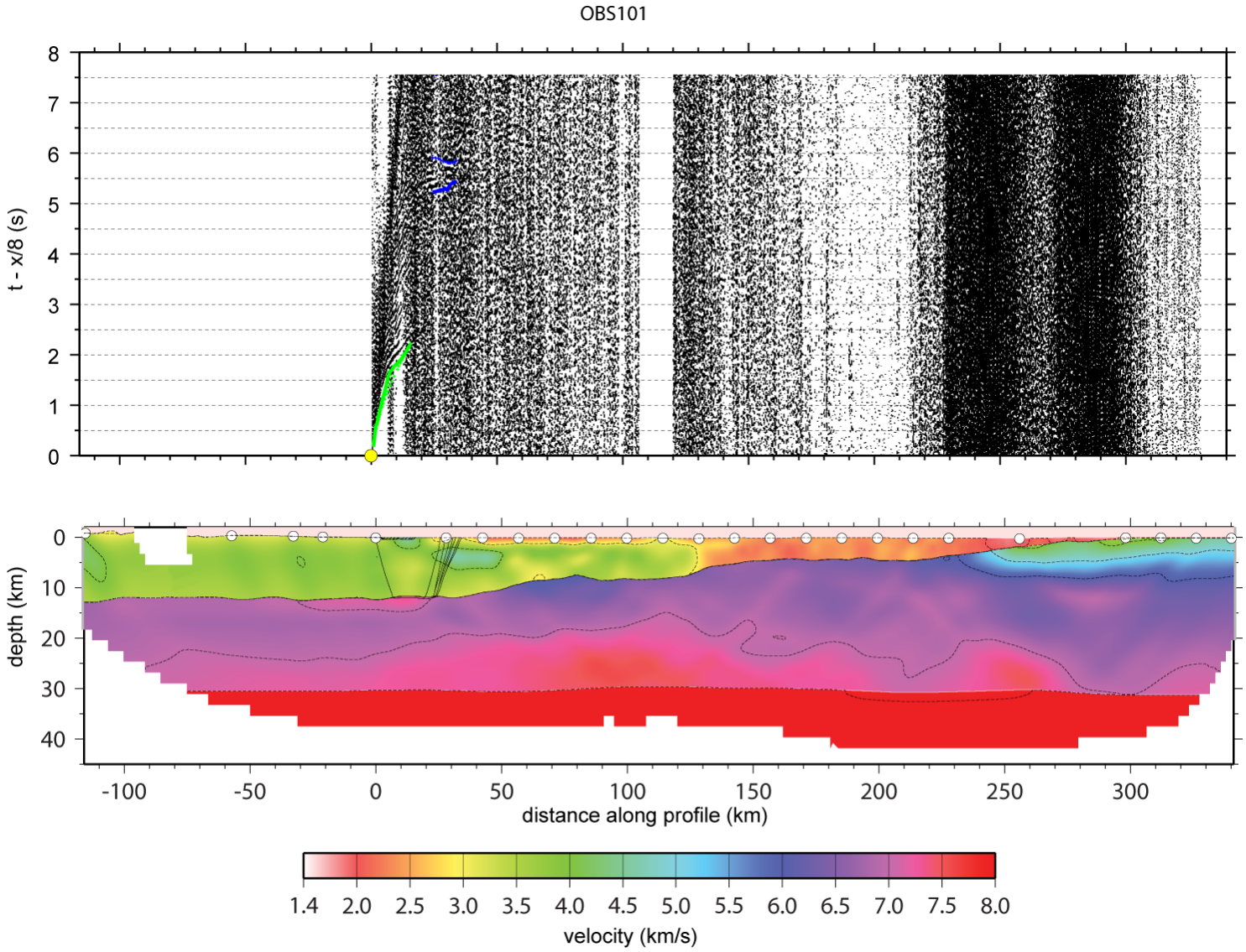
OBS101
t - x/8 (s)
depth (km)
distance along profile (km)
velocity (km/s)
1.4 2.0 2.5 3.0 3.5 4.0 4.5 5.0 5.5 6.0 6.5 7.0 7.5 8.0

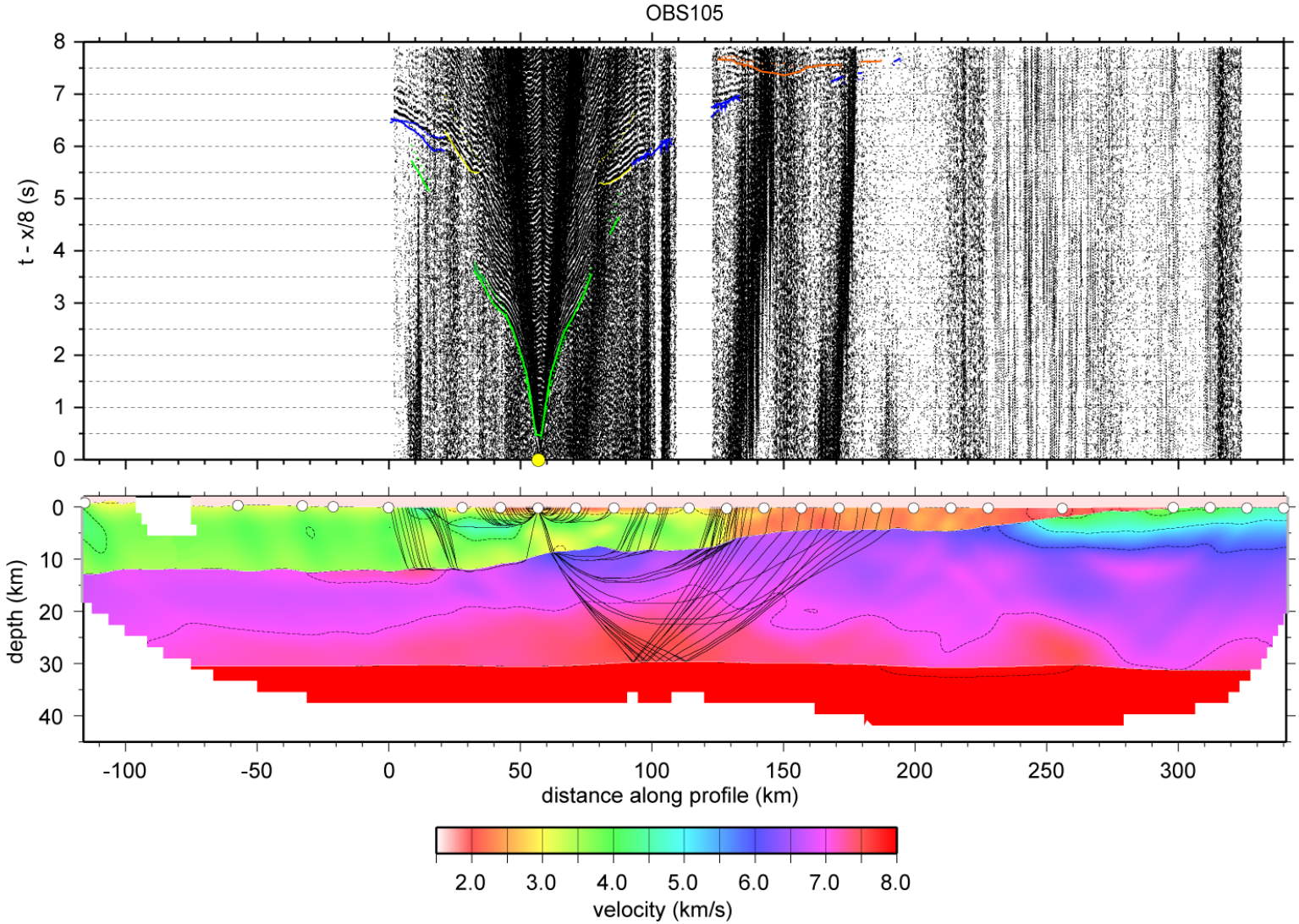
OBS105
t - x/8 (s)
depth (km)
distance along profile (km)
velocity (km/s)
2.0
3.0
4.0
5.0
6.0
7.0
8.0

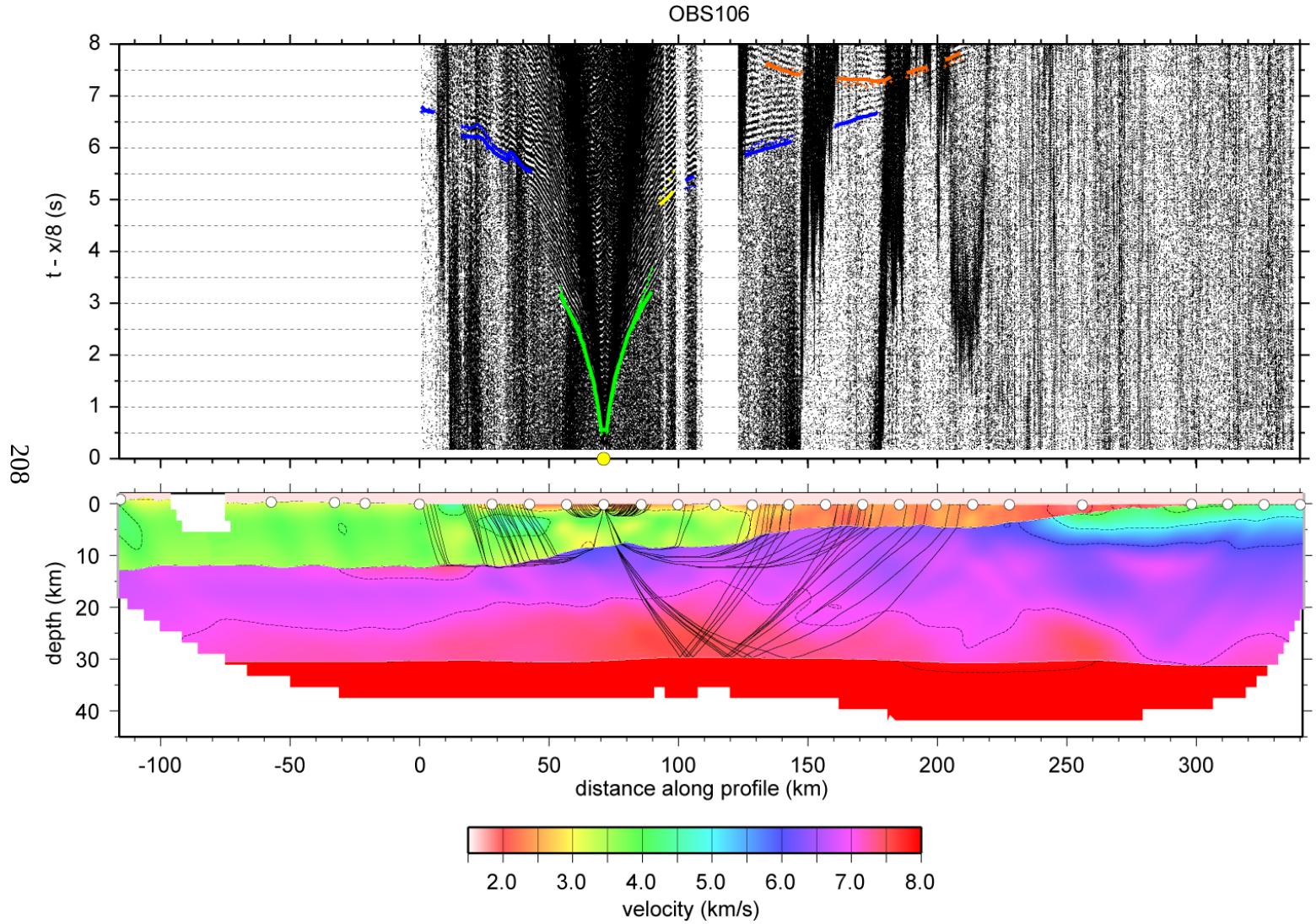
OBS106
t - x/8 (s)
depth (km)
distance along profile (km)
velocity (km/s)
2.0
3.0
4.0
5.0
6.0
7.0
8.0

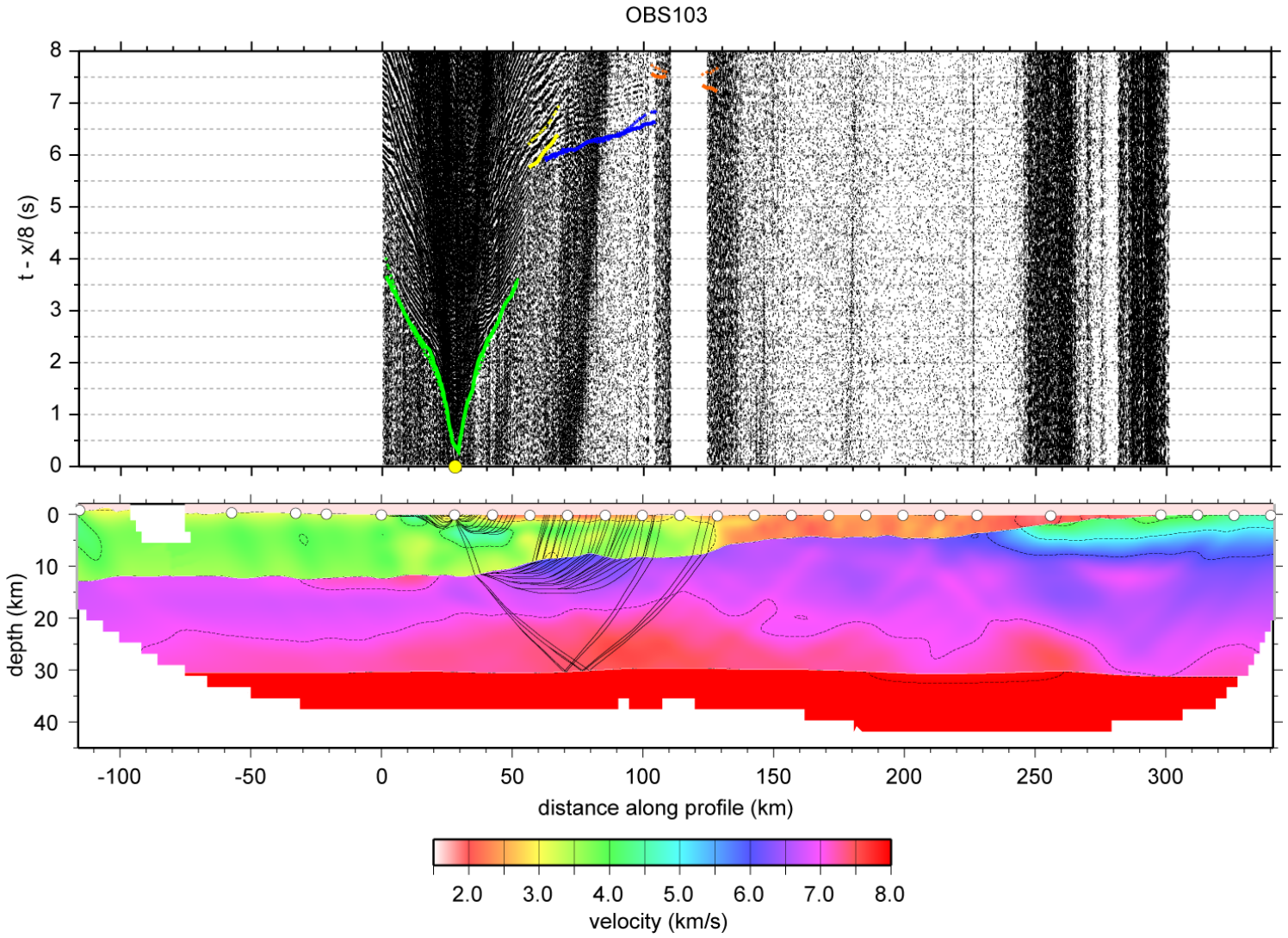
OBS103
t - x/8 (s)
depth (km)
distance along profile (km)
velocity (km/s)
2.0
3.0
4.0
5.0
6.0
7.0
8.0

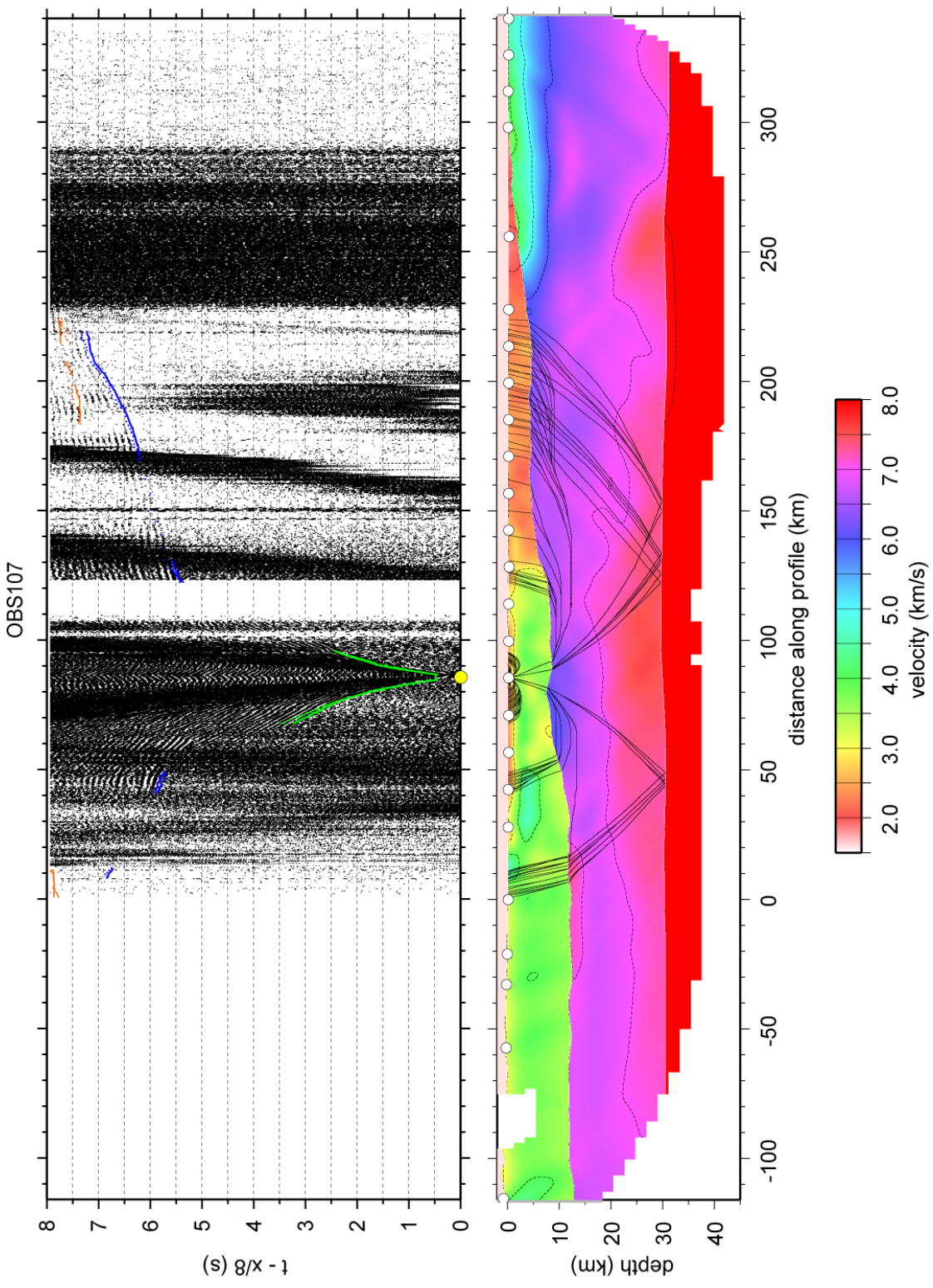
OBS107
t - x/8 (s)
depth (km)
distance along profile (km)
velocity (km/s)
2.0
3.0
4.0
5.0
6.0
7.0
8.0

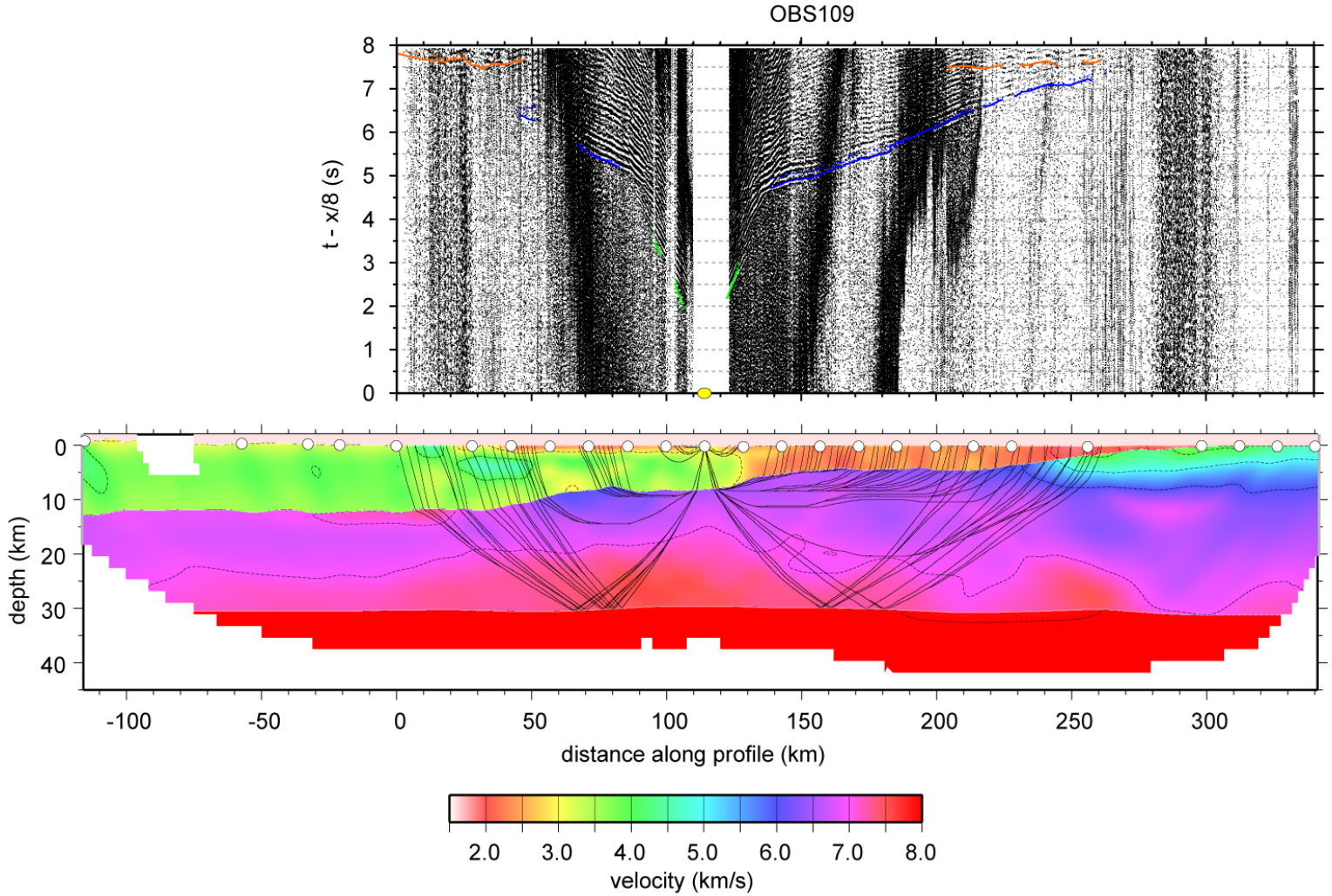
OBS109
t - x/8 (s)
0
1
2
3
4
5
6
7
8
depth (km)
0
10
20
30
40
-100
-50
0
50
100
150
200
250
300
distance along profile (km)
2.0
3.0
4.0
5.0
6.0
7.0
8.0
velocity (km/s)

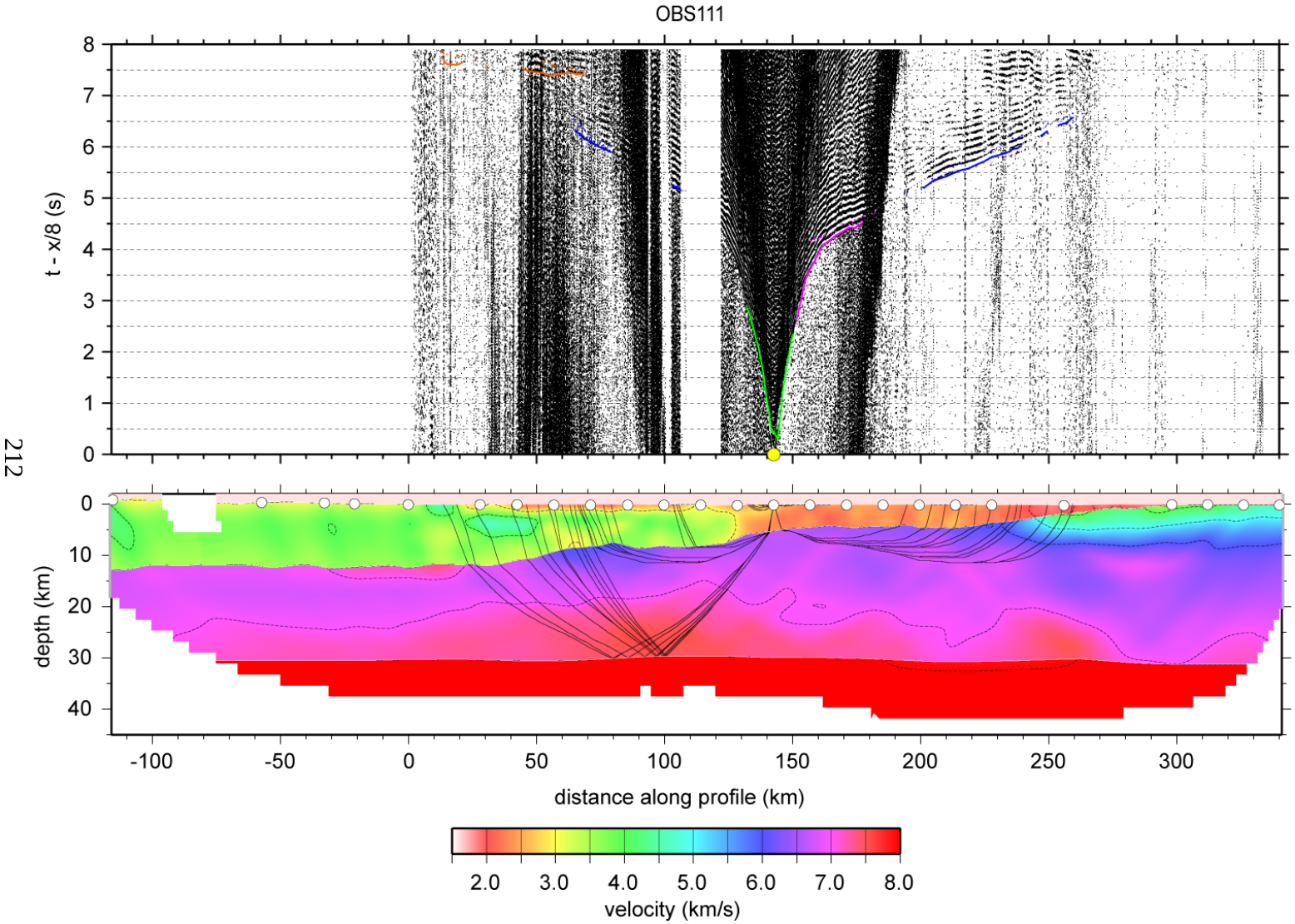
OBS111
t - x/8 (s)
depth (km)
distance along profile (km)
velocity (km/s)
2.0
3.0
4.0
5.0
6.0
7.0
8.0

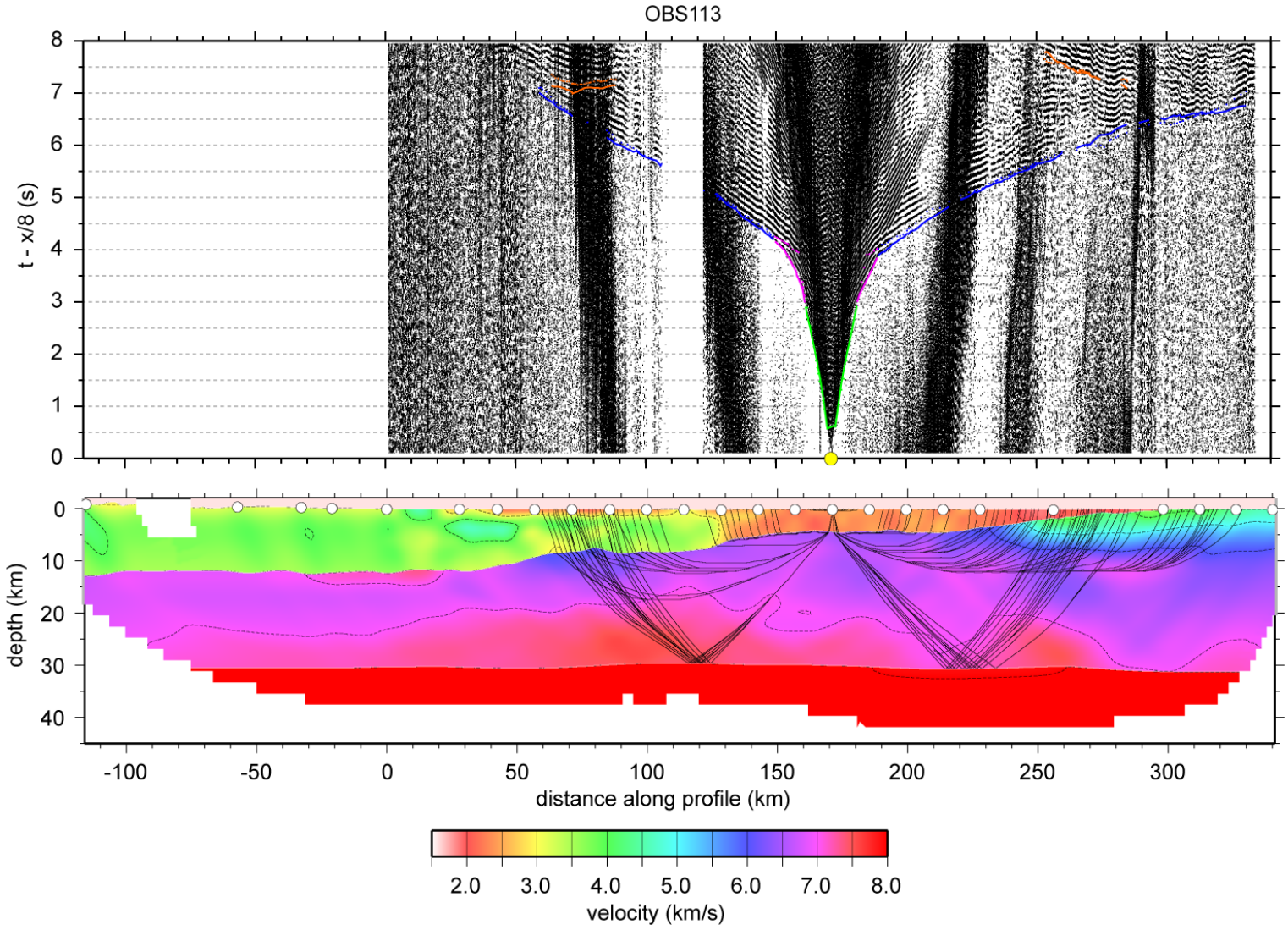
OBS113
t - x/8 (s)
depth (km)
distance along profile (km)
velocity (km/s)
2.0
3.0
4.0
5.0
6.0
7.0
8.0

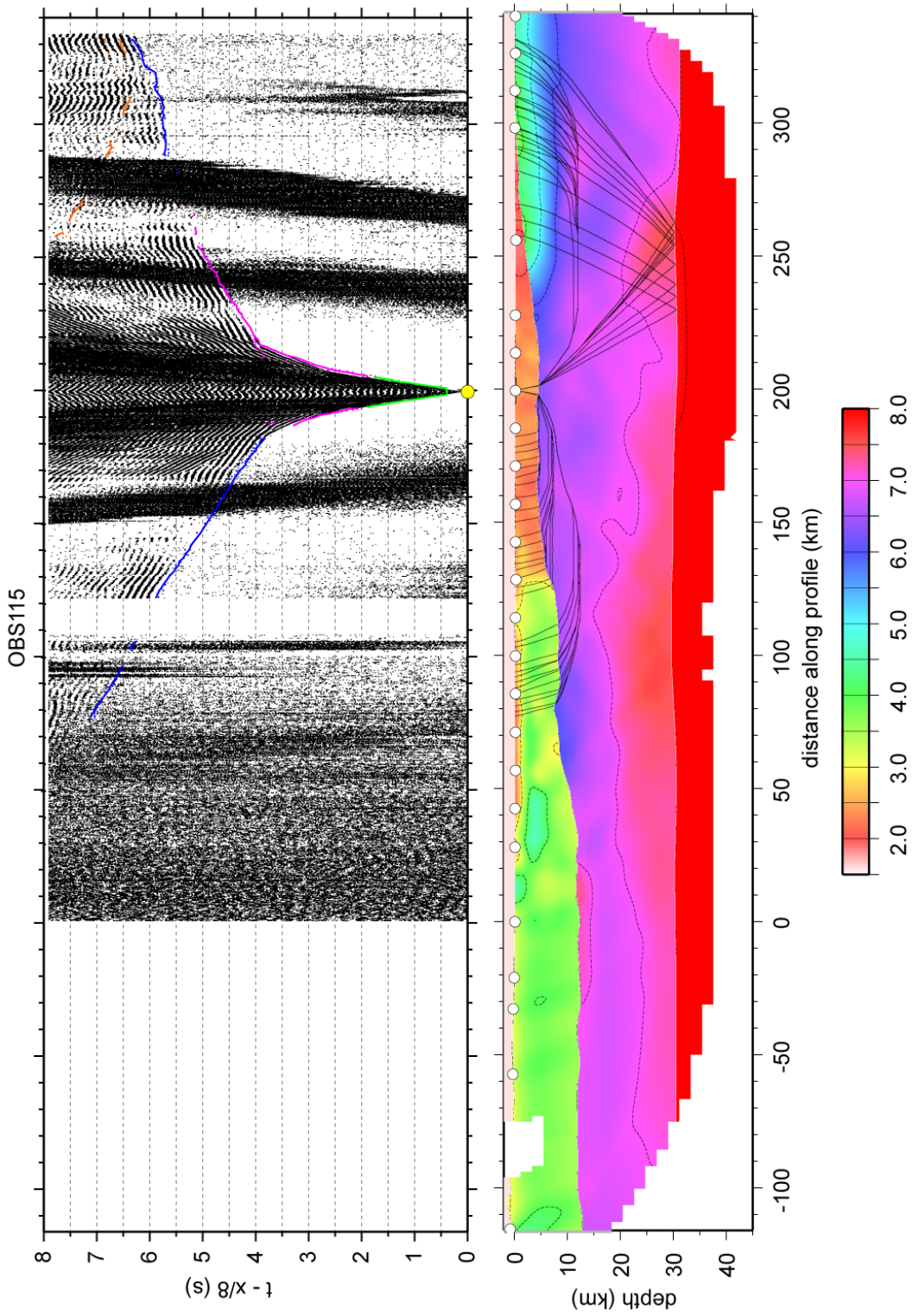
OBS115
t - x/8 (s)
depth (km)
distance along profile (km)
-100
-50
0
50
100
150
200
250
300
0
10
20
30
40
0
1
2
3
4
5
6
7
8
2.0
3.0
4.0
5.0
6.0
7.0
8.0

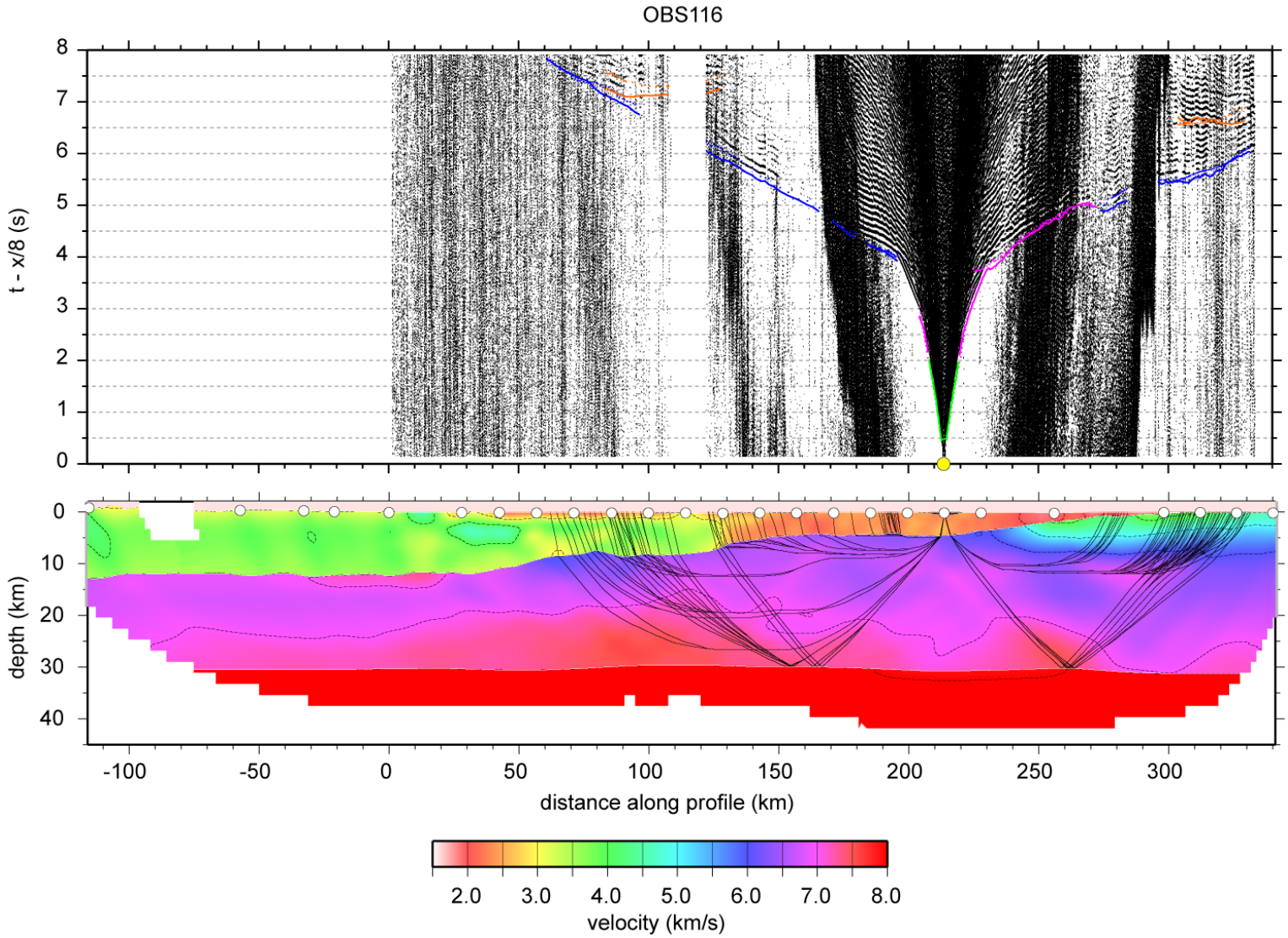
OBS116
t - x/8 (s)
depth (km)
distance along profile (km)
velocity (km/s)
2.0
3.0
4.0
5.0
6.0
7.0
8.0

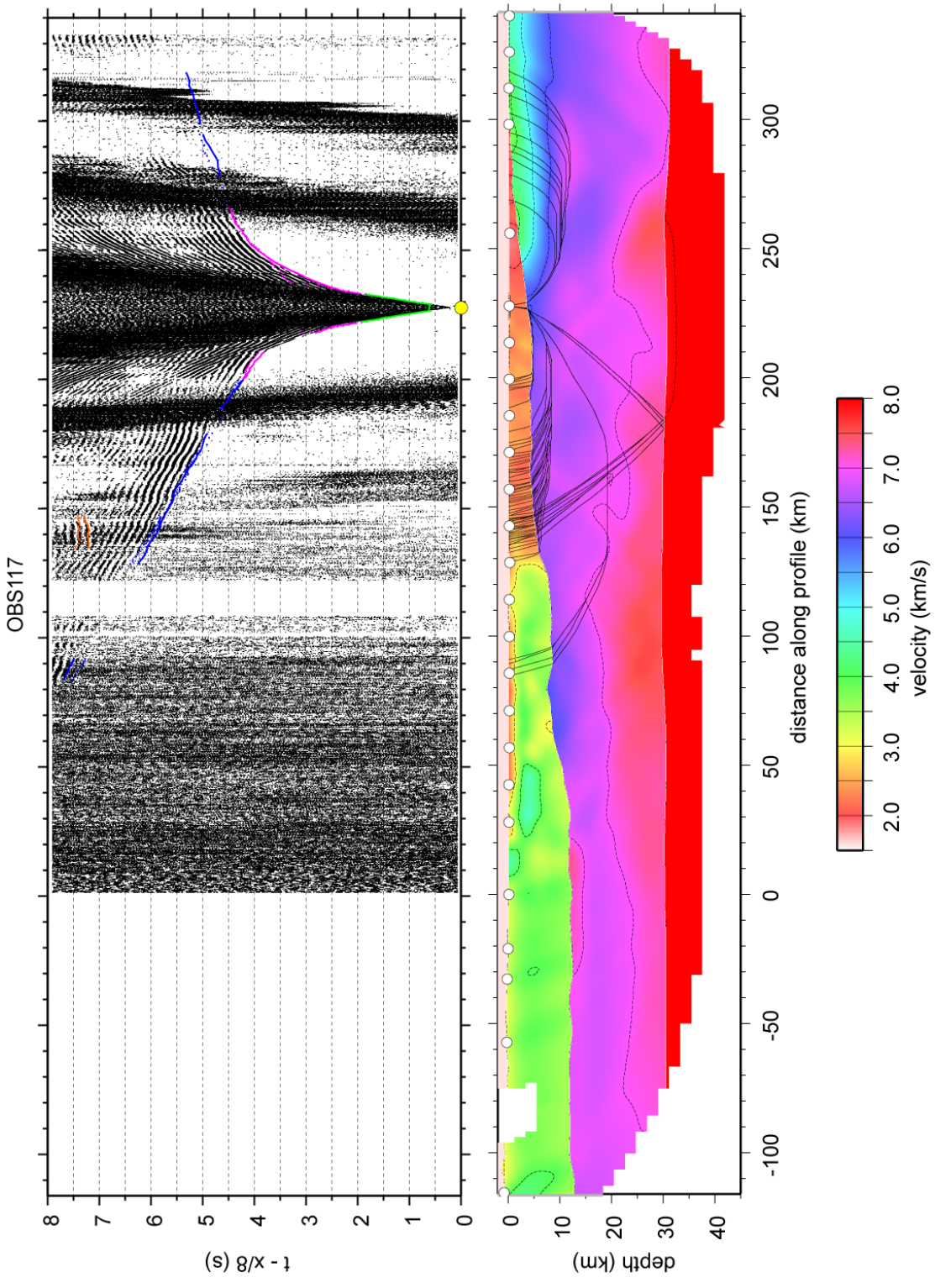
OBS117
t - x/8 (s)
depth (km)
distance along profile (km)
velocity (km/s)
2.0
3.0
4.0
5.0
6.0
7.0
8.0

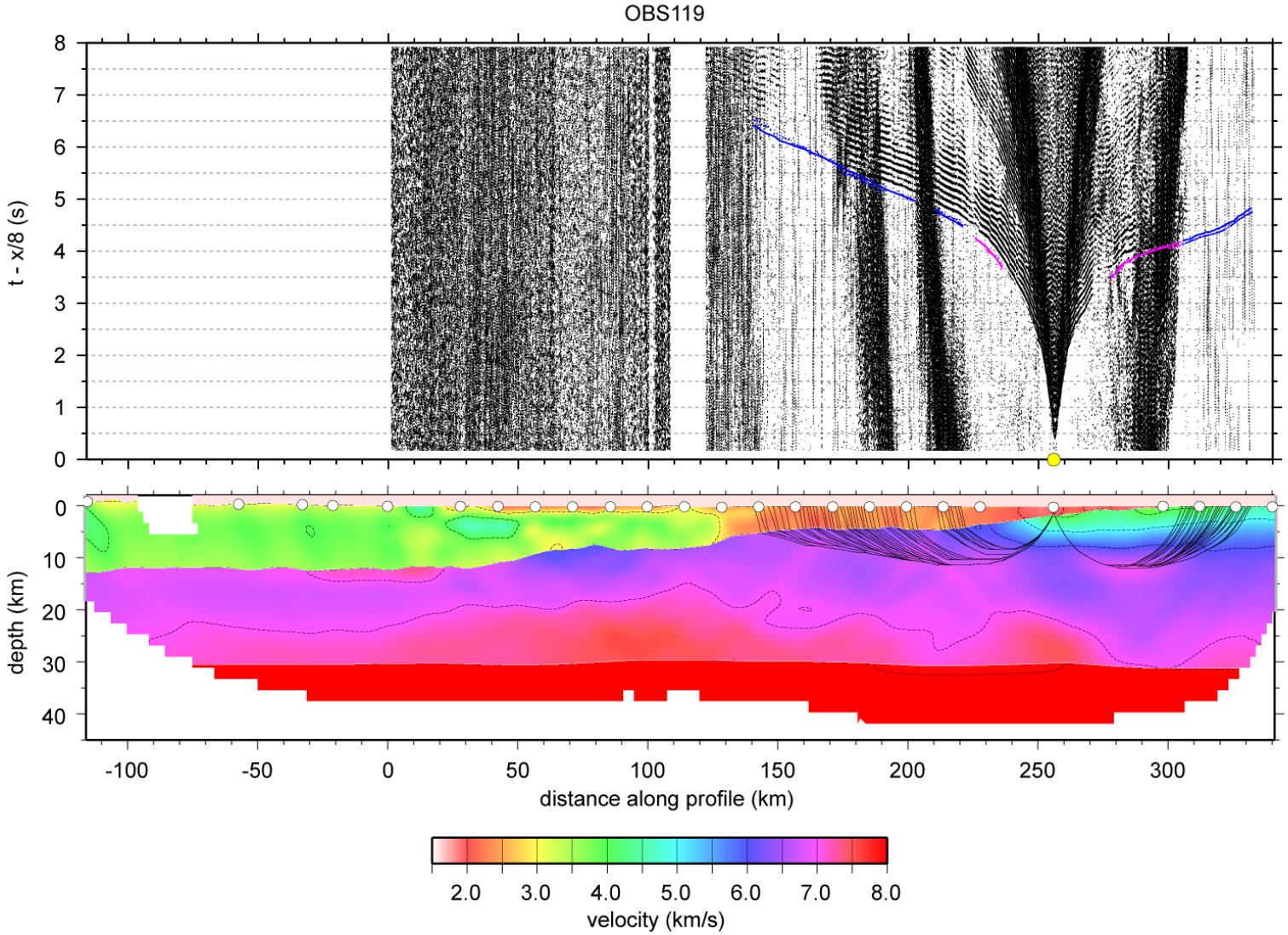
OBS119
t - x/8 (s)
depth (km)
distance along profile (km)
velocity (km/s)
2.0
3.0
4.0
5.0
6.0
7.0
8.0

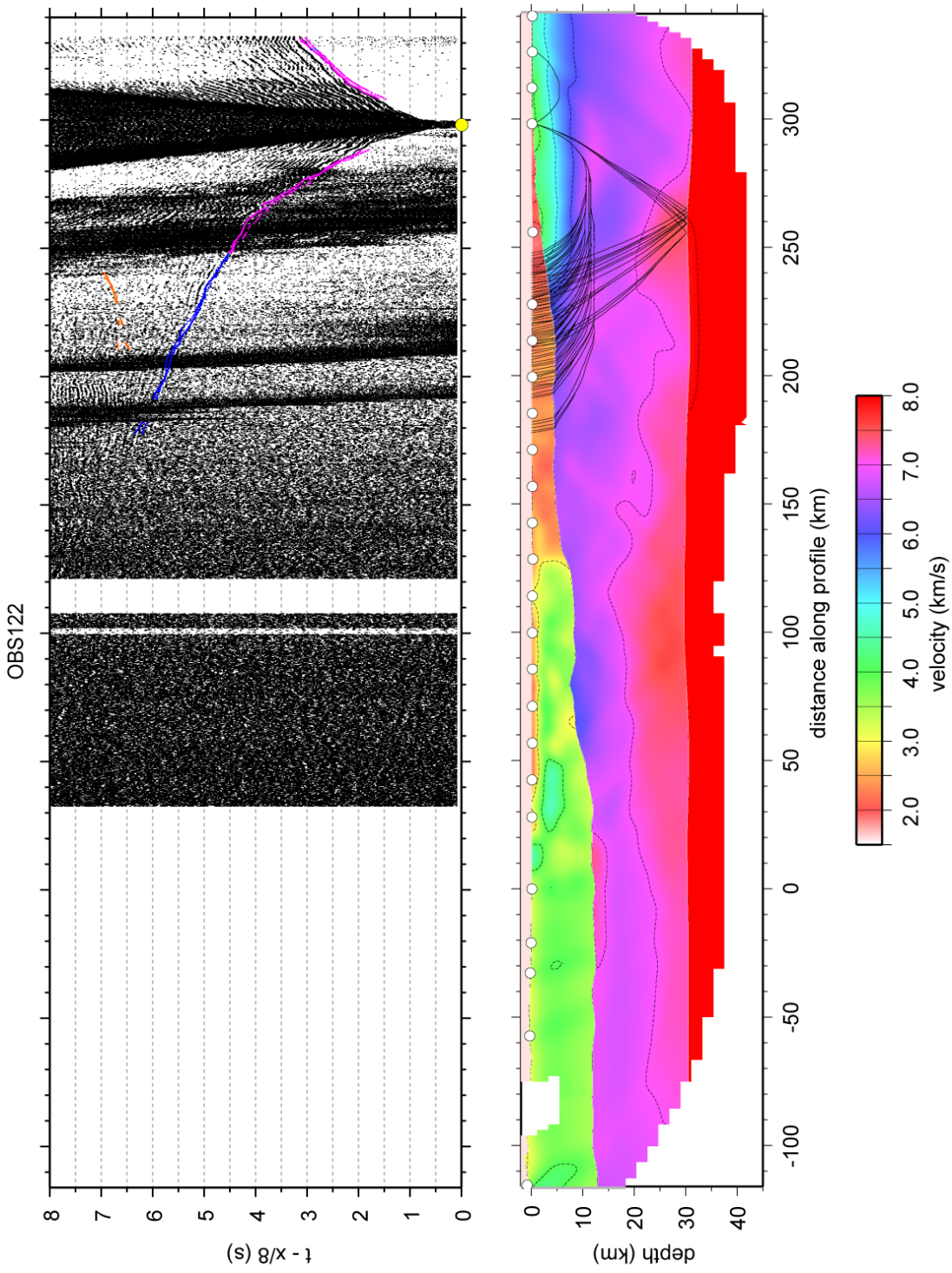
OBS122
t - x/8 (s)
depth (km)
distance along profile (km)
velocity (km/s)
2.0
3.0
4.0
5.0
6.0
7.0
8.0

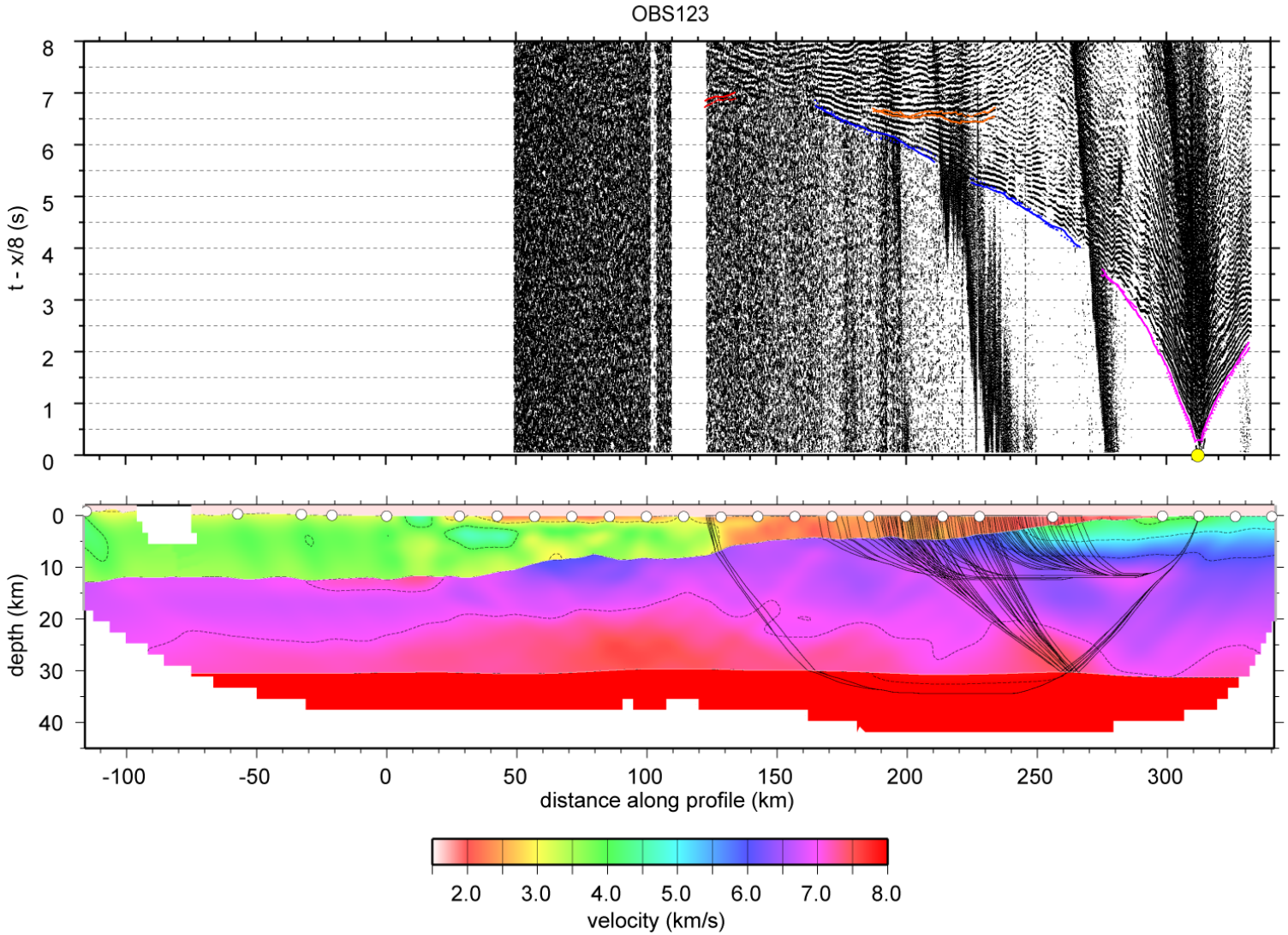
OBS123
t - x/8 (s)
depth (km)
distance along profile (km)
velocity (km/s)
2.0
3.0
4.0
5.0
6.0
7.0
8.0

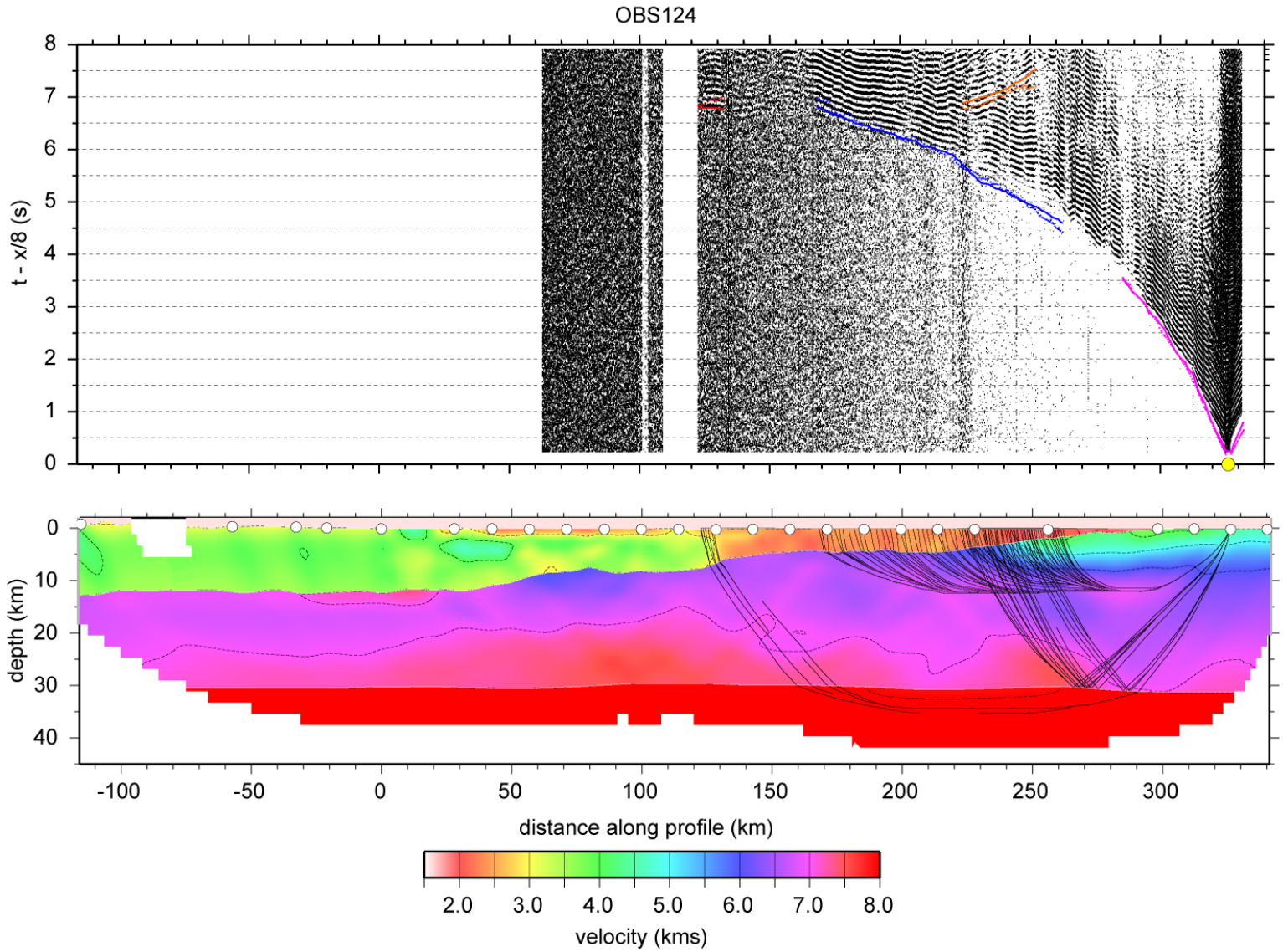
OBS124
t - x/8 (s)
depth (km)
distance along profile (km)
velocity (kms)
2.0
3.0
4.0
5.0
6.0
7.0
8.0

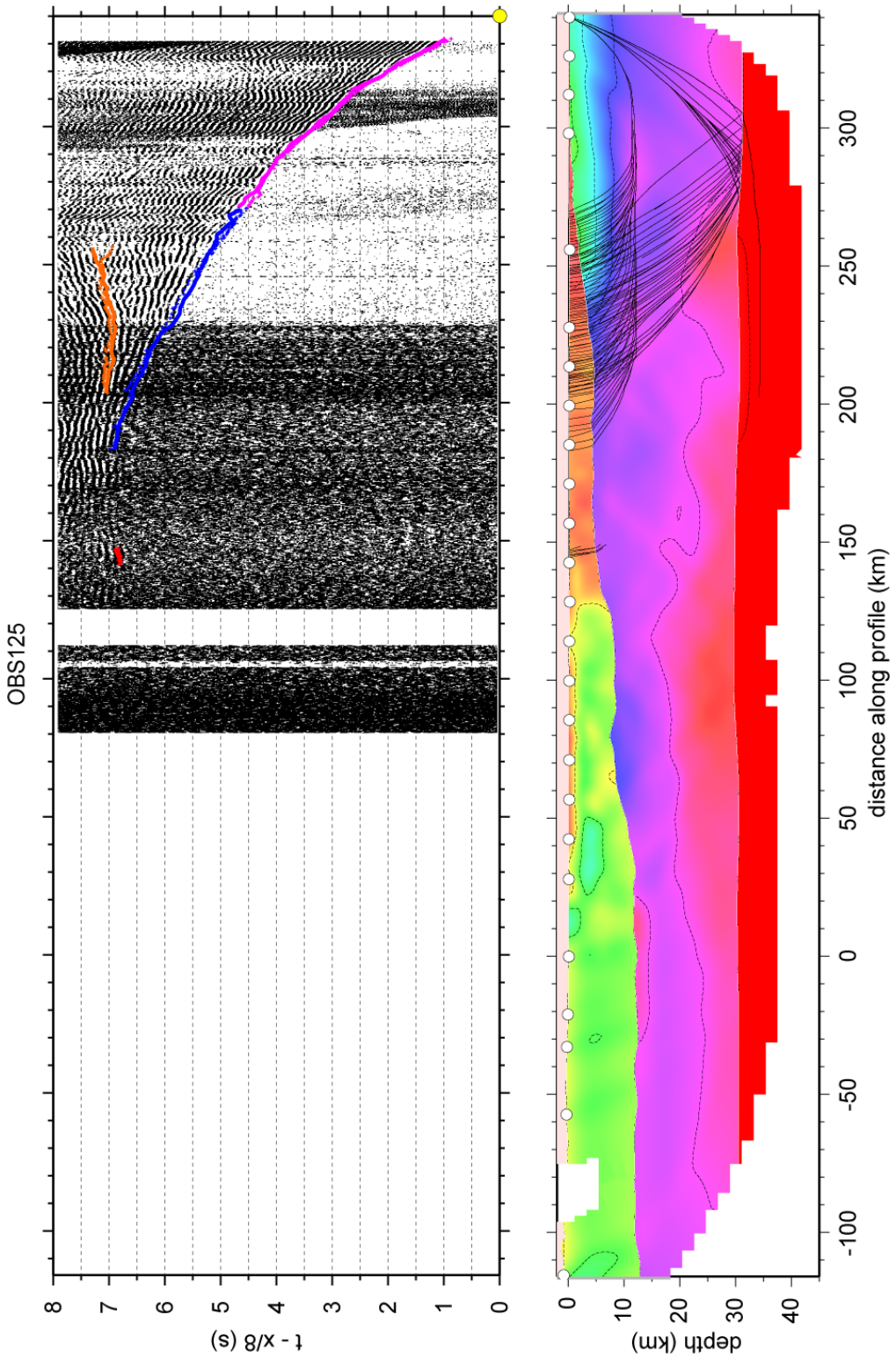
OBS125
t - x/8 (s)
0
1
2
3
4
5
6
7
8
depth (km)
0
10
20
30
40
-100
-50
0
50
100
150
200
250
300
distance along profile (km)

Appendix E: Travel Time Residuals

The following pages show normalized travel time residuals for each instrument used in the tomographic inversion described in Chapter 4. The travel time residual is calculated by subtracting picked travel times from the travel times calculated during raytracing and raybending after inversion. Then, the residuals are normalized by dividing by the assigned uncertainty.

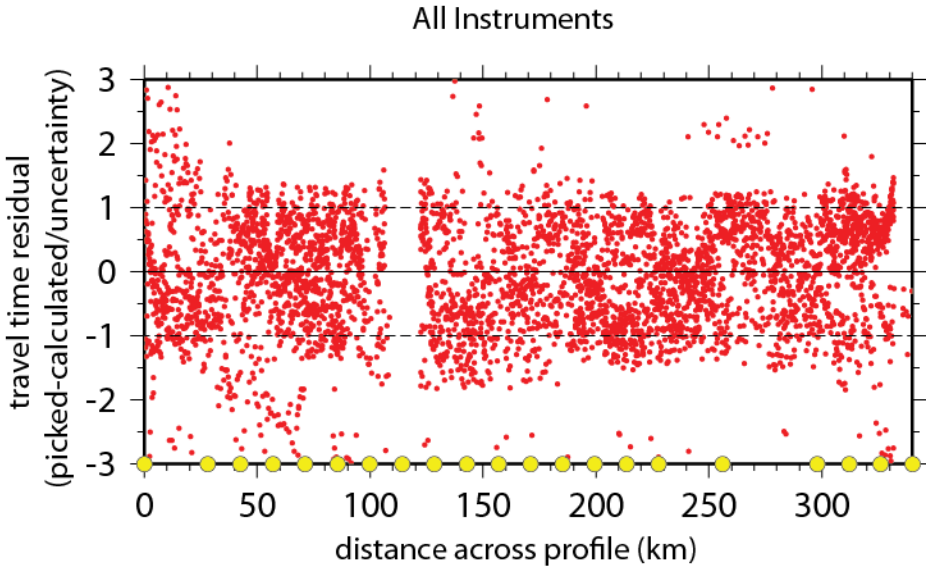
All Instruments
travel time residual
(picked-calculated/uncertainty)
3
2
1
0
-1
-2
-3
0
50
100
150
200
250
300
distance across profile (km)

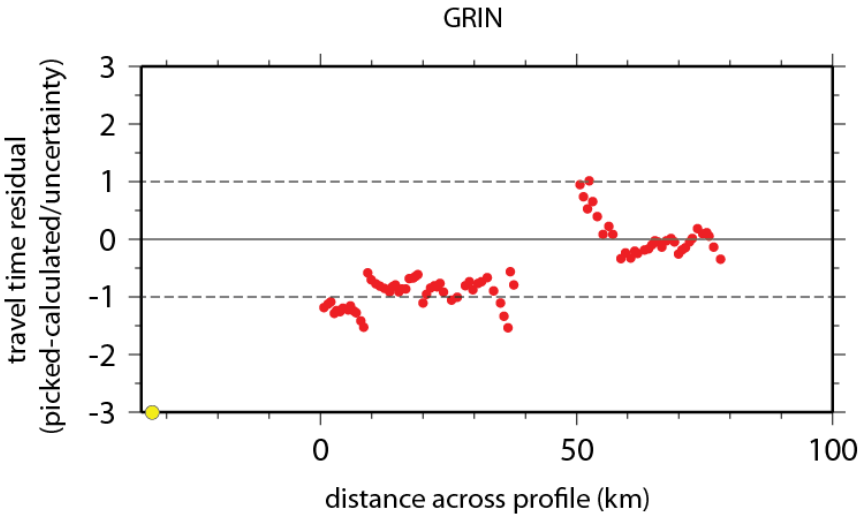
GRIN
travel time residual
(picked-calculated/uncertainty)
3
2
1
0
-1
-2
-3
0
50
100
distance across profile (km)

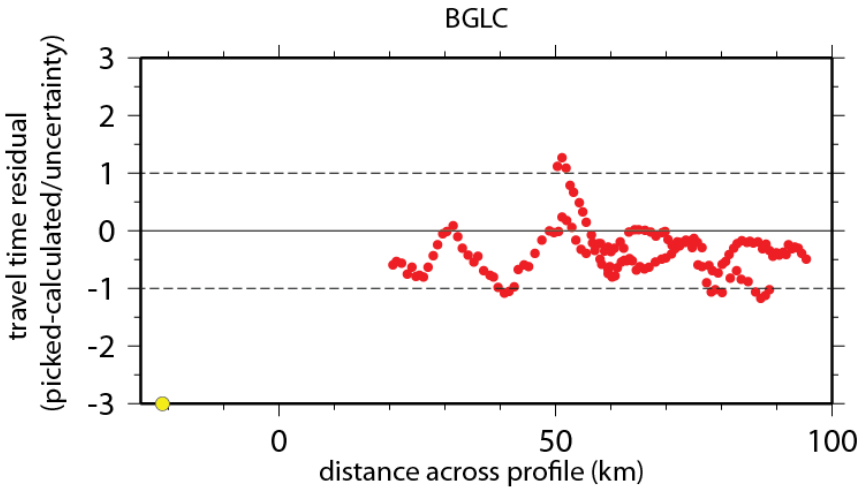
BGLC
travel time residual
(picked-calculated/uncertainty)
3
2
1
0
-1
-2
-3
0
50
100
distance across profile (km)

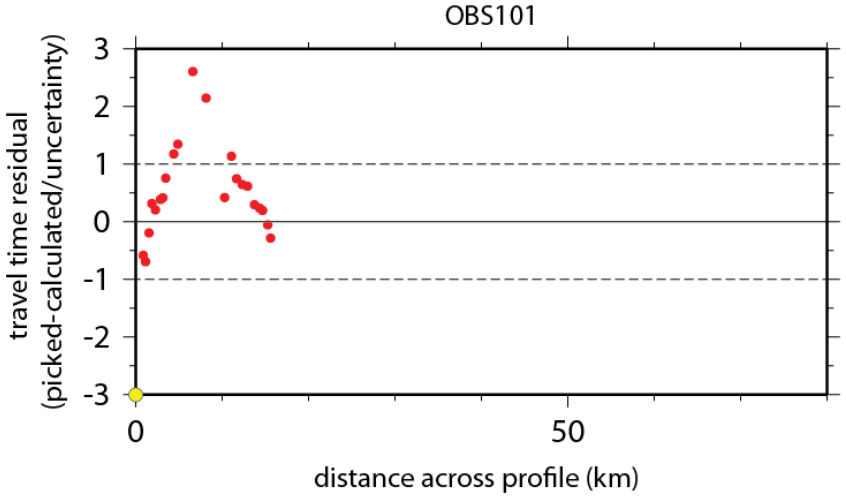
OBS101
travel time residual
(picked-calculated/uncertainty)
3
2
1
0
-1
-2
-3
0
50
distance across profile (km)

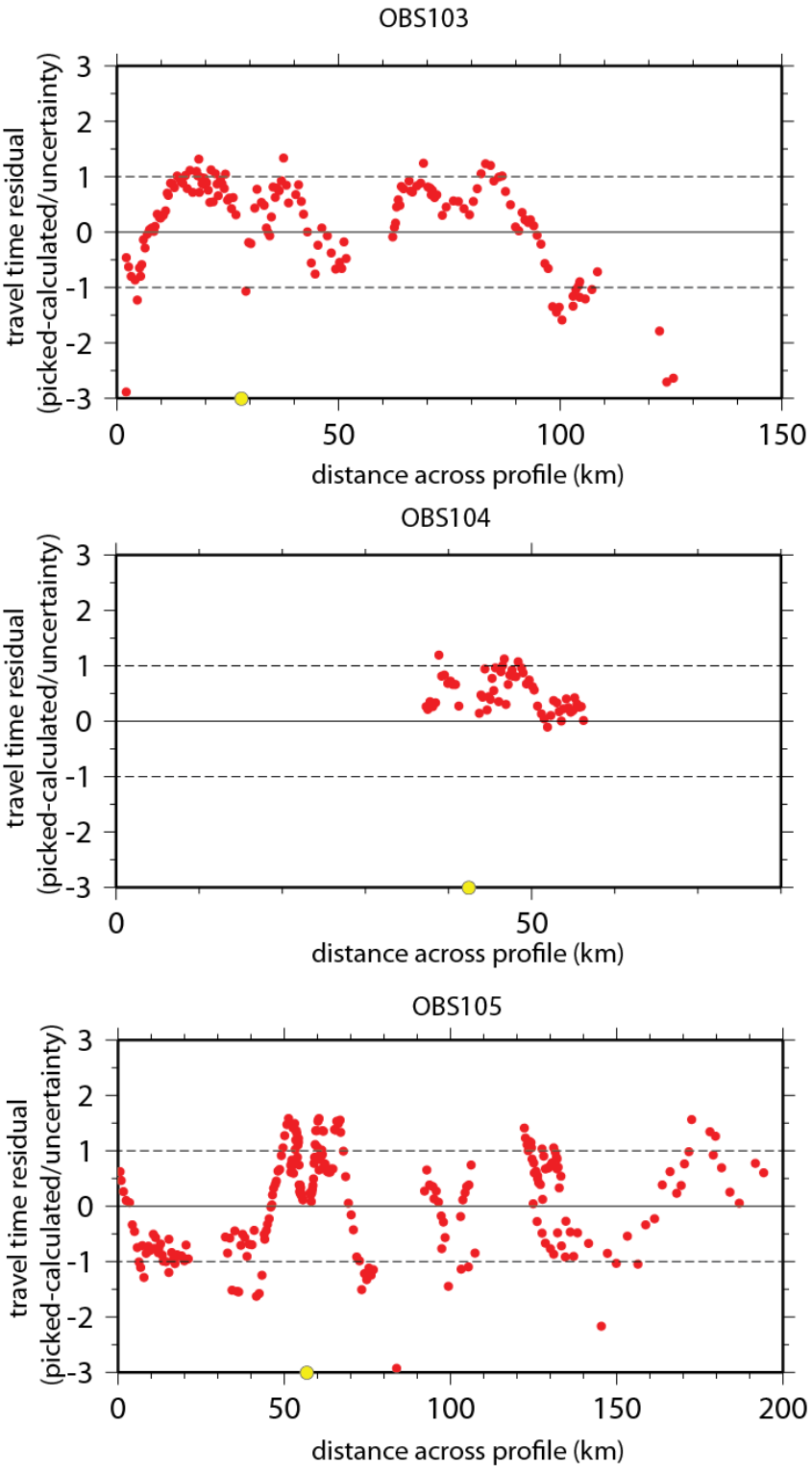
OBS103
travel time residual
(picked-calculated/uncertainty)
3
2
1
0
-1
-2
-3
0
50
100
150
distance across profile (km)
OBS104
travel time residual
(picked-calculated/uncertainty)
3
2
1
0
-1
-2
-3
0
50
distance across profile (km)
OBS105
travel time residual
(picked-calculated/uncertainty)
3
2
1
0
-1
-2
-3
0
50
100
150
200
distance across profile (km)

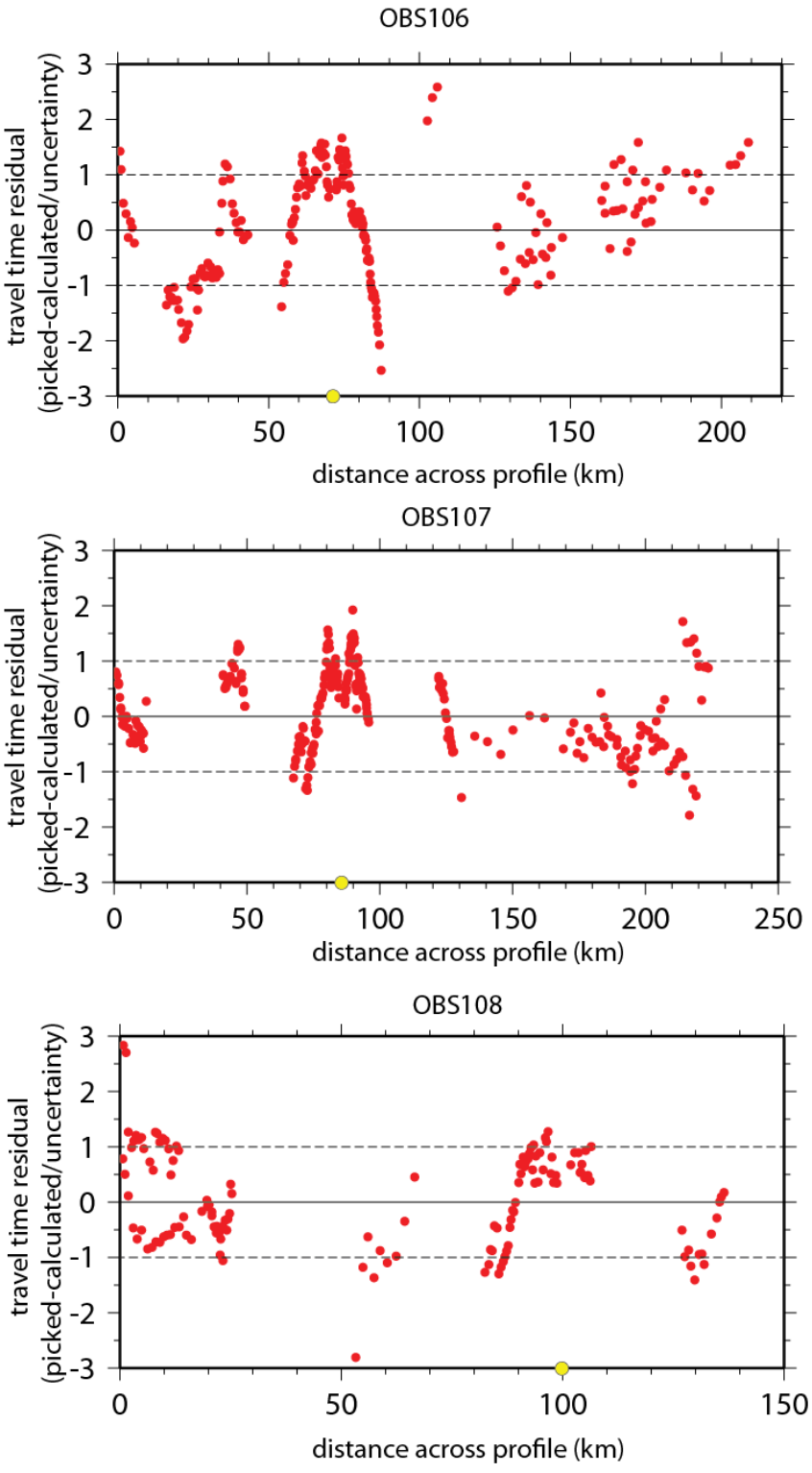
OBS106
travel time residual
(picked-calculated/uncertainty)
3
2
1
0
-1
-2
-3
0
50
100
150
200
distance across profile (km)
OBS107
travel time residual
(picked-calculated/uncertainty)
3
2
1
0
-1
-2
-3
0
50
100
150
200
250
distance across profile (km)
OBS108
travel time residual
(picked-calculated/uncertainty)
3
2
1
0
-1
-2
-3
0
50
100
150
distance across profile (km)

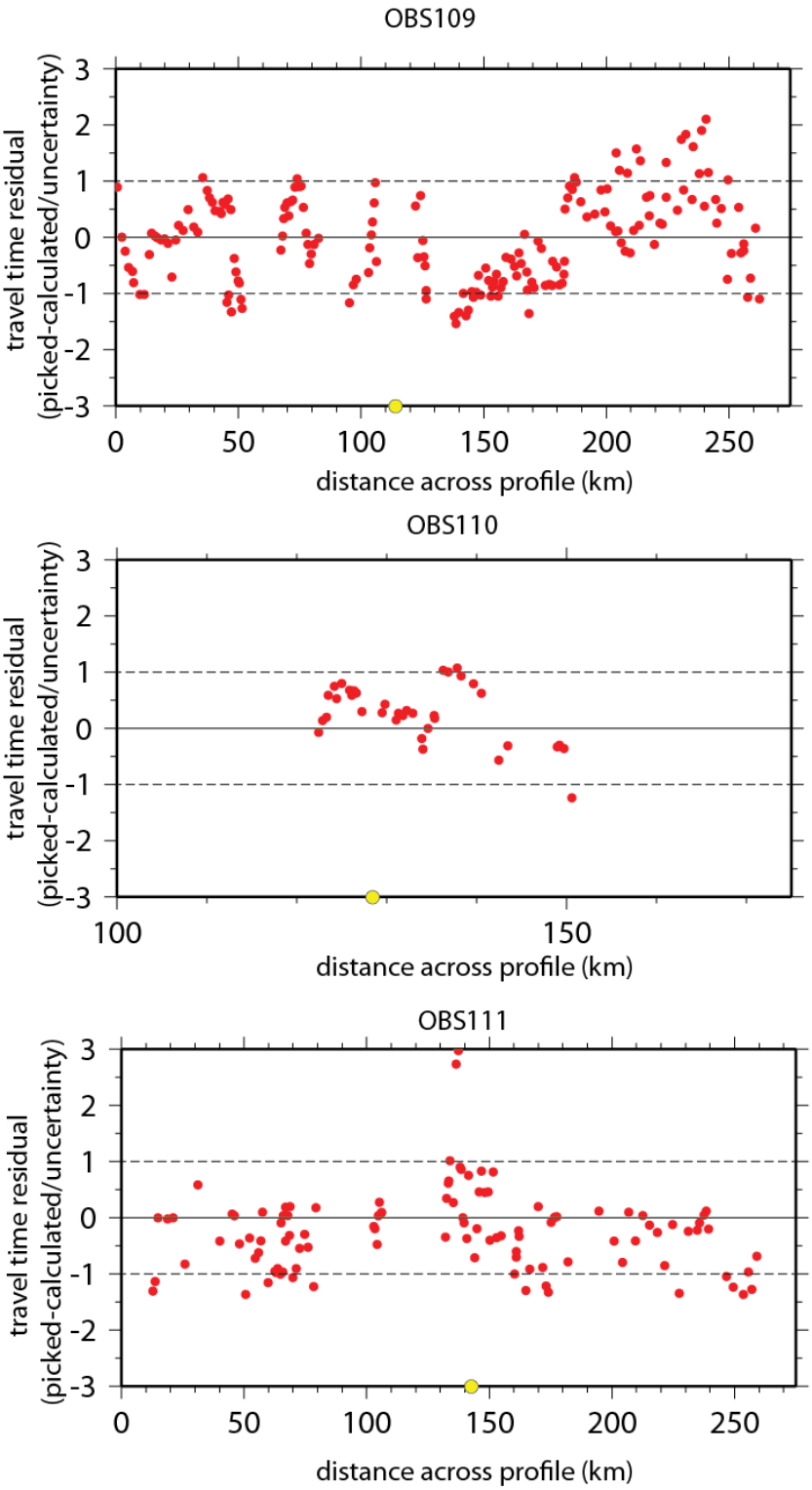
OBS109
travel time residual
(picked-calculated/uncertainty)
3
2
1
0
-1
-2
-3
0
50
100
150
200
250
distance across profile (km)
OBS110
travel time residual
(picked-calculated/uncertainty)
3
2
1
0
-1
-2
-3
100
150
distance across profile (km)
OBS111
travel time residual
(picked-calculated/uncertainty)
3
2
1
0
-1
-2
-3
0
50
100
150
200
250
distance across profile (km)

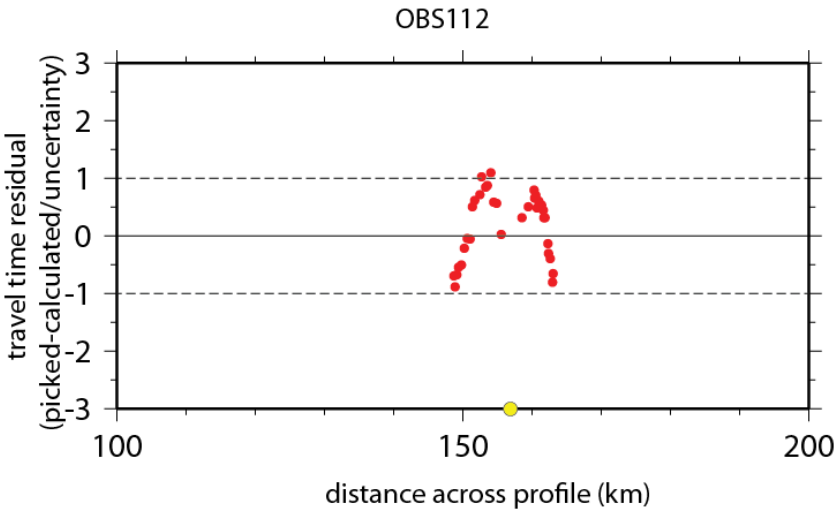
OBS112
travel time residual
(picked-calculated/uncertainty)
3
2
1
0
-1
-2
-3
100
150
200
distance across profile (km)

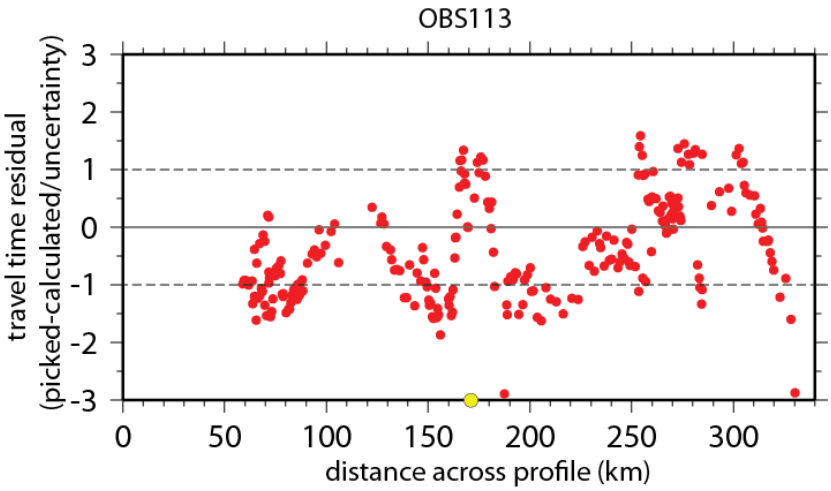
OBS113
travel time residual
(picked-calculated/uncertainty)
3
2
1
0
-1
-2
-3
0
50
100
150
200
250
300
distance across profile (km)

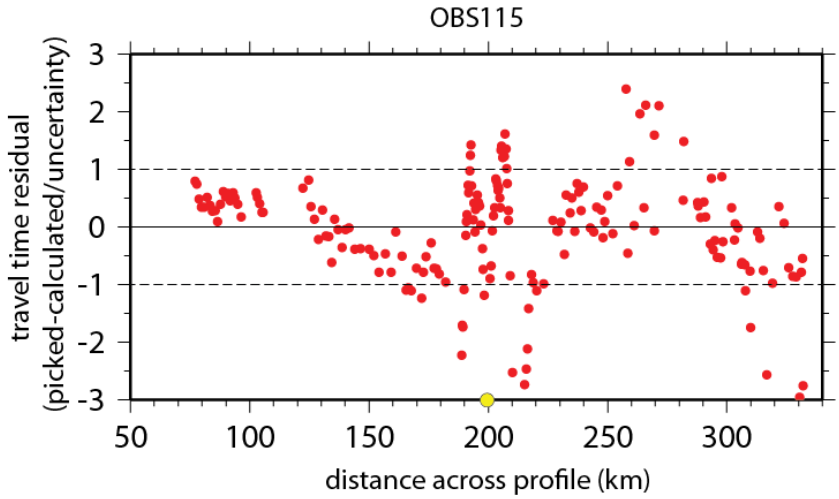
OBS115
travel time residual
(picked-calculated/uncertainty)
3
2
1
0
-1
-2
-3
50
100
150
200
250
300
distance across profile (km)

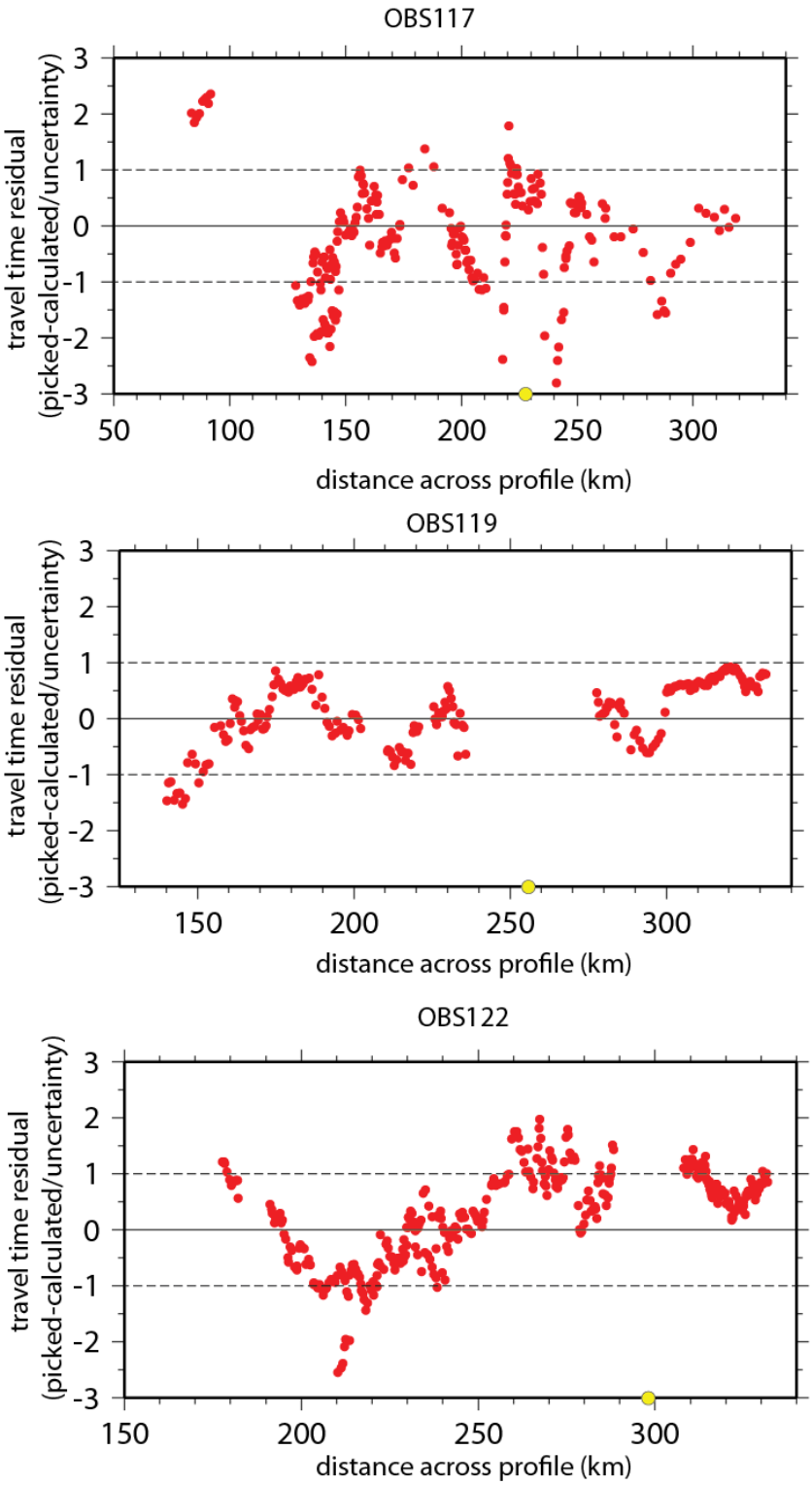
OBS117
travel time residual
(picked-calculated/uncertainty)
3
2
1
0
-1
-2
-3
50
100
150
200
250
300
distance across profile (km)
OBS119
travel time residual
(picked-calculated/uncertainty)
3
2
1
0
-1
-2
-3
150
200
250
300
distance across profile (km)
OBS122
travel time residual
(picked-calculated/uncertainty)
3
2
1
0
-1
-2
-3
150
200
250
300
distance across profile (km)

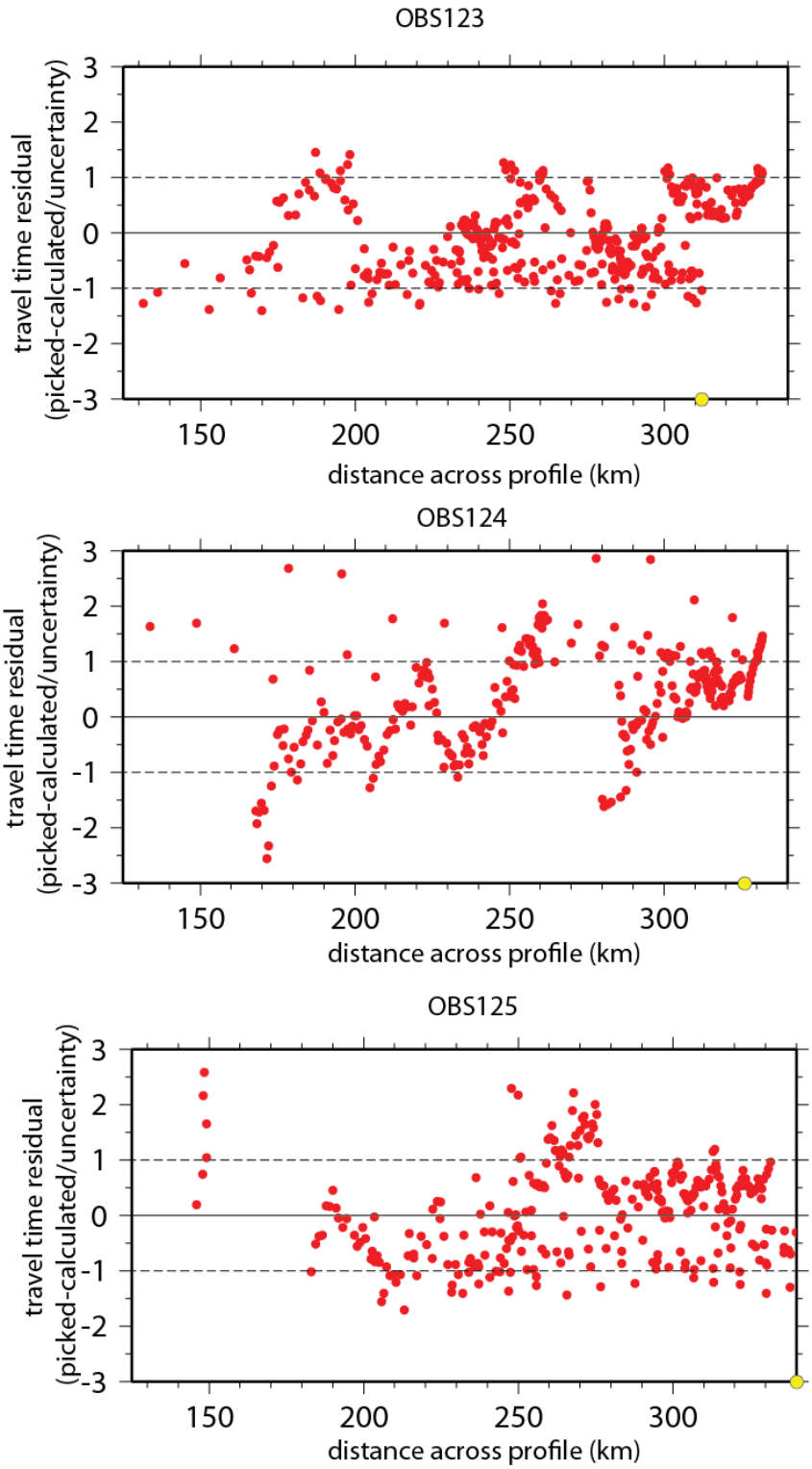
OBS123
travel time residual
(picked-calculated/uncertainty)
3
2
1
0
-1
-2
-3
150
200
250
300
distance across profile (km)
OBS124
travel time residual
(picked-calculated/uncertainty)
3
2
1
0
-1
-2
-3
150
200
250
300
distance across profile (km)
OBS125
travel time residual
(picked-calculated/uncertainty)
3
2
1
0
-1
-2
-3
150
200
250
300
distance across profile (km)

Bibliography

Berger, A. L., Gulick, S. P. S., Spotila, J. A., Upton, P., Jaeger, J. M., Chapman, J. B., Worthington, L. L., Pavlis, T. L., Ridgway, K. D., Willems, B. A., and McAleer, R. J., 2008a, Quaternary tectonic response to intensified glacial erosion in an orogenic wedge: Nature Geosciences, v. 1, no. 10, p. 793-799.

Berger, A. L., and Spotila, J. A., 2008, Denudation and deformation in a glaciated orogenic wedge; the St. Elias Orogen, Alaska, Geology [Boulder]: United States, Geological Society of America (GSA) : Boulder, CO, United States, p. 523-526.

Berger, A. L., Spotila, J. A., Chapman, J. B., Pavlis, T. L., Enkelmann, E., Ruppert, N. A., and Buscher, J. T., 2008b, Architecture, kinematics, and exhumation of a convergent orogenic wedge; a thermochronological investigation of tectonic-climatic interactions within the central St. Elias Orogen, Alaska, Earth and Planetary Science Letters: Netherlands, Elsevier : Amsterdam, Netherlands, p. 13-24.

Bird, P., 1996, Computer simulations of Alaskan neotectonics: Tectonics, v. 15, no. 2, p. 225-236.

Bishop, T. N., Bube, K. P., Cutler, R. T., Langan, R. T., Love, P. L., Resnick, J. R., Shuey, R. T., Spindler, D. A., and Wyld, H. W., 1985, Tomographic determination of velocity and depth in laterally varying media: Geophysics, v. 50, no. 6.

Brocher, T. M., Fuis, G. S., Fisher, M. A., Plafker, G., and Moses, M. J., 1994, Mapping the megathrust beneath the northern Gulf of Alaska using wide-angle seismic data: Journal of Geophysical Research, v. 99, no. B6, p. 11663-11685.

Bruhn, R. L., McCalpin, J., Pavlis, T. L., Gutierrez, F., Guerrero, J., Lucha, P., and Vorkink, M., 2006, Active Tectonics of western St. Elias Orogen, Alaska: Integration of LIDAR and Field Geology: Eos Trans. AGU, v. 87, no. 52, p. Abstract G53C-0922.

Bruhn, R. L., Pavlis, T. L., Plafker, G., and Serpa, L., 2004, Deformation during terrane accretion in the St. Elias orogen, Alaska: Geological Society of America Bulletin, v. 116, no. 7-8, p. 771-787.

Bruns, T. R., 1983a, Model for the origin of the Yakutat block, an accreting terrane in the northern Gulf of Alaska: Geology, v. 11, p. 718-721.

-, 1983b, Structure and petroleum potential of the Yakutat segment of the northern Gulf of Alaska continental margin, AK: Department of the Interior
United States Geological Survey, scale 1:500000.

-, 1985, Tectonics of the Yakutat block, an allochthonous terrane in the northern Gulf of Alaska: Department of Interior
United States Geological Survey, 85-13.

Bruns, T. R., and Schwab, W. C., 1983, Structure maps and seismic stratigraphy of the Yakataga segment of the continenetal margin, northern Gulf of Alaska: United States Geological Survey, MF-1424.

Carlson, P. R., 1989, Seismic reflection characteristics of glacial and glacimarine sediment in the Gulf of Alaska and adjacent fjords: Marine Geology, v. 85, p. 391-416.

Chapman, J. B., Pavlis, T. L., Gulick, S. P. S., Lowe, L. A., Picornell, C., Bruhn, R. L., Vorkink, M., Spotila, J. A., Berger, A. L., Ridgway, K. D., Jaeger, J. M., Koons, P., Hallet, B., and McCalpin, J., 2008, Neotectonics of the Yakutat collision: Changes in deformation driven by mass redistribution, *in* Freymueller, J. T., Haeussler, P. J., Wesson, R. L., and Ekstrom, G., eds., Active Tectonics and Seismic Potential of Alaska: Geophysical Monograph Series: Washington, D.C, American Geophysical Union, p. 65-81.

Charvis, P., Recq, M., Operto, S., and Brefort, D., 1995, Deep structure of the northern Kerguelen Plateau and hotspot-related activity: Geophysical Journal International, v. 122, no. 3, p. 899-924.

Christensen, N. I., and Mooney, W. D., 1995, Seismic velocity structure and composition of the continental crust: A global view: J. Geophys. Res., v. 100, no. B6, p. 9761-9788.

Christeson, G. L., Gulick, S. S., Van Avendonk, H. J. A., Worthington, L. L., Reece, R. S., and Pavlis, T. L., 2010, The Yakutat Terrane: Dramatic change in crustal thickness across the Transition fault, Alaska: Geology, v. in press.

Cloos, M., 1993, Lithospheric buoyancy and collisional orogenesis: Subduction of oceanic plateaus, continental margins, island arcs, spreading ridges, and seamounts: GSA Bulletin, v. 105, p. 715-737.

Coney, P. J., Jones, D. L., and Monger, J. W. H., 1980, Cordilleran suspect terranes: Nature, v. 288, no. 5789, p. 329-333.

Davis, D., Suppe, J., and Dahlen, F. A., 1983, Mechanics of fold-and-thrust belts and accretionary wedges, Journal of Geophysical Research: United States, American Geophysical Union : Washington, DC, United States, p. 1153-1172.

Dickinson, W. R., 2004, Evolution of the North American Cordillera: Annual Review of Earth and Planetary Science, v. 32.

Doser, D. I., Pelton, J. R., and Veilleux, A., M., 1997, Earthquakes in the Pamplona zone, Yakutat block, south central Alaska: Journal of Geophysical Research, v. 102, no. B11, p. 24499-24511.

Doser, D. I., Wiest, K. R., and Sauber, J., 2007, Seismicity of the Bering Glacier region and its relation to tectonic and glacial processes: Tectonophysics.

Eberhart-Phillips, D., Christensen, D. H., Brocher, T. M., Hansen, R., Ruppert, N. A., Haeussler, P. J., and Abers, G. A., 2006, Imaging the transition from Aleutian Subduction to Yakutat collision in central Alaska, with local earthquakes and active source data: Journal of Geophysical Research, v. 111, no. B11303, p. 1-31.

Elliott, J. L., Larsen, C. F., Freymueller, J. T., and Motyka, R. J., 2010, Tectonic block motion and glacial isostatic adjustment in southeast Alaska and adjacent Canada constrained by GPS measurements: Journal of Geophysical Research, v. 115.

Enkelmann, E., 2008, Rapid exhumation of ice-covered rocks of the Chugach-St. Elias Orogen, southeast Alaska, *in* Garver, J. I., and Pavlis, T. L., eds., Geology

[Boulder]: United States, Geological Society of America (GSA) : Boulder, CO, United States, p. 915-918.

Enkelmann, E., Zeitler, P. K., Garver, J. I., Pavlis, T. L., and Hooks, B. P., 2010, The Thermochonological record of tectonic and surface process interaction at the Yakutat-North American collision zone in southeast Alaska: American Journal of Science, v. 310.

Enkelmann, E., Zeitler, P. K., Pavlis, T. L., Garver, J., and Ridgway, K. D., 2009, Intense localized rock uplift and erosion in the St. Elias orogen of Alaska: Nature Geosciences, v. 2.

Ferris, A., Abers, G. A., Christensen, D. H., and Veenstra, E., 2003, High resolution image of the subducted Pacific (?) plate beneath central Alaska, 50-150km depth: Earth and Planetary Science Letters, v. 214, p. 575-588.

Fisher, M. A., Freymueller, J. T., Ruppert, N. A., Parsons, T., Eberhart-Phillips, D., Sliter, R. W., and Wong, F. L., 2006, The South Boundary of the Subducted Yakutat Terrane Seems to Affect the Distribution of Forearc Subsidence Since the 1964 Great Alaska Earthquake (Mw=9.2), *in* American Geophysical Union Fall Meeting, San Francisco.

Fletcher, H. J., and Freymueller, J. T., 1999, New GPS Constraints on the Motion of the Yakutat Block: Geophysical Research Letters, v. 26, no. 19, p. 3029-3032.

-, 2003, New constraints on the motion of the Fairweather fault, Alaska, from GPS observations: Geophysical Research Letters, v. 30, no. 3, p. 1139.

Fuis, G. S., Moore, T. E., Plafker, G., Brocher, T. M., Fisher, M. A., Mooney, W. D., Nokleberg, W. J., Page, R. A., Beaudoin, B. C., Christensen, N. I., Levander, A. R., Lutter, W. J., Saltus, R. W., and Ruppert, N. A., 2008, Trans-Alaska Crustal Transect and continental evolution involving subduction underplating and synchronous foreland thrusting, Geology [Boulder]: United States, Geological Society of America (GSA) : Boulder, CO, United States, p. 267.

Gardner, J. V., 2006, Mapping supports potential submission to U.N. Law of the Sea: Eos, v. 87, p. 157-160.

Gardner, J. V., Mayer, L. A., and Armstrong, A., 2006, Mapping supports potential submission to U.N. Law of the Sea: Eos Transactions AGU, v. 87, no. 16, p. 157.

Gerdom, M., Trehu, A. M., Flueh, E. R., and Klaeschen, D., 2000, The continental margin off Oregon from seismic investigations: Tectonophysics, v. 329, no. 1-4, p. 79-97.

Gulick, S. P. S., Bangs, N. L. B., Shipley, T. H., Nakamura, Y., Moore, G., and Kuramoto, S., 2004a, Three-dimensional architecture of the Nankai accretionary prism's imbricate thrust zone off Cape Muroto, Japan: Prism reconstruction via en echelon thrust propagation: Journal of Geophysical Research, v. 109, no. B02105.

Gulick, S. P. S., Lowe, L. A., Pavlis, T. L., Gardner, J. V., and Mayer, L. A., 2007, Geophysical insights into the Transition Fault debate: Propagating strike-slip in response to stalling subduction in the Gulf of Alaska: Geology, v. 35, no. 8, p. 763-766.

Gulick, S. P. S., Meltzer, A. S., and Clarke, S. H., Jr., 1998, Seismic structure of the southern Cascadia subduction zone and accretionary prism north of the Mendocino triple junction, Journal of Geophysical Research: United States, American Geophysical Union : Washington, DC, United States, p. 27.

Gulick, S. P. S., Willems, B., Powell, R. D., Jaeger, J., and Cowan, E. A., 2004b, High-resolution seismic images of southeast Alaskan glacial fjords and continental shelf: Is the present the key to the past?: Eos Trans. AGU, Abstract H51G-0444, v. 86, no. 52.

Gutscher, M.-A., Spakman, W., Bijwaard, H., and Engdahl, E. R., 2000, Geodynamics of flat subduction: Seismicity and tomographic constraints from the Andean margin: Tectonics, v. 19, no. 5, p. 814-833.

Hilley, G., Strecker, M. R., and Ramos, V. A., 2004, Growth and erosion of fold-and-thrust belts with an application to the Aconcagua fold-and-thrust belt, Argentina: Journal of Geophysical Research, v. 109.

Hole, J. A., 1992, Nonlinear High-Resolution Three-Dimensional Seismic Travel Time Tomography: J. Geophys. Res., v. 97, no. B5, p. 6553-6562.

Jaeger, J., Nittrouer, C. A., Scott, N. D., and Milliman, J. D., 1998, Sediment accumulation along a glacially impacted mountainous coastline: North-east Gulf of Alaska: Basin Research, v. 10, p. 155-173.

Jaeger, J. M., and Nittrouer, C. A., 1999, Sediment deposition in an Alaskan fjord; controls on the formation and preservation of sedimentary structures in Icy Bay, Journal of Sedimentary Research: United States, Society of Economic Paleontologists and Mineralogists : Tulsa, OK, United States, p. 1011-1026.

Koons, P. O., Hooks, B. P., Pavlis, T., Upton, P., and Barker, A. D., 2010, Three-dimensional mechanics of Yakutat convergence in the southern Alaskan plate corner: Tectonics, v. 29, no. 4, p. TC4008.

Kopp, C., Fruehn, J., Flueh, E. R., Reichert, C., Kukowski, N., Bialas, J., and Klaeschen, D., 2000, Structure of the Makran subduction zone from wide-angle and reflection seismic data: Tectonophysics, v. 329, no. 1-4, p. 171-191.

Krissek, L. A., 1995, Late Cenozoic ice-rafting records from Leg 145 sites in the North Pacific: late Miocene onset, late Pliocene intensification, and Pliocene-Pleistocene events.

Lagoe, M. B., Eyles, C. H., Eyles, N., and Hale, C., 1993, Timing of Late Cenozoic Tidewater Glaciation in the Far North Pacific: Geological Society of America Bulletin, v. 105, no. 12, p. 1542-1560.

Lagoe, M. B., and Zellers, S. D., 1996, Depositional and microfaunal response to Pliocene climate change and tectonics in the eastern Gulf of Alaska: Marine Micropaleontology, v. 27, no. 1-4, p. 121-140.

Lahr, J. C., and Plafker, G., 1980, Holocene Pacific-North American plate interaction in southern Alaska: Implications for the Yakataga seismic gap: Geology, v. 8, p. 483-486.

Livaccari, R. F., Burke, K., and Sengor, A. M. C., 1981, Was the Laramide orogeny related to subduction of an oceanic plateau?: Nature, v. 289, no. 5795, p. 276-278.

Mackey, K. G., Fujita, K., Gunbina, L. V., Kovalev, V. N., Imaev, V. S., Koz'min, B. M., and Imaeva, L. P., 1997, Seismicity of the Bering Strait region: Evidence for a Bering block: Geology, v. 25, no. 11, p. 979-982.

Malavieille, J., 2010, Impact of erosion, sedimentation, and structural heritage on the structure and kinematics of orogenic wedges: Analog models and case studies: GSA Today, v. 20, no. 1, p. 4-10.

Mann, D. H., and Peteet, D. M., 1994, Extent and Timing of the Last Glacial Maximum in Southwestern Alaska: Quaternary Research, v. 42, p. 136-148.

Mazzotti, S., and Hyndman, R. D., 2002, Yakutat collision and strain transfer across the northern Canadian Cordillera: Geology, v. 30, no. 6, p. 495-498.

Mazzotti, S., Leonard, L. J., Hyndman, R. D., and Cassidy, J. F., 2008, Tectonics, Dynamics and Seismic Hazard in the Canada-Alaska Cordillera, *in* Freymueller, J. T., Haeussler, P. J., Wesson, R. L., and Ekstrom, G., eds., Active Tectonics and Seismic Potential of Alaska: Geophysical Monograph Series: Washingtion, DC, American Geophysical Union.

Meigs, A., Johnston, S., Garver, J., and Spotila, J., 2008, Crustal scale structural architecture, shortening, and exhumation of an active, eroding orogenic wedge (Chugach-St Elias Range, Southern Alaska), Tectonics: United States, American Geophysical Union : Washington, DC, United States.

Meigs, A. J., and Sauber, J., 2000, Southern Alaska as an example of the long-term consequences of mountain building under the influence of glaciers: Quaternary Science Reviews, v. 19, p. 1543-1562.

Menke, W., 1984, Geophysical data analysis: Discrete inverse theory: San Diego, Academic Press, 289 p.

Miura, S., Suyehiro, K., Shinohara, M., Takahashi, N., Araki, E., and Taira, A., 2004, Seismological structure and implications of collision between the Ontong Java Plateau and Solomon Island Arc from ocean bottom seismometer-airgun data: Tectonophysics, v. 389, no. 3-4, p. 191-220.

Mooney, W. D., and Luetgert, J. H., 1982, A seismic refraction study of the Santa Clara Valley and southern Santa Cruz Mountains, west-centrat California: Bulletin of the Seismological Society of America, v. 92.

Moser, T. J., 1991, Shortest path calculation of seismic rays: Geophysics, v. 59, no. 56.

Moser, T. J., Nolet, G., and Snieder, R., 1992, Ray bending revisited: Bulletin of the seismological Society of America, v. 82, no. 1, p. 259-288.

Nakanishi, I., and Yamaguchi, K., 1986a, A numerical experiment on nonlinear image reconstruction from first-arrival times for two-dimensional island arc structure: Journal of Physics of the Earth, v. 34, p. 195-201.

-, 1986b, A numerical experiment on nonlinear image reconstruction from first-arrival times for two-dimensional island structure: Journal of Physics of the Earth, v. 34.

Nolet, G., 1993, Solving large linearised tomographic problems, *in* Iyer, J. M., and Hirahara, K., eds., Seismic Tomography: Theory and Practice: London, Chapman & Hall, p. 227-247.

Operto, S., and Charvis, P., 1996, Deep structure of the southern Kerguelen Plateau (southern Indian Ocean) from ocean bottom seismometer wide-angle seismic data: J. Geophys. Res., v. 101, no. B11, p. 25077-25103.

Paige, C. C., and Saunders, M. A., 1982, LSQR: Sparse linear equations and least squares problems: Assoc. Comput. Mach. Trans. Math. Software, v. 8, p. 195-209.

Pavlis, T. L., Hamburger, M. W., and Pavlis, G. L., 1997, Erosional processes as a control on the structural evolution of an actively deforming fold and thrust belt: An example from the Pamir-Tien Shan region, central Asia: Tectonics, v. 16, p. 810-822.

Pavlis, T. L., Picornell, C., Serpa, L., Bruhn, R. L., and Plafker, G., 2004, Tectonic processes during oblique collision: Insights from the St. Elias orogen, northern North American Cordillera: Tectonics, v. 23, no. TC3001.

Pegler, G., and Das, S., 1996, The 1987-1992 Gulf of Alaska earthquakes: Tectonophysics, v. 257, p. 111-136.

Picornell, C., 2001, Detachment folds in the Gulf of Alaska fold and thrust belt: New implications for the tectonic framework of the eastern Aleutian Arc: University of New Orleans, 117 p.

Plafker, G., 1974, Preliminary geologic map of Kayak and Wingham Islands, Alaska: U.S. Geological Survey, scale 1:31,860.

-, 1987, Regional geology and petroleum potential of the northern Gulf of Alaska continental margin, *in* Scholl, D. W., ed., Geology and Resource Potential of the Continental Margin of Western North America and Adjacent Ocean Basins: Circum-Pacific Council for Energy and Mineral Resources: Houston, p. 229-268.

Plafker, G., Moore, J. C., and Winkler, G. R., 1994, Geology of the southern Alaska margin, The Geology of Alaska: Denver, The Geological Society of America, p. 389-449.

Preece, S. J., and Hart, W. K., 2004, Geochemical variations in the <5 Ma Wrangell Volcanic Field, Alaska: implications for the magmatic and tectonic development of a complex continental arc system: Tectonophysics, v. 392, no. 1-4, p. 165-191.

Press, W. H., Teukolsky, S. A., Vetterling, W. T., and Flannery, B. P., 1986, Numerical Recipes in Fortran: The art of scientific computing: Cambridge, Cambridge University Press, 818 p.

Prueher, L. M., 1998, Rapid onset of glacial conditions in the subarctic North Pacific region at 2.67 Ma; clues to causality, *in* Rea, D. K., ed., Geology [Boulder]: United States, Geological Society of America (GSA) : Boulder, CO, United States, p. 1027-1030.

Prueher, L. M., and Rea, D. K., 1998, Rapid onset of glacial conditions in the subarctic North Pacific region at 2.67 Ma: Clues to causality: Geology, v. 26, no. 11, p. 1027-1030.

Ranero, C. R., von Huene, R., Weinrebe, W., and Barcknausen, U., 2007, Convergent margin tectonics: A marine perspective, *in* Bundschuh, J., and Alvarado, G. E., eds., Central America: Geology, Resources and Hazards: London, Taylor and Francis, p. 239-265.

Ranero, C. R., von Huene, R., Weinrebe, W., and Reichert, C., 2006, Tectonic processes along the Chile convergent margin, *in* Onken, O., ed., The Andes: Active Subduction Orogeny: Berlin, Springer-Verlag, p. 91-122.

Rea, D. K., Basov, I. A., Krissek, L. A., Janecek, T. R., Arnold, E., Barron, J. A., Beaufort, L., Bristow, J. F., deMenocal, P., Dubuisson, G. J., Gladenkov, A. Y., Hamilton, T., Ingram, B. L., Keigwin, L. D., Jr., Keller, R. A., Kotilainen, A. T., McKelvey, B. C., Morley, J. J., Okada, M., Olafsson, G., Owen, R. M., Pak, D. K., Pedersen, T. F., Roberts, J. A., Rutledge, A. K., Shilov, V. V., Snoeckx, H., Stax, R., Tiedemann, R., and Weeks, R. J., 1995, Scientific results of drilling the North Pacific Transect, Proceedings of the Ocean Drilling Program, Scientific Results: United States, Texas A & M University, Ocean Drilling Program : College Station, TX, United States, p. 577-596.

Rea, D. K., and Snoeckx, H., 1995, Sediment fluxes in the Gulf of Alaska: paleoceanographic record from Site 887 on the Patton-Murray Seamount platform, *in* Rea, D. K., Basov, I. A., Scholl, D. W., and Allan, J. F., eds., Proceedings of the Oceanic Drilling Program: Scientific Results Leg 145: College Station, TX, Ocean Drilling Program, p. 247-256.

Redfield, T. F., Scholl, D. W., Fitzgerald, P. G., and Beck, M. E., Jr., 2007, Escape tectonics and the extrusion of Alaska; past, present, and future, Geology [Boulder]: United States, Geological Society of America (GSA) : Boulder, CO, United States, p. 1039-1042.

Reece, R. S., Gulick, S. S., Christeson, G. L., and Worthington, L. L., 2009, Intraplate shearing and basin deformation in the Pacific Plate as a result of the Yakutat Block collision with North America, *in* Union, A. G., ed., Fall Meeting San Francisco.

Risley, D. E., Martin, G. C., Lynch, M. B., Flett, T. O., and Larson, J. A., 1992, Geologic report for the Gulf of Alaska Planning Area.

Roe, G. H., Stolar, D. B., and Willett, S. D., 2006, Response of a steady-state critical wedge orogen to changes in climate and tectonic forcing: Geological Society of America Special Paper, v. 398, p. 228-241.

Shackleton, N. J., Hall, M. A., and Pate, D., 1995, Pliocene stable isotope stratigraphy of Site 846, *in* Pisias, N. G., Janacek, L. A., Palmer-Julson, A., and Van Andel, T. H., eds., Proceedings of the Oceanic Drilling Program, Scientific Results Leg 138: Proceedings of the Oceanic Drilling Program Scientific Results: College Station, TX, p. 337-355.

Sheaf, M. A., Serpa, L., and Pavlis, T. L., 2003, Exhumation rates in the St. Elias Mountains, Alaska: Tectonophysics, v. 367, no. 1-2, p. 1-11.

Shennan, I., 2009, Late Quaternary sea-level changes and palaeoseismology of the Bering Glacier region, Alaska: Quaternary Science Reviews, v. 28, no. 17-18, p. 1762-1773.

Shennan, I., Bruhn, R., and Plafker, G., 2009, Multi-segment earthquakes and tsunami potential of the Aleutian megathrust: Quaternary Science Reviews, v. 28, no. 1-2, p. 7-13.

Simpson, G. D. H., 2010, Formation of accretionary prisms influenced by sediment subduction and supplied by sediments from adjacent continents: Geology, v. 38, no. 2, p. 131-134.

Spotila, J. A., and Berger, A. L., 2010, Exhumation at orogenic indentor corners under long-term glacial conditions: Example of the St. Elias orogen, Southern Alaska: Tectonophysics, v. 490.

Spotila, J. A., Buscher, J. T., Meigs, A. J., and Reiners, P. W., 2004, Long-term glacial erosion of active mountain belts: Example of the Chugach-St. Elias Range, Alaska: Geology, v. 32, no. 6, p. 501-504.

Spotila, J. A., and Meigs, A. J., 2004, Testing glacial limits to mountain building; the buzz saw in the Chugach/St. Elias Range, Alaska, Eos, Transactions, American Geophysical Union: United States, American Geophysical Union : Washington, DC, United States, p. t33d.

Stevenson, A. J., and Embly, R., 1987, Deep-sea fan bodes, terrigenous turbidite sedimentation, and petroleum geology, Circum-Pacific Council of Energy and Mineral Resources: Earth Science Series, p. 502-522.

Suppe, J., 1997, Bed-by-bed fold growth by kink-band migration; Sant Llorenc de Morunys, eastern Pyrenees, *in* Sabat, F., Munoz, J. A., Poblet, J., Roca, E., and Verges, J., eds., Journal of Structural Geology: International, Pergamon : Oxford-New York, International, p. 443-461.

Suppe, J., Chou, G. T., and Hook, S. C., 1992, Rates of folding and faulting determined from growth strata: United Kingdom, Chapman & Hall : London, United Kingdom, 105-121 p.

Tomkin, J. H., and Roe, G. H., 2007, Climate and tectonic controls on glaciated critical-taper orogens: Earth and Planetary Science Letters, v. 262, no. 3-4, p. 385-397.

Toomey, D. R., and Foulger, G. R., 1989, Tomographic inversion of local earthquake data from the Hengill-Grensdalur central volcano complex, Iceland: Journal of Geophysical Research, v. 94, no. 12, p. 497-517.

Trop, J. M., and Ridgway, K. D., 2007, Mesozoic and Cenozoic tectonic growth of southern Alaska: A sedimentary basin perspective, *in* Ridgway, K. D., Trop, J. M., Glen, J. M. G., and O'Neill, J. M., eds., Tectonic Growth of a Collisional Continental Margin: Crustal Evolution of Southern Alaska: GSA Special Paper: Boulder, Geological Society of America, p. 55-94.

van Avendonk, H. J. A., Harding, A. J., Orcutt, J. A., and Holbrook, W. S., 2001, Hybrid shortest path and ray bending method for traveltime and raypath calculations: Geophysics, v. 66, no. 2, p. 648-653.

Van Avendonk, H. J. A., Shillington, D. J., Holbrook, W. S., and Hornbach, M. J., 2004a, Inferring crustal structure in the Aleutian arc from a sparse wide-angle seismic data set: G3, v. 5, no. 8, p. Q08008.

van Avendonk, H. J. A., Shillington, D. J., Holbrook, W. S., and Hornbach, M. J., 2004b, Inferring crustal structure in the Aleutian island arc from a sparse wide-angle seismic data set, Geochemistry, Geophysics, Geosystems - G [super 3]: United

States, American Geophysical Union and The Geochemical Society, United States.
van Hunen, J., 2002, On the role of subducting oceanic plateaus in the development of shallow flat subduction, *in* van den Berg, A. P., and Vlaar, N. J., eds., Tectonophysics: Netherlands, Elsevier : Amsterdam, Netherlands, p. 317-333.
von Huene, R., 1999, Relation between the subducting plate and seismicity associated with the great 1964 Alaska earthquake, *in* Klaeschen, D., and Fruehn, J., eds., Pure and Applied Geophysics: Switzerland, Birkhaeuser Verlag : Basel, Switzerland, p. 575-591.
von Huene, R., and Ranero, C. R., 2009, Neogene collision and deformation of convergent margins along the backbone of the Americas: The Geological Society of America Memoir 204.
Wallace, W. K., 2008, Yakataga Fold-and-Thrust Belt: Structural Geometry and Tectonic Implications of a Small Continental Collision Zone, *in* Freymueller, J. T., Haeussler, P. J., Wesson, R. L., and Ekstrom, G., eds., Active Tectonics and Seismic Potential of Alaska: Geophysical Monograph Series: Washingtion, DC, American Geophysical Union, p. 237-256.
Walther, C., 2003, The crustal structure of the Cocos ridge off Costa Rica: Journal of Geophysical Research, v. 108, no. B3.
Westbrook, G. K., Ladd, J. W., Buhl, P., Bangs, N., and Tiley, G. J., 1988, Cross section of an accretionary wedge; Barbados Ridge Complex, Geology [Boulder]: United States, Geological Society of America (GSA) : Boulder, CO, United States, p. 631-635.
Whipple, K. X., 2009, The influence of climate on the tectonic evolution of mountain belts, Nature Geoscience: United Kingdom, Nature Publishing Group : London, United Kingdom, p. 97-104.
Whipple, K. X., and Meade, B. J., 2004, Controls on the strength of coupling among climate, erosion, and deformation in two-sided, frictional orogenic wedges at steady state, Journal of Geophysical Research: United States, American Geophysical Union : Washington, DC, United States.
-, 2006, Orogen response to changes in climatic and tectonic forcing: Earth and Planetary Science Letters, v. 243, p. 218-228.
White, J. M., Ager, T. A., Adam, D. P., Leopold, E. B., Liu, G., Jette, H., and Schwegger, C. E., 1997, An 18 million year record of vegetation and climate change in northwestern Canada and Alaska: tectonic and global climatic correlates: Palaeogeography, Palaeoclimatology, Palaeoecology, v. 130, p. 293-306.
White, R. S., McKenzie, D., and O'Nions, R. K., 1992, Oceanic crustal thickness from seismic measurements and rare earth element inversions: J. Geophys. Res., v. 97, no. B13, p. 19683-19715.
Willett, S. D., 1999, Orogeny and orography: The effects of erosion on the structure of moutnain belts: Journal of Geophysical Research, v. 104, p. 28957-28981.

-, 2002, On steady states in mountain belts, *in* Brandon, M. T., ed., Geology [Boulder]: United States, Geological Society of America (GSA) : Boulder, CO, United States, p. 175-178.

Worthington, L. L., Gulick, S. P. S., and Pavlis, T. L., 2008, Identifying active structures in the Kayak Island and Pamplona zones; implications for offshore tectonics of the Yakutat Microplate, Gulf of Alaska, Geophysical Monograph: United States, American Geophysical Union : Washington, DC, United States, p. 257-268.

Worthington, L. L., Gulick, S. S., and Pavlis, T. L., in press, Coupled Stratigraphic and Structural Evolution of a Glaciated Orogenic Wedge, offshore St. Elias Orogen, Alaska: Tectonics.

Yilmaz, O., 2001, Seismic Data Analysis: Processing, Inversion, and Interpretation of Seismic Data, Investigations in Geophysics: Tulsa, OK, Socity of Exploration Geophysicists.

Zapata, T. R., and Allmendinger, R. W., 1996, Growth stratal records of instantaneous and progressive limb rotation in the Precordillera thrust belt and Bermejo Basin, Argentina, Tectonics: United States, American Geophysical Union : Washington, DC, United States, p. 1065-1083.

Zellers, S. D., 1995, Foraminiferal sequence biostratigraphy and seismic stratigraphy of a tectonically active margin; the Yakataga Formation, northeastern Gulf of Alaska: Marine Micropaleontology, v. 26, p. 255-271.

Zelt, C. A., Sain, K., Naumenko, J. V., and Sawyer, D. S., 2003, Assessment of crustal velocity models using seismic refraction and reflection tomography: Geophysical Journal International, v. 153.

Zelt, C. A., and White, D. J., 1995, Crustal structure and tectonics of the southeastern Canadian Cordillera: J. Geophys. Res., v. 100, no. B12, p. 24255-24273.

Vita

Lindsay Lowe Worthington was born in Denver, Colorado on January 1, 1981, to Nancy Lindsey and Ron Lowe. She spent her childhood in Denver and graduated from Cherry Creek High School in 1999. After high school, Lindsay moved to Berkeley, California to begin her undergraduate studies at the University of California at Berkeley. During her undergraduate career, Lindsay was involved with the ultimate Frisbee and ski-racing teams. She also spent the fall semester of 2001 in Ghana volunteering teaching math and physics at a technical school in the capital city of Accra. Lindsay graduated in 2004 with a major in Earth and Planetary Science, concentration in Geophysics. After graduation, Lindsay worked at the Lawrence Livermore National Laboratory in the seismology group.

Lindsay began graduate studies at the University of Texas in the Jackson School of Geosciences in the fall of 2005. Lindsay has participated in multiple field studies during the last 5 years. She conducted work in the southern coastal mountains of Alaska in the summer of 2006 and participated in a marine seismic acquisition cruise in the fall of 2008. She also participated in a marine field class in the Gulf of Mexico in the summer of 2008 and follow-up field work there in the fall of 2008. Her dissertation work using seismic data from the Gulf of Alaska has appeared or will appear in the journal Tectonics and the Journal of Geophysical Research. She has presented her work at multiple conferences including the annual American Geophysical Union Fall Meeting and the Geological Society of America National Meeting. Lindsay has also worked as a teaching assistant during her graduate career and earned the JSG Outstanding Teaching Assistant Award for the 2007-2008 academic year. In June 2008, she married Travis Worthington in Denver, Colorado.